technische universität
dortmund

Max-Planck-Institut
für molekulare Physiologie

mpi

Deciphering the structural effect of nucleotide hydrolysis and small molecule binding on actin and myosin

Dissertation

zur Erlangung des akademischen Grades
eines Doktors der Naturwissenschaften
der Fakultät für Physik
der Technischen Universität Dortmund

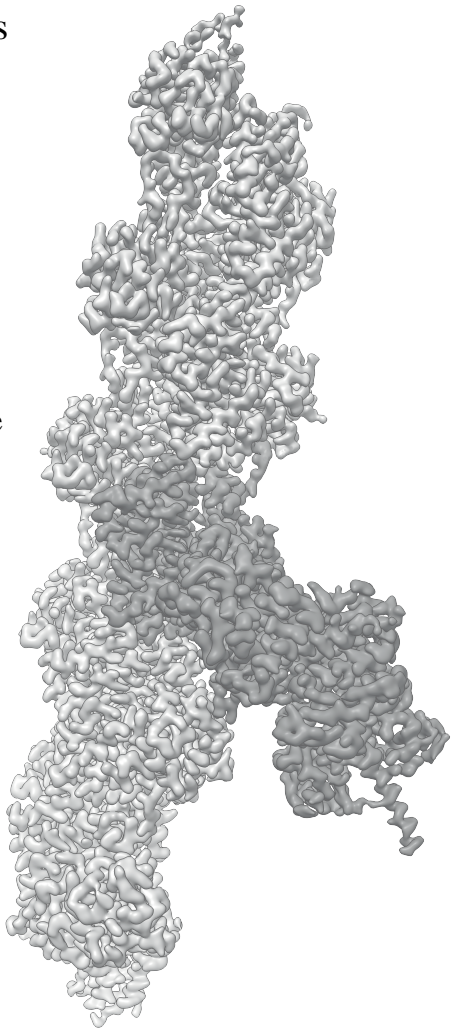

Angefertigt in der
Abteilung für Strukturbiochemie am
Max-Planck-Institut für molekulare Physiologie

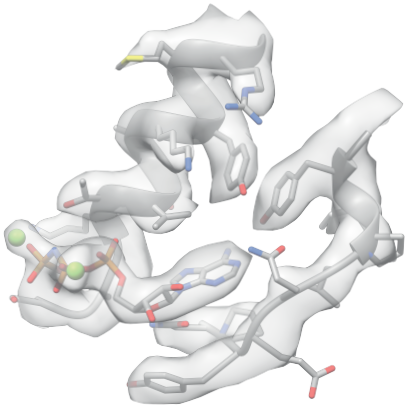

vorgelegt von

Sabrina Pospich

Februar 2021

Erstgutachter : **Prof. Dr. Metin Tolan**

Lehrstuhl für Experimentelle Physik I
Fakultät Physik
Technische Universität Dortmund

Zweitgutachter : **Prof. Dr. Stefan Raunser**

Abteilung für Strukturbiochemie
Max-Planck-Institut für molekulare Physiologie

Fakultät für Chemie und Chemische Biologie
Technische Universität Dortmund

Die vorliegende Arbeit wurde in der Abteilung für Strukturbiochemie am Max-Planck-Institut für molekulare Physiologie im Zeitraum November 2015 bis Februar 2021 erstellt.

Datum des Einreichens der Arbeit: 28. Februar 2021

Contents

d

List of Abbreviations

2D	Two-dimensional
3D	Three-dimensional
ABP	Actin binding protein
ACN	Acetonitrile, an organic solvent
ADF	Actin depolymerizing factor
ADP	Adenosine diphosphat
ADP-Be$_x$	Adenosine diphosphat-beryllium fluoride
ALP	Actin-like protein
AMP-PNP	Synonym of AppNHp
AppNHp	Adenosine-5'-[(β,γ)-imido]triphosphate, a non-hydrolyzable ATP analog
ATP	Adenosine triphosphat
ATPase	Enzyme hydrolyzing ATP to ADP and a phosphate ion
CCD	Charged coupled device
CM	Cardiomyopathy
Cryo-EM	Electron cryo microscopy
Cryo-ET	Electron cryo tomography
CTF	Contrast transfer function
DED	Direct electron detector
DDD	Direct detection device, synonym of DED
DMSO	Dimethyl sulfoxide, an organic solvent
DTT	Dithiothreitol, a reducing agent
DQE	Detector quantum efficiency
EGTA	Egtazic acid, a chelating agent
ELC	Essential light chain
EM	Electron microscopy
EMDB	Electron microscopy data bank
F-actin	Filamentous actin

FEG	Field emission gun
FIB	Focused ion beam
FSC	Fourier shell correlation
G-actin	Globular, monomeric actin
GTP	Guanine triphosphate
HEPES	4-(2-hydroxyethyl)-1-piperazineethanesulfonic acid, a buffer agent
HLH	Helix-loop-helix
IHRSR	Iterative helical real space reconstruction
IRPLC	Ion-pair reversed-phase liquid chromatography
ISAC	Iterative stable alignment and clustering
JASP	Jasplakinolide, a natural drug-like toxin
JASP-cLys	Jasplakinolide-cLys, a JASP derivative with improved solubility
LC	Light chain
LED	Light-emitting diode
MD	Molecular dynamics
MDFF	Molecular dynamics flexible fitting
MPI	Max Planck Institute
MiuA	Miuraenamide A
NCS	Non-crystallographic symmetry
NMR	Nuclear magnetic resonance
NTP	Nucleoside triphospate
OJ8	Optojasp-8, a photo-switchable JASP derivative
OM	Omecamtiv mecarbil, a myosin activator
PC	Principal component
PCA	Principal component analysis
PDB	Protein data bank
PfActin	Actin 1 of *Plasmodium falciparum*
PHD	Phalloidin, a natural drug-like toxin
Pi	Inorganic phosphate

PiR	Phosphate release
PPS	Pre-powerstroke
PRT	Post-rigor transition
RLC	Regulatory light chain
RMSD	Root mean square deviation
RT	Room temperature
SD	Subdomain
SDS	Sodium dodecyl sulfate, a strong detergent
SDS-PAGE	Sodium dodecyl sulfate polyacrylamide gel electrophoresis
SMILES	Simplified molecular input line entry specification
SNR	Signal-to-noise ratio
SPA	Single particle analysis
TCEP	Tris(2-carboxyethyl)phosphine, a reducing agent
TEM	Transmission electron microscopy/ microscope
TIRF	Total internal reflection fluorescence
Tris	Trishydroxymethylaminomethane, a buffer agent
Tween 20	Polysorbate 20, a non-ionic detergent
UV	Ultraviolet
VPP	Volta phase plate

h

List of Figures

List of Tables

List of Supplementary Figures

1 Abstract and Zusammenfassung

Abstract

The proteins actin and myosin are key role players of eukaryotic life. The µm-long dynamic filaments formed by actin are a major component of the cytoskeleton. They furthermore serve as tracks for the molecular motor myosin, which powers many essential processes, such as cargo transport and muscle contraction. According to their biological relevance, malfunctions of either actin or myosin are usually linked to serious medical issues. The function of both proteins is tightly coupled to ATP hydrolysis as well as to their structure. Resolving this structure is hence key to decipher the molecular details of actin and myosin. While the overall structure of both proteins has already been resolved previously, the structural effect of ATP hydrolysis and the subsequent release of inorganic phosphate has remained elusive. Similarly, it is poorly understood how sequence variations or binding of small molecules affect the stability of actin filaments.

In my doctoral thesis I have used transmission electron cryo microscopy (cryo-EM) to solve a total of 19 high-resolution structures of filamentous actin (F-actin) as well as myosin bound to F-actin (actomyosin). First of all, I present structures of different nucleotide states, which elucidate the structural transitions of actin and myosin along their ATPase cycle. The data suggest that the ATPase cycle of myosin is not exclusively driven by mechanical coupling, but strongly relies on structural flexibility. They furthermore illustrate the conformational changes associated with ADP release and binding of ATP. The structural changes within F-actin are generally smaller than the ones in myosin, and localize primarily to the D-loop C-terminus interface at the surface of the filament. In this way, the nucleotide state is likely communicated to interaction partners, thereby facilitating the directed remodeling of the cytoskeleton. This thesis also reveals how small sequence variations cause filament instability in actin 1 of the malaria parasite *Plasmodium falciparum*. Finally, it deciphers the structural basis by which the natural toxins jasplakinolide and phalloidin stabilize F-actin, and describes their effect on the structural transition of actin. While these small molecules already represent powerful tools for basic research, the structures of a photoswitchable jasplakinolide presented in this thesis will likely promote the structure-based design of novel functionalized derivatives with even greater potential.

Collectively, the structures solved in this thesis have brought valuable insights into the structural transition of actin and myosin and thereby will eventually lead to a better understanding of all actin- and myosin-based processes.

Zusammenfassung

Die Proteine Aktin und Myosin sind Schlüsselakteure des eukaryotischen Lebens. Während Aktin µm-lange, dynamische Filamente formt, die eine Hauptkomponente des Zytoskeletts sind, läuft der molekulare Motor Myosin entlang dieser Filamente und treibt so eine Vielzahl essentieller Prozesse, wie beispielsweise den intrazellulären Transport und die Muskelkontraktion, an. Entsprechend ihrer biologischen Relevanz sind Fehlfunktionen von Aktin und Myosin meist mit schwerwiegenden medizinischen Problemen verbunden. Die Funktion beider Proteine ist eng mit der Hydrolyse von ATP, wie auch mit ihrer Struktur verknüpft. Die Aufklärung dieser Struktur ist daher entscheidend für die Entschlüsselung der zugrunde liegenden molekularen Details. Obwohl die Struktur beider Proteine bereits zuvor aufgeklärt wurde, ist der strukturelle Effekt der ATP Hydrolyse und der anschließenden Freisetzung des anorganischen Phosphats noch unbekannt. Weiterhin ist der Einfluss von Sequenzvariationen und der Bindung kleiner Moleküle auf die Stabilität des Aktinfilaments bisher nicht aufgeklärt.

In meiner Doktorarbeit habe ich mit Hilfe der Transmissionselektronen-Kryomikroskopie (Kryo-EM) insgesamt 19 hochaufgelöste Strukturen von Aktinfilamenten (F-Aktin) sowie von aktingebundenem Myosin (Aktomyosin) gelöst. Anhand von Strukturen verschiedener Nukleotidzustände präsentiere ich zunächst den strukturellen Wandel von Aktin und Myosin entlang ihres ATPase-Zyklus. Die Daten deuten darauf hin, dass der ATPase-Zyklus von Myosin nicht ausschließlich auf mechanischer Kopplung basiert, sondern zu großen Teilen auf struktureller Flexibilität beruht. Sie veranschaulichen außerdem die Konformationsänderungen, die mit der Freisetzung von ADP und der Bindung von ATP einhergehen. Die strukturellen Veränderungen in F-Aktin sind im Allgemeinen kleiner als die in Myosin und beschränken sich hauptsächlich auf das D-Loop-C-Terminus-Interface an der Oberfläche des Filaments. Auf diese Weise wird der Nukleotidzustand wahrscheinlich an Interaktionspartner übermittelt, wodurch ein gerichteter Umbau des Zytoskeletts ermöglicht wird. Diese Arbeit zeigt außerdem, wie kleine Sequenzänderungen die Filamentinstabilität des Aktin 1 vom Malariaparasiten *Plasmodium falciparum* verursachen. Schließlich wird die strukturelle Grundlage der aktinstabilisierenden natürlichen Toxine Jasplakinolid und Phalloidin entschlüsselt und ihre Wirkung auf den Strukturwandel von F-Aktin beschrieben. Während diese Moleküle bereits wertvolle Werkzeuge für die Grundlagenforschung darstellen, werden die hier vorgestellten Strukturen eines photoschaltbaren Jasplakinolids wahrscheinlich das strukturbasierte Design neuartiger, funktionalisierter Derivate mit noch größerem Potenzial vorantreiben.

Insgesamt haben die in dieser Arbeit gelösten Strukturen wertvolle Einblicke in den strukturellen Wandel von Aktin und Myosin gebracht und werden dadurch letztendlich zu einem verbesserten Verständnis aller auf Aktin und Myosin beruhender Prozesse führen.

2 Introduction

Within this thesis the structural effect of nucleotide hydrolysis and small molecule binding on actin and myosin was studied using electron cryo microscopy (cryo-EM). This chapter initially presents methods for high-resolution structure determination and reasons why cryo-EM is the optimal choice for studying actin and myosin (Section 2.1). Next, it gives a concise introduction into the field of actin and myosin, focusing on their structure-function relationship and how it relies on the binding of small molecules (Sections 2.2 to 2.3). Afterwards, the theory of transmission electron microscopy and the reconstruction of a 3D protein structure is established with special emphasize on filamentous protein samples (Section 2.4 to 2.4.5). Finally, this chapter closes with an overview of recent advances in the field of cryo-EM (Section 2.4.6).

2.1 Structural biology at atomic resolution

The function of a protein is tightly coupled to its three-dimensional (3D) structure. Basically all interactions, both protein-protein and protein-ligand interactions, rely not only on specific, hydrophobic or electrostatic interactions, but also on shape complementarity. In some cases, proteins even have pronounced grooves, into which a complementary shaped binding partner can insert, resembling a “lock-and-key“ interaction (Reece et al., 2011). For this reason, a high-resolution 3D structure of a protein is essential to fully understand its function and how it is affected by disease-causing mutations. Furthermore, structures do not only promote our understanding of the effects of drug-like molecules, but can even facilitates the development of new drugs by structure-based drug design (Anderson, 2003).

Every protein is composed of a specific number of amino acids, which are chained together according to their construction plan encoded in the genome. Parts of this chain of amino acids, also known as the primary structure of a protein, fold either spontaneously or with the help of chaperones into secondary structure elements, namely α-helices and β-sheets. A further spatial packing of the protein chain is energetically favorable, resulting in a distinctive 3D arrangement of secondary structure elements and flexible loop regions, which is known as tertiary structure. Single protein molecules can further assemble into higher-order complexes such as multimers or filaments, thereby defining the quaternary structure of a protein (Reece et al., 2011). Even though the human genome was successfully decoded (Lander et al., 2001) and the primary structure of most proteins is thus known, the prediction of their corresponding 3D structure remains a difficult task, often resulting in inaccurate solutions (Kuhlman and Bradley, 2019). For this reason, the 3D

structure of proteins has been studied experimentally using methods of structural biology for decades (Curry, 2015).

A number of different methods is available to study the 3D structure of proteins, the achievable resolution, however, varies significantly from method to method. In the following, an overview of high-resolution methods, which facilitate the building of an atomic model and the analysis of specific interactions between residues, is given (Figure 2.1).

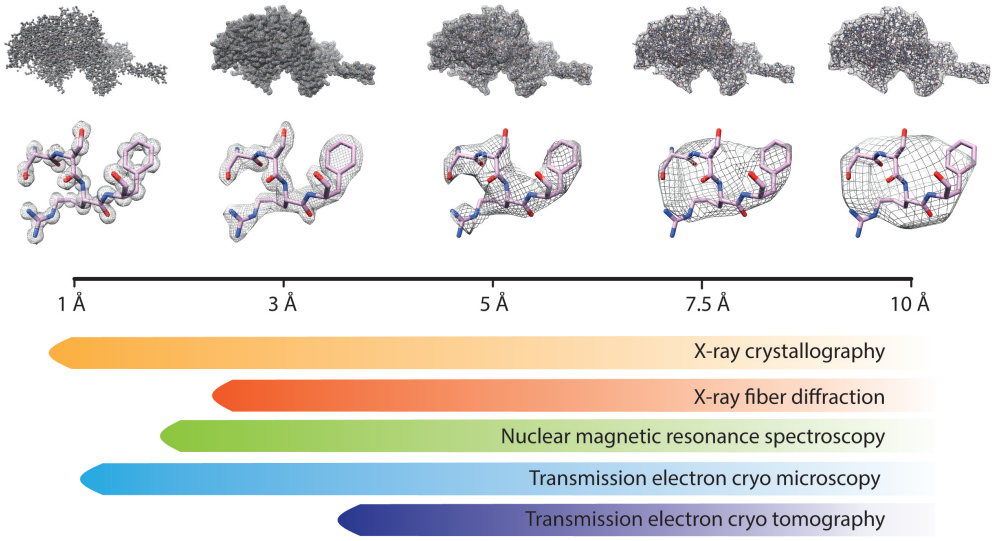

Fig. 2.1: **(Top)** Simulated electron density illustrating the amount of molecular details resolved at 1 Å to 10 Å resolution (PDB 1OE9). **(Bottom)** Schematic overview of high-resolution structural biology methods and their current resolution range.

X-ray crystallography The highest resolution protein structures available today were obtained using X-ray crystallography (0.5-1.0 Å). Here, a diffraction pattern of a 3D protein crystal is collected using X-rays, based on which the 3D protein structure, i.e., corresponding electron density map, can be computationally reconstructed (Ilari and Savino, 2008). While the majority of high-resolution structures was solved using this method, it is not applicable to all proteins, primarily due to the requirement of crystallization (Curry, 2015). Crystallization of proteins is in general not straight forward and relies on the controlled precipitation of purified proteins from solution into a highly-ordered crystal, which is stabilized by protein-protein interactions. Because of this, crystallization often requires the biochemical stabilization or modification of proteins, such as the removal of flexible loops. Still, some proteins including many filamentous and also membrane proteins, which are of special interest for drug design, are recalcitrant to crystallization (McPherson and Gavira, 2014). Furthermore, buffers used for crystallization are often far from native conditions and crystal packing can introduce additional interactions resulting in artificial protein conformations. For this reasons, X-ray crystallography is a powerful, yet limited method.

X-ray fiber diffraction The structure of helical filaments that are recalcitrant to crystallization efforts can be studied by X-ray fiber diffraction. This method also relies on the reconstruction of a 3D electron density map from a X-ray diffraction pattern, but does not require any crystallization (Marvin and Nave, 1982). Instead, the diffraction pattern of a single, aligned fiber or filament is collected. The 3D structure is then refined by maximizing the similarity of a simulated diffraction pattern of a 3D reference structure with the experimental pattern. In this way, the helical symmetry parameters of the respective filament can be directly determined. While this method was successfully applied to determine the first structure of filamentous actin (F-actin) (Oda et al., 2009), there is a persistent concern that the model built to match the experimental diffraction pattern might not be unique (Egelman, 2007a). In addition, the achieved resolution is anistropic and considerably worse along the axis of the filament. Finally, filaments need to be oriented, straightened and controlled in length, requiring the addition of actin binding proteins like gelsolin (Oda et al., 2009).

Nuclear magnetic resonance spectroscopy In contrast to the other methods presented in this section, the 3D structure of a protein cannot be directly determined by nuclear magnetic resonance (NMR) spectroscopy. Instead, the distances of neighboring atomic nuclei of a protein are measured in an aqueous solution, allowing the computational reconstruction of the 3D protein structure (Curry, 2015). While this approach comes with the benefit of direct information about the dynamics of the protein as well as protein-protein interactions, its indirect concept also strongly limits its applicability. Specifically, the complexity and overlap of a NMR spectrum increases dramatically with the protein size, impairing the corresponding analysis. Therefore, NMR spectroscopy is routinely only used for small proteins with a molecular weight $\leq$ 30 kDa (corresponding to $\sim$300 amino acids). While traditional in-solution NMR is limited to hydrophilic proteins (Curry, 2015, Wüthrich, 1990), solid-state NMR also has the potential to study insoluble proteins (Sun et al., 2012).

Transmission electron microscopy Transmission electron microscopy, in particular electron cryo microscopy (cryo-EM) has become increasingly popular in recent years. Thanks to significant improvements in both hardware and software (also see Section 2.4.6), the achievable resolution has increased within the last years and lately has reached 1.2-1.3 Å (Nakane et al., 2020, Yip et al., 2020). Hence, cryo-EM has now almost drawn level with X-ray crystallography in terms of resolution.
Cryo-EM does neither require the crystallization of proteins nor orientation and straightening of filaments. Instead, proteins are vitrified in aqueous solution and thereby preserved in a near-native condition (also see Section 2.4.3). In this way, cryo-EM can also

be applied to membrane proteins, which are reluctant to crystallization, but can be vitrified using a model membrane system such as detergent micelles, amphipols and nanodiscs (Mio and Sato, 2018). The 3D protein structure is reconstructed from many real-space 2D transmission images, depicting a variety of 2D projections of the protein, using single particle analysis (SPA, also see Section 2.4.4) (De Rosier, 1997, Dubochet, 2011). As proteins are not stabilized or fixed in a specific conformation by crystal packing, cryo-EM can also directly resolve structural heterogeneity, i.e., different structural states associated with the biological function of the protein. In contrast to X-ray crystallography and NMR spectroscopy, cryo-EM is especially well suited to determine the structure of huge molecular complexes. The 3D reconstruction of small proteins $\leq$ 100 kDa, however, remains challenging because of a reduced image contrast. The contrast of cryo-EM data is generally weak due to the small scattering cross-sections of biological samples as well as the low electron doses required for the imaging of proteins (also see Section 2.4.3). In case of small proteins, the contrast is additionally decreased as fewer atoms are available for interactions (Glaeser, 2019, Glaeser and Hall, 2011, Henderson, 1995).

Transmission electron tomography Transmission electron tomography has been used to study the *in situ* organization and localization of proteins for many years. However, as a method for protein structure determination it has been limited to low- to medium-resolutions $\sim$10-20 Å for a long time and only recently advanced to a high-resolution method. This is especially, but not exclusively, due to advances in the sample preparation, the imaging strategy and data analysis. First, vitrified thick samples, such as tissues or cells, can now be thinned by focused ion beam (FIB) milling which, in contrast to previous thinning or sectioning approaches, preserves high-resolution features and introduces less artifacts (Marko et al., 2006, Rigort et al., 2012). Second, sophisticated data acquisition schemes have become available, which apply a tilt dependent electron dose and thereby reduce the overall beam damage within tomograms (Hagen et al., 2016). Besides beam damage, the specimen drift was also reduced by improvements of the specimen stage. Finally, software packages for the advanced processing of tomograms and especially for sub-tomogram averaging, the tomographic analog of SPA, have become available. While these advances culminated in structures at $\sim$3-4 Å resolution (Dick et al., 2020, Schur et al., 2016, Turoňová et al., 2017), comparable resolutions are not yet routinely achieved by electron cryo tomography (cryo-ET). Still, these advances and currently ongoing research with the aim to improve the complete cryo-ET pipeline, make cryo-ET a very promising technique for the high-resolution structure determination of proteins in their natural environment.

Most of the methods presented in this section are not suitable to determine the structure of

the actin and actomyosin filaments studied in this thesis. First of all, F-actin does not readily crystallize because its helical symmetry is incompatible with crystal packing, which would require exactly two, three, four or six subunits per turn (Egelman, 2007a). Despite considerable efforts to stabilize short actin filaments in their native conformation to enable their crystallization (Kudryashov et al., 2005, Qu et al., 2018, Sawaya et al., 2008), F-actin remains recalcitrant to crystallization attempts excluding X-ray crystallography as a potential method for structure determination. Although fiber diffraction does not require any crystallization, it suffers from other drawbacks including the strong dependence on the reference model and the requirement to orient and straighten the filaments (Egelman, 2007a). Consequently, X-ray fiber diffraction is also not an optimal tool to study F-actin, whose flexibility is thought to be of biological relevance. NMR spectroscopy is also not suitable, as a single actin monomer (42 kDa) already exceeds the molecular weight limit of this method ($\sim$ 30 kDa). Consequently, cryo-EM and cryo-ET are the only two methods to be considered. Although significant advances have been made in the field of cryo-ET, the achievable resolution still falls behind cryo-EM. Answering of the biological questions asked within this thesis requires at least near-atomic resolution ($\leq$ 4 Å) and greatly benefits from even higher resolutions. For this reason, cryo-EM was chosen as the prime experimental method to study the structural effect of ATP hydrolysis and small molecule binding on F-actin and actomyosin.

2.2 Actin

Actin is a highly abundant structural protein making up to 10 % of the overall weight of a cell (Lodish et al., 2000). It is expressed in basically all eukaryotic organisms and essential for their survival (Pollard and Cooper, 2009). Both bacteria and archae express actin-like or actin-related proteins, which fulfill similar biological functions (Erickson, 2001, Pospich and Raunser, 2018). Actin is involved in a plethora of key cellular processes including the maintenance of the cell shape, cell motility, cell division, intracellular cargo transport and endocytosis (reviewed in Svitkina (2018)). In particular, actin is a key role player in muscle cells, where force is generated through the interplay of actin filaments and the associated molecular motor myosin. Furthermore, actin is a main component of the cytoskeleton, which is a highly dynamic network of filaments within the cytoplasm of cells (also see Secton 2.2.2). To fulfill its diverse functions, actin participates in more protein-protein interactions than any other known protein (Dominguez and Holmes, 2011). In line with this, a multitude of actin binding proteins (ABPs, $\geq$ 160) has been identified over the years, which tightly control the structure and dynamics of actin (Pollard, 2016) (also see Section 2.2.2).

Actin is an ATPase, which means that it can hydrolyse adenosine triphosphate (ATP) to

adenosine diphosphate and inorganic phosphate (ADP and P_i) in its active site (Straub and Feuer, 1989). The chemical energy that is stored in ATP thereby gets transferred to the protein and eventually gives rise to conformational changes, which are linked to the biological function of the protein (mechanochemical coupling, also see Section 2.2.1). Another prominent ATPase is the motor protein myosin, which uses the energy of ATP to generate the force driving muscle contraction and cargo transport (Robert-Paganin et al., 2020) (also see Section 2.3).

2.2.1 The structure-function relationship

In 1990 Kabsch and colleagues solved the first structure of monomeric actin in complex with DNase I by X-ray crystallography (Kabsch et al., 1990). The ∼42 kDa protein consists of four subdomains (SD1 to SD4) and has an overall size of approximately 55 Å x 55 Å x 35 Å (Figure 2.2A) (Dominguez and Holmes, 2011). In the center of the molecule resides the nucleotide binding pocket, which is also known as active site. Here, an adenonucleotide (ATP, ADP-P_i or ADP) binds alongside to a divalent metal ion, which is mostly Mg^{2+}, but can also be Ca^{2+}. The metal-nucleotide complex is not only coupled to the ATPase activity of actin, but also stabilizes the fold of the protein (Asakura, 1961). The cleft between SD1 and SD3 is commonly referred to as hydrophobic cleft and serves as a hub for the binding of many ABPs. Additional structural features of particular importance are the DNase-I-binding loop (D-loop) in SD2 as well as the N- and C-terminus in SD1, which can often not be structurally resolved due to their intrinsic flexibility (Figure 2.2). The D-loop has been shown to be highly flexible and adopts a variety of conformations in crystal structures ranging from not resolved, over various loop conformations to an α-helix and β-turn (Kudryashov and Reisler, 2013).

Under physiological conditions, i.e., pH and ionic strength, actin spontaneously polymerizes into µm-long helical filaments, provided that the concentration is above the critical concentration ($\geq$1 µM, exact value depends on the actin isoform and identity of the divalent metal ion) (Pollard, 1986). Polymerization goes along with a transition of actin from its monomeric, globular conformation (G-actin) to its filamentous conformation (F-actin). This transition was first described by Oda and colleagues based on their X-ray fiber diffraction structure of F-actin (Oda et al., 2009) and was later confirmed by a high-resolution cryo-EM structure (von der Ecken et al., 2015). Upon polymerization, subdomains SD2 and SD4 rotate by ∼20 ° relative to SD1 and SD3, resulting in an overall flattening of the actin monomer and closure of the nucleotide cleft (Figure 2.2B). While G-actin is a weak ATPase with a neglectable catalytic rate of $7 \cdot 10^{-6}$ s^{-1} (Rould et al., 2006), the transition to F-actin dramatically increases the ATPase activity to 0.3 s^{-1} (Blanchoin and Pollard, 2002). Although it is assumed that the G- to F-transition estab-

lishes a hydrolysis-potent geometry at the active site, the structural details remain to be resolved.

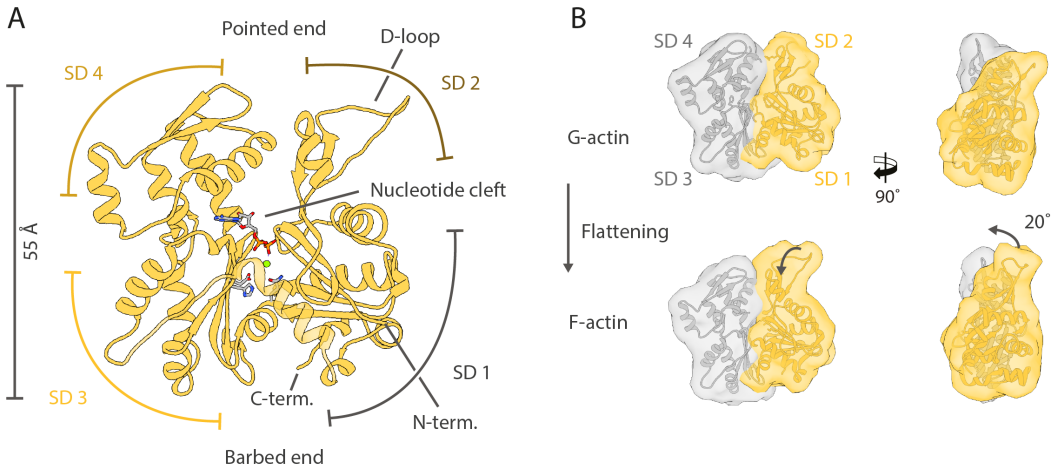

Fig. 2.2: Architecture and structural transition of actin upon polymerization. **(A)** Illustration of the actin domain architecture consisting of four subdomains (SDs) and the central nucleotide binding cleft. Important structural features, such as the D-loop and the N- and C-terminus, are labeled. **(B)** Structural rearrangement upon polymerization, also known as G- to F-actin transition. SD1 and SD2 (yellow) rotate ∼20 ° relative to SD3 and SD4, resulting in a flattening of the monomer and closing of the nucleotide cleft. Figure was originally published in Merino et al. (2019), and was rearranged and modified.

Polymerization is a highly cooperative process that has to initially overcome the unfavourable formation of a tetrameric nucleus (Oda et al., 2016). Once ATP-bound G-actin adds to the filament, it transitions to F-actin and ATP hydrolysis is triggered (Figure 2.3). The association and dissociation kinetics of the two ends of the filament are not identical (Pollard, 2016). Instead, actin monomers preferentially add to the so-called "+" end (SD1 and SD3), while the "–" end (SD2 and SD4) is prone to depolymerization. Based on the arrow-shaped appearance of F-actin decorated with myosin, the ends are also referred to as barbed ("+") and pointed ("–") end (Pollard, 2016). While ATP hydrolysis is fast, the release of inorganic phosphate is slow (0.003 s^{-1}) (Carlier and Pantaloni, 1988). Therefore, at least three different nucleotide states exist in the filament, namely the initial ATP, the intermediate ADP-P_i and the final ADP state (Carlier and Pantaloni, 1986, 1988). Although hydrolysis and P_i release are both first-order processes, the large difference in kinetic constants and the faster growth from the "+" end results in a characteristic nucleotide gradient along the filament, which marks the local age of the polymer (Figure 2.3) (Merino et al., 2018). Specifically, F-actin encompasses a young ATP/ADP-P_i-bound and an old ADP-bound end. The depolymerization tendency of the "–" end directly relates to the nucleotide state, as ADP-bound F-actin is thermodynamically and mechanically less stable than ATP or ADP-P_i F-actin. (Isambert et al., 1995, Kardos et al., 2007).

F-actin forms a double-stranded, polar helical filament with a diameter of ∼7 nm (Figure 2.3) (Holmes et al., 1990). The filament is stabilized by interactions between the two strands (interstrand) as well as interactions of subunits within one strand (intrastrand) (Oda et al., 2009, von der Ecken et al., 2015). Intrastrand contacts are large and primarily mediated through the hydrophobic D-loop, which inserts into a hydrophobic cavity between SD1 and SD3 of the consecutive subunit. By inserting into the D-loop, Tyr169 additionally stabilizes this contact through a lock-and-key interaction. Additional ancillary interactions occur between SD3 and SD4 of consecutive subunits. Interstrand contacts are sparser and also contribute less to the overall filament stability. The most prominent interaction is between the plug (historically also referred to as hydrophobic plug, despite its charged nature) and the base of the D-loop of the adjacent subunit (Galkin et al., 2015, Oda et al., 2009, von der Ecken et al., 2015).

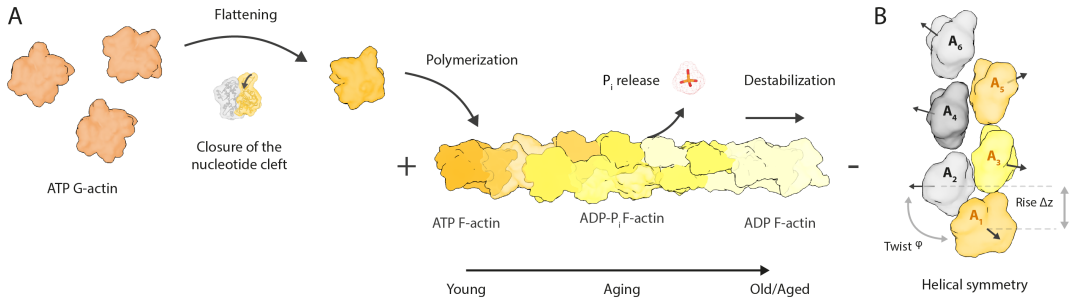

Fig. 2.3: Schematic illustration of polymerization and aging of actin due to ATP hydrolysis and P_i release as well as the helical symmetry of F-actin. **(A)** Scheme of actin polymerization and filament aging. ATP-G-actin adds to the barbed (+) end of the the filament undergoing a structural transition to F-actin, which promotes ATP hydrolysis. Due to the slow release of inorganic phosphate (P_i), F-actin has a characteristic nucleotide gradient along the filament, which marks the local age and can be sensed by ABPs. **(B)** Actin filaments can either be described as a right-handed, double-stranded (long pitch), or left-handed single start (short pith) helix. The helical symmetry is defined through the rotation (twist, φ) and shift (rise, Δz) between consecutive subunits. The two strands are colored in shades of yellow and gray, respectively, and subunits are numbered along the short pitch helix. Figure was originally published in Merino et al. (2019), and was rearranged and modified.

The D-loop, which was reported to be highly flexible in G-actin (Kudryashov and Reisler, 2013), is ordered in F-actin and forms the key interface (Galkin et al., 2015, Oda et al., 2009, von der Ecken et al., 2015). However, the D-loop does not only play an essential role in polymerization and filament stability, but also serves as a binding hub for many ABPs that bind to actin filaments (Dominguez and Holmes, 2011). Some of these proteins, including coronin (Cai et al., 2007b), cofilin (Muhlrad et al., 2006) and specific myosins (Zimmermann et al., 2015), have been reported to be nucleotide sensitive. This means, that their binding affinity depends on the nucleotide state of F-actin, facilitating the directed remodeling of the actin cytoskeleton (also see Section 2.2.2). As the binding site of these ABPs is far from the nucleotide pocket of actin, it has long be accepted that

the nucleotide state has to be transmitted to the surface of the filament. Biochemical data indicate that the D-loop is highly flexible, adopting a variety of conformations in both G-actin and F-actin, which are probably linked to the nucleotide state (Kudryashov et al., 2010, Oztug Durer et al., 2010, 2012). Consequently, the conformation of the D-loop could possibly be used by ABPs to sense the nucleotide state of F-actin. However, the conformational changes associated with ATP hydrolysis and release of inorganic phosphate as well as the recognition mechanism used by ABPs remain elusive.

The symmetry of F-actin can by described by two helical symmetry parameters, specifically the rise Δz and twist $\Delta\varphi$. The rise represents the longitudinal distance between two consecutive actin subunits, while the twist describes the azimuthal rotation between these two subunits (around the filament axis, Figure 2.3). As F-actin is a double-stranded filament, consecutive subunits are always located on different strands. Independent cryo-EM studies determined values of $\Delta z = 27.7$ Å and $\Delta\varphi = 166.6°$ (Fujii et al., 2010) and $\Delta z = 27.5$ Å and $\Delta\varphi = 166.4°$ (von der Ecken et al., 2015), respectively. Yet, F-actin is not rigid but flexible and the symmetry can change due to, for example, sheering forces (Egelman et al., 1982, Galkin et al., 2012) or the binding of ABPs such as cofilin (Huehn et al., 2020, McGough et al., 1997). In addition, the determination of symmetry parameters is not straight-forward and sensitive to small errors in the pixel size of cryo-EM data (Pospich and Raunser, 2018). Hence, reported symmetry parameters should be carefully considered and understood as averages.

The dynamics of actin have been studied extensively since the discovery of the protein by Straub in 1942 (Straub, 1942). Due to limitations in methodology, it was not before 1990 that the first high-resolution structure of G-actin was solved (Kabsch et al., 1990). Since then, a multitude of crystal structures of G-actin in complex with different nucleotides or ABPs has been published. Further advances in the field of structural biology eventually enabled the structural characterization of F-actin at high-resolution, first by X-ray fiber diffraction in 2009 (Oda et al., 2009) and later by cryo-EM (von der Ecken et al., 2015). Since then, cryo-EM has become the standard method for studying actin filaments (Pospich and Raunser, 2018). At the beginning of this thesis in 2015, the knowledge was limited to high-resolution structures of F-actin in the ADP state (Galkin et al., 2015, Oda et al., 2009, von der Ecken et al., 2015), leaving many questions about the structural transition of actin and its recognition by ABPs unanswered. In the meantime, many groups including the Raunser lab, in which this thesis was prepared, have contributed with high-resolution cryo-EM structures (≤ 4 Å) of actin alone and in complex with ABPs including myosin (Belyy et al., 2020, Chou and Pollard, 2019, 2020, Das et al., 2020, Doran et al., 2020, Galkin et al., 2015, Grintsevich et al., 2017, Huehn et al., 2018, 2020, Iwamoto et al., 2018, Kumari et al., 2020, Mei et al., 2020, Mentes et al., 2018, Merino et al., 2018, Oda et al., 2020, Pospich et al., 2021, 2017, 2020, Ren et al., 2019, Risi et al., 2020, Shaa-

ban et al., 2020, Tanaka et al., 2018, Vahokoski et al., 2020, von der Ecken et al., 2016, Xu et al., 2020, Yamada et al., 2020, Zimmet et al., 2020).

2.2.2 The actin cytoskeleton

Actin is a main component of the cytoskeleton, which is a dynamic network of filaments and a key component of every eukaryotic cell. Within the actin cytoskeleton a phlethora of ABPs fine-tune the dynamics and structure of actin filaments (Figure 2.4). Preferential binding of ABPs to either a certain nucleotide or oligomeric state of actin, i.e., G-actin or F-actin, enables the directed remodeling of the cytoskeleton according to the specific

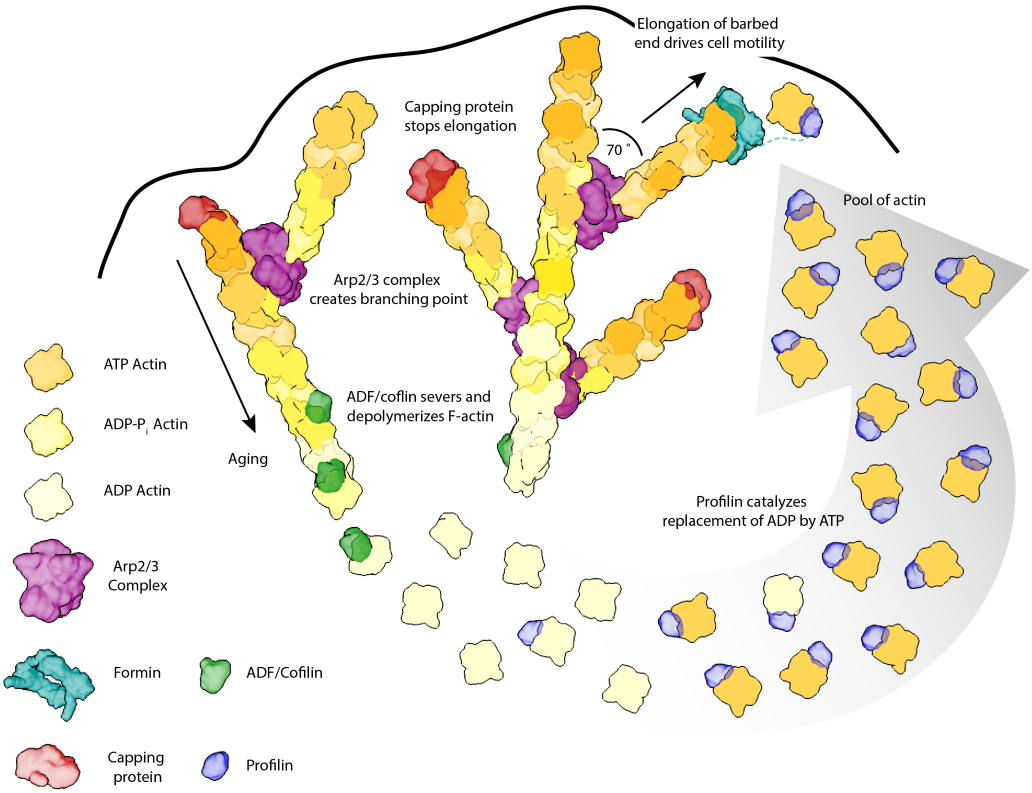

Fig. 2.4: Schematic overview of the actin cytoskeleton, which is tightly organized by ABPs both spatially and temporally, to facilitate a dynamic remodeling. Proteins like capping protein (red) and the Arp2/3 complex (purple) remodel the cytoskeleton by either capping the barbed end or by introducing a branch point from which a new filament can grow. Other proteins like ADF/cofilin (green) and profilin (blue) depolymerize and sever actin or maintain a constant pool of polymerizable actin, respectively. The ATPase activity of actin itself is also essential for the regulation as it results in a nucleotide gradient along the filament which can be sensed by accessory proteins. Actin is depicted in shades of yellow depending on its nucleotide state. The color gradient represents the nucleotide gradient along the filament from the darkest shade (ATP) to brightest shade (ADP). Figure and legend were originally published in Merino et al. (2019).

biological function (Merino et al., 2019, Pollard, 2016). Within this section, only a short overview of key ABPs will be presented. A more detailed presentation can be found in the following reviews Dominguez and Holmes (2011), Merino et al. (2019).

ABPs fulfill very distinct functions within the cytoskeleton and *inter alia* sever, sequester, polymerize, cap and branch actin filaments (Pollard, 2016). Through the concerted action of all ABPs, the actin cytoskeleton can provide mechanical stability to the cell, but also produce force through the directed polymerization of actin filaments (Figure 2.4) (Blanchoin et al., 2000, Kovar and Pollard, 2004, Pollard and Borisy, 2003). In this process, cofilin (also known as actin depolymerizing factor, ADF) preferentially severs the aged ADP-bound "–" end of filaments, which eventually results in depolymerization (Suarez et al., 2011). Subsequently, profilin binds to the free monomers and catalyses the nucleotide exchange from ADP to ATP (Funk et al., 2019). Thereby, a polymerization-potent pool of actin is maintained, that contains the majority of cellular actin. The directed elongation of actin filaments, which is essential for cell motility, is promoted by formins, which bind to the "+" end (Funk et al., 2019). In contrast, capping protein inhibits the elongation by blocking the "+" end interface. Although single actin filaments can produce pN-magnitude forces (Kovar and Pollard, 2004), they are likely to buckle under stress with growing length. Nature has circumvented this restriction, by building a branched cytoskeleton with improved stability. Here, the Arp2/3 complex binds to F-actin and creates a branch point, from which a daughter filament can assemble (Amann and Pollard, 2001). The preference of Arp2/3 for young, ATP/ADP-P_i-bound F-actin results in increased branching at the "+" end accompanied by debranching at the "–" end of filaments.

2.2.3 Sequence conservation and unusual actins

Actin is exceptional in many ways. It is not only one of the most abundant proteins, but also one of the most conserved proteins (Gunning et al., 2015). While the human genome encodes three different isoforms (α, β and γ-actin) in six genes, only very few of the 374 to 375 actin residues differ (Firtel, 1981). Specifically, the sequence of human actins is 94 % identical, with differences localizing mostly to the N-terminus. The sequence conservation is not limited to human actins, but expands to the whole eukaryotic kingdom (Pollard, 2016). For instance, the human skeletal muscle actin (α-actin) is 100 % identical with rabbit skeletal muscle actin and 87 % identical to the actin of baker's yeast. Different explanations for the remarkable sequence conservation have been proposed. The most widely accepted one suggests the evolution of actins from an ancestral, archeal actin (Gunning et al., 2015, Merino and Raunser, 2016b). The existence of actin-like proteins (ALPs) which form filaments similar to F-actin in both archae and bac-

teria is in line with this model (Pospich and Raunser, 2018). Yet, the sequence of ALPs has diverged significantly from eukaryotic actins, resulting in a sequence identity as little as 20 %. So, why are eukaryotic actins highly conserved while prokaryotic ALPs are not? This can be answered by the different degree of evolutionary pressure within these organisms. Proteins that are highly expressed, generally evolve more slowly as incorrect folding leads to cell death (Galkin et al., 2010). In addition, the evolution is further restricted by protein-protein interactions. Eukaryotic actins participate in more protein-protein interactions than any other known protein and today more than 160 ABPs have been identified (Dominguez and Holmes, 2011, Pollard, 2016). In contrast, prokaryotic organism express only very few ABP-like proteins on their own, thereby leaving more room for evolutionary divergence (Merino et al., 2019).

The probably most divergent actins can be found within unicellular eukaryotic apicomplexan parasites. A hallmark of these parasites is their complex life cycle including an obligatory change of host, i.e., transmission from a vector organism to the target organism and vice versa (World Health Organization, 2020). Prominent representatives of this protozoan phylum are the species *Plasmodium* and *Toxoplasma*, which are the causatives of malaria and toxoplasmosis, respectively. While most apicomplexan parasites express only one actin isoform, two different actins have been identified in the human-pathogen *Plasmodium falciparum* (*Pf*actin1 and *Pf*actin2) (Wesseling et al., 1988, 1989). *Pf*actin1 is the major isoform and expressed throughout the complex life cycle of the malaria parasite. It is closely related to the actins found in other apixomplexan parasite, sharing 93 % of its sequence with the actin of *Toxoplasma gondii* (Dobrowolski et al., 1997). In contrast, *Pf*actin1 shares less than 80 % of its sequence with ophistokont (animal and yeast) and plant actins, making it one of the most divergent actins known so far (Wesseling et al., 1988). While the sequence of homologous proteins often differs by more than 20 %, the general structure and function of these proteins is usually conserved. This is, for example, the case for prokaryotic actin-like proteins, which share as little as 20 % of their sequence with eukaryotic actin, but still polymerize into actin-like filaments (Pospich and Raunser, 2018). It is therefore all the more surprising that *Pf*actin1 does not form µm-long filaments, but is intrinsically unstable (Schmitz et al., 2005, Skillman et al., 2011, Vahokoski et al., 2014). In line with this, the direct visualization of a actin-cytoskelton within *P. falciparum* proved challenging and required super-resolution microscopy (Hliscs et al., 2015). Previously, only short filamentous structures in equilibrium with G-actin were reported (Angrisano et al., 2012a,b, Kudryashev et al., 2010, Sidén-Kiamos et al., 2012, Webb et al., 1996). Addition of high concentrations of the filament-stabilizing agent jasplakinolide (JASP, also see Section 2.2.4) were shown to inhibit parasite growth and to impair cell invasion (Mizuno et al., 2002). Hence, the unstable nature of *Pf*actin1 filaments was proposed to be essential for the invasion strategy and parasite survival (Skillman et al.,

2011). Within the cytoskeleton, ABPs such as formin and coronin are thought to stabilize actin filaments (Hliscs et al., 2015, Olshina et al., 2015). However, only very few ABPs have been identified in *Plasmodium* and further studies are required to fully understand actin organization and remodeling in parasites (Bhargav et al., 2013).

A crystal structure of monomeric *Pf*actin1 illustrated that while the overall fold of mammalian G-actin is conserved, small but appreciable structural deviations exist (Vahokoski et al., 2014). These localize primarily to the binding interface of ABPs, the nucleotide binding pocket and the D-loop, which represents a key interface of actin filaments. Due to the conformational change coupled to filament formation (G- to F-transition, also see Section 2.2), one cannot predict how these differences influence the structure and stability of *Pf*actin1 filaments. For this reason, the same group also studied the structure of filamentous *Pf*actin1 using cryo-EM (Vahokoski et al., 2014). To overcome the intrinsic filament instability and reduce the very high critical concentration of parasite actin, filaments were stabilized by JASP. While the analysis of interfaces was impeded by the low-resolution of this cryo-EM structure (∼25 Å), it indicated a stronger twisting of *Pf*actin1 filaments (helical symmetry parameters: Δz=27.7 Å and $\Delta\varphi$=167.5 °) compared to mammalian actin (Δz=27.7 Å and $\Delta\varphi$=166.6 °) (Fujii et al., 2010, Vahokoski et al., 2014). The deviating helical symmetry was confirmed by both atomic force microscopy data (Schmitz et al., 2010) and a medium-resolution cryo-EM structure (∼9 Å) originating from research conducted during a master degree project preceding this doctoral thesis (Pospich, 2015). Unfortunately, the achieved resolution was not sufficient to explain how small sequence variations translate to the altered properties of *Pf*actin1. Considering the essential role *Pf*actin1 plays in the host cell invasion strategy and thus infectivity of *Plasmodium*, it poses a promising target for structure-based drug design. Already today, malaria is a threat to half of the global population (World Health Organization, 2020). This number will in future even increase, as global warming enables the spread of the vector mosquito species to regions of previously moderate climate. A growing resistance of *Plasmodium* species against anti-malaria drugs as well as vector resistance to insecticides additionally complicates the control of the live-threatening fever disease (World Health Organization, 2020). This urges the need for the development of innovative, possibly structure-based, drugs.

All apixomplexan parasites use a unique actin-myosin-based molecular machine called glideosome to actively invade host cells (Drewry and Sibley, 2015, Keeley and Soldati, 2004, Kumpula and Kursula, 2015, Skillman et al., 2011). Therefore, knowledge about functional aspects of *Pf*actin1 would likely be transferable to other apixomplexan parasites such as *Toxoplasma*, which primarily infects cats but is also a threat to humans. Insights about the structural basis of filament instability in *Pf*actin1 would furthermore facilitate the identification of common and specific features in the actin superfamily.

2.2.4 Inhibition of actin by drug-like small molecules

Over the years many small molecules that bind to actin have been identified (Fenteany and Zhu, 2003). A majority of them are either natural products themselves, or were derived from natural products, which are produced by organisms like fungi, marine sponges and myxobacteria for self-defense purposes (Figure 2.5). This section gives an overview about the most popular compounds that directly bind to actin. An elaborate review of small molecule inhibitors, which can also affect the interactions with ABPs and myosin, can be found in Fenteany and Zhu (2003).

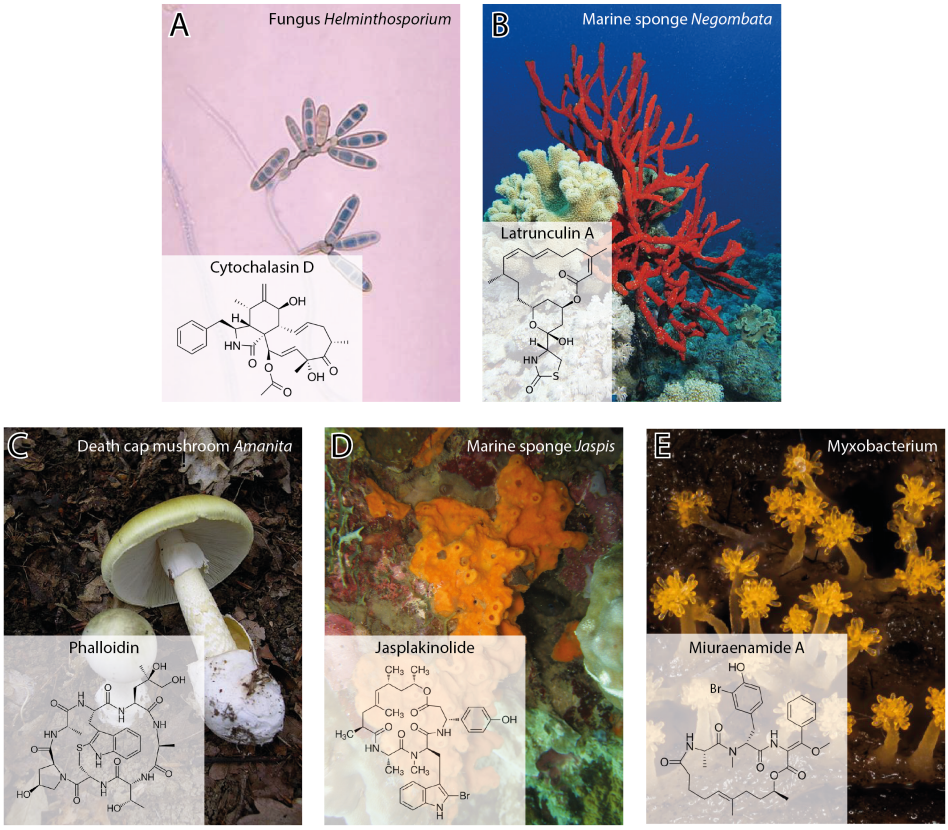

Fig. 2.5: Illustration of source organisms and chemical structures of selected natural drugs that either destabilize **(A-B)** or stabilize **(C-E)** actin filaments. Figure was assembled from images published by **(A)** organism: CDC (1970), chemical structure: Edgar181 (2010), **(B)** organism: Vasenin (2010), chemical structure: Edgar181 (2015), **(C)** organism: Archenzo (2005), chemical structure: Chem Sim 2001 (2020), **(D)** organism: Crews (2019a), chemical structure: Crews (2019b) (with permission from Prof. P. Crews) and **(E)** organism: Pollack (2020) (with permission from A. Pollack, Instagram @marin_mushrooms), chemical structure: Gemperlein et al. (2018).

Actin binding compounds are usually referred to as inhibitors, as they have dramatic effects on basically all actin based processes and thereby inhibit the various cellular functions of actin (also see Section 2.2). Known inhibitors can be divided into two groups based on their effect on actin: destabilizers and stabilizers (Fenteany and Zhu, 2003,

Wang et al., 2019). While destabilizers typically inhibit filament elongation or cause depolymerization (Dominguez and Holmes, 2011), stabilizers increase the filament stability and can even promote polymerization (Fenteany and Zhu, 2003). In the following, the most widely-used destabilizers and stabilizers will be briefly introduced (Figure 2.5).

Cytochalasins are well-studied fungal toxins that bind to the barbed end of F-actin and thereby inhibit polymerization and eventually cause depolymerization (dissociation constant $K_D \approx 5$ µM, Goddette and Frieden (1986)) similar to capping protein (also see Section 2.2.2) (Cooper, 1987, Dominguez and Holmes, 2011, Katagiri and Matsuura, 1971). Cytochalasin B and D are the most prominent and widely used compounds of this group (Figure 2.5A). Both compounds are known to accelerate the ATPase activity of actin. Yet, their precise effect on actin slightly differs. While the more selective cytochalsin D was also reported to sequester actin monomers and possibly dimers, cytochalsin B was shown to sever F-actin (Fenteany and Zhu, 2003).

Latrunculins are marine macrolides which were first isolated from a red sea sponge (Figure 2.5B) (Spector et al., 1983). In contrast to the less potent cytochalasins, they bind in the nucleotide-binding cleft of G-actin ($K_D \approx 0.2$ µM, Yarmola et al. (2000)). In this way, latrunculins inhibit nucleotide exchange and elicit a structural conformation that is incompatible with polymerization (Dominguez and Holmes, 2011). Latrunculin A is the most potent member of the latrunculin family and binds G-actin in a stochiometric ratio. Its mechanism is thereby reminiscent of the one of the actin sequestering protein β-thymosin (Fenteany and Zhu, 2003, Yarmola et al., 2000).

Additional actin destabilizers have been identified including swinholide A, misakinolide A, mycalolide B, which probably binds covalently, halichondramide and dihydrohalichondramide, aplyronine A and pectenotoxins (reviewed in in Fenteany and Zhu (2003)). Despite their non-conserved chemical structure, most destabilizers bind to the target-binding cleft of actin and mimic the function of ABPs such as capping protein or β-thymosin (Dominguez and Holmes, 2011, Fenteany and Zhu, 2003). In contrast, no resemblance of ABPs has been reported for common actin stabilizing small molecules.

Phalloidin (PHD) is one of many phallotoxins found in the death cap mushroom *Amanita phalloides* (Figure 2.5C) (Lynen and Wieland, 1938). The bicyclic heptapeptide binds stochiometrically and with a high specificity to F-actin (Estes et al., 1981, Wieland and Govindan, 1974). PHD does not only stabilize actin filaments, but also considerably reduces the critical concentration, thereby promoting polymerization and preventing de-

polymerization even under harsh conditions (Dancker et al., 1975, Estes et al., 1981, Faulstich et al., 1977, Lengsfeld et al., 1974). The increased filament stability is possibly linked to a considerably delayed release of P_i after ATP hydrolyis, while the hydrolysis rate remains unaffected (Barden et al., 1987, Dancker and Hess, 1990, Vig et al., 2011). The high-affinity ($K_D \approx 36$ nM, Faulstich et al. (1977)) binding site of PHD at the interface of three actin protomers within F-actin was identified early (Belmont et al., 1999, Drubin et al., 1993, Lorenz et al., 1993, Oda et al., 2005, Steinmetz et al., 1998). The exact position and underlying molecular interactions, however, were only recently revealed by cryo-EM, both by other groups (Das et al., 2020, Kumari et al., 2020, Mentes et al., 2018), and within the research performed for this thesis (Pospich et al., 2020) (also see Section 4.3). PHD is widely used in structural studies and is a common marker for F-actin in fluorescence light microscopy, when conjugated to fluorophores (Melak et al., 2017).

Jasplakinolide (JASP) is a cyclic depsipetide produced by marine sponges of the genus *Japsis* (Figure 2.5D) (Crews et al., 1986). It not only competes with PHD for actin binding, but also shares most if its effects with it, including filament stabilization, promotion of polymerization and delay of inorganic phosphate release (Dancker et al., 1975, Estes et al., 1981, Faulstich et al., 1977, Lengsfeld et al., 1974). Yet, the stabilization effect of JASP has been reported to be stronger than the one of phalloidin (Bubb et al., 2000, Visegrády et al., 2004, 2005). While the competition of PHD and JASP enabled a rough delimitation of the JASP binding site, details about the stabilizing interactions were not available prior to this thesis. JASP is, in contrast to PHD, cell-permeable, making it a useful tool for cellular studies (Fenteany and Zhu, 2003). Surprisingly, JASP derivatives are rarely used, possibly with the exception of Sir-actin, a silicon-rhodamine JASP derivate designed for super-resolution fluorescence microscopy (Lukinavičius et al., 2014).

Miuraenamide A (MiuA) is a myxobacterial toxin, which is structurally related to JASP (Figure 2.5E) (Fenteany and Zhu, 2003, Gemperlein et al., 2018, Wang et al., 2019). Similiar to JASP, MiuA competes with PHD for its binding site, promotes actin polymerization and stabilizes F-actin (Wang et al., 2019). At the same time MiuA was reported to differ from JASP in its down-stream effects such as binding of ABPs and eventually cell migration and transcriptional regulation (Wang et al., 2019). While molecular docking of MiuA and molecular dynamics simulation suggested that an altered conformation of the D-loop gives rise to the observed different effects (Wang et al., 2019), a high-resolution structure is required to finally answer this question.

Less common small-molecule actin stabilizers are doliculide, dolastatin 11 and hectochlorin, whereby the latter two do not compete with PHD and therefore likely bind to a differ-

ent interface (Fenteany and Zhu, 2003).

Small molecule actin inhibitors are an invaluable tool in cell biology and have greatly promoted our current understanding of the actin structure and dynamics (Dominguez and Holmes, 2011, Fenteany and Zhu, 2003). The future identification of additional natural actin-targeting toxins as well as the chemical design of novel functionalized compounds promise further insights.

Considering the essential role of actin in basically all eukaryotic organisms (also see Section 2.2), it is not surprising that anti-proliferative, anti-fungal and anti-cancer activity has been reported for many actin inhibitors. Within the field of anti-cancer drug development, regulators of the cell cycle including cytoskeletal proteins have been of special interest (Fenteany and Zhu, 2003). Today, the natural-metabolites taxol and colchicine are routinely used to inhibit the microtubule-driven cell division in cancer chemotherapy. While these compounds are highly effective, they come at the cost of inevitable side effects, as cell division is also blocked in non-cancer cells (Fenteany and Zhu, 2003). Although actin inhibitors are currently not used in anti-cancer therapy, the actin cytoskeleton also presents a valid drug target. Yet, a possible drug would have similarly severe side effects as actin is essential for all cell types. With the aim to reduce side effects in chemotherapy, photoswitchable microtubule inhibitors were recently introduced (Borowiak et al., 2015). The activity of these inhibitors can be switched on and off by visible light (changed isomeric state) and can thereby be restricted to a region of interest, i.e., a solid tumor. The concept of photoswitching was successfully transferred to actin inhibitors lately, giving rise to cell-permeable photoswitchable JASP derivates (optojasps) (Borowiak et al., 2020). Optojasps were reported to provide direct optical spatiotemporal control of the actin cytoskelton and to affect cell viability, motility and division in an isomer-dependent way. While these results are promising, a compound that is completely inactive in one isomeric state and only becomes active upon illumination is still missing. A high-resolution structure of an optojasp-F-actin complex would allow a structure-based drug design of new derivatives and in this way promote future design efforts.

2.3 Myosin

Myosin is a motor protein, which uses the energy stored in ATP to generate force. In analogy to actin, the function of myosin is tightly coupled to its structure, which in turn is coupled the nucleotide bound to its active site (reviewed recently by Sweeney et al. (2020) and Robert-Paganin et al. (2020)). Initially, ATP hydrolysis primes the motor in a stable high-energy conformational state. Binding to F-actin starts a cascade of conformational changes, which eventually give rise to a large force-producing structural rearrangement

known as powerstroke. A subsequent exchange of the bound ADP to ATP results in the detachment of myosin and initiates a new ATPase cycle starting with the re-priming of myosin via the recovery stroke (for details see Section 2.3.2). Trough repetitive cycles of binding and detachment, myosin can "walk" along polar actin filaments, thereby creating directed motion (Houdusse and Sweeney, 2016, Sweeney et al., 2020). While the underlying principle of allosteric chemo-mechanical transduction has been identified early, the complex molecular mechanism by which myosin produces force remains to be fully understood (Robert-Paganin et al., 2020).

2.3.1 Diversity and conservation within the myosin family

Muscle contraction is undoubtedly the most prominent and archetypical example of a myosin-dependent process (Reedy et al., 1965). Yet, myosin is involved in many more critical processes in eucaryotic cells including cytokinesis, cell adhesion and crawling, endo- and exocytosis as well as signal transduction and transcription (Behrmann, 2012, Coluccio, 2020, Robert-Paganin et al., 2020). The diversity in function is well reflected by the diversity of the myosin protein family itself (Figure 2.6). In contrast to the conserved actin family, whose function is tuned by ABPs, evolution has produced a multitude of highly specialized myosins, which differ remarkably in their sequence and cellular localization (Sellers, 2000). Over the years, great efforts have been put forward to classify the myosin superfamily based on the sequence, structure, function and cellular localization of its members (Coluccio, 2020). For example, myosins can be divided into 17 distinct classes based on the sequence similarity of their functional motor domains (Figure 2.6) (Hodge and Cope, 2000)). For historical reasons, class II myosins, which are highly abundant in muscle cells and were first discovered, are referred to as conventional myosins, whereas all other myosins are known as unconventional myosins (Sellers, 2000). In addition to their sequence similarity, myosins can be grouped corresponding to their function in either muscle contraction (class II), cargo transport (e.g., class V, VI) or as molecular anchors (e.g class I). Today, the dimeric myosins V and VI are probably the best-characterized unconventional myosins, both structurally and biochemically (Coluccio, 2020). Interestingly, myosin VI is the only myosin reported to walk in reverse direction and thus towards the "–" instead of the "+" end of F-actin (Wells et al., 1999).

Despite the pronounced divergence of the myosin family (Figure 2.6), the underlying mechanism of force production, involving ATP hydrolysis and actin binding, is conserved (Robert-Paganin et al., 2020). In agreement with a tight coupling of the structure and function, myosins share a common architecture consisting of a force-generating motor domain ($\sim$100 kDa), as well as a regulating neck and a tail domain (Figure 2.7A). The C-terminal tail domain is primarily responsibly for the formation of a functional myosin

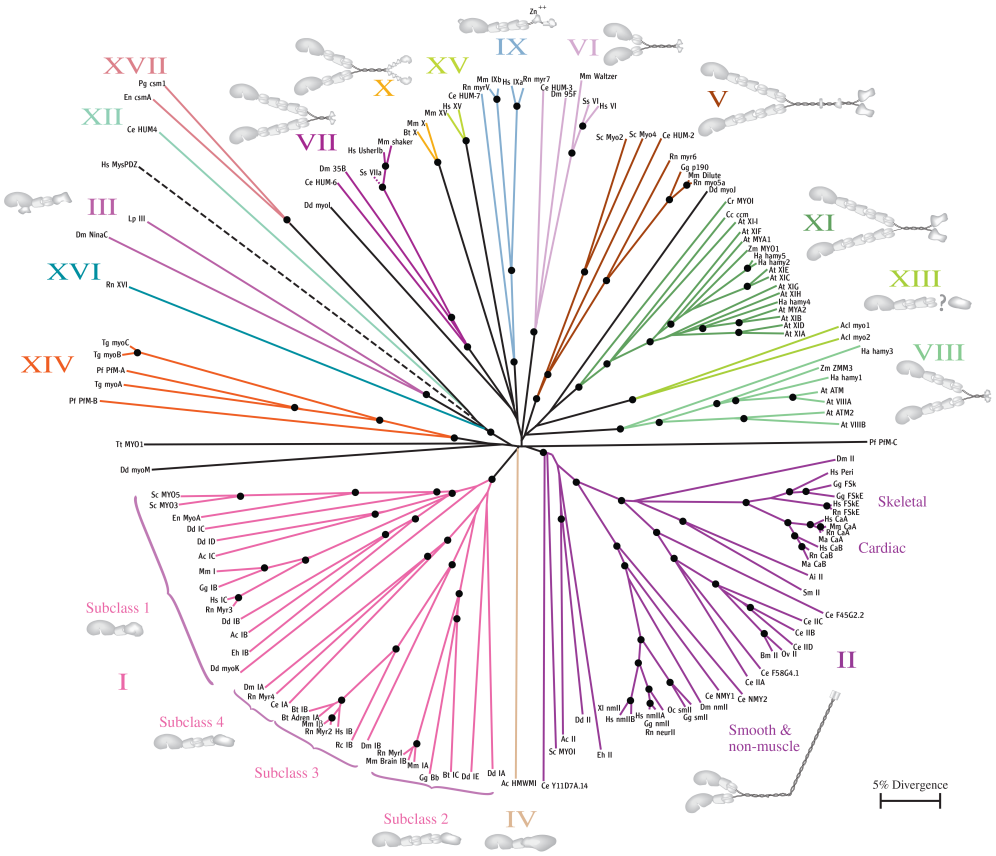

Fig. 2.6: Phylogenetic tree illustrating the complexity and diversity of the myosin family. Myosins are divided into classes based on the sequence similarity of their motor domain, which correlates with their functionality and cellular localization. The typical architecture of myosins within a specific class, e.g., monomeric vs. dimeric, is shown in grey. Figure reprinted from Hodge and Cope (2000) with permission from The Company of Biologists.

complex and varies significantly between myosin classes (Hartman et al., 2011, Robert-Paganin et al., 2020). For example, the tail domain of cargo-transporting myosins, which are typically double-headed to facilitate processive movement on F-actin by walking hand-over-hand (Yildiz et al., 2003), contains a coiled-coil motif promoting dimerization. The specificity of myosins is provided by varying cargo-binding domains at the C-terminus of myosin. For full functionality, most myosins furthermore require the binding of up to six light chains (LC, ∼15-20 kDa), which can be either essential (ELC) or regulatory light chains (RLC), to their neck region (Figure 2.7A) (Sellers, 2000). The tail domain of muscle myosins (class II, Figure 2.6) is exceptionally long, facilitating the assembly of myosin filaments from dimers. In the sarcomere, which is the smallest contractile unit within a muscle fiber, these filaments, also known as thick filaments, are aligned parallelly to thin filaments, which are composed of F-actin and regulatory ABPs such as tropomyosin and troponin. By concerted interactions of the thick filaments with the thin filaments, the two filament systems slide past each other, resulting in an effective shortening of the sarcomere and hence muscle contraction (Huxley, 2004).

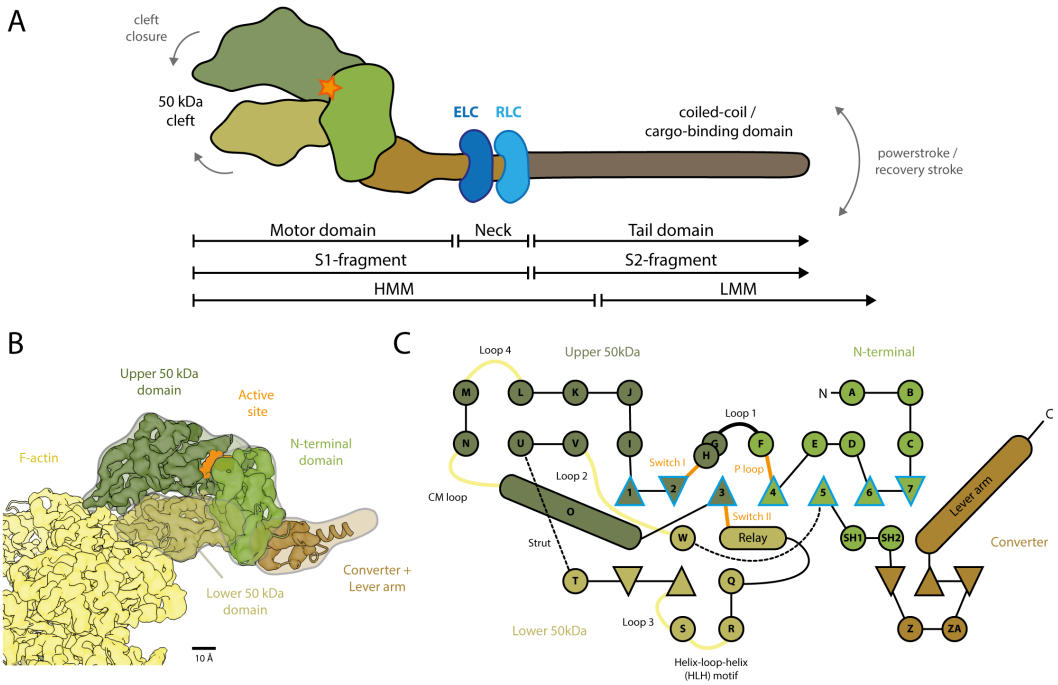

Fig. 2.7: Overall architecture of myosin with focus on the motor domain. **(A)** Schematic of a full-length myosin illustrating the coverage of commonly used myosin fragments originating from limited proteolysis (HMM: heavy meromyosin, LMM: light meromyosin). The U50 and L50 kDa domains are separated by a large cleft, which has to close to facility strong binding to F-actin. Light chains such as the essential light chain (ELC, dark blue) and regulatory light chain (RLC, light blue) depicted, promote complex assembly and force generation for many myosins. The extended tail domain of myosin significantly varies between myosins and is essential for specific cargo binding and assembly of functional myosin complexes. For color code and labels see B). **(B)** Schematic illustrating the conserved architecture of the myosin motor domain consisting of the actin-binding upper (U50, dark green) and lower 50 kDa domains (L50, tan), as well as the N-terminal domain (light green) and the converter domain which includes the lever arm (brown). The active site resides at the interface of the U50 and N-terminal domain (orange). Figure was adapted from Merino et al. (2019). **(C)** Full topology model of the motor domain illustrating the spatial organization of secondary structure elements. α-helices are shown as circles and β-strands as triangles. Important loops are shown in bold. Loops involved in the binding of F-actin are shown in yellow, while nucleotide-coordinating loops are highlighted in orange. The central seven-stranded β-sheet is essential for the mechanochemical coupling and commonly known as transducer (blue outlines). Model was reproduced from Behrmann (2012).

In contrast to the tail domain, the structure of the N-terminal motor domain is highly conserved in the myosin family, following a common blueprint (Figure 2.7). It consists of four domains, which are connected by flexible linkers: the upper and lower 50 kDa domains (U50 and L50), the N-terminal domain and the converter domain including the elongated lever arm (Figure 2.7B-C) (Houdusse et al., 1999, Rayment et al., 1993b). Biochemical studies suggested early on that surface loops from both the U50 and L50 domain are involved in actin binding (Figure 2.7C) (discussed in detail in Behrmann (2012)). Pioneering cryo-EM studies later confirmed the importance of these loops and reported a closure of the central actin-binding cleft (50 kDa cleft, separating the U50 and L50 domains) upon actin binding (Behrmann et al., 2012a, von der Ecken et al., 2016). The active site of myosin is located at the end of this cleft, at the interface of the U50 and

N-terminal domain (Figure 2.7B). It is composed of three loops, the P-loop, switch I and switch II, which are key for the coordination and hydrolysis of the adenonucleotide and accompanying Mg^{2+} ion (Figure 2.7C) (Coureux et al., 2004, 2003). While cleft closure directly affects the organization of the active site, the identity of the bound nucleotide is thought to dictate the conformation of the central seven-stranded β-sheet (transducer) (Coureux et al., 2003). The conformation of the transducer in turn affects the conformation of both the N-terminal and the converter domain, effectively controlling the orientation of the mobile converter domain and the connected lever arm. In this way, not only the nucleotide state is allosterically coupled to peripheral regions, but small conformational changes at the active site also get amplified eventually resulting in a large conformational change of the lever arm known as powerstroke (Figure 2.7A). While the basic concept of mechanochemical transduction in myosin is well-accepted, the structural details are only partially understood, primarily due to the lack of high-resolution structures of actin-bound intermediate states (recently reviewed in Robert-Paganin et al. (2020) and Schröder (2020), also see Section 2.3.2). In addition, it is currently unclear how sequence variations in myosin classes fine-tune the motor activity and give rise to divergent functions.

Due to its abundance in muscle, the actin-myosin (actomyosin) complex was the first track-motor system to be discovered and is therefore also best understood today (Needham et al., 1942). However, myosin is not the only molecular motor expressed in eukaryotic cells, but there are two more motors using microtubules as tracks. One of them is dynein, which belongs to the AAA-type ATPase family and forms a large ($\sim$ 2 MDa) multiprotein complex (Cho and Vale, 2012). The other molecular motor is the much smaller kinesin ($\sim$ 120 kDa), which walks in reverse direction compared to dynein (Stenoien and Brady, 1999). Interestingly, kinesin closely resembles myosin with respect to its structure and function. Specifically, the two proteins share a common core structure covering all nucleotide binding loops as well as the central β-sheet (Kikkawa et al., 2001, Sablin et al., 1996). Even more intriguingly, the same overall architecture and several conserved motifs such as the Walker A motif (Walker et al., 1982) were also found in some distinct ATPases and finally G-proteins, a family of guanine triphosphate (GTP)-binding molecular switches known to be critical for cellular signaling (Kull and Endow, 2013, Vale, 1996). For this reason, myosin, kinesin and finally G-proteins have been suggested to have evolved from a common evolutionary ancestor (Kull and Endow, 2013, Vale, 1996). In this context, the ancestral molecular unit resembles an universal chemomechanical engine. In combination with different gear wheels, i.e., varying insertions and extensions within the protein sequence, the same engine can power a plethora of molecular machines and thus processes.

2.3.2 The motor cycle

Myosin generates force via a complex and highly dynamic multi-step process. Different models of force generation have been proposed and refined over the years, ultimately giving rise to our current understanding of the myosin motor cycle (Figure 2.8, for a historical discourse see Behrmann (2012) and Koubassova and Tsaturyan (2011)). It combines the "swinging lever arm" hypothesis (Hanson and Huxley, 1953, Holmes, 1997, Huxley and Niedergerke, 1954), which first identified the central role of the lever arm in muscle contraction, with the ATP-hydrolysis cycle of myosin, also known as Lymn-Taylor-cycle according to its first in-detail description by Lymn and Taylor (1971). Based on the interactions of myosin filaments with F-actin in the muscle, the myosin motor cycle is also commonly referred to as the cross-bridge cycle (Koubassova and Tsaturyan, 2011).

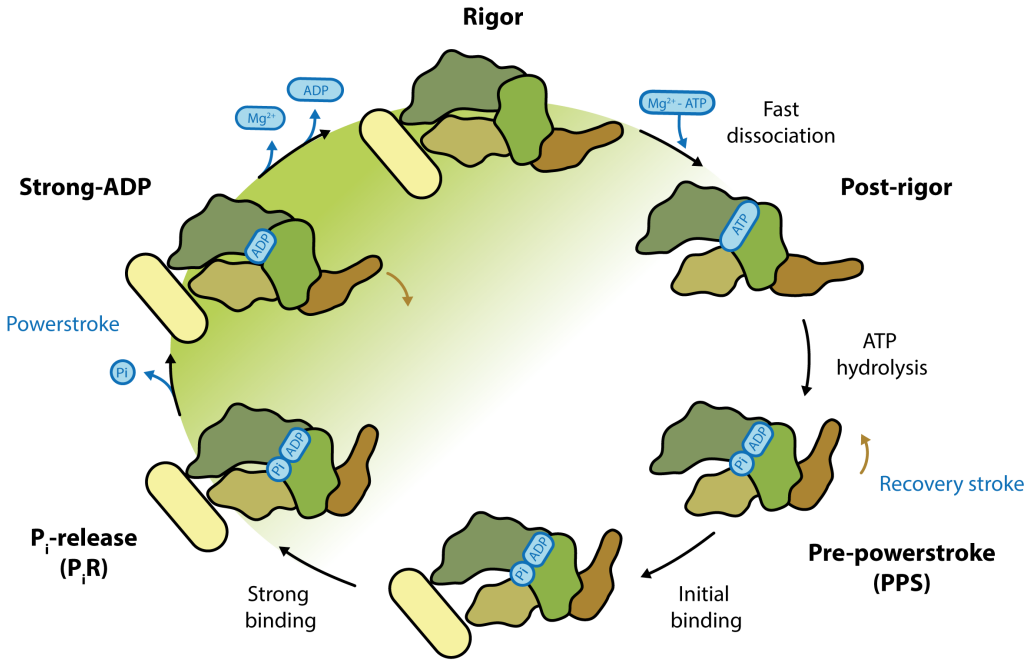

Fig. 2.8: Schematic of the force-generating ATPase cycle of myosin. ATP hydrolysis initially primes myosin in a high-energy pre-powerstroke state (bottom right). Binding to F-actin (yellow) promotes cleft closure and eventually triggers the release of P_i and the force-producing powerstroke (bottom left). The sequential release of Mg^{2+} and ADP leaves myosin strongly bound to F-actin in the rigor state (top left). Finally, binding of Mg^{2+}-ATP causes cleft opening and eventually dissociation of myosin (top right). The subsequent ATP hydrolysis gives rise to the recovery stroke, which re-primes myosin for a new ATPase cycle. Only key structural states are included for simplicity. ATP, Mg^{2+} and hydrolysis products are shown in blue. The motor domain of myosin is colored according to Figure 2.7. The transition from weak to strong binding states is illustrated by a color gradient (white to green). Figure adapted from (Merino et al., 2019), based on the model proposed by Robert-Paganin et al. (2020).

The myosin motor cycle (Figure 2.8) describes the structural transition of myosin throughout its ATPase cycle. In dependence of the bound nucleotide, myosin passes through

several, distinct structural states. Binding to F-actin eventually activates and further on regulates the motor activity, enabling effective force production (Robert-Paganin et al., 2020). The binding affinity of myosin for F-actin is defined by its structural state and hence the bound nucleotide. The myosin motor cycle can be divided into regimes of weak and strong actin binding (Figure 2.8). While this classification is valid for all myosin classes, the cycle kinetics, i.e., transition rates between states and the life-times of specific states, differ significantly between myosin classes, reflecting the distinct properties of the respective myosins (Greenberg et al., 2016). For example, release of P_i is rate limiting for fast myosins as found in muscle, while ADP release is limiting the ATPase activity of myosins acting as processive cargo transporters (Robert-Paganin et al., 2020). Consequently, cargo transporters spend more time in strongly bound states than muscle myosins. This time span is additionally prolonged under load, effectively ensuring that one myosin head always remains attached to facilitate processive hand-over-hand walking (Greenberg et al., 2016, Yildiz et al., 2003). The fraction of the motor cycle in which myosin remains bound to F-actin and hence in force-producing states is known as the duty-ratio (Coluccio, 2020). Prominent high duty-ratio myosins are myosin I, V and VI, which serve as molecular anchor and cargo transporters, respectively. Low duty-ratio myosins are typically found in muscle (class II), as they allow fast cycling, going along with high velocities and rapid movement (Robert-Paganin et al., 2020).

In the following paragraphs the myosin motor cycle (Figure 2.8) and associated key structural states will be briefly described. Furthermore, limitations of our current understanding and open research questions will be pointed out.

The pre-powerstroke state When detached from F-actin, myosin rapidly hydrolizes the bound ATP to ADP-P_i. The cleavage energy does not dissipate, but transfers to the protein. A series of conformational changes in key structural elements including the untwisting of the transducer, kinking of the relay helix and finally rotation of the converter domain (also see Figure 2.7) triggers a large swing of the lever arm known as recovery stroke (Robert-Paganin et al., 2020). The resulting primed lever arm is a hallmark of the high-energy pre-powerstroke state (PPS) of myosin (Figure 2.8), as determined by several crystal structures in complex with ADP-P_i analogs (Fisher et al., 1995, Smith and Rayment, 1996, Wulf et al., 2016). While the actin binding cleft is open in the PPS state, the nucleotide cleft is closed, facilitating a tight coordination of Mg^{2+}-ADP and P_i. As this conformation is incompatible with the structural rearrangements required for the relaxation to a lower-energy state, myosin is auto-inhibited in the PPS state and has to be activated through interactions with F-actin.

Eventually binding to F-actin triggers a cascade of conformational changes facilitating the efficient release of hydrolysis products and thereby progression of the ATPase cy-

cle. Although no structural data is available yet, biochemical studies suggest a multi-step binding process in which the closure of the actin binding cleft is essential for the transition from an initial weak binding state (μM affinity) to a force-producing strong (nM affinity) binding state (Figure 2.8, recently reviewed in Robert-Paganin et al. (2020) and Sweeney et al. (2020)).

The P_i-release state The sequential release of hydrolysis products, in particular P_i, destabilizes the high-energy state of myosin, promoting the release of conformational strain. This process culminates in a large force-producing swing of the lever arm, known as powerstroke (Figure 2.8). By rotating by approximately 60 °, the end of the lever arm gets significantly displaced, giving rise to step lengths as large as 74 nm in case of the double-headed myosin V (Fischer et al., 2005, Yildiz et al., 2003).

While the milestones of force generation are well-accepted, the relative timing of critical events, i.e., cleft closure, P_i release and the powerstroke, remains controversial. Based on recent functional studies and crystal structures of myosin in a putative P_i-release (P_iR) state, Robert-Paganin et al. lately proposed a unifying model of force generation. They suggested, that initial weak binding of myosin to F-actin elicits a structural transition from the PPS to the P_iR state. A hallmark of this transitions is the partial closure of the central 50 kDa cleft, resulting in a structural intermediate between the PPS and strong-ADP state with moderate binding affinity. Cleft rearrangements are furthermore coupled to a large switch II movement, which opens an exit tunnel for P_i (Llinas et al., 2015), in agreement with a previously proposed back door mechanism (Cecchini et al., 2010, Lawson et al., 2004, Yount et al., 1995). Interestingly, opening of the tunnel only marginally changes the lever arm orientation; thus is not directly coupled to the force producing powerstroke (Llinas et al., 2015). In line with this, the transducer and relay helix are in a strained conformation, as seen in the PPS state (Llinas et al., 2015). Yet, these findings are in contradiction to convincing biochemical evidence suggesting that the powerstroke precedes the release of P_i (recently reviewed in Robert-Paganin et al. (2020)). In their unifying model Robert-Paganin et al. propose that P_i release from the active site is a gating event for both the powerstroke and the complete closure of the 50 kDa cleft required for strong binding. P_i is, however, not directly set free, but rebinds to a second binding site at the mouth of the exit tunnel near the solvent (Llinas et al., 2015). Here it possibly remains bound until the powerstroke has completed, explaining why P_i cannot be detected in the solvent earlier (Robert-Paganin et al., 2020). While this model convincingly summarizes our current knowledge of how myosin gets activated by actin, it is also incomplete. We still lack details on how actin interacts with myosin in the PPS and P_iR states and hence promotes cleft closure. Moreover, it is unclear how the cleft closure and the lever arm swing are coupled and timed. Solving high-resolution structures of weakly-bound myosin

states will likely be key to answer these questions.

The strong-ADP state Closure of the actin binding cleft significantly increases the binding affinity of myosin for F-actin from previously µM to nM (Robert-Paganin et al., 2020). Due to its strong binding and bound nucleotide, the associated state is commonly referred to as strong-ADP state (Figure 2.8). It represents the major force-generating state and is particularly long-lived in myosins serving as anchors or cargo transporters such as myosin I, V and VI. For this reason, these myosins have been preferentially chosen when studying the structure of the actomyosin complex in the ADP state by cryo-EM (Gurel et al., 2017, Mentes et al., 2018, Wulf et al., 2016). Today only one high-resolution structure of this state is available (Mentes et al., 2018), showing that ADP is primarily bound to the P-loop and comes with a twisted transducer. The lever arm adopts a relaxed, post-powerstroke conformation, which is accompanied by a partial unwinding of the C-terminus of the relay helix, but no kinking as it is the case in the PPS state.

The exact mechanism by which Mg^{2+}-ADP is released from the active site remains to be elucidated. Yet, it is known that Mg^{+2} is released first. In this way, it can no longer mediate interactions between ADP, the P-loop and switch I, possibly resulting in an insufficient coordination of ADP, which eventually leads to its loss (Robert-Paganin et al., 2020).

The rigor state Once ADP is released, myosin remains strongly bound to F-actin in the rigor state until Mg^{2+}-ATP binds to its active site (Figure 2.8). As ATP is readily available in living cells, the rigor state is in general short-lived. After cell death, however, ATP gets quickly depleted resulting in the primary population of the rigor state, which is for this reason named after the associated pathological muscle stiffness known as rigor mortis (Vanderwee et al., 1981). Due to its stability in absence of ATP, the rigor state was not only the first to be solved by cryo-EM in pioneering studies (Behrmann, 2012, Behrmann et al., 2012a, von der Ecken et al., 2016), but also remains the most studied state of the actomyosin complex (Banerjee et al., 2017, Doran et al., 2020, Fujii and Namba, 2017, Gurel et al., 2017, Mentes et al., 2018, Risi et al., 2020, Vahokoski et al., 2020, Wulf et al., 2016). Interestingly, several myosins (I, II, V, VI, XIV) have been successfully crystallized in a rigor-like state in the absence of F-actin (Coureux et al., 2003, Ménétrey et al., 2005, Robert-Paganin et al., 2019, Shuman et al., 2014, Yang et al., 2007), suggesting that this conformation is also accessible in solution (Sweeney et al., 2020).

In agreement with strong binding, the central 50 kDa cleft is closed in the rigor state, whereas the nucleotide binding cleft is unoccupied and therefore open. Opening of

the nucleotide cleft requires a substantial shift of the P-loop coupled to pivoting of the N-terminal domain (Mentes et al., 2018). Furthermore, ADP release gives rise to an even more twisted conformation of the central transducer β-sheet. While there is no kink in the relay helix, as characteristic for a relaxed lever arm position, the lever arm position is not identical in the strong-ADP and rigor states, but slightly changes (also see Figure 2.9) (Mentes et al., 2018). Assuming that this swing is required for ADP release, it directly offers an explanation how load can stall force-sensitive myosins in the strong-ADP state (Mentes et al., 2018, Robert-Paganin et al., 2020).

The post-rigor state Binding of Mg^{2+}-ATP to the active site is thought to open the central 50 kDa cleft, resulting in a significantly reduced binding affinity and rapid detachment of myosin from actin (Figure 2.8) (Bagshaw and Trentham, 1974, Goody et al., 1977). Myosin now populates the post-riogr state, which was the first state that was successfully crystallized and was originally referred to as near-rigor (Rayment et al., 1993a). Within this state, an open actin binding cleft is accompanied by an untwisted transducer and a relaxed, post-powerstroke position of the lever arm, which yet slightly deviates from its position in the rigor state. Evntually, hydrolysis of ATP to ADP-P_i gives rise to the recovery stroke, re-priming the lever arm for another force-generating motor cycle (Figure 2.8).

Despite half a century of research dedicated to the motor cycle of myosin, its details are still not fully uncovered. In particular, the field lacks knowledge about the nature and timings of the transitions between key structural states (Figure 2.8). How does actin activate myosin? How is the powerstroke coupled to the cleft closure and phosphate release? What initiates ADP release? And how does ATP binding cause dissociation? Answering these questions is challenging, as most transitions involve weak actin-binding states, such as the actin-bound PPS/ P_iR and post-riogr state, which are intrinsically short lived. This characteristic has so far inhibited all structural characterization attempts. Stabilization of these states by, for example, nucleotide analogs, small molecules or mutations could help to overcome this bottle neck. In addition, future advances in the method of time-resolved cryo-EM could make a structural characterization of short-lived states feasible (Frank, 2017).

To ultimately unravel force-generation by myosin, one would need to reconstruct a high-resolution molecular movie of the full myosin motor cycle from a number of cryo-EM and crystal structures supplemented by functional and kinetic data. A comparison of the structures already available illustrates that the complete cycle would ideally be solved for a single myosin, as the rigor states of different myosins are in general similar but do not superimpose (Figure 2.9) (Merino et al., 2019). While many studies are dedicated to conventional myosins for both historical reasons and their eminent medical relevance,

actin-bound states other than the rigor are difficult to trap for low duty-ratio myosins due to their short lifetime. Consequently, high duty-ratio myosins such as myosin I, V and VI are better choices. Especially, the latter two represent promising candidates considering the vast number of crystal structures of different states already available (for an overview see Sweeney et al. (2020)). Moreover, myosin V and VI were reported to by sensitive to the nucleotide state of F-actin (Zimmermann et al., 2015), adding another interesting research aspect. Eventually, it would be optimal to have complete cycles for a number of myosins from distinct classes, as their comparison would help to decipher how differences in sequence translate into different motor properties.

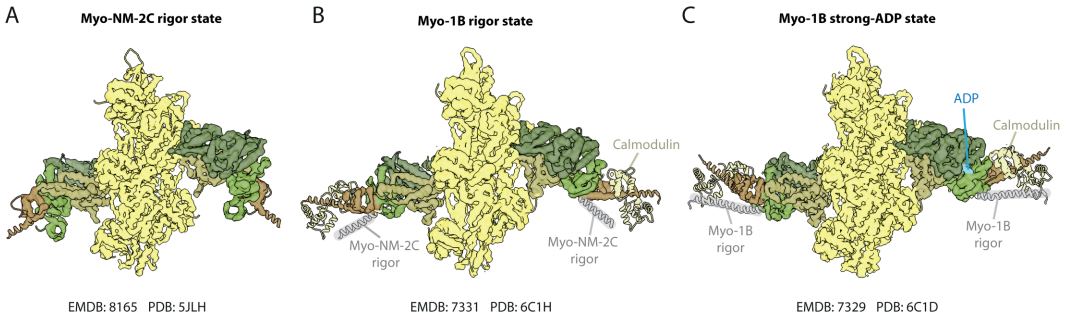

Fig. 2.9: Comparison of high-resolution actomyosin complexes solved by cryo-EM. **(A)** Structure of myosin NM2c in the rigor state (von der Ecken et al., 2016). **(B)** Superposition of the rigor states of myosin 1B (colored, Mentes et al. (2018)) and myosin NM2C (grey, atomic model only, von der Ecken et al. (2016)), highlighting distinct lever arm positions. **(C)** Superposition of the strong-ADP (colored) and rigor (grey) states of myosin 1B (Mentes et al., 2018), illustrating the small swing of the lever arm associated with ADP release. Figure adapted from (Merino et al., 2019).

The nature and function of structural flexibility within myosin is an additional aspect that is waiting to be further investigated. A number of studies have reported structural dynamics that are possibly not represented in crystal structures due to crystal packing (Klein et al., 2008, Nesmelov et al., 2008, Sun et al., 2008, Thompson et al., 2008). Intriguingly, spectroscopic (Klein et al., 2008) and cryo-EM data (Behrmann, 2012, Behrmann et al., 2012a) even suggest different degrees of cleft opening within the low-energy rigor state. Moreover, a conformation similar to the rigor state has been found alongside the strong-ADP state for ADP-bound myosin 1B, suggesting that at least one stable intermediate state exists (Mentes et al., 2018). Further cryo-EM studies of actomyosin complexes are required to elucidate the extent and role of structural heterogeneity and dynamics in the myosin family. Recent developments in cryo-EM (also see Section 2.4.6) have now also made this method suitable for the characterization of monomeric myosin, which was previously limited to crystallography. In this way, the structural dynamics could also be assessed in the absence of F-actin. Finally, cryo-EM can also give invaluable insight into the structure of full-length, dimeric myosin, instead of just the motor domain or the S1

fragment, as lately demonstrated by two independent pioneering studies (Scarff et al., 2020, Yang et al., 2020).

2.4 Transmission electron microscopy

Different imaging techniques which rely on electrons are available, including transmission electron microscopy (TEM), the main experimental method used in this thesis, scanning electron microscopy and scanning transmission electron microscopy. While TEM was first primarily applied in the field of material sciences, its potential for biological samples was soon recognized. Nowadays, TEM of vitrified, biological samples (cryo-EM) is considered a standard method for high-resolution structure determination. The importance of this technique is also reflected by the Nobel price recently awarded for the development of cryo-EM. Overall, two Nobel prizes were granted for developments associated with TEM. On the one hand, Ernst Ruska and colleagues were awarded in 1986 for their fundamental work in electron optics, which led to the design of the first electron microscope (The Nobel Foundation, 1986). On the other hand, Jacques Dubochet, Joachim Frank and Richard Henderson jointly received a Nobel prize in 2017 for developing the methods of high-resolution cryo-EM dedicated to biological samples (The Nobel Foundation, 2017). Despite these breakthroughs and the establishment of TEM in the field of structural biology, cryo-EM and especially cryo-ET have surely not yet reached their peak potential.

Transmission images collected with an electron microscope are commonly referred to as micrographs. In contrast to the data generated by X-ray diffraction, the micrographs represent real space projections of the sample. Thus, they include not only amplitude, but also phase information, thereby allowing a direct reconstruction of the underlying 3D structure. Within this chapter, the basic setup of a transmission electron microscope (TEM) is presented (Section 2.4.1). Next, the principles of image formation are introduced, followed by sections focusing on the imaging of biological samples (Section 2.4.2 to 2.4.3). Consecutively, the theoretical basis of the 3D reconstruction from 2D TEM micrographs is given and extended by details on the challenges of helical samples (Section 2.4.4 to 2.4.5). Finally, this chapter closes with an overview of recent advances in the field of cryo-EM (Section 2.4.6).

2.4.1 The microscope

The basic setup of a transmission electron microscope (TEM) closely resembles the one of a light microscope (Figure 2.10). By using electrons instead of photons, the theoretical

resolution limit of the microscope is significantly improved from $\sim$ 300 nm for visual light (500 nm) to $\leq$ 1 Å (300 kV acceleration voltage, corresponding to a wavelength of $\sim$ 2 pm) according to the Abbe criterion (Williams and Carter, 2009). In reality, the resolution one can achieve for a 3D reconstruction from TEM data is not limited by the wavelength, but by other factors such as the pixel size, lens aberrations, sample drift and beam damage. While the latter factors are difficult or even impossible to control, the pixel size can be easily adjusted to allow high-resolution. According to the sampling theorem, the achievable resolution is limited to two times the pixel size, e.g., a resolution of 2 Å requires at least a pixel size of 1 Å. The corresponding spatial frequency $f_{\text{Nyquist}} = (2 \cdot \text{pixel size})^{-1}$ is also known as Nyquist frequency and defines the highest frequency that can be sampled without loss of information at a given pixel size (Nyquist, 1928).

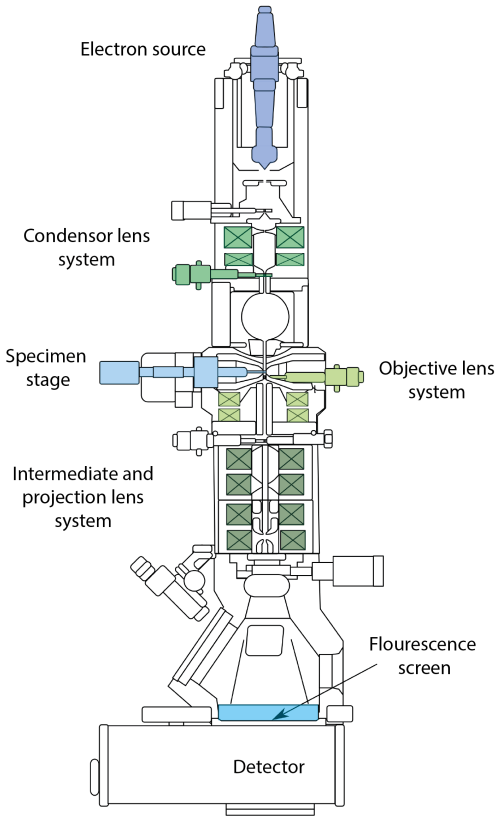

Fig. 2.10: Schematic illustrating the internal components of a basic transmission electron microscope. Lens systems are highlighted in hues of green, while the electron source, specimen stage and florescence screen are colored in shades of blue. Figure adapted from Gringer (2009), according to the creative commons license.

When using electrons instead of photons for imaging, the microscope has to be tailored to negatively charged particles. First, glass lenses need to be replaced by electromagnetic lenses. Second, the microscope column has to be evacuated to a high vacuum, to avoid

unwanted scattering of the electron beam with the residual gas. Finally, an electron detector has to be installed. In the following, the basic components of a TEM and their function are described.

A number of electron sources, which exploit different mechanism for electron generation, i.e., thermal emission or the tunnel effect, are available (Egerton, 2005). They do not only strongly vary in their pricing, but also in the coherence and brightness of the emitted electrons. For instance, the coherence of a lanthanum hexaboride (LaB_6) cathode, a standard thermal emitter, is ΔE=1.5-3 eV, while a high-brightness field emission gun (FEG) reaches a coherence up to ΔE=0.2 eV (Reimer and Kohl, 2008). As a high coherence is essential to achieve high-resolution, only FEGs are used in microscopes dedicated to data acquisition, while LaB_6 cathodes are routinely used in small screening microscopes (Williams and Carter, 2009).

Emitted electrons are accelerated along the column and towards the sample by applying a high voltage (Figure 2.10). While higher acceleration voltages increase the theoretical resolution, they can also reduce the overall contrast of TEM images. Therefore, the voltage needs to be adjusted to radiation-sensitive biological samples (Williams and Carter, 2009). Voltages of 120 keV for screening microscopes and 200 keV or 300 keV for high-end microscopes dedicated to data acquisition have prevailed in the field of structural biology.

Every TEM comprises four lens systems, including a condensor, objective, intermediate and projector system (top to bottom, Figure 2.10) (Reimer and Kohl, 2008). The condensor system at the top of the microscope is used to achieve a parallel and homogeneous illumination of the sample. The consecutive objective system either directly follows the specimen stage (Figure 2.10), or in case of a three lens system even encloses it. The objective system is the most important lens system in the microscope and defines both the central axis of the beam path and the achievable resolution (Reimer and Kohl, 2008). Therefore, all other lens systems are aligned relative to the objective system. Towards the end of the column, the intermediate and projection lens systems are used to magnify the real space transmission image of the sample up to 10^6-times and eventually project it onto either a florescence screen or an electron detector (also see Section 2.4.6) (Reimer and Kohl, 2008). Each lens system consists of several lenses, at least two to three, whose electromagnetic field can be tuned by the current applied. Thereby, lenses can among others shift and tilt the electron beam, or correct for astigmatism without changing the energy of electrons (Williams and Carter, 2009). The condenser and objective systems include additional apertures to remove off-axis electrons (Figure 2.10). The objective pinhole aperture is of particular relevance, as it retains elastically scattered electrons with a comparably large scattering angle (Egerton, 2005). Thereby, it directly increases the

contrast (amplitude contrast, also see Section 2.4.2) of the acquired image. Yet, the usage of an objective aperture, especially a small one, has to be considered thoroughly, as the increased contrast comes at the cost of a reduced overall resolution.

Some TEMs have additional energy filters installed to increase the contrast of the micrographs. Here, electrons with altered energy due to inelastic scattering are removed from the electron beam (also see Section 2.4.2) (Reimer and Kohl, 2008). For this purpose, a Wien filter is used, which utilizes a magnetic field to deflect the electron beam in dependence of its energy (Reimer and Kohl, 2008). Once the beam is split according to its energy, the fraction of the beam with the desired energy can be selected by insertion of a slit, with a typical slit width of 12 eV to 20 eV. By selecting electrons which have not deposited energy onto the sample by inelastic scattering, the noise of the transmission images can be considerably reduced, resulting in an increased signal-to-noise ratio (SNR).

2.4.2 Image formation and the contrast transfer function

A TEM image is created through interactions of the electron beam with the sample. These interactions can be categorized into two types, namely elastic and inelastic scattering (Reimer and Kohl, 2008). In case of elastic scattering, electrons only change their direction when interacting with the atoms of the sample, while their energy transfer can be neglected. In contrast, inelastically scattered electrons are hardly deflected from their path, but their energy and thus wavelength is altered, as they deposit energy into the sample (Egerton, 2005). Elastically scattered electrons contribute constructively to the image contrast, while inelastically scattered electrons primarily cause noise and furthermore beam damage in radiation-sensitive biological samples (also see Section 2.4.3) (Williams and Carter, 2009).

Elastic scattering gives rise to two kinds of contrast, known as amplitude contrast (or scattering contrast) and phase contrast (Reimer and Kohl, 2008). The amplitude contrast is simply created through the presence or absence of electrons at a specific position of the micrograph. Specifically, electrons that have interacted with the sample and are scattered at large angles do not hit the detector. Thus, the image appears dark at the corresponding position as in a shadow image (Williams and Carter, 2009). The amplitude contrast can be enhanced through an objective aperture, which retains electrons with large scattering angles, that would still have hit the detector (also see Section 2.4.1). In contrast to the amplitude contrast, which can be understood using classical physics, electrons need to be considered as waves in case of the phase contrast (Reimer and Kohl, 2008). Here, elastic interactions cause a phase shift of a electron, while its wavelength remains unchanged. This allows the scattered electron wave to interfere with the unscattered, primary electron

wave. In this way, the differences in phases are translated into changes, i.e., amplification or reduction, of the amplitude of the resulting electron wave, which eventually contributes to the real space transmission image (Egerton, 2005). A maximum phase contrast is achieved for phase shifts which are integral multiples of π (180 °), resulting in constructive or destructive interference. Biological samples, however, cause phase shifts of $\sim \frac{\pi}{2}$ (90 °) (Reimer and Kohl, 2008), which only marginally change the amplitude. Hence, the phase shift needs to be increased to generate sufficient contrast (also see Section 2.4.3). An additional constant phase shift is, on the one hand, introduced through the spherical aberration C_s of the specific microscope (Reimer and Kohl, 2008). On the other hand, a variable phase shift can be applied by defocusing. The overall phase shift $\gamma(k,\Delta z)$ can be described through

$$\gamma(k,\Delta z) = \frac{\pi}{2}\left(\lambda^3 C_s k^4 - 2\lambda\Delta z k^2\right)$$

with the spatial frequency k, defocus Δz and wavelength λ (Scherzer, 1949). The contrast enhancement achievable by defocusing is, however, limited, as defocusing negatively affects the high-resolution information (Glaeser et al., 2021). Therefore, only a small defocus is routinely used in the field of structural biology, typically $\leq$ 3-4 µm. Alternatively or complementary to defocusing, an additional phase shift can nowadays also be introduced using a phase plate (Glaeser, 2013), which, however, has other drawbacks (also see Section 2.4.6).

All imaging systems have in common, that they are imperfect. Thus, they do not produce an image that is completely identical to the original object. Instead, the contrast of the object is altered by the contrast transfer function (CTF), according to the following relation

$$\text{Image contrast} = \text{CTF} \cdot \text{Object contrast}$$

In an ideal case the CTF would be a constant value, in reality, however, it is usually frequency depended. Specifically, the CTF for TEM oscillates with the spatial frequency k according to its effect on the phase shift $\gamma(k,\Delta z)$ (Frank, 1973, Wade and Frank, 1977). In addition, the amplitude decreases with the frequency, thereby dampening high-resolution information. Mathematically the CTF can be described as

$$CTF(k,\Delta z) = \left(\sqrt{1-A^2}\cdot\sin\left(\gamma(k,\Delta z)\right) - A\cdot\cos\left(\gamma(k,\Delta z)\right)\right)\cdot e^{-\frac{B}{4}\cdot k^2}$$

with the amplitude contrast A and the B-factor B (Penczek, 2010a). While the first term accounts for the frequency depended oscillation of the CTF, the latter, also known as

envelope function, represents the exponential decay of the amplitude. The B-factor summarizes a number of imaging factors that negatively affect the transmission of the high-resolution signal, including the limited coherence of the beam, the energy dispersion and the sample drift. The overall B-factor of a TEM data set can be further increased through alignment and interpolation errors during the processing.

In practice, the CTF causes a frequency dependent inversion of the contrast and dampening of fine details (Figure 2.11). Moreover, the squared 2D Fourier transform, knows as power spectrum, illustrates that all information is lost at the zero crossings of the CTF, resulting in disconnected rings of information within the spectrum, which are also known as Thon rings (Thon, 1971). Hence, it is necessary to vary the defocus during a data collection, to collect information for all frequencies within one data set (Penczek, 2010a). In addition, the CTF needs to be computationally corrected for to enable the reconstruction of a high-resolution 3D structure. While the information at the zero crossings cannot be recovered, the CTF correction, on the one hand, rectifies the signal (to all positive values, phase flipping) and, on the other hand, boosts the amplitudes with the aim to not only counteract the envelope function, but also enhance the signal close to the zero-crossings (Penczek, 2010a,b) As the number of zero crossing increases considerably with the defocus, the usage of low defocus values is essential to reach high-resolution.

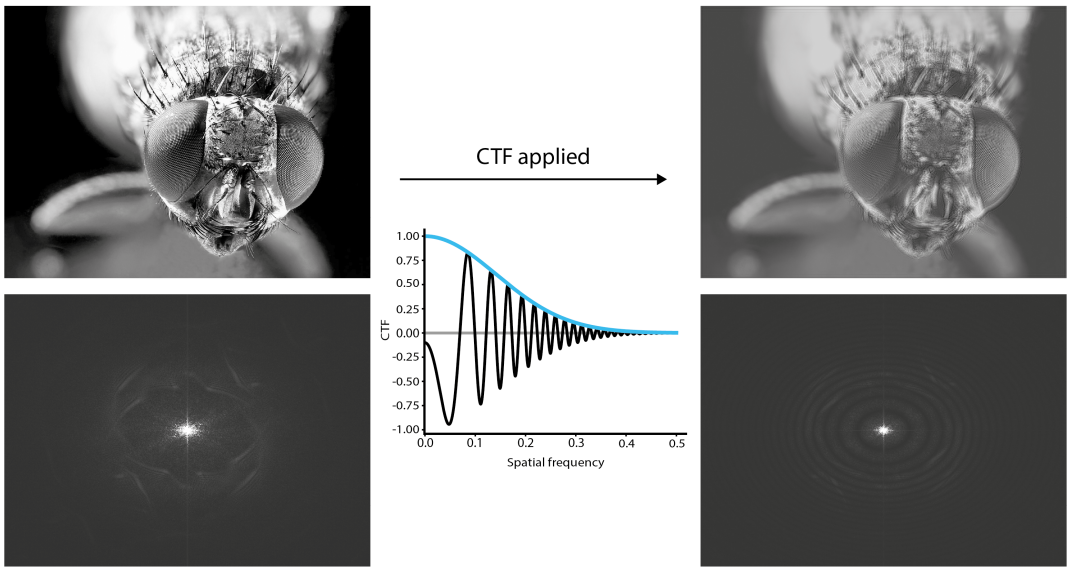

Fig. 2.11: Illustration of the effect of the CTF on the image contrast. **(Left)** Photograph of a fly (top, kindly provided by Rainer Pospich) and the corresponding power spectrum (bottom). A typical CTF with a defocus of 0.5 µm and a mild B-factor of 100 Å^2 (envelope function in blue) was simulated and multiplied with the original image **(Right)**, resulting in a frequency dependent inversion of the contrast and dampening of high-resolution features (top). The information at the zero-crossings of the CTF is lost, as visualized by the Thon rings in the power spectrum (bottom).

2.4.3 TEM for biological samples

Samples for TEM need to be fixed to a specimen holder (typically a grid, also see Section 3.2) to withstand the high-vacuum in the column. While this is straight forward for solid materials, liquid biological samples can, for example, be fixed by negative staining or vitrification. While biological samples range from whole tissues, over sections to isolated proteins, this section focuses on the handling and imaging of isolated proteins.

Negative staining The easiest and fastest way to fix a biological sample onto a grid is to stain it with a heavy metal solution like uranylformate or uranylacetate and air-dry it (Orlova and Saibil, 2011). The stain accumulates on the surface of the protein, forming a 3D imprint. Due to the high atomic number, the heavy metal atoms cause strong scattering (amplitude contrast, also see Section 2.4.2) resulting in a dark silhouette around the bright protein on the micrograph. Thanks to the enhanced contrast, even small proteins can be imaged (Booth et al., 2011). Although negative stain TEM has many advantages, such as high image contrast as well as insensitivity and durability of samples, it also has some serious drawbacks. Specifically, the achievable resolution is limited to $\sim$ 18-20 Å by the grain size of the heavy metal stain (Scarff et al., 2018). In addition, only the surface of a protein can be depicted, as the stain cannot penetrate into cavities. Finally, the acidic pH of most staining solutions and the drying process can cause aggregation of the protein or artificial conformations (Booth et al., 2011). For these reasons, negative stain TEM is not suitable for high-resolution structure determination. Still, it is indispensable for the initial evaluation of the sample quality and protein structure.

Vitrification Alternatively, biological samples can be vitrified in an aqueous buffer solution. Here, the protein solution is applied to a grid and cooled so rapidly that ice crystals, which would destroy the sample, have no time to form. In this way, the protein is embedded in a thin amorphous ice layer in a near-native condition allowing the determination of a high-resolution structure (Dubochet et al., 1988). In practice, the grid is plunged into a liquid, such as ethane or a propane-ethane mixture, which is cooled to at least the glass phase transition temperature ($T = -137°C$ at normal pressure, Dubochet et al. (1988)). While liquid nitrogen ($T = -196°C$) would be a more obvious cooling agent, it is not suitable due to the Leidenfrost effect (Leidenfrost, 1796). Liquid nitrogen quickly evaporates when in contact with a warm surface, resulting in a layer of vapour, which delays the cooling process. Although vitrification is the standard and sole fixation method for high-resolution structural biology, it is not straightforward requiring *inter alia* the optimization of plunging conditions, careful handling of the fragile grids and constant cooling (Orlova and Saibil, 2011). Furthermore, the imaging of vitrified samples using cryo-EM struggles

with an intrinsically weak contrast, as discussed in the next paragraphs. Details on the implementation of both fixation methods are given in Sections 3.2.1 to 3.2.2.

The overall contrast and suitable imaging conditions are dictated by the nature and composition of biological samples. In general, elastic scattering of electrons gives rise to both amplitude and phase contrast within TEM micrographs (see Section 2.4.2). In case of biological samples, the contrast is intrinsically weak resulting in a low signal-to-noise ratio (SNR). This is primarily due to the composition of the sample, with carbon, oxygen and nitrogen as main elements. These light atoms have comparably small cross sections. Thus, they are less likely to interact with electrons and also give rise to smaller scattering angles (Williams and Carter, 2009). Consequently, the amplitude contrast is weak for biological samples and the phase contrast is the predominant contrast.
The amplitude contrast can be enhanced considerably by negative staining of samples with heavy atoms, as the cross section and hence the probability of elastic and inelastic scattering is proportional to $Z^{\frac{4}{3}}$ and $Z^{\frac{1}{3}}$, respectively, with the atomic number Z (Robenek, 1995). However, the resolution of negatively stained samples is limited. For this reason, proteins are instead vitrified in an aqueous buffer solution to preserve their native structure for high-resolution studies. As buffers are also composed of light elements, they cannot produce a sufficient amplitude contrast. Imaging of vitrified samples therefore relies on the phase contrast.

Unfortunately, biological samples are also weak phase objects, shifting the phase of the scattered electron beam by approximately $\frac{\pi}{2}$ (90 °) (Reimer and Kohl, 2008). Interference of the scattered and primary electron wave consequently only changes the amplitude of the resulting wave minimally, making the introduction of an additional phase shift indispensable. For this reason, micrographs are routinely collected in underfocus (also see Section 2.4.2). Alternatively, a phase plate can be used, to alter the phase shift of the unscattered, primary electron beam. This strategy is especially beneficial for small proteins with a molecular weight $\leq$ 50-100 kDa, as the scattering probability decreases with the molecular weight (also see Section 2.4.6).

Not all electrons that interact with the sample are elastically scattered. On the contrary, a majority of electrons is inelastically scattered resulting in a deposition of energy into the sample. There are three times more inelastic scattering events than elastic ones at 300 kV acceleration voltage (Henderson, 1995, Smith and Langmore, 1992). This is especially disadvantageous for biological samples, as they are radiation-sensitive, i.e., are damaged by the deposited energy. An increment of the acceleration voltage would reduce the amount of inelastic scattering. At the same time, it would also reduce the probability of elastic scattering and thereby the overall contrast and is therefore not optimal (Williams and Carter, 2009). Instead, biological samples are imaged using low electron doses to

keep the beam damage to a minimum. Furthermore, the sample thickness is reduced, as the probability of inelastic scattering is proportional to the sample thickness. By doing so, harmful multi-scattering events can also be avoided.

Besides beam damage, specimen drift is a major impediment of high-resolution cryo-EM. The drift of the specimen stage and beam-induced motion of the vitreous ice layer due to charging and energy deposition cause motion blurring within micrographs (Brilot et al., 2012). The beam-induced drift can be reduced by using, for example, lower electron dose rates or gold grids, which have superior conductivity compared to the standard copper grids (Russo and Passmore, 2016). Yet, the problem of motion blurring persists. For this reason, a movie consisting of $\sim$ 30-100 frames is nowadays collected instead of a single image integrating over the whole exposure time. The drift can then be corrected by alignment of the individual frames prior to averaging (Li et al., 2013). Another advantage of collecting movies is that the total electron dose can be computationally reduced during the processing to mitigate the effect of beam damage.

In summary, a weak contrast and low SNR are representative for cryo-EM micrographs, despite and also because of the adjustments required for the imaging of biological samples, i.e., low electron dose. An untrained eye can often not identify the protein molecules on a micrograph, but only sees grey noise. Moreover, beam damage and specimen drift are major impediments that need to be taken care of. Therefore, sophisticated processing strategies and algorithms are key for the reconstruction of a high-resolution structure.

2.4.4 Single particle analysis

Each cryo-EM micrograph depicts a number of 2D projection images of individual protein particles, which can be extracted as 2D particle images. The reconstruction of a 3D structure from many 2D particle images is the heart of the structural analysis. The workflow is commonly referred to as single particle analysis (SPA) and is based on the Fourier slice theorem (Bracewell, 1956). According to the theorem, the 2D Fourier transforms of projection images of the same object represent 2D slices of the 3D Fourier space (perpendicular to the projection direction, Figure 2.12). Although we do not have several transmission images of the same object, as it would be the case in tomography, the individual protein particles are assumed to be identical, i.e., to represent a single particle, allowing the combination of all 2D Fourier transforms. Hence, the 3D real-space structure can be reconstructed through an inverse 3D Fourier transformation provided that the 3D Fourier space is sufficiently filled. Incomplete filling corresponds to missing information and will result in an inaccurate 3D structure. Specifically, the structure will be elongated perpendicular to the missing view, i.e., if only side-views are present, there is no information about the depth of the structure. For this reason, a uniform distribution

of the protein orientation on the grid is essential to receive projection images of all possible views. Some proteins adopt a preferred orientation on the grid due to, for example, their shape or unspecific interactions with the air-water interface, which can also cause denaturation (D'Imprima et al., 2019, Glaeser, 2018). In these cases, the usage of grids with a continuous support layer such as carbon or graphene oxide, onto which the protein molecules can attach, might be necessary (Glaeser, 2018, Russo and Passmore, 2016). Alternatively, the addition of detergents or surfactants such as polylysine can positively affect the orientation of protein particles within the amorphous ice layer (Bernecky et al., 2016, Chen et al., 2019). Finally, tilting of the specimen stage during the data acquisition can be used to capture additional views. This comes, however, at the cost of a lower contrast and a more complex analysis process (due to the increased sample thickness and defocus variation within the image) (Tan et al., 2017).

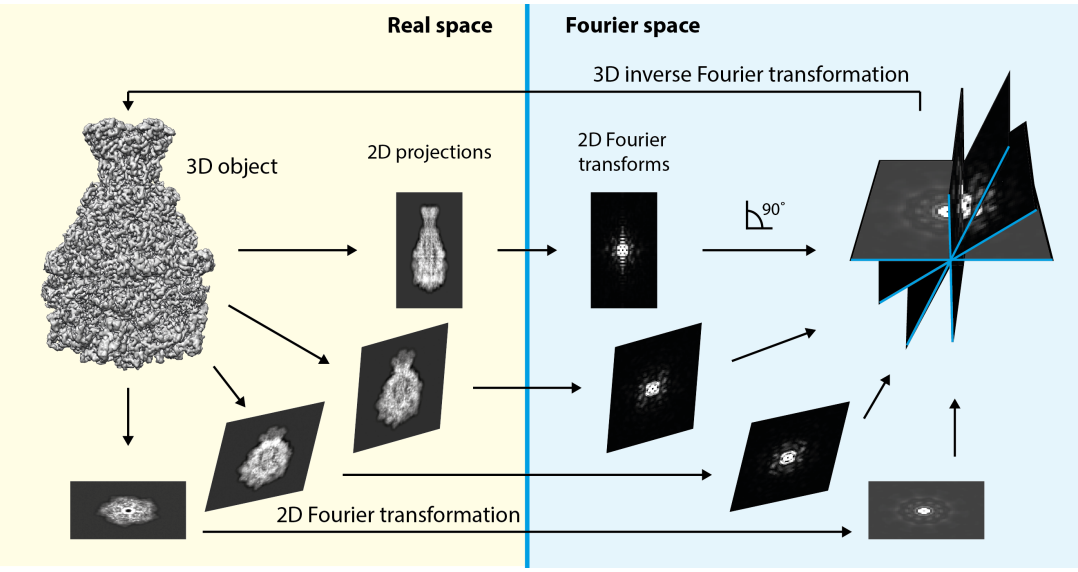

Fig. 2.12: Schematic illustration of the Fourier slice theorem using the 3D density of a bacterial Tc Toxin (EMDB 10034, Leidreiter et al. (2019)). The 3D structure can be reconstructed by an inverse 3D Fourier transformation, as the Fourier transforms of 2D projection images represent slices of the 3D Fourier space.

The 3D reconstruction requires the knowledge of the 3D projection parameters of each projection image. In contrast to tomography, these are unknown in case of single particle cryo-EM and have to be determined during the SPA. Each view can be described by a set of 3D projection parameters, also known as pose $\vec{x}$, which consist of the three Euler angles φ, θ and ψ as well as two shift values s_x and s_y (Figure 2.13). The pose $\vec{x}_i = (\varphi_i, \theta_i, \psi_i, s_{x,i}, s_{y,i})^T$ of each particle i is determined by projection matching (Frank, 2005). Here, each 2D projection image is compared to simulated 2D projection images of a 3D reference density to find the best match with regard to the cross-correlation. The set of poses $\vec{x}_i$ is then used to reconstruct a 3D reconstruction of the protein, which is used

as a reference in a consecutive iteration of projection matching and 3D reconstruction. In this way, the 3D projection parameters and the 3D electron density map are iteratively refined until the parameters converge. Simultaneously, the sampling angle, i.e., the angle between adjacent sampling points on the Euler sphere used to compute 2D projection images from the 3D reference, is decreased with increasing angular accuracy throughout the 3D refinement.

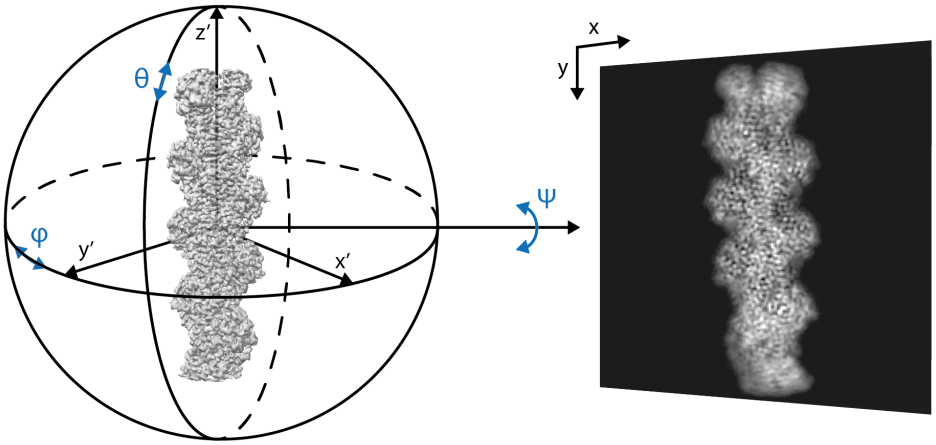

Fig. 2.13: Schematic illustration of the projection parameters on a sphere of Euler angles φ (central axis rotation), θ (tilt), ψ (in-plane rotation) enclosing F-actin. Shifts in x and y direction are determined on the level of 2D projection images. Figure is based on Behrmann (2012).

In earlier times, only the poses $\vec{x_i}$ with the highest cross-correlation were used for the reconstruction ("pure projection matching") (Frank, 2005). With the introduction of maximum likelihood methods, all poses n of one particle with a likelihood higher than a defined threshold are used for the reconstruction and weighted in accordance to their likelihood $L(\vec{x_{i,n}})$ (Sigworth et al., 2010). Thereby, the risk of converging to a local minimum is significantly decreased, making the 3D refinement more robust and less biased by the initial 3D reference. The smear, which describes the spread of the likelihood distribution, is usually large at the beginning and decreases throughout the refinement, when the resolution and accuracy improves. Consequently, the smear also represents a measure for the "alignability" and unambiguousness of a cryo-EM data set.

Nowadays, data sets are commonly split into two halves and processed independently during the 3D refinement according to the gold standard (Henderson et al., 2012). In this way, the resolution of a data set can be assessed based on the correlation of the two half maps within individual shells in Fourier space (Fourier shell correlation - FSC). While only the overall FSC curve provides reliable information about the quality of a data set, in particular whether there is overrefinement, the reporting of a single resolution value has prevailed. There is a persistent controversy about the resolution criterion that

should be used (Penczek, 2020, Sorzano et al., 2017, van Heel, 2020, van Heel and Schatz, 2017). Still, the most widespread and accepted one is the $FSC_{0.143}$ criterion that reports the frequency at which the correlation has dropped to a value of 0.143 (Rosenthal and Henderson, 2003). All resolutions reported within this thesis comply with this criterion.

2.4.5 Challenges in the processing of helical samples

According to its name, SPA was originally tailored to single particles, i.e., globular proteins, and therefore assumes that the protein is centered in each 2D particle image, taking up ∼2/3 of the image area (Frank, 2005). Furthermore, particles are considered randomly distributed and thereby all views should be equally represented. Filamentous samples do not fulfill these assumptions, thus the processing of filaments requires a number of adjustments to the SPA pipeline.

First, the selection of 2D particles has to be adapted. Instead of picking individual proteins, filaments need to be traced on the 2D micrographs (Figure 2.14). Importantly, crossings of filaments or bundles need to be excluded, as they would not only interfere with the 3D reconstruction, but likely also locally alter the filament structure. In principle, every unique subunit of a filament could be handled as a single particle. However, the size of a single subunit is in most cases insufficient for robust projection matching. To guide the alignment several, subunits are thus usually included into one 2D particle image, e.g., 10-12 subunits in case of F-actin. In practice, traced filaments are segmented into overlapping particle images, where neighboring particles along one filament are shifted by the rise Δz of the filament, i.e., the height of one unique subunit (Egelman, 2000). In this way, every particle image depicts a small stretch of the filament consisting of several subunits, while only containing one "new", unique subunit (Figure 2.14). If the rise is unknown, it can either be estimated from micrographs or more reliably be determined from the diffraction pattern of the respective filament (Egelman, 2014). Segmenting filaments by their rise has the great advantage, that the projection parameters of a particle can be predicted from the parameters of its neighbor particle, when the helical symmetry parameters are known. While the alignment of all particles has proven superior to sole predictions based on the symmetry, this knowledge can still be exploited to, for example, restrain the views considered during projection matching, or assess the alignment performance and identify outliers. Therefore, the helical affiliation and particle order should be included into the metadata of particle images. Due to the identity of ∼80-95% of neighboring particles within one filament, it is crucial to group all particles coming from one filament into the same half set for the gold-standard refinement (also see Section 2.4.4) to avoid self-correlation.

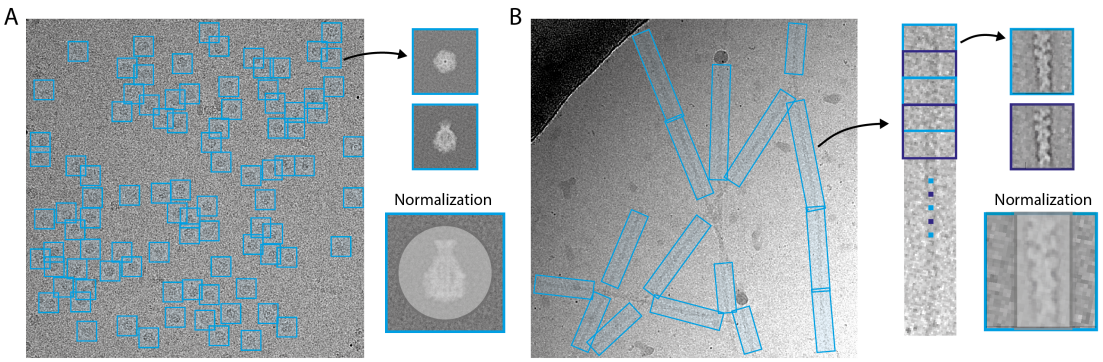

Fig. 2.14: Schematic illustrating the differences of cryo-EM data of **(A)** globular, single particles and **(B)** filaments. **(A)** Micrograph of a bacterial Tc toxin, kindly provided by Dr. Peter Njenga Ng`Ang`A. Particles are selected and extracted using squared boxes. **(B)** Micrograph of F-actin with traced filaments. The rectangular filament boxes are afterwards segmented into individual, overlapping particles. As the contrast of 2D particle images would be insufficient for visualization, higher contrast particles were simulated using 2D class averages (F-actin) and projections (for the Tc toxin, EMDB 10034, Leidreiter et al. (2019)) with additional noise.

Once filaments are successfully segmented and extracted, their normalization needs to be adjusted. Usually, a spherical mask is used for the normalization, which includes the central protein, but excludes the majority of the surrounding noise. In case of filaments, a spherical mask cannot properly separate the signal from the background and hence needs to be replaced by a cylindrical mask (Figure 2.14). This also applies to consecutive normalization steps in 3D. Masking adapted to filaments is also crucial for all alignment steps in 2D and 3D. By segmenting a filament, its structure is cut at the edges of the particle images. The thereby introduced sharp edge represents a strong feature which can strongly bias the alignment of filamentous particles, i.e., the edge is aligned rather than the protein features. While the negative effect is limited in 2D, the larger degree of freedom in a 3D alignment makes it more prone to edge effects. Specifically, the cross-correlation during projection matching can be maximized by artificially tilting the filament, bringing the sharp edge into the center of the box. This behavior can be prevented by applying a mask containing only a central fraction, e.g., 85% of the filament, throughout the 3D refinement. This mask needs to be very soft, i.e., its values need to fall smoothly from 1 to 0, to not introduce another sharp feature that could deteriorate the refinement.

The 2D and 3D alignment of filaments is further impeded through the comparably high correlation generated through the alignment of two featureless cylinders. For this reason, a successful alignment of helical filaments often requires high initial sampling rates, to consider features of the protein rather than its overall shape. This is especially true for filaments that are polar and do not additionally exhibit a C-symmetry (rotational symmetry) such as F-actin, as the orientation of the filaments within the 2D particle images needs to be identified correctly.

Finally, cryo-EM data of helical filaments significantly differs from single particle data

in the number of views they include. SPA assumes that the particles are distributed randomly within the amorphous ice layer, giving rise to a variety of 2D projection views which are ideally distributed homogeneously over the sphere of Euler angles. Strongly preferred views, e.g due to interactions of the protein with the air-water interface, impede the reconstruction of 3D structure and in worst case can completely prevent it (also see Section 2.4.4). In case of filaments, the orientation of filaments is tightly restricted to side-views and tilted side-views by the thickness of the amorphous ice layer. Still, reconstructions of helical filaments usually do not suffer from reconstruction artefacts due to missing views. While the tilt angle θ is limited to values close to the equator of the Euler sphere (90 °), the helical symmetry ensures a homogeneous distribution of all side views (rotation around the filament axis, φ).

Different 3D refinement strategies for helical filaments have been introduced over the years. Initially, structures were determined from layer lines (helical diffraction pattern computed from TEM images) using Fourier-Bessel inversion (Moore and De Rosier, 1970). Later, an iterative helical real space reconstruction (IHRSR) strategy was introduced (Egelman, 2000, 2007b), which adapted the principle of projection matching and Fourier 3D reconstruction to the needs of helical samples. Here, the electron density map and the helical symmetry parameters are iteratively refined to achieve a symmetrized high-resolution 3D structure. Helical symmetry has been traditionally applied within all refinements strategies. While the application of symmetry is in general advantageous, especially when the number of particles is limited, it also is a non-neglectable source of possible bias (Pospich and Raunser, 2018). Particularly, the determination of the helical symmetry parameters is not straight-forward and the application of even slightly wrong parameters can result in severe overrefinement or, even worse, an artificial 3D structure (Egelman, 2014). While the risk of the latter is limited to low-resolution structures, the remaining aspects also persist at higher resolution. In addition, filaments usually exhibit a resolution gradient due to their intrinsic flexibility and alignment inaccuracies. Consequently, symmetrization results in an overall improvement of the map quality at the cost of lost fine details in the central region, which is best resolved.

At the time this thesis was prepared, only one software package offered a maximum-likelihood helical refinement strategy, which is based on the IHRSR algorithm (He and Scheres, 2017). While one can deactivate the refinement of helical symmetry parameters, they are always applied. For the reasons listed before, the application of helical symmetry is not the optimal strategy when reconstructing a high-resolution structure of F-actin or actomyosin (Pospich and Raunser, 2018). Therefore, two different hybrid SPA processing strategies were used for the processing of the data analyzed in this thesis (see Sections 3.3.1.3 to 3.3.1.4).

Most of the challenges associated with the processing of helical samples have been successfully met. However, there are yet some to be overcome. On the one hand, the *ab initio* reconstruction of filaments still poses a major obstacle, caused by the missing of top and bottom views. Therefore, structures of homologous proteins or cylinders filled with Gaussian noise are routinely used as reference structures for the 3D refinement. On the other hand, methods for classification, in particular 3D classification are in many cases not powerful enough to classify heterogeneous filaments (Pospich and Raunser, 2018). Biologically relevant conformational changes within filaments are often subtle, due to the constraints binding partners impose on the structure, and therefore require sensitive and robust algorithms. Moreover, the possibility to classify data based on the presence or identity of a small molecule would dramatically promote the structural research focused on nucleotide hydrolysis and drug interactions.

2.4.6 Recent advances in cryo-EM

About seven years ago, the field of cryo-EM experienced a first "resolution revolution" (Kühlbrandt, 2014). While previously the achievable resolution was limited to $\geq$ 4-6 Å, advances in the technology of electron detectors and software including the introduction of maximum-likelihood methods led to a significant improvement of the achievable resolution to $\sim$2-3 Å (Figure 2.15A). Specifically, the routinely used charged coupled device (CCD) detectors were replaced by direct electron detectors (DEDs, also direct detection devices, DDDs). Now, electrons no longer needed to be converted into photons at the cost of a low detector quantum efficiency (DQE) prior to detection. Instead, DEDs can directly detect electrons with a high spatiotemporal accuracy and are furthermore fast enough to allow the collection of movies, which in turn allow the correction of the specimen drift (Faruqi and Henderson, 2007, Jin et al., 2008). In the meantime, the development of DEDs went on and new, faster detectors with an even higher DQE have become available (Figure 2.15B). In addition, new detection modes were introduced. Previously, all incident electrons were integrated within the exposure time of a single frame (linear mode). Later, single electrons could be detected (counting mode) and recently the localization of an electron impact can be computationally estimated with sub-pixel accuracy (super-resolution mode). In this way, the DQE of especially the high-resolution signal could be significantly increased (Figure 2.15B).

Additional advances have been made in the field of software development. Improved data acquisition software, supporting *inter alia* faster file handling and aberration-free image shifts (AFIS), considerably increased the speed of the data acquisition. The increase of speed combined with a growing chip size, i.e., larger field of view, also led to a drastic increase in the size of data sets, making in particular the preprocessing (also see Section

3.3.1.1) laborious and time consuming. Recently, TRANSPHIRE (Stabrin et al., 2020), a fully-automated on-the-fly processing pipeline, was introduced. By automatically preprocessing the data using a deep-learning based optimization strategy, TRANSPHIRE significantly eases the handling of big data sets as well as the monitoring of key parameters of an ongoing data acquisition. Besides software dedicated to automation, deep-learning based particle picking and image selection software (Stabrin et al., 2020, Wagner et al., 2020, 2019) was introduced to the field of cryo-EM, making the manual selection of hundred thousands of particles obsolete. Moreover, novel methods, on the one hand, improved the handling of beam damage and fitting of CTF parameters (Zivanov et al., 2018, 2019); On the other hand, higher order aberrations and beam tilt, which negatively affect the high-resolution signal, can now be corrected for (Zivanov et al., 2020). A combination of individual advances finally culminated in cryo-EM structures at 1.2-1.3 Å (Nakane et al., 2020, Yip et al., 2020). Consequently, cryo-EM has today almost drawn level with X-ray crystallography with regard to the achievable resolution.

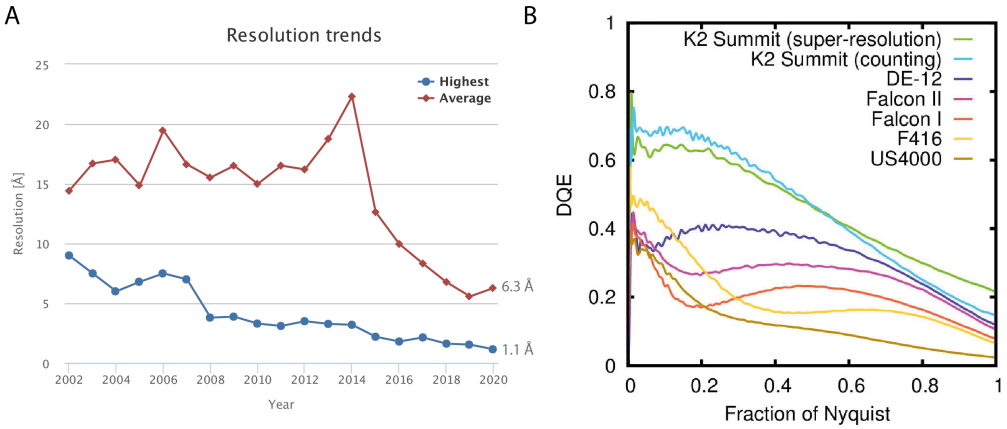

Fig. 2.15: **(A)** Resolution trends of all SPA cryo-EM structures deposited to the electron microscopy data base (EMDB, downloaded from the EMDB website on 17.11.2020, Lawson et al. (2011)). **(B)** Comparison of the detector quantum efficiency (DQE) of CCD cameras - US400 (Gatan), F416 (TVIPS)- and DEDs operated in linear mode - Falcon I, Falcon II (Thermo Fisher), DE-12 (Direct Electron) - as well as counting and super-resolution mode - K2 Summit (Gatan). Figure reprinted from Ruskin et al. (2013) with permission from Elsevier.

The greatest weakness of cryo-EM is probably its limitation to large protein complexes ($\geq$ 50-100 kDa), which generate sufficient contrast for the successful reconstruction of a high-resolution 3D structure. Biological samples are in general weak scattering objects (also see Section 2.4.3) and their scattering properties cannot be changed without altering the protein itself. Yet, the contrast can be enhanced considerably by changing the phase of the unscattered beam, resulting in a more distinct change of amplitudes after interference of the scattered and unscattered beam (phase contrast). This principle has been exploited in light microscopy for many years, but was only recently successfully implemented in the

field of cryo-EM with the Volta phase plate (VPP) (Danev and Baumeister, 2016, Danev et al., 2014, Khoshouei et al., 2016). While the enhancement of contrast is remarkable, the VPP is unfortunately not an all-purpose solution. Although the VPP in general would allow for in focus imaging, the stability of the specimen stage and the accuracy of focusing routines is insufficient for reliable focusing. The application of a small defocus, or even worse, overfocus is a major problem, as it cannot be properly corrected for. Thus, the VPP is nowadays mostly used in combination with mild defocusing to allow CTF correction. As the phase shift increases with the total electron dose deposited on the VPP, the position on the phase plate has to be changed regularly to ensure a suitable range of phase shifts. Besides additional demands on the data acquisition, image analysis is also more complicated, due to a dominating low-resolution signal, which requires the adjustment of processing algorithms.

2.5 Aim of this thesis

Actin and myosin are key role players in eukaryotic cells powering many essential processes such as cell motility, cargo transport and muscle contraction. The biological functionality of both proteins relies on the coupling of their conformational state to ATP hydrolysis. While sequence variations are known to fine-tune the molecular properties of actin and myosin, genetic mutations can cause malfunctions, which are often associated with severe medical conditions. Although actin and myosin have been studied biochemically for decades and pioneering studies preceeding this thesis have culminated in first high-resolution structures, many questions about the structure-function relationship of actin and myosin await to be answered.

How do sequence variations fine-tune the structure and function of actin and myosin? How is ATP hydrolysis and the subsequent release of inorganic phosphate coupled to the conformational state and finally functionality? By which mechanism do nucleotide-sensitive ABPs read the nucleotide state of actin? What is the structural basis of known actin inhibitors and how can we use them most efficiently?

With the ultimate aim to answer some of these key research questions, I planned to solve a number of high-resolution structures of actin alone and in complex with myosin. My plans included the structural characterization of a distinct actin from *Plasmodium* as well as complexes of actin and myosin in different nucleotide states and bound to small-molecule inhibitors of known function. For this purpose, protein complexes of interest would first need to be reconstituted from purified proteins. After a successful reconstitution, the focus would be on the preparation, optimization and imaging of cryo-EM samples. Finally, the reconstruction of three-dimensional electron density maps and, in case of a sufficient resolution, building and analysis of atomic models, would shed light on the effects of ATP hydrolysis, phosphate release and small molecule binding. A comparison of these atomic models with available structures of other actins and myosins would furthermore help to identify common or sequence-specific features within these protein families. Ultimately, the results of this thesis project would help to explain the structural mechanism of actin inhibitors and could possibly guide the structure-based design of novel functionalized compounds.

3 Materials and Methods

3.1 Protein biochemistry

All protein complexes studied in this doctoral thesis were reconstituted from purified proteins. To answer the biological questions of interest (also see Section 2.5), near-atomic resolution ($\leq$4 Å) structures are required. For this reason, most proteins were chosen based on their stability during sample preparation. Specifically, α-actin and myosin Va were chosen for studying the structural effect of ATP hydrolysis and small-molecule actin inhibitors. While α-actin is an established model system (Behrmann et al., 2012a, Galkin et al., 2015, von der Ecken et al., 2015), the high-duty ratio cargo-transporter myosin Va is well-suited for cryo-EM studies of the actomyosin complex as it binds strongly to F-actin in both the rigor and ADP-state (Volkmann et al., 2005, Yengo et al., 2002). Additionally, myosin Va has been reported to be nucleotide-sensitive (Zimmermann et al., 2015). Thus, structures of the F-actin-myosin Va complex can possibly shed light on the mechanism by which ABPs sense the nucleotide state of actin. Finally, extensive previous knowledge is available for α-actin and myosin Va, including a number of crystal structures (Coureux et al., 2004, 2003, Wulf et al., 2016), promoting the analysis of cryo-EM structures. An overview of all proteins studied within this thesis with corresponding taxonomy information and purification details is given in Table 3.1.

	Protein	Gene	Organism	UniProt ID	Purified from
Actin	α-actin, skeletal muscle	*ACTA1*	*Oryctolagus cuniculus* (Rabbit)	P68135	Native source at RUB & MPI
***Pf* Actin**	Actin 1	PFL2215w[1]	*Plasmodium falciparum*	P86287	Baculovirus/SF21 cells Kursula Lab
Myosin	Unconventional myosin Va	*MYO5A*	*Gallus gallus* (Chicken)	Q02440	Baculovirus/SF9 cells Houdusse lab
ELC	Myosin light chain 6B	*MYL6B*	*Homo sapiens* (Human)	P14649	Co-expressed with myosin Houdusse lab

Table 3.1: Summary of protein samples, corresponding taxonomy and purification details.
[1]Based on an identical protein isolated from a different strain, UniprotID: Q8I4X0.

Protein samples expressed in and purified from insect cells were kindly provided from collaborating laboratories:

***Pf* Actin**	Prof. Dr. Inari Kursula Department of Biomedicine, University of Bergen, Bergen, Norway Faculty of Biochemistry & Molecular Medicine, University of Oulu, Oulu, Finland
Myosin and ELC	Prof. Dr. Anne Houdusse Structural motility, Institut Curie, CNRS, Paris, France
	Prof. Dr. Lee Sweeney Departmental of Pharmacology & Therapeutics, University of Florida, Florida, USA

Prof. Dr. W. Linke and Dr. A. Unger (Cardiovascular Physiology, Ruhr-Universität Bochum - RUB, Germany) kindly provided me with muscle acetone powder, which was purified natively from rabbit skeletal muscle based on the protocol of Pardee and Spudich (Pardee and Spudich, 1982). The subsequent purification of G-actin from muscle acetone powder was carried out at the MPI in Dortmund as described in the following section.

3.1.1 Purification of actin

Rabbit skeletal muscle acetone powder can be stored at $-20°C$, where it remains stable for several months up to years. α-actin filaments were purified from stored acetone powder in a two step process. First, G-actin was purified from the actin-rich muscle acetone powder, flash-frozen in liqid nitrogen and stored at $-80°C$. Second, F-actin was freshly polymerized and, if necessary, additionally purified starting from thawed G-actin aliquots. This approach guarantied a high yield of stable, helical actin filaments. The purification protocols exploit the highly distinctive sedimentation characteristics of G-actin and F-actin, that allow purification of actin through cycles of polymerization and depolymerization in combination with ultra centrifugation. The details of the protocol are given in the next sections and are based on the protocols described by von der Ecken (2016).

The following buffers are used throughout the purification protocols:

G-actin buffer / G-buffer	5 mM Tris-HCl pH 7.5, 1 mM DTT, 0.2 mM $CaCl_2$, 0.5 mM ATP, 2 mM NaN_3
F-actin buffer / F-buffer	5 mM Tris-HCl pH 7.5, 1 mM DTT, 100 mM KCl, 2 mM $MgCl_2$
F-HEPES-buffer	10 mM HEPES pH 7.5, 1 mM DTT, 100 mM KCl, 2 mM $MgCl_2$

When nucleotides or small molecules were added, the respective concentration is stated in the protocol. Buffers containing ATP and DTT were either frozen or used directly after preparation, due to the limited stability of compounds at room temperature.

Purification of G-actin from muscle acetone powder

1 g of acetone powder was resuspended in 20 ml freshly prepared G-buffer and stirred for 25 min at 4 °C. The solution was separated from solid material by vacuum-filtering (filter paper: QT 205, Fisherbrand) and kept at 4 °C. Remaining solid material was resuspended in another 20 ml of fresh G-buffer, stirred for 25 min at 4 °C and vacuum-filtered. The filtered solutions were pooled (40 ml) and centrifuged for 30 min at 4 °C to remove debris and solid impurities (Beckmann Rotors, Ti 70, 100.000 g). By increasing the salt concentration to a total of 2 mM $MgCl_2$ and 100 mM KCl polymerization of actin was induced. Addition of 0.5 mM ATP can improve the filament formation, but was not required. After 1 h of polymerization at room temperature (RT), the solution was highly viscous and appeared cloudy due to the presence of actin filaments. Addition of 700 mM solid KCl, resulting in a total KCl concentration of 0.8 M, and incubation for 1 h at RT ensured the release of all bound ABPs such as tropomyosin. Afterwards, filaments were collected by centrifugation for 2-3 h at 4 °C (Beckmann Rotors, Ti 70 or TLA 100.4, 100.000 g). The pellet was carefully separated from the supernatant, washed several times with fresh G-buffer, resuspended in 10 ml of G-buffer and homogenized with a glass douncer. The solution was transferred to a dialysis membrane tube (SpectraPor-4, cut-off 12-14 kDa, SpectrumLabs) and dialysed against 2 l of fresh G-buffer at 4 °C for 1.5 days, changing the dialysis buffer once after approximately 12 h. Actin filaments should now be depolymerized. Inactive filaments and aggregates were removed by centrifugation for 1 h at 4 °C (Beckmann Rotors, Ti 70 or TLA 100.4, 100.000 g). In the following, the supernatant was further purified by another cycle of polymerization and depolymerization, starting with the induction of actin polymerization as described before. At the end of the cycle, the concentration c of actin in the supernatant was estimated by absorption spectroscopy (Spectrophotometer DS-11, DeNovix) according to $c = E_\lambda \cdot \varepsilon_\lambda^{-1} \cdot d^{-1}$, where E_λ is the measured extinction and ε_λ the extinction coefficient at the given wavelength λ and $d = 1$ cm. The absorption was measured at 290 nm ($\varepsilon_{290\,\mathrm{nm}} = 0.62$ ml mg^{-1} cm^{-1} $\approx 22{,}000$ M^{-1} cm^{-1}) (Hertzog and Carlier, 2005), as the bound adenonucleotide also absorbs close to 280 nm and thereby falsifies the measured actin concentration at this wavelength.

The progression of the purification and especially the final purity of actin was evaluated by SDS-PAGE (see Section 3.1.5 and Figure 3.6 for details). If required, actin can be further purified by additional cycles of polymerization and depolymerization or size exclusion chromatography. Both was not necessary for the purifications performed in this thesis.

G-actin can either be stored at 4 °C in dialysis conditions or flash-frozen and stored at -80 °C. As the adenonucleotide is crucial for the structural stability of actin, the dialysis buffer needs to be replaced regularly by fresh G-buffer with ATP. Therefore, it was more convenient to flash-freeze 50-100 µl aliquots of G-actin in liquid nitrogen allowing the long-term storage at -80 °C. To ensure, that the concentration of actin is above the critical concentration required for polymerization, even after freezing and thawing, the G-actin concentration should be at least 2 mg/ml ($\sim$ 50 µM). If required, G-actin can be concentrated prior to flash-freezing using an Amicon concentrator (Amicon ultra, Merck Millipore, cut-off 30 kDa). The addition of cryoprotectants was not necessary and also not recommended, as they would need to be removed prior to cryo-EM experiments. The yield of G-actin purified from muscle acetone powder depends on the quality of the powder itself and thus the preceding purification. Typical yields for 1 g of the muscle acetone powder used in this thesis ranged from 12 mg to 21 mg.

Purification of F-actin from frozen G-actin

F-actin is not stable when frozen and thawed, thus, the actin filaments studied in this thesis were always prepared freshly from frozen G-actin aliquots according to the following protocol.

100 µl of frozen G-actin were thawed and properly mixed. Aggregates and remaining polymerized actin was removed by centrifugation for 1 h at 4 °C (Beckmann Rotors, TLA 120.1, 100.000 g). By increasing the salt concentration to a total of 2 mM $MgCl_2$ and 100 mM KCl polymerization of actin was induced. As the ATP within the sample might have partially hydrolyzed while stored, additional 0.5 mM ATP were added to promote filament formation. After 2 h of incubation at RT, the sample was transferred to 4 °C for further polymerization overnight. In the morning, F-actin was separated from inactive G-actin by centrifugation for 2 h at 4 °C (Beckmann Rotors, TLA 120.1, 100.000 g). Depending on the sample purity, F-actin was be either directly prepared for subsequent experiments or further purified by another cycle of depolymerization and polymerization. In case of the latter, the pellet was carefully washed and resuspended in 50-100 µl of freshly prepared G-buffer. The solution was then transferred to a dialysis button (Hampton Research) covered with a piece of dialysis membrane (SpectraPor-4, cut-off 12-14 kDa, SpectrumLabs) which was previously equilibrated in G-buffer for 1-2 h. The actin sample was depolymerized by dialysis against 100 ml of G-buffer overnight. To promote depolymerization, the dialysis buffer was exchanged once in the evening. On the next day, the solution was carefully recovered from the dialysis button with the tip of a pipette and centrifuged for 1 h at 4 °C to remove remaining aggregates (Beckmann Rotors, TLA 120.1,

100.000 g). Afterwards, polymerization of G-actin was induced by increasing the salt concentration to 2 mM $MgCl_2$ and 100 mM KCl and incubation at RT for 2 h followed by overnight polymerization at 4 °C. Finally, actin filaments were collected by centrifugation for 2 h at 4 °C (Beckmann Rotors, TLA 120.1, 100.000 g) closing the depolymerization and polymerization cycle.

The F-actin pellet was carefully washed and resuspended in 50 µl of F-buffer using a pipette tip to loosen the pellet and homogenize the solution, avoiding strong sheering forces that could break filaments. Filaments were stored for 1-2 h at 4 °C before preparation of samples for TEM to allow reassembly of fragmented filaments. Addition of 0.5 mM ADP has a positive effect on the stability of filaments, was, however, avoided when studying complexes of F-actin with ABPs that are ATPases themselves such as myosin. F-actin can be stored in solution at 4 °C for a few days at the cost of an increasing amount of aggregates and fragmented filaments. For longer storage times, up to 2-4 weeks, the F-actin pellet was stored at 4 °C properly protected from drying out.

The concentration of F-actin cannot be measured reliably by absorption spectroscopy, due to the viscosity of the sample (von der Ecken, 2016). Thus, the concentration of G-actin before the final polymerization was determined allowing a rough estimation of the final F-actin concentration. This estimate served as a starting point for the experimental adjustment of the F-actin concentration in TEM experiments. The yield of F-actin purified from frozen G-actin strongly depends on the purity and successful depolymerization of the starting sample. Furthermore, stabilizing small molecules like phalloidin and jasplakinolide promote polymerization (also see Sections 2.2.4 and 3.1.2) and thereby actively increase the yield of actin filaments. When starting from 100 µl at 50 µM, the yield was typically 50 µl with a concentration ranging from 30 - 80 µM.

3.1.2 Preparation of ligand-bound F-actin

In this thesis the structure of F-actin in complex with different ligands including nucleotides and stabilizing small molecules like phalloidin and jasplakinolide was studied. Preparation of these samples requires some modifications to the basic F-actin preparation protocol outlined in the previous section, which results in ADP-bound F-actin (von der Ecken et al., 2015).

Nucleotides

With the aim to study the structural transition of F-actin upon ATP-hydrolysis, F-actin in complex with AppNHp, ADP-BeF_x, ADP-P_i and ADP was prepared in collaboration with Dr. Felipe Merino. Details of the samples prepared by Dr. Merino (ADP, AppNHp and

ADP-BeF$_x$) can be found in the methods section of the corresponding publication.

> Merino, F.*, Pospich, S.*, Funk, J., Wagner, T., T. Küllmer, F., Arndt, H.-D., Bieling, P. and Raunser, S. (**2018**) Structural transitions of F-actin upon ATP hydrolysis at near-atomic resolution revealed by cryo-EM. *Nature structural & molecular biology*, 25(6):528-537

F-actin in complex with ADP-P$_i$ was prepared following the protocol described in Section 3.1.1 without the additional cycle of depolymerization and polyermization. Instead of resuspending the F-actin pellet in F-buffer in the final step, the pellet was resuspended in 50 µl of freshly prepared phospatae buffer (5 mM HEPES pH 7.5, 50 mM KCl, 2 mM $MgCl_2$, 0.5 mM TCEP, 2 mM NaN_3, 0.2 mM ADP and 50 mM potassium phosphate pH 7.5). The pH of potassium phosphate was adjusted by adding K_2HPO_4 to KH_2PO_4.

Phalloidin and jasplakinolide

Within this thesis the structural effects of phalloidin (PHD) and jasplakinolide (JASP) on F-actin were studied. Afterwards, this knowledge was exploited to stabilize specific functional states of F-actin for the structural characterization of actomyosin filaments.

Small molecules were either commercially purchased or synthesized and provided by the lab of

JASP derivatives Prof. Dr. Hans-Dieter Arndt
Chair for Organic Chemistry I, Friedrich-Schiller-Universität Jena, Germany

A summary of all compounds studied in this thesis and corresponding chemical information is given in Table 3.2.

PHD is routinely conjugated to fluorescent probes enabling the visualization of the actin cytoskeleton by light microscopy (also see Section 2.2.4). In this thesis, Alexa Fluor^{TM} 546 Phalloidin was chosen as a representative compound of phalloidin-dyes for studying the structural effect of PHD on F-actin. The Alexa fluorophore 546 is a bright, photostable fluorescent dye with an excitation wavelength of 556 nm and an emission wavelength of 570 nm (also see Figure 3.1).

Compound	Chemical Formula	Molecular Weight	Source
Phalloidin	$C_{35}H_{48}N_8O_{11}S$	788.87 kDa	Sigma Aldrich (MERCK) CAS:17466-45-4
Alexa Fluor^{TM} 546 Phalloidin	$C_{75}H_{89}Cl_3N_{12}O_{21}S_4$	$\sim$ 1800 kDa	ThermoFisher Scientific
Jasplakinolide	$C_{36}H_{45}BrN_4O_6$	709.67 kDa	Sigma Aldrich (MERCK) CAS: 102396-24-7
JASP-cLys	$C_{38}H_{52}ClN_5O_6$	710.31 kDa	Arndt lab
Optojasp-8	$C_{58}H_{72}N_8O_{12}$	1073.26 kDa	Arndt lab

Table 3.2: Summary of F-actin stabilizing small molecule inhibitors studied in this thesis.

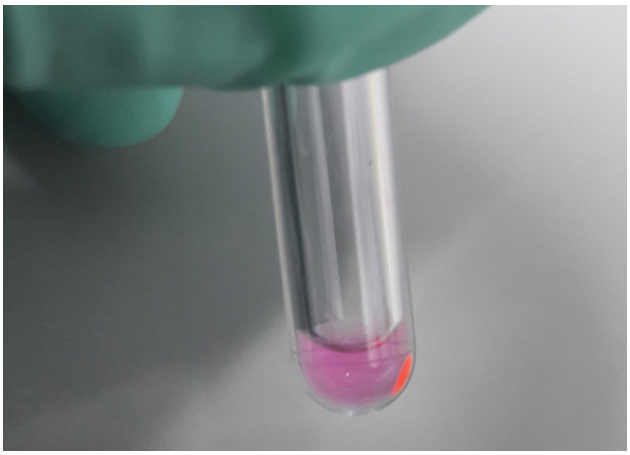

Fig. 3.1: Addition of Alexa Fluor^{TM} 546 Phalloidin to G-actin resulted in a colorful pellet in the final centrifugation illustrating the successful binding to F-actin with only little unbound toxin in the supernatant.

JASP-cLys is a synthetic analog of JASP with improved solubility due to the removal of a methyl group and the introduction of a cationic lysine side chain. Both modifications have been shown to result in compounds with function similar to that of JASP itself (Lukinavičius et al., 2014, Milroy et al., 2012, Tannert et al., 2010).

All small-molecules were shipped as powder and solved in dimethyl sulfoxide (DMSO, JASP) and methanol (PHD). Solvents should in general be avoided in cryo-EM samples, as they can negatively affect the protein, image contrast and the vitrification process (see Section 3.2.2.1 for details). For this reason, the final solvent concentration was kept to a minimum by preparing high concentration stock solutions of 2-3 mM, so that the addition of very small volumes (<µl) to actin samples was sufficient to reach a 2-fold molar excess of stabilizing small molecules.

In case of commercially purchased inhibitors, which were delivered in larger quantities, aliquots containing 0.025 to 0.15 µmol were dessicated for 1 h at RT (Eppendorf concentrator plus, Mode V-AL) and stored at −20°C. Aliquots were freshly thawed and resuspended (JASP: DMSO, PHD: methanol) shortly before addition to actin. As the final concentration was not experimentally determined, the actual concentration might be lower than the reported value based on the initial concentration.

PHD and JASP both drastically reduce the critical concentration of actin polymerization and even have the capacity to polymerize actin at low salt conditions (G-buffer, see Figure 3.2 and Section 2.2.4). Thus, the toxins can be added at any time point to either G-actin or F-actin resulting in stable filaments with minimal G-actin in the background.

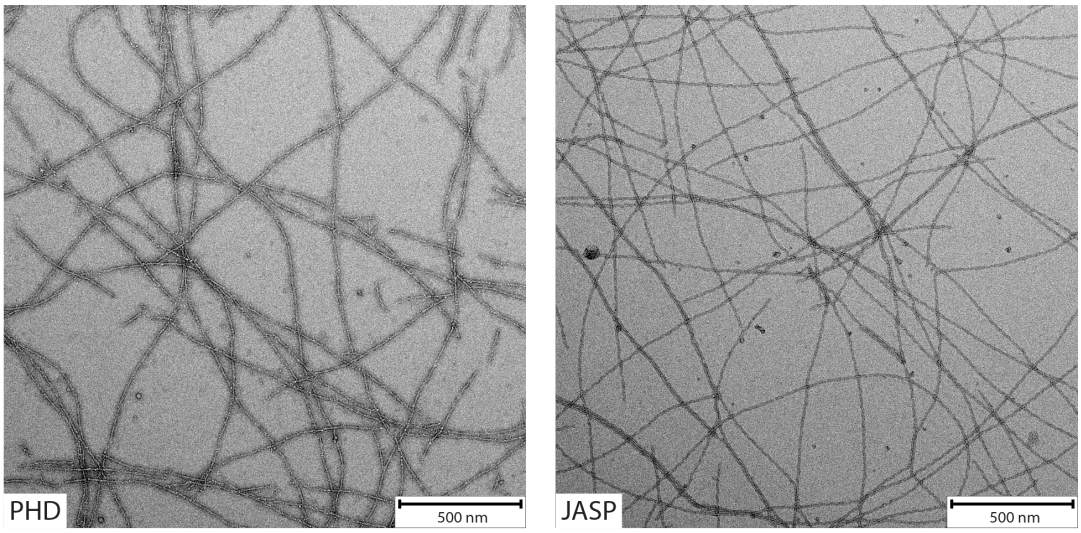

Fig. 3.2: Overnight incubation of G-actin in G-buffer with either PHD **(left)** or JASP **(right)** results in long and stable actin filaments with minimal background as illustrated by negative stain EM.

To systematically study the structural effect of PHD and JASP on F-actin, the toxins were added at different time points during the preparation of actin filaments. Specifically, toxins were either added to G-actin when polymerization was induced (in parallel to or immediately before the salt concentration was increased to 2 mM $MgCl_2$ and 100 mM KCl) or to F-actin after overnight polymerization and the subsequent centrifugation and resuspension. In the first case, the nucleotide pocket of actin still accommodates ATP or ADP-P_i when the small molecule binds. On the contrary, ATP hydrolysis and phosphate release has completed in the second case resulting in ‘aged‘ actin filaments with ADP bound. In both cases, the respective toxin was added in a 2-fold molar excess. When the toxin was added to G-actin, a small amount of extra toxin was added after the final centrifugation and resuspension to reach a concentration guaranteeing the saturation of

actin with the respective small molecule. Detailed information on how each sample was prepared including the final ligand and solvent concentration is provided in the Results and Discussion.

Photo-switchable jasplakinolide

To facilitate the development of functional photo-switchable small molecules targeted to F-actin, an optojasp photoswitch bound to actin filaments was characterized structurally in both switch states within this thesis.

Optojasp-8 (OJ8) is a photo-switchable small molecule derived from JASP-cLys (see previous paragraph and Table 3.2). A bistable azobenzene is attached via a linker to the cyclodepsipetide macrocycle of JASP (Figure 3.3). The azobenzene can be isomerized from its *trans* configured ground state to a high-energy *cis* form by photo-activation at 380 nm. Eventually, the photoswitch thermally reverts back to its *trans* state with a specific half life. Alternatively, relaxation can be stimulated by irradiation with green light (Borowiak et al., 2020).

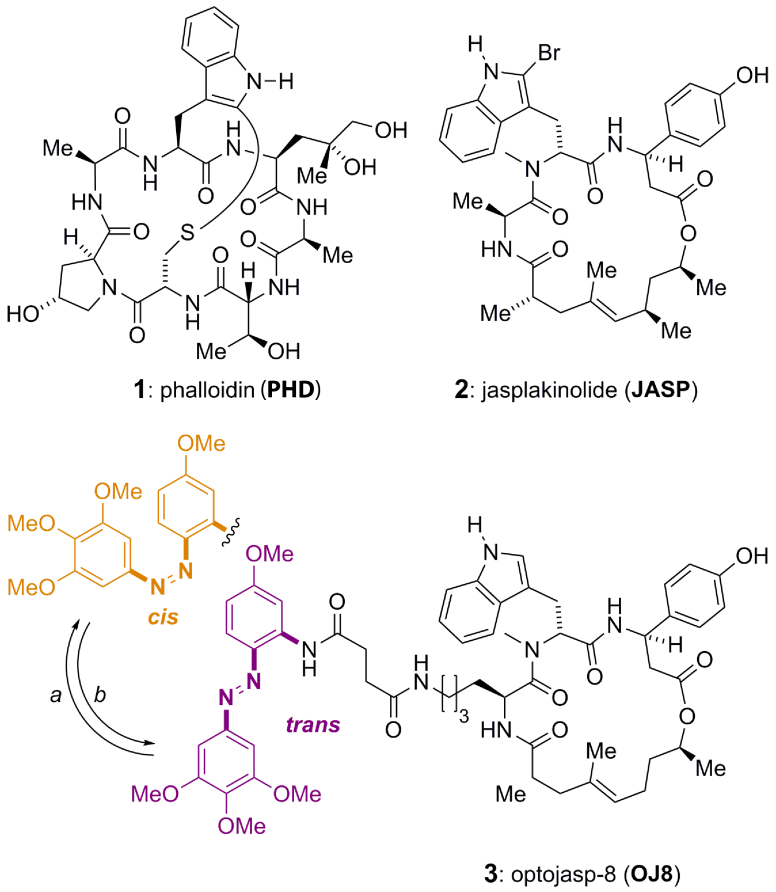

Fig. 3.3: Chemical structures of F-actin stabilizing natural product toxins PHD and JASP, and OJ8. Conditions: a) $h\nu$= 380 nm; b) $h\nu$ = 520 nm or ΔT ($t_{1/2}$ = 15 min in PBS buffer at 37°C (Borowiak et al., 2020).) Figure adapted from Pospich et al. (2021).

As cryo-EM relies on averaging of thousands of helical segments that cannot be classified based on the presence or conformation of a small molecule, it was crucial to avoid mixing of the isomeric states of OJ8 within actin filaments. All sample preparation and imaging steps for the *trans* state (dark state) were therefore conducted using red light only and residual light was minimized to prevent activation of OJ8. On the contrary, OJ8 was repetitively activated by UV light throughout the sample and specimen preparation process in case of the *cis* state (bright state). While it is not possible to activate OJ8 to completion (100% *cis*), this procedure maximizes the relative population of *cis*-OJ8 up to the photo stationary state (Pospich et al., 2021).

The F-actin samples were prepared as described in the previous Sections 3.1.1 to 3.1.2 and OJ8 was added to G-actin. When preparing the bright state, OJ8 was activated for $\sim$ 3 min using LEDs with a wavelength of 380 nm immediately before addition to G-actin (3 LEDs operated with an ARDUINO, consecutively pulsing for 1 s every 3 s to avoid over-heating, see Figure 3.4). To suppress relaxation of *cis*-OJ8 to *trans*-OJ8, the sample was flashed with UV light for 1 s every 3 s during overnight polymerization at 4 °C. Finally, OJ8 was activated for another $\sim$ 3 min using the same setup directly before vitrification (also see Section 3.2.2.1). To minimize the time in which OJ8 could possibly relax back into the *trans* state, grids were directly screened at a high-end microscope, that was immediately afterwards used for data collection.

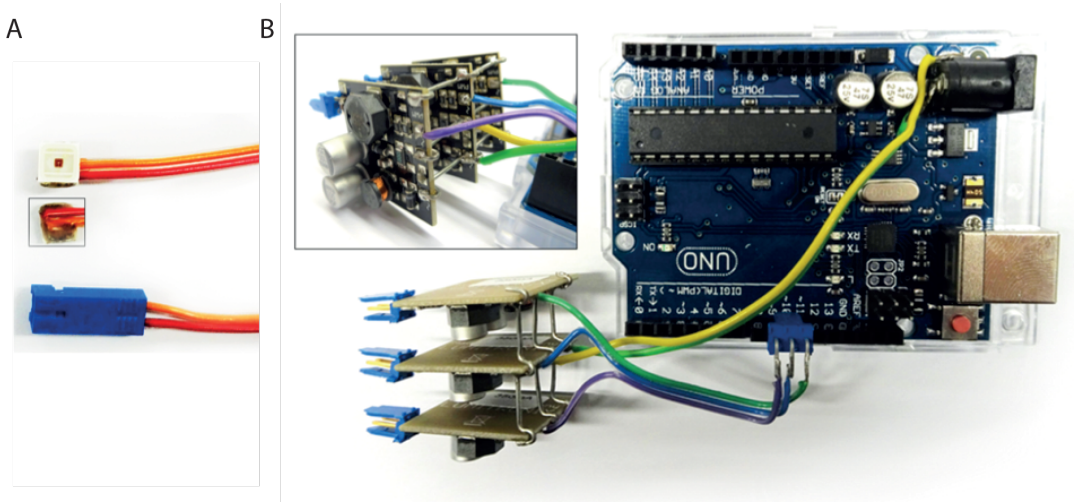

Fig. 3.4: Illumination setup used to photo-activate OJ8 consisting of **(A)** LEDs with a wavelength of 380 nm (activation) or 520 nm (stimulated emission) (Roithner Lasertechnik GmbH) attached to a two pin plug and **(B)** a microcontroller (Arduino UNO) powering and modulating three parallel-connected constant current sources (Lumitronix). This setup was assembled and kindly provided by F. Küllmer. Figure originally published as supplementary figure in Pospich et al. (2021).

3.1.3 Preparation of *Pf* Actin filaments

Pf Actin was purified in and provided by the Kursula lab (also see Table 3.1). Details of the expression system and purification protocol can be found in the corresponding publication.

> Pospich, S., Kumpula, E.-P., von der Ecken, J., Vahokoski, J., Kursula, I. and Raunser, S. (**2017**) Near-atomic structure of JASPlakinolide-stabilized malaria parasite F-actin reveals the structural basis of filament instability. *Proc. Natl. Acad. Sci. USA*, 114(40):10636-10641

Pf Actin is not stable when frozen, also in its globular form. Thus, stabilized actin filaments were prepared freshly in the Kursula lab, shipped to the MPI Dortmund and directly vitrified. *Pf* Actin was polymerized for 16 h at 20 °C in 10 mM HEPES pH 7.5, 0.2 $CaCl_2$, 50 mM KCl, 4 mM $MgCl_2$,5 mM DTT and 0.5 mM ATP. To overcome the inherent instability of *Pf* Actin filaments, JASP (Sigma Aldrich) was added in a stoichiometric molar ratio during the polymerization.

Non-stabilized *Pf* Actin filaments were prepared at the MPI in Dortmund, starting from 10 µM of fresh G-actin shipped on ice. To stabilize G-actin, the buffer (10 mM HEPES pH 7.5, 0.2 mM $CaCl_2$, 0.5 mM TCEP, 0.5 mM ATP) was supplemented with 0.3 M ammonium acetate at pH 7.3. Ammonium acetate was removed using a desalting column (G-25 Spin Trap, GE Healthcare) before polymerization was induced by adding 50 mM KCl, 4 mM $MgCl_2$ and 1 mM EGTA. The sample was polymerized for 2 h at RT, followed by overnight polymerization at 4°C.

3.1.4 Preparation of myosin

Myosin co-expressed with ELC (referred to as myosin in the following) was kindly provided by the Houdusse lab (see Table 3.1 for details). It was flash-frozen in liquid nitrogen and shipped on dry ice, allowing further storage at -80 °C. The protein complex is frozen in F-HEPES-buffer without additional cryoprotectants or nucleotides. For each experiment, a 15 µl aliquot of myosin at 86 µM or 110 µM (different batches), was used. The sample was diluted to a total volume of 30 µl using F-HEPES-buffer. Aggregates were removed by centrifugation for 5 min at 4 °C (Eppendorf centrifuge 5424R for 1.5 ml tubes, 21,000 g). The protein concentration of the supernatant was measured by absorption spectroscopy (Spectrophotometer DS-11, DeNovix) with $\varepsilon_{280\,\mathrm{nm}} = 106{,}580\ \mathrm{M}^{-1}\ \mathrm{cm}^{-1}$ and a

molecular weight of 109.45 kDa. Typical yields ranged from 30 µM to 50 µM.

A co-sedimentation assay was used to evaluate the binding of myosin to F-actin and saturation of myosin with ELC. For this purpose, 6 µM of F-actin were mixed with 6 µM or 12 µM of myosin adding either no or 0.6 µM, 1.5 µM or 3 µM of extra ELC. All samples were incubated for 30 min at RT in a total volume of 10 µl. Afterwards, samples were diluted to a total volume of 20 µl. F-actin and bound myosins were pelleted by centrifugation for 30 min at 4 °C (Beckmann Rotors, TLA 120.1, 100.000 g). Pellets were separated from supernatants, carefully washed and resuspended in 20 µl F-HEPES-buffer resulting in a final actin concentraion of 3 µM. Samples were mixed with 4x SDS-PAGE sample buffer and 12 µl loaded to a SDS-PAGE (see Section 3.1.5 for details).

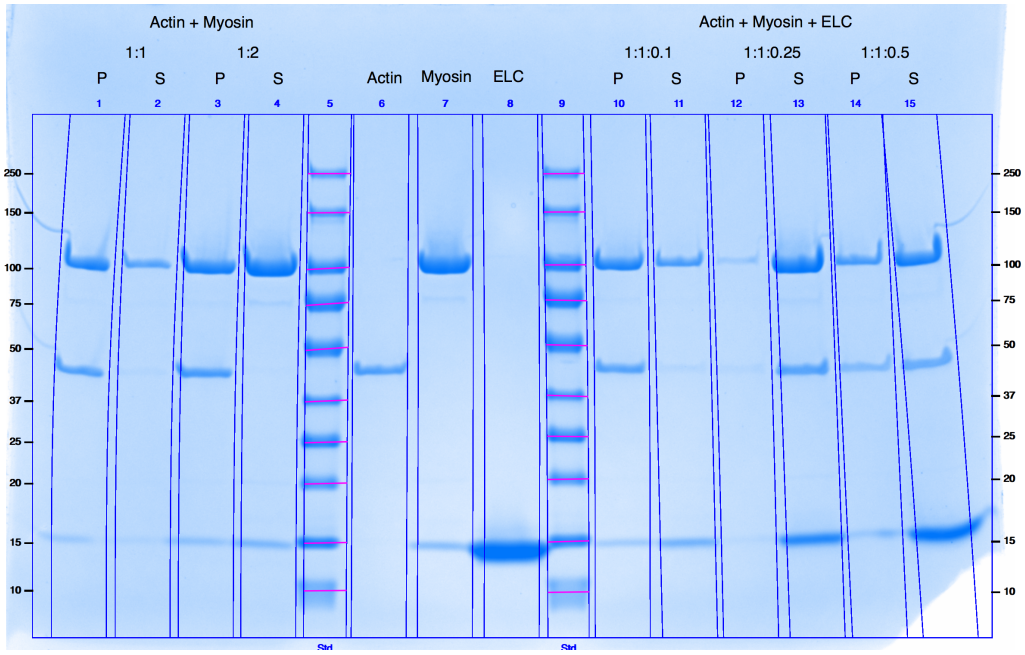

Fig. 3.5: Comassie-blue stained SDS-PAGE of pellets (P) and supernatants (S) of the co-sedimentation assay. Lanes are labeled according to the proteins and their stochiometric ratios in each sample. Lanes 6-8 are control lanes of actin, myosin and ELC alone. Lanes 5 and 9 were loaded with protein markers with known molecular weights.

Analysis of the SDS-PAGE confirms the presence of ELC in the myosin sample (lane 7) and attests a high purity of all protein samples (Figure 3.5). The presence of both myosin and ELC in lanes 1 and 3, proves the binding of myosin to F-actin. A relative increase of the myosin concentration does not result in a significant increase of myosin in the pellet (lane 3 vs lane 1), indicating that F-actin is already saturated when incubated with stoichiometric ratios of myosin. In agreement with this, unbound myosin can be found in the supernatant at stoichiometric protein ratios (lane 2). The saturation of myosin with

ELC can only be judged based on a comparison of lanes 1-2 with 10-11, as the pellet could not successfully be separated from the supernatant for lanes 12-15. The intensity of the ELC band ($\sim$ 15 kDa) in lane 1 and lane 10 is comparable. The extra ELC that was added can be found in the supernatant (lane 11) and is thus unbound. Hence, the co-sedimentation assay indicates that myosin is already saturated with ELC. Consequently, no additional ELC was added in all TEM experiments.

Preparation of ADP- and AppNHp-bound myosin

Studying the conformational changes of myosin during its hydrolysis cycle, requires the preparation of myosin in different nucleotide states. Following the protocol described in the previous section and starting from nucleotide-free myosin results in myosin in its rigor state. While myosin was complexed with ADP to study the strong-ADP state, a AppNHp-bound myosin was prepared with the aim to solve a weak binding state such as the post-rigor or PPS/P_iR release state.

Preparation of ADP-bound myosin requires the saturation with 2 mM ADP and 20 mM $MgCl_2$. As the high concentration of magnesium chloride results in the aggregation of myosin and also bundles F-actin (Gao et al., 2015), a 2x ADP-buffer (10 mM HEPES pH 7.5, 1 mM DTT, 100 mM KCl, 40 mM $MgCl_2$, 4 mM ADP and 0.04% Tween 20) was used to dilute myosin immediately before grid preparation for cryo-EM (for details see Section 3.2.2.1). Nucleotide binding is almost instantaneous guaranteeing that the majority of myosins has bound ADP.

Binding of AppNHp to myosin requires additional modifications. AppNHp hydrolyzes spontaneously up to 1% per month when stored at -20 °C. The hydrolysis rate is significantly enhanced at higher temperatures. Thus, fresh or recently frozen AppNHp was used to prepare AppNHp-bound myosin in this thesis. AppNHp (10 mg, Jena Bioscience) was solved in 200 µl of 10 mH HEPES pH 8.0, 1 mM DTT, 1 mM NaN_3 and 2 mM $MgCl_2$. As a pH below pH 7 dramatically increases hydrolysis, the pH was controlled with pH-indicator strips (MQuant, pH 6.5 - pH 10.0, Merck Millipore) and if required adjusted to $\sim$ pH 8.0. The concentration of AppNHp was measured by absorption spectroscopy with $\varepsilon_{259\,\mathrm{nm}} = 15{,}400\,\mathrm{l\,mmol^{-1}\,cm^{-1}}$ (Spectrophotometer DS-11, DeNovix). Small aliquots of $\sim$ 30 µl and $\sim$ 50 mM were stored for a maximum of 6 month at -20 °C. Ion-pair reversed-phase chromatography of freshly solved AppNHp showed the presence of 1.5 % $AppNH_2$ (hydrolysis product). Furthermore, results indicate that $AppNH_2$ does not preferentially bind to myosin, as it is the case for F-actin (Cooke and Murdoch, 1973, Merino et al., 2018), and thus does not get enriched.

To increase the binding affinity of AppNHp to myosin, the overall concentration of potassium chloride within the myosin sample was reduced to $\sim$ 10-13 mM KCl by dilution.

Finally, 5 mM of AppNHp and 4 mM of $MgCl_2$ to reach a total of 6 mM of $MgCl_2$ were added immediately before grid prepartion for cryo-EM (for details see Section 3.2.2.1).

3.1.5 Protein gel electrophoresis

The purity and composition of a protein sample can be analysed by protein gel electrophoresis (Figure 3.6). Sodium dodecyl sulfate polyacrylamine gel electrophoresis (SDS-PAGE) separates proteins according to their electrophoretic mobility which depends on their molecular weight. SDS is a strong detergent resulting in a partial to complete denaturation of proteins. Additional thermal denaturation of the sample completes the unfolding process and thereby increases the accessibility of the protein backbone to the detergent.

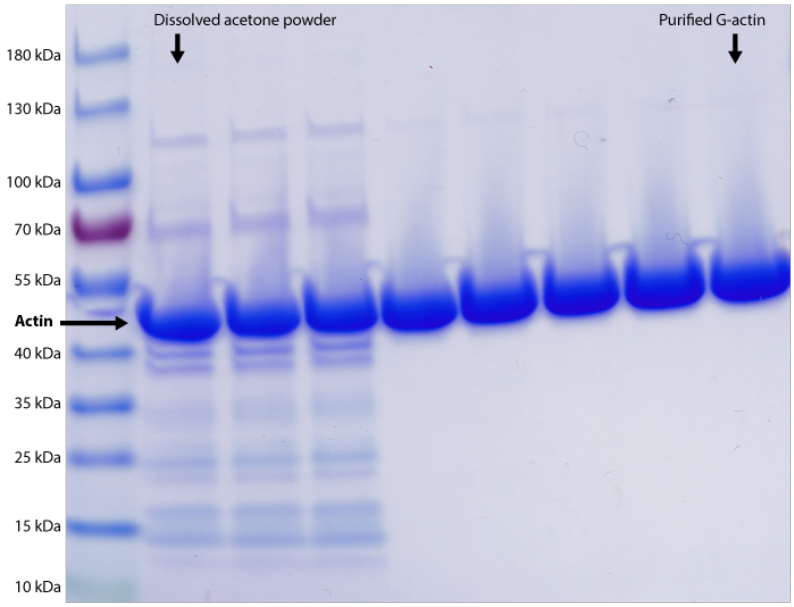

Fig. 3.6: SDS-PAGE illustrating the increase in purity throughout the purification of G-actin from muscle acetone powder (from left to right) as described in Section 3.1.1.

In this thesis, precast gradient protein gels (4-15 % Mini-PROTEAN TGX Stain-free Gels, Bio-RAD) were used that allow the separation of proteins ranging from 4 kDa to 300 kDa. Initially, samples were diluted to a suitable concentration (< 0.5 mg/ml for F-actin), mixed with 4x SDS-PAGE sample buffer (250 mM Tris-HCl pH 8, 100 mM DTT, 6 % SDS, 40% glycine, 0.2 mg/ml bromophenool blue) and optionally denatured by heating to 95 °C for 1-2 min followed by removal of aggregates in a table-top centrifuge. 5 µl of sample was loaded to each lane using a glass syringe (Hamilton). Additionally, two

protein markers (stained and stain-free) were loaded to guide the identification of protein bands (PageRuler Prestrained Protein Ladder, #26616, Thermo Fisher Scientific and Unstained Protein Molecular Weight Marker, #SM0431, Fermentas). Gels were run at a constant voltage of 175 V (0.05 A, 8 W) for 30 to 60 min in SDS running buffer (25 mM Tris-HCl pH 8, 14.4 mg/ml glycine, 1 mg/ml SDS).

Stain-free gels exploit a trihalo compound to enhance the fluorescence of tryptophan amino acids. Thus, these gels can directly be imaged after a short photoactivation. However, some ABPs including tropomyosin cannot be visualized stain-free due to the absence of tryptophan residues. Thus, all gels prepared in this thesis were stained with Coomassie blue. For this purpose, gels were covered with staining solution (50 % (v/v) ethanol, 10% (v/v) acetic acid, 0.1 % (w/v) Coomassie brilliant blue R-250), shortly boiled in a microwave to accelerate the staining process and incubated for $\sim$ 5 min under gentle agitation. Excess dye was removed by incubation with destaining solution (5 % (v/v) ethanol, 10% (v/v) acetic acid) for $\sim$ 5 min. Afterwards the solution was exchanged and the gel shortly boiled in a microwave, before it was left for incubation on a shaker for 30 min. If required, the destaining solution was replaced one more time, before the gel was left for further destaining until only protein bands remained visible. Stained gels were then imaged using a ChemiDoc Imaging System (Bio-RAD).

3.1.6 Ion-pair reversed-phase chromatography

Ion-pair reversed-phase liquid chromatography (IRPLC) was used to identify the isomeric state of OJ8 and visualize photoswitching in solution and when bound to F-actin. IRPLC can separate organic compounds according to their charge. In this process, small molecules bind to the column material by ion-pairing. In the subsequent elution step, these molecules elute successively according to their binding strength.

Before each experiment, the system (In-Line Degasser AF, 600s Controller, 626 Pump and 2487 Dual λ Absorbance Detector, Waters) and column (Prontosil 120-5-C18, 5 µm, Bischoff Chromatography) were properly washed and equilibrated with 50 % acetonitrile (ACN, Buffer A: millipore water, Buffer B: 100 % ACN). Buffers were degassed by sonication for 15 min before usage to avoid the introduction of bubbles into the system. When analysing the isomeric state of OJ8, 30 µl of 50 µM sample were loaded manually onto the column using a glass syringe (Hamilton). F-actin present in the samples was not denatured by heating or chemicals prior to loading to avoid relaxation of OJ8, but directly loaded onto a C18 pre-column which traps the protein. Samples were eluted from the column by a gradient from 50 % to 100 % ACN within 10 min (flow rate 1.5 ml/min). The absorption at 280 nm and 370 nm was monitored, allowing the distinction of the *trans* and *cis* isomer of OJ8. After each run, the column was washed and equilibrated

until a stable baseline was reached again. The chromatography system was operated and monitored using EMPower (Waters). As ACN is hazardous, experiments were performed with special attention to proper disposal of all waste solutions.

During sample preparation, OJ8 was protected from light, solved in DMSO and diluted in F-buffer to 50 µM resulting in a final DMSO concentration of 1.6 %. F-buffer supplemented by 1.6 % DMSO was used as a control allowing the identification of signal due to buffer compounds. OJ8-stabilized F-actin was prepared as described for *trans*-OJ8 cryo-EM sample (see Section 3.1.2), but without adding extra OJ8 after resuspension of the pellet, as larger amounts of unbound ligand would falsify the results. A control sample containing only F-actin (no JASP ligand) was prepared in analogy. OJ8, in solution or bound to F-actin, was activated for 5 min using one LED with a wavelength of 380 nm flashing for 1 s every 3 s using the illumination setup described in Section 3.1.2 (Figure 3.4). Samples were activated before dilution (OJ8: 1 µl of 3 mM, OJ8-stabilzed F-actin: 10 µl of 150 µM), as smaller volumes can be activated more efficiently. Relaxation of *cis*-OJ8 to its *trans* state was stimulated by a subsequent illumination for 5 min using one LED with a wavelength of 520 nm again flashing for 1 s every 3 s.

3.2 Structural biology

When studying the structure of filamentous proteins at high-resolution, transmission electron microscopy (TEM) is the method of choice (also see Section 2.1). Due to the high vacuum in the column of the microscope, biological samples that are typically prepared in liquid buffer solutions, are fixed onto a specimen holder (grid, Figure 3.7). Standard grids consist of copper and are covered with a thin layer of carbon. This layer can be either continuous (for negative stain EM or for proteins that suffer from preferred orientations or require a support film) or holey (for cryo-EM, also see Figure 3.7). For stability reasons each grid is divided into hundreds of squares. A variety of grids is available commercially, offering different grid materials, additional substrate layers, mesh and hole sizes.

The surface of grids is generally hydrophobic. Thus, it has to be rendered hydrophilic prior to applying a liquid sample. For this purpose, grids were glow discharged using a plasma-cleaner (FEMTO, Diener electronics) immediately before sample application for both negative stain and cryo-EM.

Fixation of TEM samples can either be achieved by drying in combination with staining (negative stain EM) or by vitrification (cryo-EM) (also see Section 2.4.3). While the sample preparation for negative stain EM is straightforward and results in high-contrast images, the achievable resolution is limited to $\sim$ 20 Å due to the grain size of the staining solution. In contrast, sample preparation for cryo-EM is more complicated and cryo-EM

images of lower contrast requiring the usage of sophisticated software for data acquisition and analysis. Yet, only cryo-EM allows the reconstruction of high-resolution structures (also see Section 2.4.3). For this reason, negative stain EM was only used for an initial sample check and optimization within this thesis. Consecutively, all samples were further studied by cryo-EM.

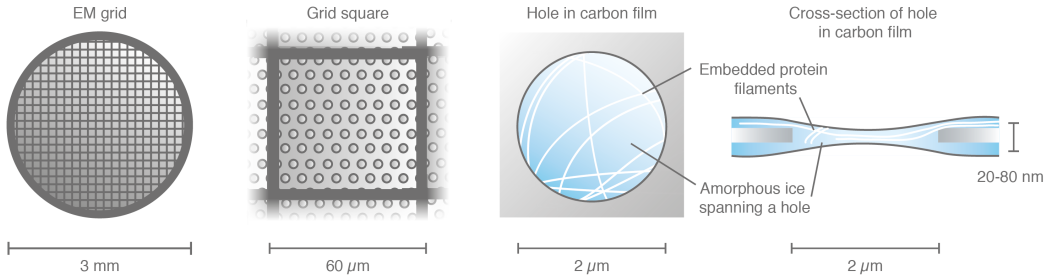

Fig. 3.7: Schematic illustrating the layout of a typical EM specimen holder (grid). The grid is divided into squares and either covered with a continuous or holey carbon layer (as depicted). The latter allows the vitrification of protein filaments in a thin layer of amorphous ice, which results in minimal background during imaging. This figure was created based on Wang and Sigworth (2006)

Within this chapter, methods of negative stain EM including sample preparation and sample screening are described (Section 3.2.1). Afterwards, vitrification protocols for cryo-EM are presented, followed by sample screening and optimization strategies and finally details on the high-resolution data acquisition of cryo-EM samples (Section 3.2.2). The subsequent section deals with the computational methods used to analyze the cryo-EM data within this thesis, including not only details on the 3D reconstruction, but also on model building and structural analysis (Section 3.3).

3.2.1 Negative stain EM

Negative stain EM was used to assess the sample quality and adjust the protein concentration prior to cryo-EM. Details on the sample preparation and screening procedure are given in the following Sections 3.2.1.1 to 3.2.1.2.

3.2.1.1 Sample preparation

Carbon coating of grids Fixation of protein samples by negative staining requires grids with a continuous carbon film. These grids were prepared manually, by first applying a polymer film to bare copper grids (G2400C, Plano GmbH), which was later covered with a thin carbon film. For this purpose, filtered water was filled into a clean glass beaker

with a diameter of $\sim$ 30 cm. As soon as the water surface had calmed down, 2-3 droplets ($\sim$25 µl) of collodion solution (Sigma) were carefully applied to the surface, taking care not to disturb it. Evaporation of the solvent resulted in the formation of a continuous polymer film on the water surface. Individual grids were carefully placed onto the film upside-down with inverted forceps. Perturbations of the surface would result in creases in the final carbon film and were thus avoided. Grids were placed close to each other without overlap to ease the subsequent transfer. Once a patch of grids ($\sim$ 40-60) was placed, a piece of lint-free blotting paper covering the area of grids was gently applied onto the surface. When the paper was completely soaked, the surrounding polymer film was disrupted and the paper together with the grids and polymer film carefully lifted from the water surface. Grids (polymer film pointing upwards) were left to dry for 2-3 days in a Petri dish in the presence of additional filter paper, before they were carbon coated using a high-vacuum carbon coater (Leica EM ACE600). For optimal stability and contrast, a carbon layer of $\sim$5-10 nm was applied. Coated grids can be stored at room temperature for months to years when kept dry.

Preparation of stain solution In this thesis a 0.75 % uranyl formate solution was used for negative staining of protein samples. It generates high contrast and has a relative small grain size compared to other heavy metal stains. This advantage comes at the cost of acidity ($\sim$ pH 4), which has a negative impact on pH-sensitive proteins. Furthermore, uranyl formate is highly toxic and should thus be handled carefully including proper disposal of hazardous waste. The staining solution was prepared by dissolving 37.5 mg of uranyl formate (SPI-Chem / Science Services) in 5 ml of boiling water. After 5 min of stirring protected from light, 4.5 µl of 5 M NaOH were added to adjust the pH to $\sim$ pH 4, followed by another 5 min of stirring in the dark. Finally, the solution was filtered using a 0.22 µm filter syringe to remove debris. When stored at room temperature and protected from light the staining solution is stable up to one week before it starts to precipitate. Freezing of small aliquots extends the shelf life.

Negative staining of protein samples Negative stain samples were prepared according to a standard protocol (Pospich et al., 2020, von der Ecken et al., 2015). Specially, 4 µl of sample was applied onto a freshly glow-discharged copper grid, which was previously coated with a thin continuous carbon film. The sample was incubated for 60 s before excess solution was blotted away using filter paper (Whatman no. 4, the grid should never dry out). For the following washing and staining steps, two droplets (10 µl) of sample buffer and two droplets of 0.75 % uranyl formate staining solution were applied onto a clean piece of Parafilm (Bemis). The grid was washed twice with buffer and once with stain by adsorbing a droplet to the grid, followed by direct blotting of excess solution.

Finally, the sample was stained by incubating the second drop of staining solution for 30 s before blotting. The grid was left to dry for several minutes before imaging. Negative stain grids can be stored for years when not exposed to direct light or humidity.

3.2.1.2 Screening and sample optimization

In this thesis negative stain EM was only used to assess the sample quality and empirically adjust the protein concentration prior to cryo-EM, although this technique can also be used to structurally characterize proteins at low-resolution.

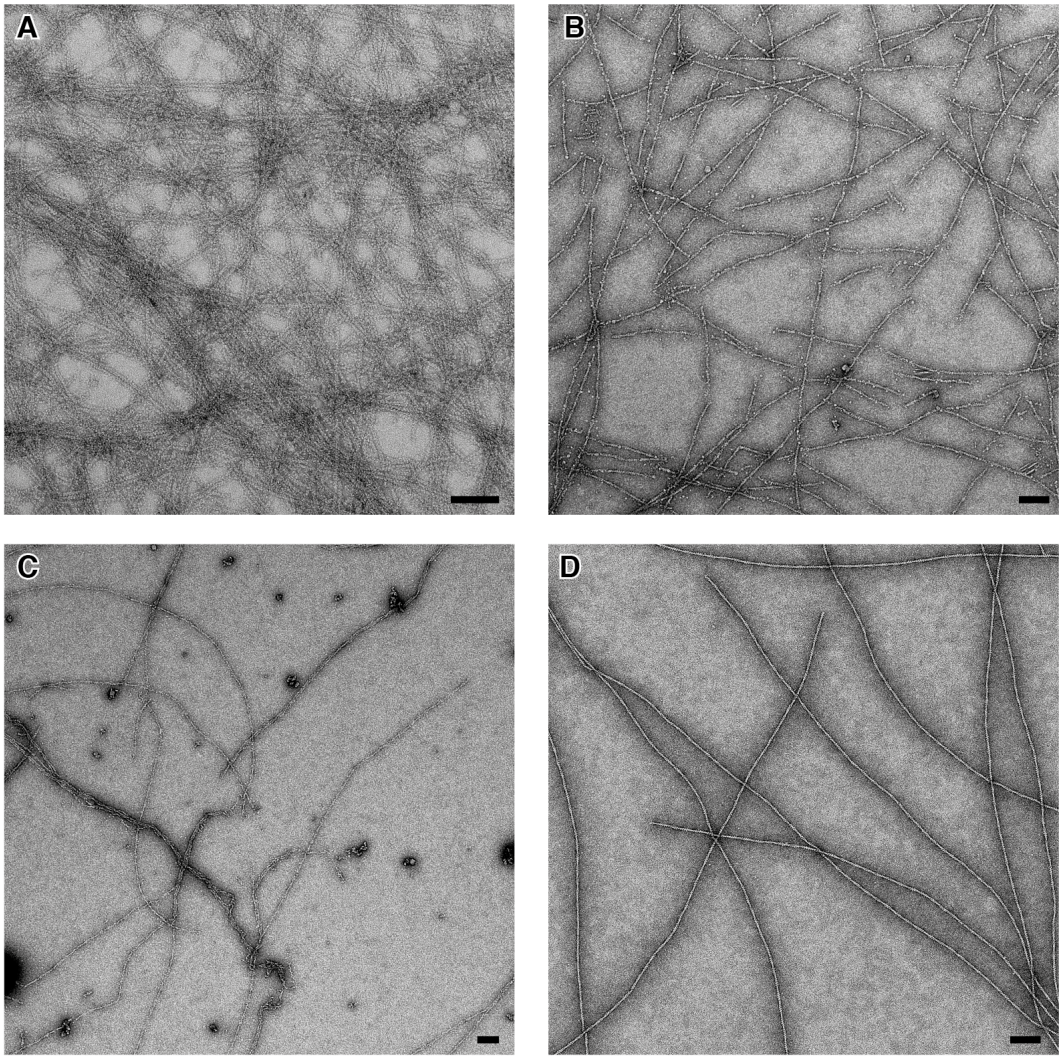

Fig. 3.8: Negative stain micrographs illustrating **(A)** a too high protein concentration, **(B)** fragmented filaments, **(C)** aggregates and bundled filaments and **(D)** an optimized F-actin sample. Scale bar 200 nm.

Negative stain grids were either screened on a JEOL JEM-1400 electron microscope or a Tecnai G2 Spirit microscope (Thermo Fisher). Both microscopes are equipped with a

4k x 4k CMOS TemCam F416 detector (TVIPS) and a LaB_6 cathode operated at 120 kV. Microscopes and cameras were operated using the EMMENU software (TVIPS).

While ∼1 µM is a good starting concentration when preparing negative stain grids of F-actin, the concentration has to be adjusted empirically for every sample, not least because the concentration of F-actin cannot be measured reliably (also see Section 3.1.1). The protocol described in the previous section works well for most samples. Yet, the staining procedure, e.g., incubation and blotting time, might require optimization. Once a suitable concentration and staining conditions are found, negative stain EM can give valuable insights about the quality of the sample. Filaments might, for example, be fragmented or partially aggregated (Figure 3.8).

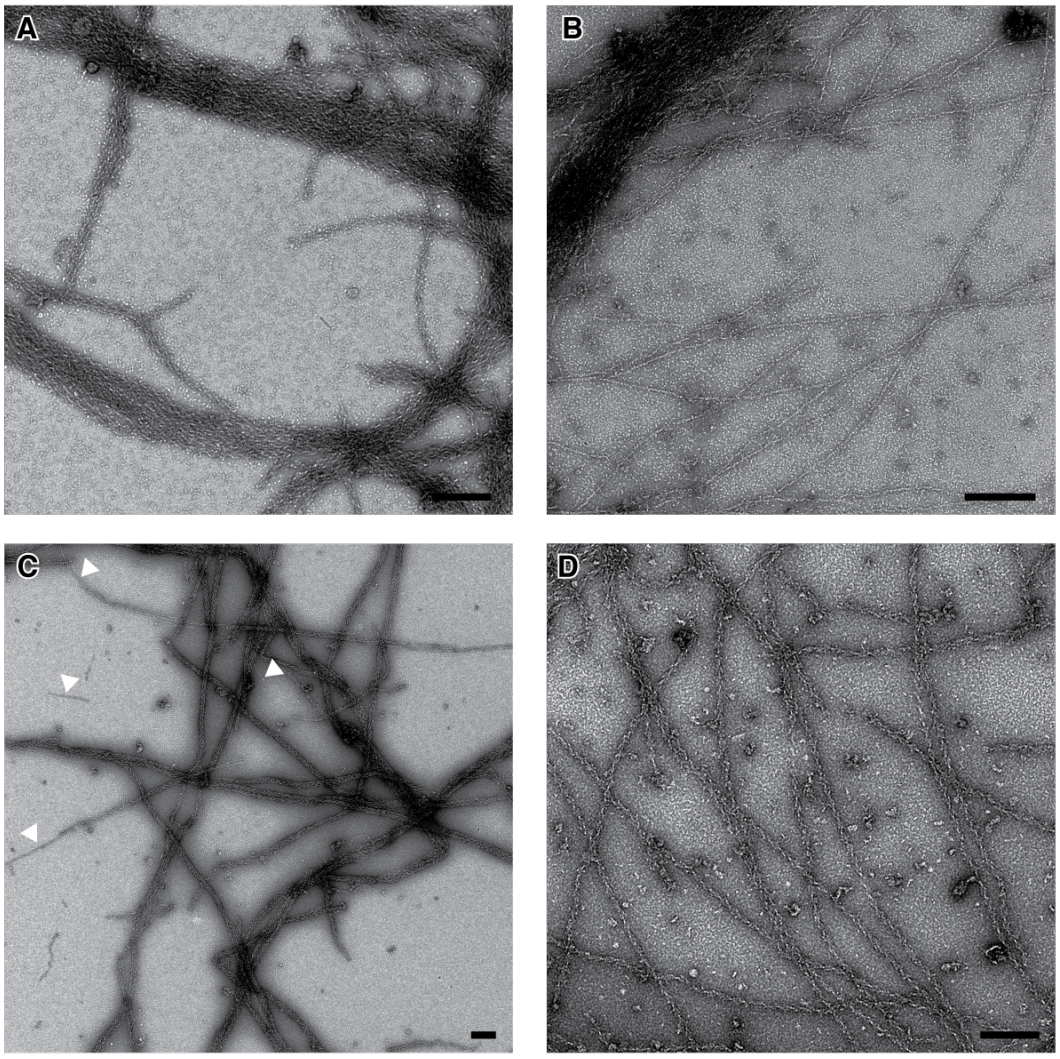

Fig. 3.9: Negative stain micrographs illustrating **(A)** bundled actomyosin filaments, **(B-C)** bundled and partially decorated filaments and **(D)** an optimized actomyosin sample. White arrow heads highlight undecorated F-actin in **(C)**. Scale bar 100 nm.

Whereas the bare F-actin filaments studied in this thesis required little to no sample optimization, the preparation of actomyosin filaments proved to be more complex. Incubation of F-actin with myosin always resulted in thick bundles of actomyosin filaments (Figure 3.9A-B). This behavior was independent of the stoichiometry, and reduction of the myosin concentration resulted in only partially decorated or undecorated F-actin (Figure 3.9B-C). Changing the buffer composition, i.e., the ionic strength, did also not abolish bundling. Finally, this problem was overcome by using a previously reported on-grid decoration strategy (von der Ecken, 2016, von der Ecken et al., 2016). Here, F-actin is first applied onto the grid and incubated, before excess solution is blotted away, resulting in a network of "fixed" filaments spanning over the complete grid. Due to nonspecific interaction with the carbon surface of the grid, filaments will not bundle, even when myosin is afterwards added and incubated. This strategy was successfully applied to prepare the actomyosin filaments studied within this thesis (Figure 3.9D). To achieve a full decoration of F-actin, filaments need to be saturated with myosin at a concentration above the dissociation constant K_D, which depends on both the nucleotide state and buffer composition. In this thesis, the myosin concentration was adjusted empirically by maximizing the number of decorated filaments. Usually filaments needed to be over-saturated, inevitably resulting in a higher background consisting of unbound myosin (Figure 3.9D).

3.2.2 Cryo-EM

The focus of this thesis was on the reconstruction of high-resolution structures; thus, cryo-EM was the predominant method used (also see Section 2.1). Cryo-EM samples need to be vitrified to avoid formation of ice crystals, which would destruct the protein structure. Thin biological samples are routinely vitrified using a method called plunge freezing. Details on plunge freezing, strategies for cryo screening and sample optimization as well as for the final high-resolution data acquisition are given in the following Sections 3.2.2.1 to 3.2.2.3.

3.2.2.1 Plunge freezing

To reach high-resolution, protein samples should ideally contain no detergents, cryo-protectants or electron-dense buffer components such as phosphate or high salt concentrations, as they negatively impact the vitrification process and sample contrast. In reality, these additives can often not be omitted, but should still be reduced to a minimum. For this reason, only small volumes of high-concentration JASP and PHD were added to cryo-EM samples, so that the final DMSO and methanol concentrations were usually <1 %. However, there are also additives that can have a positive effect on either plunge freezing or

the protein distribution on the grid. For instance, small amounts of Tween 20, a non-ionic detergent, improve the spreading of the sample droplet on the grid and thereby result in a more homogeneous ice distribution after plunge freezing. Therefore, 0.02-0.04 % (weight/volume) Tween 20 were added to all cryo-EM samples described within this thesis.

A multitude of grids with varying material, surface layer, hole and mesh sizing is available commercially, meeting the different needs of protein samples. For the vitrification of F-actin and actomyosin filaments standard holey carbon grids with a hole size of 2 µm (2/1 300 mesh Quantifoils or 2/1 C-flats, Protochips) were used (Figure 3.7). After rendering the surface hydrophilic by glow-discharging (also see Section 3.2), an individual grid was mounted to the forceps of a cryo plunger. A small volume of protein sample was then applied onto the grid and excess solution blotted away after a short incubation time. Finally, the grid was plunged into liquid ethane (∼-167 C°). In this way, the grid was cooled down so quickly that ice crystals could not form, resulting in an amorphous, glass-like ice layer, also known as vitrified water.

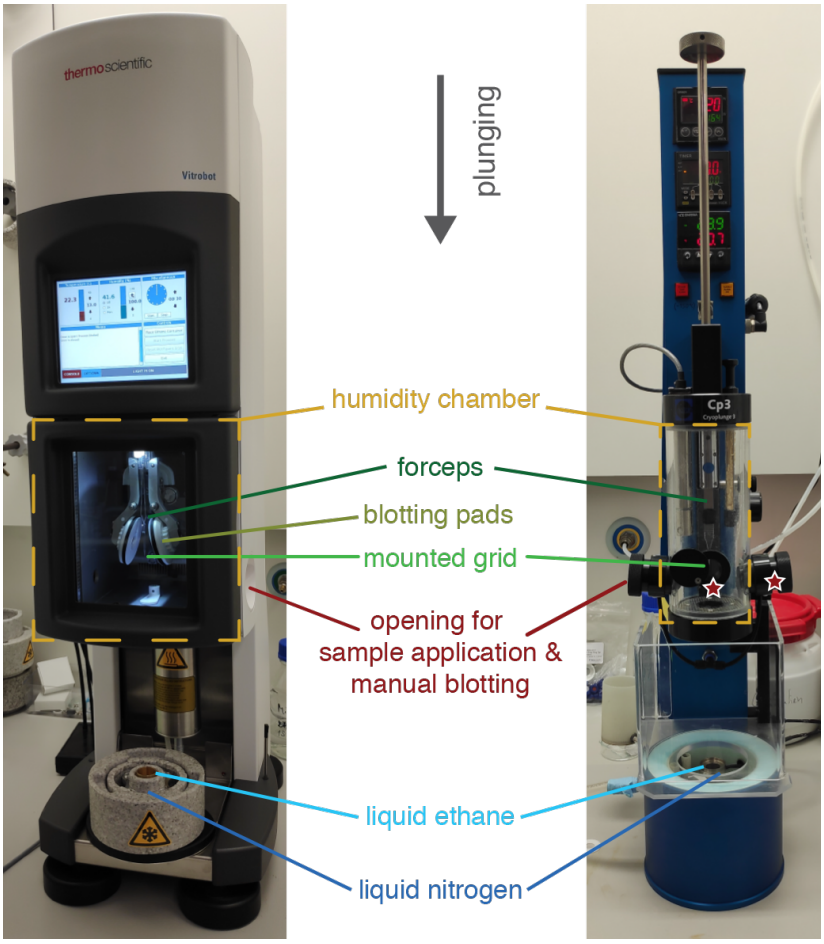

Fig. 3.10: Composition of cryo-EM plungers used for vitrification **(Left)** Vitrobot (Thermo Fisher) and **(Right)** Cryoplunge CP3 (Gatan). Additonal openings for sample application and manual blotting at the front and side of the CP3 cryo plunger are highlighted by red stars.

Two different cryo plungers were used in this thesis, namely the Cryoplunge CP3 (Gatan) and the Vitrobot (Thermo Fisher). Both share a similar overall architecture (Figure 3.10), consisting of an interface to adjust key parameters (top), a humidity chamber which encloses the forceps and automatic blotting pads (center) and a pot of liquid ethane surrounded by liquid nitrogen for cooling (bottom). A humidity of ∼90-100 % is crucial to minimize the evaporation of the sample during the plunging process. While the humidity within the chamber of the CP3 comes from a small sponge soaked with hot water and is thus difficult to fine tune, the humidity chamber of the Vitrobot is automated and furthermore temperature controlled, increasing the reproducibility of the plunging process. Another advantage of the Vitrobot is that it has an exchangeable ethane-nitrogen pot, which is lifted to the opening of the humidity chamber for plunging, thereby significantly reducing the plunging path. Whereas the ethane pot of the CP3 is fixed, and thus can neither be lifted nor exchanged, it is temperature controlled and equipped with an additional heater to circumvent freezing of the ethane in contrast to the Vitrobot.

The usage of either plunger requires the careful handling of the ethane as it is explosive and will directly cause frostbite when in contact with skin. Furthermore, the cool surfaces and liquids act as a cooling trap, effectively attracting all kinds of particles from the air which accumulate into severe contamination over time. Thus, plunging was performed in a humidity controlled room, using a face mask, and all tools were heated before usage to completely dry them.

After plunging, excess ethane was manually blotted using filter paper (Whatman No. 4) and individual grids were transferred into a grid box resting within the liquid nitrogen surrounding the ethane pot. As the vitrified ice-layer easily breaks when under stress, grids were carefully handled and always held at their outer rim. To avoid contamination and devitrification, only clean liquid nitrogen was used and grids were directly transferred to a liquid nitrogen cooled dewar for long-term storage, if not directly screened or imaged.

In general, the grid type and parameters of plunge freezing, i.e., sample concentration, volume, incubation and blotting time, need to be optimized for every protein sample. The plunging of F-actin and actomyosin filaments furthermore required the optimization of the blotting strategy as described in the following paragraphs.

Manual blotting Samples plunged with the CP3 cryo plunger were blotted manually, as the automatic blotting of this device was not gentle enough, resulting in fragmented, broken filaments. 1.5-2 µl of sample was applied onto the front of a freshly glow-discharged cryo grid using the front opening of the plunger. After an incubation time of 30-60 s, the solution was manually blotted from the backside using a small piece of blotting paper (Whatman No. 5) fixed in a pair of forceps. For this purpose, the forceps were first in-

serted through the right opening of the plunger, before the filter paper was gently brought into even contact with the entire backside of the grid. The blotting process was guided by directed backlight and monitored by a timer. After the desired blotting time had elapsed (∼4-11 s), the forceps with the blotting paper were pivoted away and the grid directly plunged into liquid ethane. By blotting from the backside, the buffer solution is sucked away, while the majority of filaments that span over the grid square, do not fit through the holes. Thereby, this strategy effectively "enriches" the filament concentration, so that protein concentrations of $\sim$ 0.2-1.0 µM give a suitable filament concentration.

Automatic blotting The Vitrobot plunger has a very gentle blotting mechanism and the blot force can additionally be adjusted, enabling the automatic blotting of F-actin samples when using a relative blot force of -20 to -25 (minimum possible). Initially, critical values including the temperature (13 °C), incubation time (0 s), blotting time (6-9 s), blot force and drain time (0.5-1.0 s, delay between blotting and plunging) were set in the interface of the plunger. Then, 1.5-3.0 µl of sample was applied to the front of a freshly glow-discharged cryo grid using the side opening of the plunger. Immediately afterwards, the automatic plunging process was started. Since both sides of the grid are in contact with blotting paper during automatic blotting, a noteworthy fraction of filaments gets blotted away. Therefore, the protein concentration required for automatic blotting is in general higher than for manual blotting and ranges from 5 µM to 10 µM.

On-grid decoration To avoid bundling of actomyosin filaments, F-actin was decorated with myosin on the grid (also see Section 3.2.1.2) using the Vitrobot plunger. Therefore, 3 µl of the F-actin sample was applied onto the front of a freshly glow-discharged cryo grid using the side opening of the plunger. After an incubation time of 60 s, the solution was manually blotted from the side using a small piece of blotting paper (Whatman No. 4) fixed in a pair of forceps. Blotting from the backside might be favorable, but would require the folding of the blotting paper as the orientation of the grid is fixed in the Vitrobot (front facing to the side). The grid and forceps are in general very sensitive and easily damaged. Thus, blotting with a folded paper would significantly reduce the reproducibility of the process. Hence, the blotting paper was oriented perpendicularly to the grid and gently brought into contact with the surface of the droplet sitting on the grid. As the grid should not dry out, the blotting was stopped just when the meniscus of the water surface reached the filter paper. Next, 3 µl of the myosin sample was applied onto the grid. From here on, the automatic blotting procedure described in the previous paragraph was carried out (temperature 13 °C, incubation time 30-60 s, blotting time 9 s, blot force -15 to -25 and drain time 0-1 s). Nucleotides and associated buffer components - 2 mM ADP and 20 mM $MgCl_2$, and 5 mM AppNHp and 4 mM $MgCl_2$, respectively - were added to

myosin immediately before applying the sample onto the grid. In this way, F-actin and myosin had minimal contact with each other's buffers, effectively reducing the harmful effects they might have. For example, the high Mg^{2+} concentration in the ADP-bound myosin sample would bundle F-actin (see Section 3.1.4). With the aim to trap different structural states within the ATPase cycle of myosin, the temperature of the humidity chamber was set to 4 °C and 25 °C, respectively, when preparing the AppNHp-bound actomyosin complex. The concentration of F-actin required for this plunging strategy ranged from 3-6 µM and was thus comparable to that required for automatic blotting. The required myosin concentration strongly depended on the nucleotide state of myosin. While 3-4 µM of myosin was sufficient to get full decoration for the strong-binding rigor and ADP states, 10-13 µM was required in case of the weak-binding AppNHp state, even though the salt concentration was lowered to increase the binding affinity (see Section 3.1.4).

Details on the vitrification of the individual samples studied in this thesis are summarized in Tables 4.2 to 4.11 in the Results and Discussion.

3.2.2.2 Cryo screening and sample optimization

Cryo-EM samples were either screened on a Tecnai G2 Spirit microscope (Thermo Fisher) equipped with a 4k x 4k CMOS TemCam F416 detector (TVIPS) and a LaB_6 cathode operated at 120 kV or a Talos Arctica (Thermo Fisher) operated at 200 kV and equipped with a Falcon III direct detector (Thermo Fisher).

The Spirit microscope is not primarily designed for the screening of cryo-EM samples and requires the usage of a liquid nitrogen cooled single-tilt cryotransfer holder 626 (Gatan). This holder enables the screening of one cryo-EM grid at a time. Due to long vacuum-pumping cycles and increasing contamination of the holder and transfer station, a maximum of $\sim$ 5-8 grids can be screened per day using the Spirit microscope. While grids cannot be recovered after screening using this setup (mostly because of devitrification and contamination), cryo screening at the Spirit microscope was sufficient to determine suitable vitrification conditions to prepare fresh cryo-EM grids for subsequent data collection.

A new instrument dedicated to the screening of cryo-EM samples significantly eased the process of screening and cryo sample optimization. The Talos Arctica comes with a fully-automated sample loader ("autoloader") and software that takes care of laborious tasks such as vacuum pumping and cooling. Furthermore, it runs EPU (Thermo Fisher), an advanced data acquisition software package which was also used for the acquisition of data presented in this thesis. To screen samples at this microscope, individual grids need

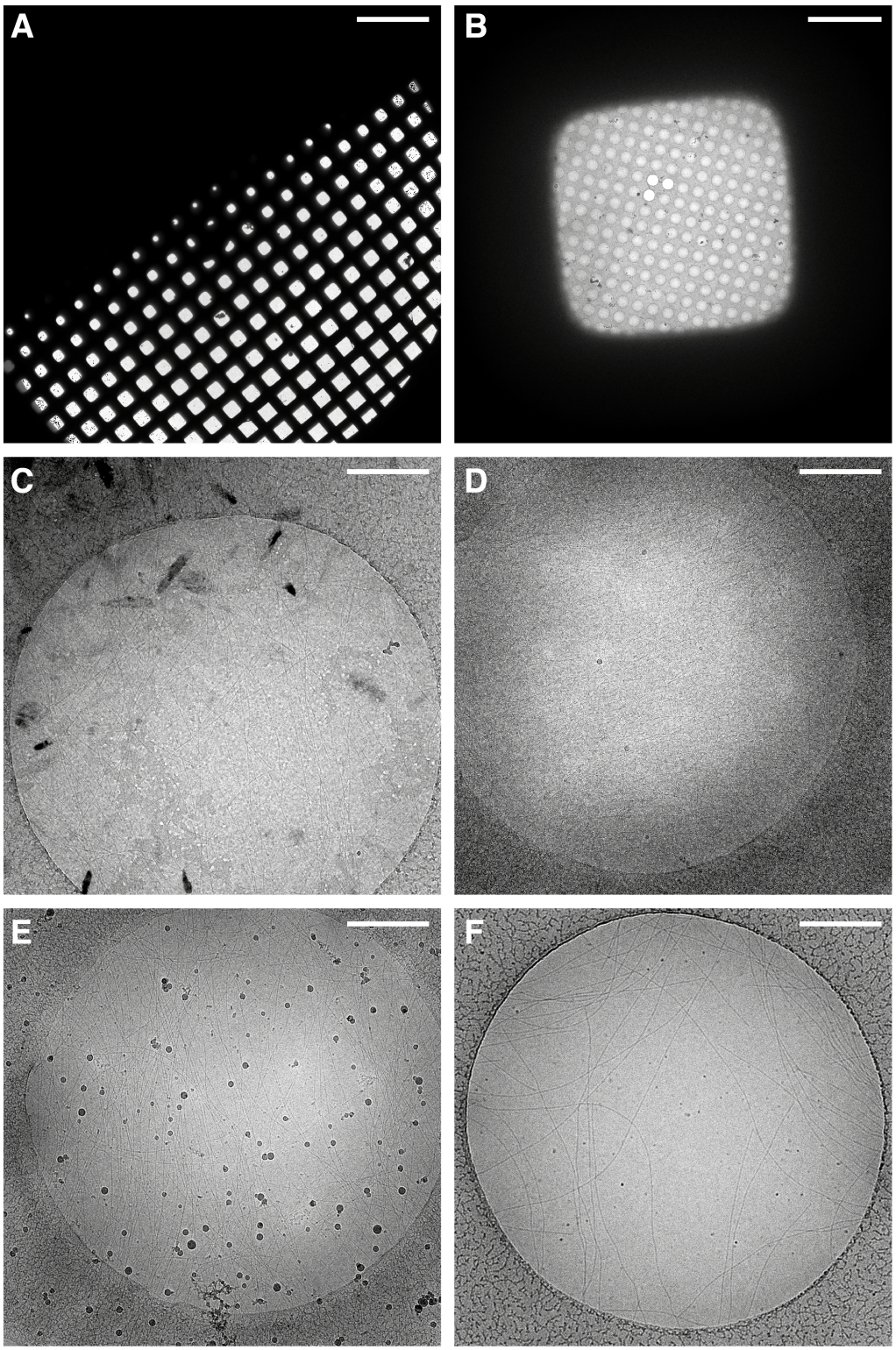

Fig. 3.11: Cryo screening and sample optimization of F-actin using the Spirit microscope. **(A)** Grid overview illustrating the typical gradient of ice thickness over the grid. **(B)** Overview image of a square with good ice thickness and distribution. The three bright holes in the center of the square have dried out and do not contain an ice layer. **(C-F)** Representative images of holes with **(C)** partially devitrified ice, **(D)** a too thick ice layer, **(E)** contamination and a too-high filament concentration and **(F)** after sample optimization. Scale bars **(A)** 250 µm, **(A)** 15 µm and **(C-F)** 0.5 µm.

to be “clipped“, i.e, transferred and fixed in a specific grid holder, and loaded to a cartridge that can hold a total of 12 grids. To avoid devitrification and contamination of grids, all these steps have to be conducted at least in liquid nitrogen atmosphere. Thanks to the automation and improved cooling, the number of grids one can screen per day drastically increased to $\sim$ 20-40. Moreover, grids screened with an Arctica microscope can be recovered, stored in liquid nitrogen and eventually imaged using a high-end microscope (Titan Krios, also equipped with an autoloader system, see next paragraph).

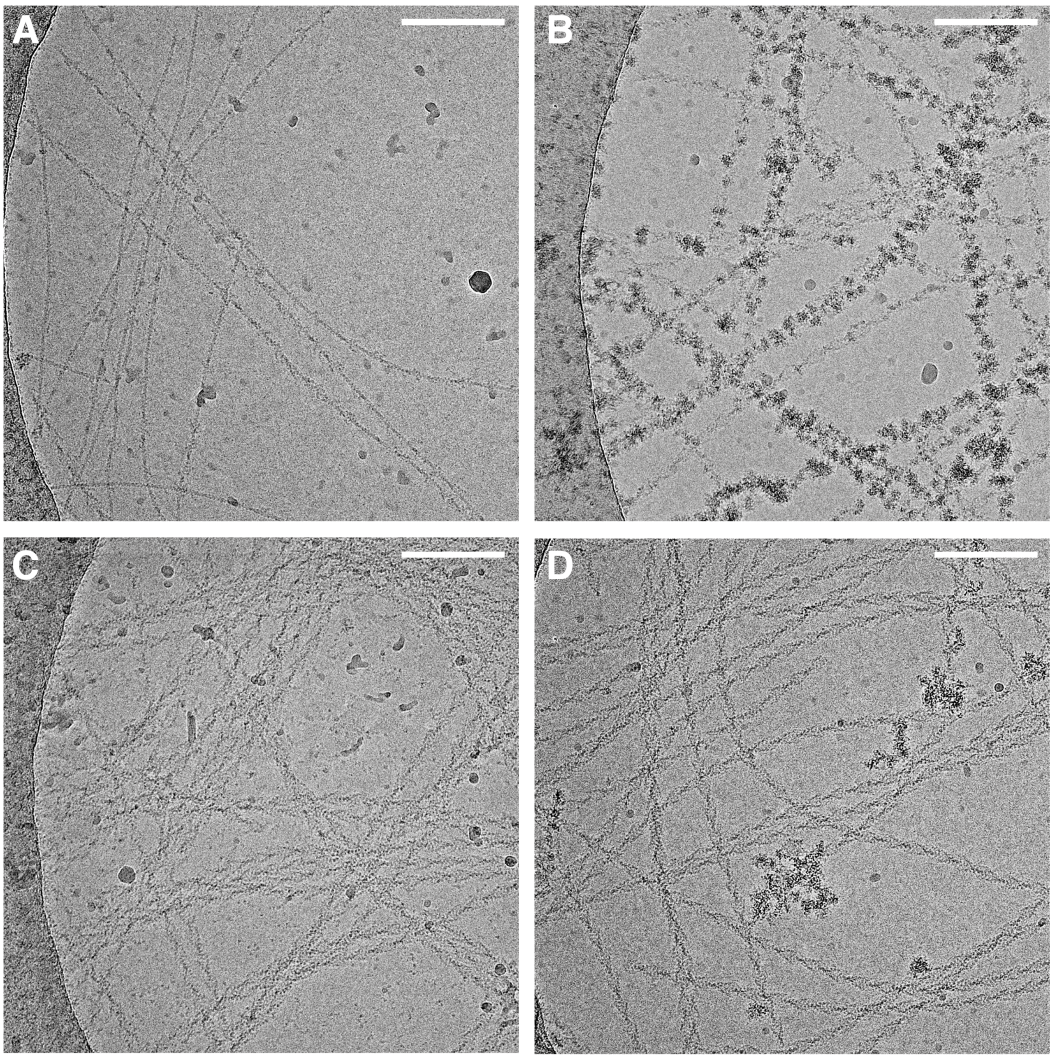

Fig. 3.12: Cryo screening and sample optimization of the actomyosin complex using the Arctica microscope. **(A-D)** Representative images of holes with **(A)** partially decorated filaments, **(B)** aggregated protein, **(C)** partially bundled filaments with high background and **(D)** after sample optimization. Scale bars 100 nm.

During cryo screening several aspects were assessed and optimized (Figure 3.11). First, the thickness, distribution and homogeneity of the amorphous ice layer was optimized by

changing, i.e., the blotting and drain time, blot force, sample volume and buffer composition. This step is crucial as the ice layer has a significant effect on the overall contrast and achievable resolution. Next, the protein sample, specifically the concentration and distribution of filaments, was optimized. For actomyosin samples, the plunging conditions and the concentration of F-actin were first optimized using the on-grid decoration plunging strategy (also see Section 3.2.2.1) but applying buffer instead of myosin. Once suitable conditions were found, myosin was added and its concentration adjusted empirically, aiming for fully decorated filaments with minimal unbound myosin in the background (Figure 3.12).

3.2.2.3 Data Acquisition

In principle, the Talos Arctica microscope used for cryo screening could have also been used for high-resolution data acquisition as it is equipped with a direct electron detector. However, its performance is inferior compared to high-end microscopes, which were designed for the high-resolution data acquisition of biological samples. For this reason, data sets were collected on Titan Krios microscopes (Thermo Fisher), equipped with a X-FEG operated at 300 kV. While one of the microscopes used in this thesis has a spherical aberration constant C_s of 2.7 mm, the other microscope is equipped with a Cs-corrector, which allows the correction of spherical aberration. Different direct detectors were used for data acquisition including a Falcon II (Thermo Fisher), a Falcon III (Thermo Fisher) and a K2 Summit (Gatan) camera. The Falcon detectors were always operated in linear mode, whereas the K2 camera was used either in counting or super-resolution mode (also see Section 2.4.6). To further improve the contrast of images, K2 data sets were collected using an additional GIF quantum energy filter (slit width of 15-20 eV, zero loss peak), which removes inelastically scattered electrons that would primarily contribute to noise. An overview of the data acquisition conditions used for every individual sample is given in Tables 4.2 to 4.11 in the Results and Discussion.

Data acquisition was carried out automatically using the EPU software (Thermo Fisher). First, a multi-tile overview image (“atlas“) of the complete grid was acquired. Next, grid squares of suitable ice thickness and corresponding holes were manually selected (Figure 3.13A-B). Finally, an acquisition pattern for the automated data collection was set up, defining critical aspects such as the imaging area, defocus values, and the drift measurement criterion (Figure 3.13C). A total of four, non-overlapping micrographs was collected per hole (“spot scan“), using a range of defocus values ($\sim$ 0.5-3.0 µm) to collect information for all frequencies within one data set (also see Section 2.4.2).

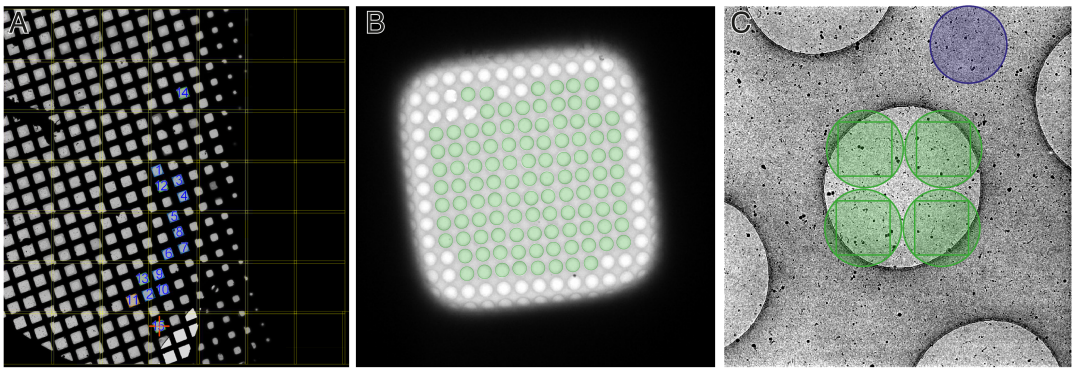

Fig. 3.13: Setting up of an automatic data acquisition in EPU. **(A)** Squares of suitable ice thickness were selected on the atlas grid overview. **(B)** Holes with a thin homogeneous ice layer were selected (green circle), while holes with broken, thick or contaminated ice layer were omitted. **(C)** Within the acquisition pattern, the acquisition areas (green) and the area for the defocus and drift estimation were defined (blue).

3.3 Computational methods in cryo-EM

An intrinsic feature of cryo-EM data is their low signal-to-noise ratio (SNR), which is mostly due to the weak scattering characteristics of biological samples combined with the low electron dose required for radiation sensitive samples. Thus, the structural information one can gain from raw cryo-EM data is strongly limited to the general appearance of the protein, i.e., elongated or round and its approximate dimensions. To harvest all the structural information, the computational analysis of a cryo-EM data set is indispensable. While 2D classification can already give valuable insight, the reconstruction of a 3D electron density map is the heart of the analysis. Within this section the principles and methods of image processing as well as atomic model building and analysis are described (Sections 3.3.1 to 3.3.3, Figure 3.14). Details on the processing and analysis of individual data sets can be found in the corresponding methods sections. Software packages used for the processing of cryo-EM data and the subsequent model building and analysis are summarized in Tables 3.3 to 3.4 at the end of this chapter.

3.3.1 Image processing and 3D reconstruction

Image processing is essential for the reconstruction of a 3D electron density map from cryo-EM data. First, a data set needs to be preprocessed with the aim to correct for the negative effects of specimen drift, beam damage and the CTF (also see Section 2.4.3). Preprocessing closes with the selection and extraction of 2D particle images and cleaning of the corresponding 2D particle stack by 2D classification (Figure 3.14). The unknown projection parameters of each particle within this stack are then determined by projection matching with 2D projections of a 3D reference volume. Based on these parameters, a

3D reconstruction of the electron density map can be computed and iteratively refined by backprojecting the 2D particles (also see Section 2.4.4). Additional processing steps can further improve the quality of the reconstructed 3D volume and allow the separation of heterogeneous 3D clusters within one data set.

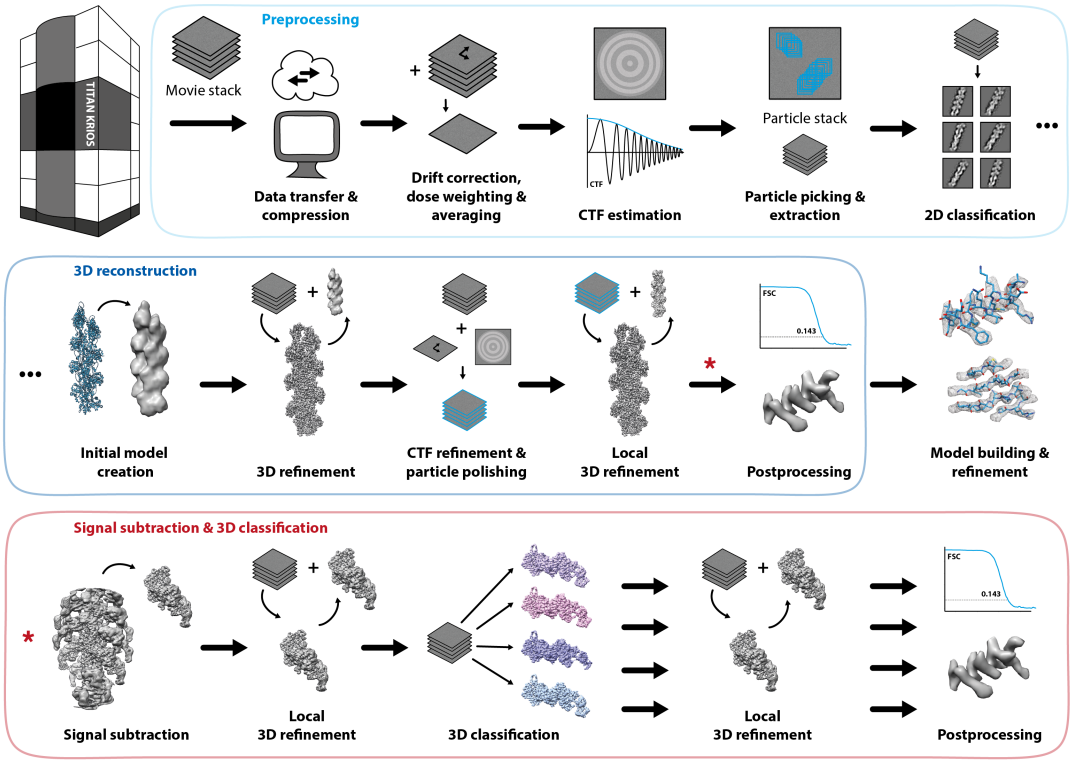

Fig. 3.14: Schematic of the cryo-EM processing pipeline consisting of preprocessing (light blue box), 3D reconstruction (dark blue box) and model building tasks. Due to the heterogeneity of the actomyosin complex additional processing steps were essential (red asterisk and box) including signal subtraction, 3D classification and a local 3D refinement of each subset.

3.3.1.1 Preprocessing

A standard cryo-EM data set consists of thousands to ten thousands of gigabyte-sized movie stacks. Consequently, the first and inevitable preprocessing step is the loss-free compression, the transfer to a data storage server and/or a computer cluster and the archiving of data for long-term storage (Figure 3.14). Afterwards, image processing starts with the correction of the specimen drift by aligning individual movie frames. Furthermore, movie frames are dose-weighted prior to averaging to reduce the effect of beam damage on the high-resolution information within the aligned micrographs (Figure 3.14). The software MOTIONCOR2 (Zheng et al., 2017) was used for this purpose for all data sets except the very first one (*Pf* Actin), where this software was not yet available. Instead, movies were aligned with UNBLUR (Grant and Grigorieff, 2015) and averaged with

SUMMOVIE (Grant and Grigorieff, 2015). While UNBLUR only supports the alignment of full frames, MOTIONCOR2 also supports the alignment of overlapping patches within frames. This option was, however, not used for the alignment of filamentous data, as F-actin usually spans over the complete micrograph and patch alignment might cause discontinuities within filaments. To further mitigate the negative impact of beam damage, the total electron dose was reduced for some data sets by averaging only a fraction of all available movie frames, i.e., only the first 15 instead of all 30 frames were averaged. As the exclusion of frames comes at the cost of an overall loss of contrast, these dose-reduced micrographs were only used for the final iterations of 3D refinement (also see Section 3.3.1.3). For the correction of the CTF during the 3D refinement, the CTF parameters, i.e., defocus and astigmatism, are required (also see Section 2.4.2) and thus need to be estimated during preprocessing (Figure 3.14). CTF estimation was performed with GCTF (Zhang, 2016) or CTFFIND4 (Rohou and Grigorieff, 2015) on aligned micrographs or movie frames (only for CTFFIND4).

In the following step, individual particles are selected (also known as particle picking) and extracted from aligned dose-weighted micrographs (Figure 3.14). In case of protein filaments, each individual subunit represents a particle. Thus, whole filaments are selected and automatically split into overlapping segments (also see Section 2.4.5). Initially, filaments were picked manually using *sxhelixboxer* in SPARX (Behrmann et al., 2012b) or *e2helixboxer* in EMAN2 (Tang et al., 2007). Later, this laborious task was automated and from there on filaments were either picked with SPHIRE STRIPER (Wagner et al., 2020), which is based on a ridge detection algorithm, or SPHIRE crYOLO (Wagner et al., 2020), a deep-learning based particle picker, which needs to be trained on a small subset of manually picked data. Filaments were segmented based on the rise of F-actin $\Delta z = 27.5$ Å, so that each box contained one unique actin subunit. The box size of the particle boxes depended on the pixel size and was adjusted to enclose 10-12 actin subunits. Only filaments containing at least six segments were considered. After successful picking, particle images were extracted into a stack of 2D images using either SPARX (Behrmann et al., 2012b), SPHIRE (Moriya et al., 2017) or RELION (He and Scheres, 2017, Scheres, 2012). Although the picking performance of crYOLO and STRIPER is exceptionally good (Wagner et al., 2020), false positive picks can usually not be prevented completely. For this reason, particle stacks coming from automatic picking were cleaned by 2D classification using ISAC (Iterative Stable Alignment and Clustering) (Yang et al., 2012) within SPHIRE (Moriya et al., 2017) or *relion_refine* within RELION (He and Scheres, 2017, Scheres, 2012). During 2D classification, particles are first aligned in 2D and then clustered by similarity, specifically the view of the protein represented. Finally, all members of one cluster are averaged into a higher contrast class average (Figure 3.14). The quality of resulting class averages was assessed manually and only particles con-

tributing to classes showing high-resolution features were kept.

The whole preprocessing pipeline described here was recently automated in TRANSPHIRE (Stabrin et al., 2020). But TRANSPHIRE does not only automate these laborious tasks, but also runs on-the-fly and monitors all key parameters. In this way, it returns first results while the data acquisition is still ongoing and also facilitates the identification problems the moment when they arise. Furthermore, TRANSPHIRE comes with a deep-learning driven feedback loop that automatically retrains the crYOLO picking model to match the needs of an individual protein sample. To accelerate the computationally costly 2D classification, TRANSPHIRE makes use of a GPU accelerated version of ISAC called *sp_isac2_gpu* (Stabrin et al., 2020) within SPHIRE (Moriya et al., 2017). Finally, TRANSPHIRE also supports the 3D refinement of small batches of particles (∼20,000). Different alpha and beta versions of TRANSPHIRE (Stabrin et al., 2020) were used for automatic preprocessing of cryo-EM data within this thesis.

3.3.1.2 3D Reconstruction

While the processing and in particular the 3D refinement of filamentous proteins requires a number of adjustments to the SPA (single particle analysis) workflow (also see Section 2.4.5), it still relies on projection matching to determine the projection parameters followed by a 3D backprojection in Fourier space. Consequently, an initial 3D reference map is required. While different methods for the computation of an *ab initio* 3D electron density map are available, e.g., *sp_rviper* within SPHIRE (Moriya et al., 2017), they all struggle with filamentous data, due to the unequal distribution of views, i.e., the data only consist of side views and lacks all top and bottom views. Alternatively, previously solved structures of similar proteins can be used to computationally create a 3D reference map. In some cases, a cylinder filled with Gaussian noise can also serve as a 3D reference, however, alignments are usually less robust due to the missing polarity and handedness within the reference. Within this thesis an initial 3D reference map was always created from published atomic models of F-actin or actomyosin filaments using SPHIRE (Moriya et al., 2017), SPARX (Behrmann et al., 2012b) and EMAN2 (Tang et al., 2007) (Figure 3.14).

A number of software packages offering helical refinement strategies is available (also see Section 2.4.5). However, all of these apply the helical symmetry to the data during the 3D refinement. While the application of symmetry can increase the resolution of a 3D reconstruction by practically mimicking a larger number of particles, the symmetry parameters of helical filaments are not straightforward to determine, change significantly with small errors on the pixel size and can easily cause overrefinement when determined incorrectly (Pospich and Raunser, 2018). Furthermore, F-actin is not rigid but can bend, which translates into a drop of resolution towards the ends of the filament within the

3D reconstruction. Symmetrization would flatten this gradient, improving the resolution at the ends of the filament, but simultaneously worsening the resolution at the center (Pospich and Raunser, 2018). Thus, two alternative hybrid SPA processing strategies that do not apply any symmetry were used for the 3D refinement within this thesis.

3.3.1.3 Hybrid SPA 3D refinement of F-actin in RELION

At the beginning of the research performed for this thesis, F-actin data sets were 3D refined using an in-house developed hybrid SPA processing strategy (Merino et al., 2018) in RELION (He and Scheres, 2017, Scheres, 2012, Zivanov et al., 2018). Initially, extracted and pre-cleaned particle stacks were manually split into half sets, i.e., split by filament, to avoid artificially high FSC values due to self-correlation of particles originating from the same filament, as consecutive particle images are ∼90 % identical. For this refinement strategy the affiliation of particles to filaments needs to be included into the metadata file (.star file). Therefore, this information was either manually added to the particle star file (`_rlnHelicalTubeID, _rlnHelicalTrackLength`), or particles were directly extracted using helical RELION (He and Scheres, 2017). In case of the latter, information about the orientation of the filaments (`_rlnAngleTiltPrior, _rlnAnglePsiPrior, _rlnAnglePsiFlipRatio`) is automatically added to the metadata. As these priors would interfere with the hybrid SPA processing strategy, they were removed manually. Next, dose-weighted binned particles (to speed up the refinement) were 3D refined using *relion_refine* with a sampling of $\Delta = 3.75°$ (`--healpix_order 3`). By considering only sampling points close to the equator of the sampling sphere (`--limit_ tilt 89`), projection matching was restricted to side views in accordance to the relative orientation of F-actin within the ice layer (Figure 3.15). Subsequently, the resulting projection paramters and the 3D electron density map were passed to a local 3D refinement using a fine sampling ($\Delta = 0.9375°$, `--healpix_order 5`), reducing the shift range to 2 px (`--offset_ range 2`) and releasing the constraint on the tilt angle θ. In this way, the refinement of poses was allowed to locally relax and move away from the equator, while inhibiting unreasonable, erroneous poses due to artificially high correlations of, e.g., the edge of the filament (also see Section 2.4.5). The resulting distribution of poses resembles a Gaussian distribution around the equator in agreement with the orientation of F-actin on the grid.

To further guide the refinement and clean the data set from outlier particles not contributing to high-resolution, prior knowledge of the particle affiliation to a specific filament was exploited. Running averages of the in-plane rotation angle ψ and tilt angle θ were calculated per filament (Figure 3.15). Particles with poses significantly deviating from the

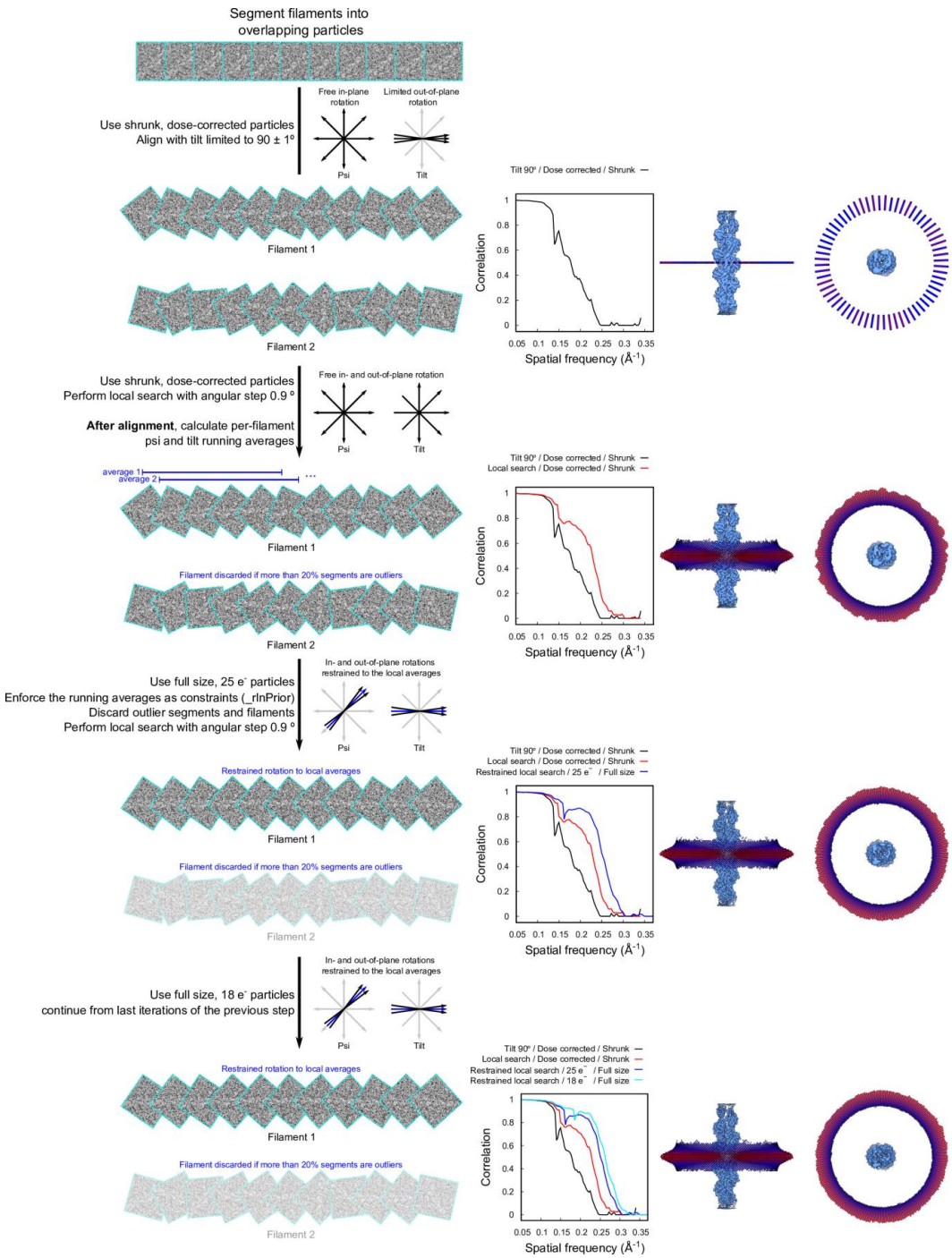

Fig. 3.15: Schematic representation of the modified single-particle analysis method used to obtain the F-actin models. For each step, possible filament segment alignments are represented along with the development of the Fourier shell correlation curves and the maps with their corresponding distribution of angular assignments. Originally published as supplementary figure of Merino et al. (2018).

running average were handled as outliers and discarded. Similarly, filaments containing more than 20 % outlier particles were discarded. For the remaining particles, the running averages were introduced as constraints in form of prior values (`_rlnAngleTiltPrior`, `_rlnAnglePsiPrior`), which were added to the metadata file. For the subsequent local 3D refinement, particles were replaced by dose-reduced (25 e^{-}), unbinned particles and the 3D electron density map was rescaled accordingly, to be used as a reference. Further-

more, the previously determined shift values (in pixels) were rescaled to account for the smaller pixel size of the unbinned particles. During the refinement, poses were loosely restricted to the prior values (`--sigma_psi 1 --sigma_tilt 1`). In this way, the resolution and map quality could be significantly improved. Finally, the last iteration of this 3D refinement was continued using particles with an even lower dose (18 e^{-}), thereby effectively reducing the negative effect of beam damage without suffering from weak alignments due to the lower contrast. Once particle polishing became available (Zivanov et al., 2018, 2019), polished particles were used instead of dose-reduced ones. Yet, the refinement strategy and settings remained unchanged, also when using CTF-refined particle stacks. Removal of particles that could not be aligned properly by 2D classification without alignment improved the overall map quality for some of the data sets.

The edge introduced through boxing of filamentous proteins represents a strong feature, which tends to negatively impact the 3D refinement (also see Section 2.4.5). Therefore, a soft mask enclosing ∼85 % of the filament, in particular excluding the ends of the filament, was used for all 3D refinements within this thesis. In addition, the FSC was determined using this mask throughout local refinements (`--solvent_correct_fsc`).

The following command is representative for the initial 3D refinement limiting the tilt to the equator:

```
relion_refine_mpi --o OUTPUT_DIR --auto_refine --split_random_halves
--i PARTICLES_woHelicalInfo_HelicalSubset.star --ref reference.mrc
--firstiter_cc --ini_high 25 --dont_combine_weights_via_disc
--no_parallel_disc_io --pool 3 --ctf --ctf_corrected_ref
--particle_diameter 260 --flatten_solvent --zero_mask
--solvent_mask mask.mrc --oversampling 1 --healpix_order 3
--auto_local_healpix_order 4 --offset_range 5 --offset_step 2
--sym C1 --low_resol_join_halves 40 --norm --scale --limit_tilt 89
```

A command similar to the one below was used for the local refinement without constraints:

```
relion_refine_mpi --o OUTPUT_DIR --auto_refine --split_random_halves
--i PARTICLES_limittilt89.star --ref reference.mrc --ini_high 7
--dont_combine_weights_via_disc --no_parallel_disc_io --pool 3
--ctf --ctf_corrected_ref --particle_diameter 260 --flatten_solvent
--zero_mask --solvent_mask mask.mrc --solvent_correct_fsc --oversampling 1
--healpix_order 5 --auto_local_healpix_order 4 --offset_range 2
--offset_step 2 --sym C1 --low_resol_join_halves 40 --norm --scale
```

Particles were locally refined applying prior values using the following command:

```
relion_refine_mpi --o OUTPUT_DIR --auto_refine --split_random_halves
--i PARTICLES_PriorPsiTilt.star --ref reference.mrc --ini_high 4.5
--dont_combine_weights_via_disc --no_parallel_disc_io --pool 3
--ctf --ctf_corrected_ref --particle_diameter 260 --flatten_solvent
--zero_mask --solvent_mask mask.mrc --solvent_correct_fsc --oversampling 1
--healpix_order 5 --auto_local_healpix_order 4 --offset_range 2
--offset_step 2 --sym C1 --low_resol_join_halves 40 --norm --scale
--sigma_tilt 1 --sigma_psi 1
```

3.3.1.4 3D refinement of filaments with helical SPHIRE

Towards the end of this thesis, a helical processing strategy tailored to the needs of F-actin was implemented in SPHIRE (Stabrin et al., 2020). Consequently, all data sets acquired afterwards, including F-actin-*cis*-OJ8 and the actomyosin complexes, were processed with helical SPHIRE. The maximum-likelihood 3D refinement implemented in *sp_meridien_alpha* is based on the SPHIRE (Moriya et al., 2017) program *sp_meridien*, which was modified to match the needs of filamentous samples (Figure 3.16). Usually, particles get assigned to the two half sets (chunks) per micrograph, e.g., all particles on micrographs with even numbers are assigned to half one, while particles from micrographs with uneven numbers end up in the second half. For the helical 3D refinement, the half set assignment was changed to per-filament (`--chunk_by=filament_id`, Figure 3.16). Furthermore, the round mask that is usually used for the normalization of 2D particles was replaced by a cylindrical mask to properly separate the protein signal from the background noise (`--filament_width=120 --radius=144`, the radius should be set to 45 % of the box size). As each 2D particle contains only one unique subunit within a total of 10-12 subunits, projection matching tends to self-correlate identical subunits in consecutive particle images along one filament. This results in strong shifting of the complete particle along the filament axis, which is accompanied by reconstruction artifacts. To prevent strong shifting, the shift along the filament axis (composed of both x and y shift, s_x, s_y) is wrapped in helical SPHIRE (`--helical_rise=27.5`, Figure 3.16). Specifically, shifts larger than half the rise $\pm\frac{1}{2}\Delta z$, which would correspond to an alignment to the next actin subunit, are mapped into this range, thereby effectively keeping the central actin

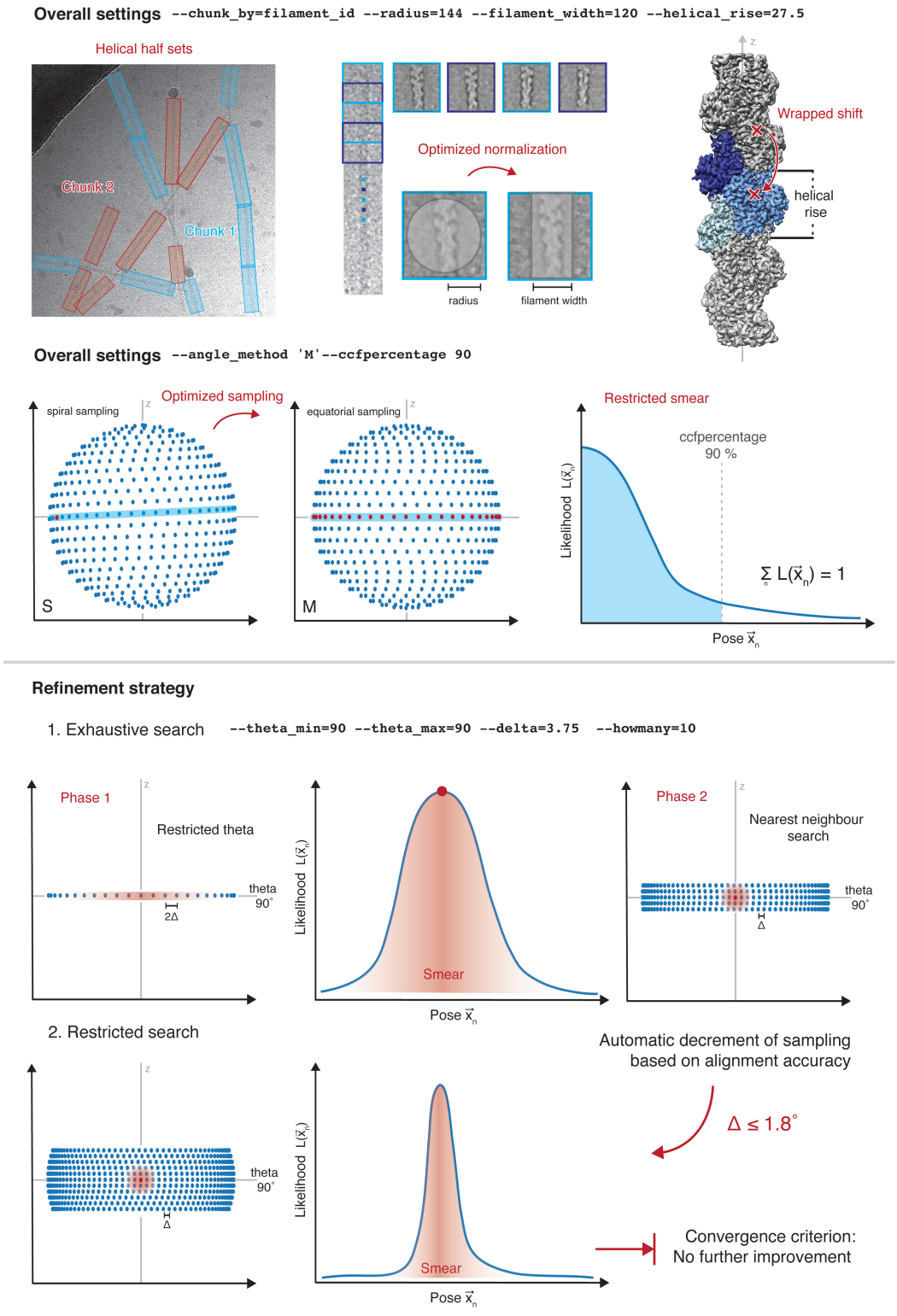

Fig. 3.16: Schematic representation of the helical 3D refinement in SPHIRE. **(Top)** Summary of overall refinement settings representing the adjustments introduced to match the needs of filaments. Also see Figure 2.14. **(Bottom)** Refinement strategy of helical SPHIRE with emphasis on the initial restriction of the sampling space to the equator and the distribution of the likelihood throughout the refinement. The likelihood of sampling points is indicated by a color gradient (red), with darker values representing a higher likelihood. Due to the low SNR of 2D particle images, 2D class averages with additional noise are shown instead.

subunit from moving too far from its position. A suitable sampling grid is essential for the successful determination of the 3D projection parameters (poses $\vec{x_n} = (\varphi_n, \theta_n, \psi_n, s_{x,n}, s_{y,n})^T$, also see Section 2.4.4). While spiraling sampling points are a good choice for equally distributed views, they are unsuitable for filamentous data, which primarily consist of side views mapping onto the equator of the sampling sphere. For this reason, a new, equatorial sampling method was introduced in helical SPHIRE, ensuring a reliable sampling of side views (`--angle_method='M'`, Figure 3.16).

While the consideration of alternative poses in accordance to their likelihood through weighted backprojection is indispensable for a high-resolution refinement, it also increases the computational cost of the 3D refinement. In case of filaments the smear (uncertainty of poses, spread of the likelihood distribution) is usually higher than for standard single particles, as the cylindrical shape of the filament itself already results in a high correlation. Therefore, the number of poses considered during the backprojection was reduced from the default cumulative value of 99 % to 90 % of the overall probability (`--ccfpercentage=90`), effectively reducing the running time, without adversely affecting the refinement (Figure 3.16).

Besides adjustments to the overall settings of the 3D refinement, the refinement strategy was also modified. Each 3D refinement in SPHIRE consists of several iterations within two different modes, i.e., exhaustive and restricted search, each consisting of two phases. Initially, an exhaustive search is performed, during which each particle is assigned to a sampling point of a coarse grid with a certain likelihood (Phase 1, angular distance between sampling points 2Δ, Figure 3.16). Next, the assignment of likely postures is reevaluated considering only sampling points in the nearest neighborhood of the previously determined points, using a finer grid (angular distance of Δ, Phase 2). Afterwards, all projections parameters and their likelihoods are used to compute a 3D electron density map, which serves as a reference in a subsequent iteration. While the distribution of the likelihood is initially very broad, it narrows throughout the refinement when the resolution and accuracy increases (Figure 3.16). The angular distance Δ of sampling points is automatically decreased during the refinement, based on the achieved alignment accuracy. Once $\Delta \leq 1.8°$, the program moves from the exhaustive search mode to the restricted search. Now, the poses determined in the previous iteration are used as a starting point and the parameters are refined locally instead of globally. The likelihood distribution further narrows throughout the iterations, until there is no more overall improvement and the refinement converges. While helical SPHIRE uses the same overall strategy, it additionally allows to restrict the sampling to points on the equator (`--theta_min=90 --theta_max=90`) during phase 1 of the exhaustive search (Figure 3.16). Thereby, the refinement is loosely restricted to side views and the robustness of the refinement is increased. To map the details necessary for a successful alignment, i.e.,

polarity of the filament, a finer initial sampling is furthermore often required for helical samples (`--delta=3.75 --howmany=10`).

The following command is representative for those used for the 3D refinement with helical SPHIRE:

```
sp_meridien_alpha.py bdb:STACK OUTPUT_DIR 3D_reference.hdf
--mask=mask.hdf --radius=144 --theta_min=90 --theta_max=90
--angle_method='M' --howmany=10 --delta=3.75 --helical_rise=27.5
--filament_width=120 --chunk_by=filament_id --ccfpercentage=99
```

To reduce the bias introduced through the usage of a reference not coming directly from the data, initially one refinement was performed without applying any mask. The resulting 3D electron density map and a corresponding 3D mask were then used as inputs for a new global 3D refinement, i.e., not taking into account the previously determined projection parameters. Considering the convergence of the refinement and the already near-atomic resolution of the 3D electron density maps computed in this way, the resulting final projection parameters were assumed to be close to their optimum. Therefore, all subsequent refinements, e.g., refinements of CTF-refined, polished or signal subtracted particles, were performed locally. Here, the previously determined poses and 3D electron density map filtered to its nominal resolution (e.g., `--inires=4.0`) were used as starting values and 3D reference, respectively. In addition, a fine sampling grid with $\Delta = 0.9375°$, a total shift range of $xr = 2.0$ and shift step size of $ts = 0.5$ was used. In this way, the change of projection parameters is restricted, making additional restraints due to the helical nature of the sample superfluous. For this reason, local refinements were performed with the standard 3D refinement program *sp_meridien*, using a command similar to the following:

```
sp_meridien.py --local_refinement bdb:STACK OUTPUT_DIR --inires=4.0
--delta=0.9375 --radius=144 --mask3D=mask.hdf --xr=2.0 --ts=0.5
```

3.3.1.5 CTF refinement and particle polishing

At the beginning of the data processing pipeline all micrographs were drift corrected and dose-weighted. Furthermore, the defocus of each micrograph was determined by CTF estimation (Section 3.3.1.1, Figure 3.14). While both steps are essential for the successful reconstruction of a 3D protein structure, they are based on simplified assumptions and thus return imperfect results.

The defocus initially estimated for each micrograph is an average value. It disregards that the ice layer is usually thicker than the protein dimensions would require. Because of this, embedded particles localize in different depths within this layer, and consequently also have different defocus values. A per-particle defocus estimation can be determined by CTF refinement (Figure 3.14). However, the fitting method is less robust than the initial CTF estimation, which takes advantage of a bootstrapping strategy. Thus, high-resolution signal is crucial for a successful CTF refinement. In case of a filamentous sample, the validity of the result can be assessed easily. Due to the continuity of filaments, the defocus value of individual particles should change smoothly along one filament (Figure 3.17A). CTF refinement was either performed with RELION (Zivanov et al., 2018) or SPHIRE (Moriya et al., 2017) (Table 3.3). While in both cases individual outlier values were observed, the usage of per-particle defocus values yielded an overall improved 3D reconstruction in most cases.

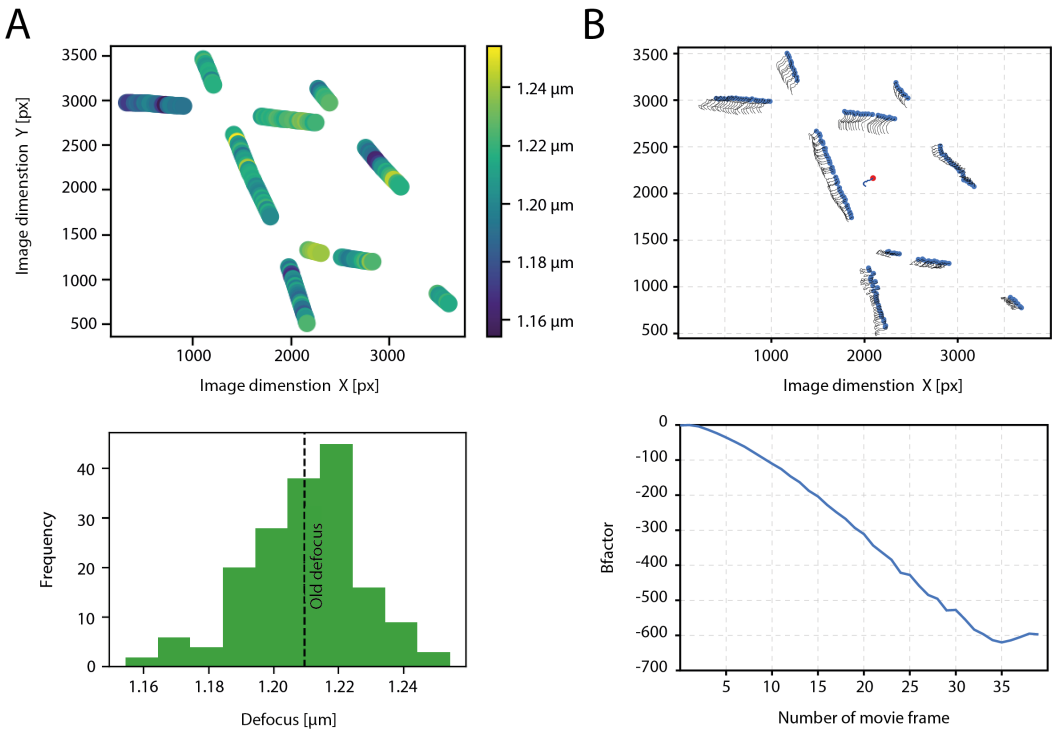

Fig. 3.17: Representative results of **(A)** per-particle CTF refinement in SPHIRE and **(B)** particle polishing in RELION. **A)** Color-coded per-particle defocus values **(top)** and histogram of defocus values **(bottom)** illustrating a considerable spread of defocus values around the average defocus determined for the full micrograph (old defocus). **B)** Per-particle drift trajectories highlighting the non-uniform movement of particles within one micrograph **(top)**. The central red dot and accompanying trajectory represent the results of the full frame motion correction. **(Bottom)** Estimated B-factors of individual movie frames used for dose-weighting.

Within the initial motion correction step the relative drift of full frames was corrected. In addition, the beam damage was accounted for by dose-weighting individual frames before

averaging. While the drift correction is imperfect by assuming a homogeneous drift within the imaging area, the B-factors used for dose-weighting are based on one representative cryo-EM sample (Grant and Grigorieff, 2015, Zheng et al., 2017) and are thus unlikely to be accurate for all imaging conditions and all cryo-EM samples. Providing a high-resolution data set, particle polishing can be used to correct the drift per-particle and apply customized dose-weighting (Figure 3.17B). Therefore, the software assesses the amount of beam damage in the individual movie frames and calculates per-frame B-factors for the given data set. These are then applied to the frames from which each particle is extracted, aligned and finally averaged. In this way, the adverse effects of beam damage can be minimized, while simultaneously maintaining the high-resolution information. Particle polishing was performed in RELION (Zivanov et al., 2019) (Table 3.3). For data sets processed in SPHIRE (Moriya et al., 2017), the programs *sp_sphire2relion* and *sp_relion2sphire* were used to convert the data format to RELION and back to SPHIRE, respectively. Similar to CTF refinement, particle polishing is not robust for all data sets. For the data sets studied within this thesis particle polishing yielded an improved 3D reconstruction in ∼50 % of the cases. In all other cases dose-weighted or dose-reduced particles were used.

3.3.1.6 Signal subtraction

The majority of 3D refinement and classification strategies are based on the matching of 2D projections of a 3D reference volume with the experimental 2D particle images. A mask can be applied to the reference volume to exclude noise or even focus on a certain region of the protein. For instance, a soft mask including only ∼85 % of the filament was routinely used when processing the F-actin data sets within this thesis, effectively focusing the alignment on F-actin rather than on the edges of the box. Yet, the scope of simple masking is limited, as the original 2D particle images still contain full, unmasked information. This is especially unfavorable in the case of filaments, when one wants to focus the refinement or classification on one unique subunit. Specifically, applying a mask that includes only the central subunit would result in the desired 2D projections of this particular subunit. However, the original 2D particle images contain several subunits and thereby give rise to several high correlation poses during projection matching. To truly focus the refinement on the desired subunit, the signal corresponding to the unwanted subunits needs to be excluded from the original 2D particle images. This is done in a multi-step workflow commonly referred to as signal subtraction (Bai et al., 2015). The benefit of signal subtraction is not limited to filaments, but also extends to heterogeneous protein complexes, where it enables the focused refinement of individual domains. However, due to the intrinsic difficulty to align protein complexes below 100 kDa, the minimum size of

domains is strongly restricted and currently also presents the main limitation of focused, signal subtracted refinements in general (Nakane et al., 2018).

Within this thesis, signal subtraction was essential for the processing of actomyosin filaments which display pronounced conformational heterogeneity. The subtraction and subsequent centering of subtracted 2D particles was performed in SPHIRE (Moriya et al., 2017), particularly using the method *sp_signalsubtract --mode projsubtract*. Initially, a 3D mask of the central subunit was created (region of interest), which was afterwards

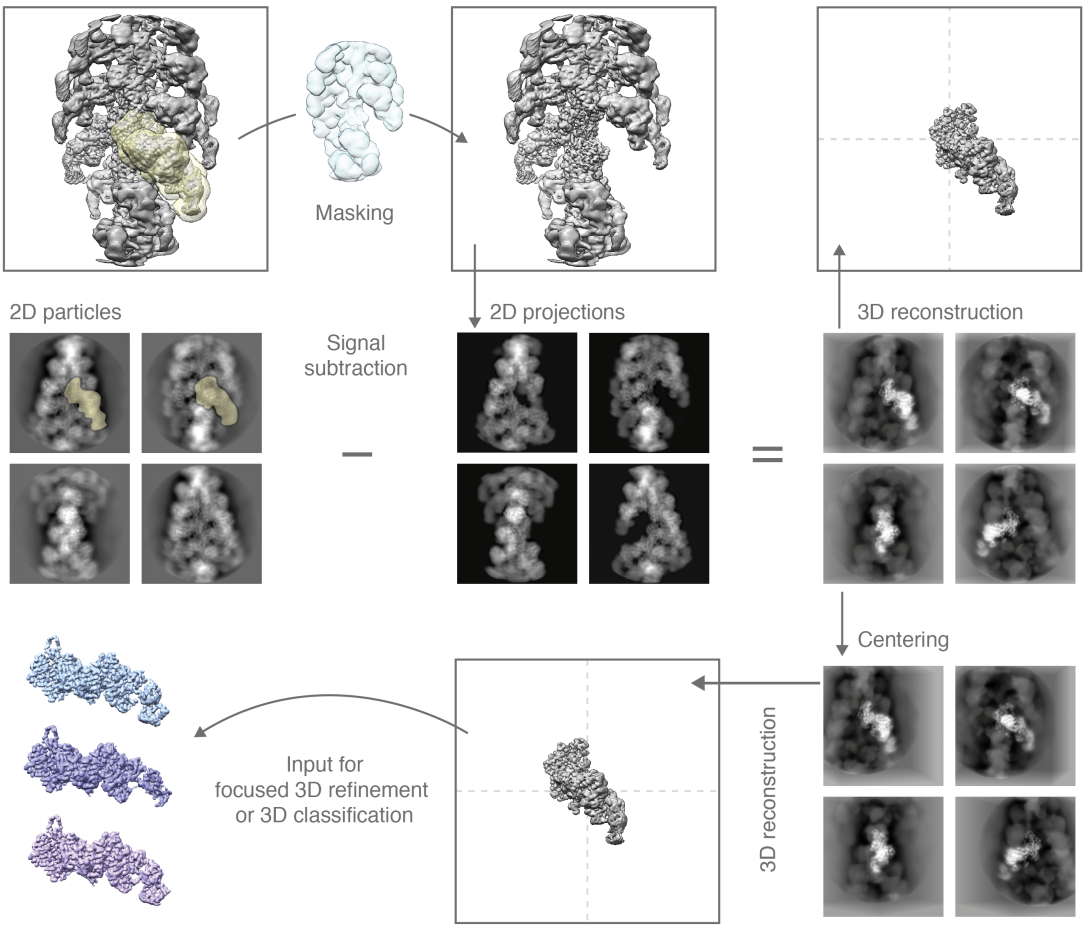

Fig. 3.18: Scheme illustrating the principle of signal subtraction. The region of interest is highlighted by a transparent yellow mask in the 3D density and some of the 2D particles. First, an inverted mask is multiplied with the full-filament density to create the volume that needs to be subtracted. 2D projections of this density are then subtracted from the original 2D particle images. Finally, these signal subtracted particles are re-centered to place the actin-myosin interface in the center of the box. As the low SNR of particle images would not allow the identification of features, 2D projections of the displayed 3D densities are shown instead.

subtracted from a mask of the full filament to generate an inverted mask which includes all protein density that needs to be subtracted (Figure 3.18). Next, this mask was applied to an unsharpened and unfiltered map (averaged half maps) creating a map which contains

all regions that need to be subtracted and has image statistics matching the experimental data. Finally, 2D projections of this map were automatically generated according to provided projection parameters and subtracted from the original particle stack. As the subtraction process strongly depends on the masks and map used, the result was assessed by computing a 3D reconstruction (with smear using *sp_meridien --do_final*) of the signal subtracted particles (Figure 3.18). When the signal subtraction was successful, the corresponding particles were lastly semi-automatically centered to bring the region of interest into the center of the box and thereby improve the refinement accuracy. The signal subtracted and centered particles were then used for subsequent focused 3D refinements or classifications (Figure 3.18)

3.3.1.7 3D classification

Classification is a powerful tool that not only allows the separation of particles from contamination during the initial assessment of picked particles, but also enables the separation of different oligomeric and conformational states. While strongly pronounced differences, i.e., monomer vs. dimer or very distinct, discrete structural states, can also be classified in 2D, more subtle and complex heterogeneity can only be addressed in 3D.

The 3D classification of filaments is especially challenging, as oligomeric (decorated vs. undecorated) or conformational differences of individual subunits are *per se* not cooperative. Consequently, the number of classes required to map all possible combinations of conformations within one filament is extremely high and difficult to handle computationally. Therefore, signal subtracted particles were used for all 3D classifications in this thesis (Figure 3.14).

3D classifications were performed in RELION (Scheres, 2012) using signal subtracted particle stacks and corresponding projection parameters generated in SPHIRE and converted to RELION .star format using *sp_sphire2relion*. As the preceding results indicated that the conformational changes are rather small and local, alignment was deactivated for all 3D classifications, in this way reducing not only the bias of this method but also reducing the runtime. A mask of the central subunit was provided to exclude noise and focus the classification on the protein. The regularization parameter T is a critical value within the maximum-likelihood implementation of RELION (Scheres, 2016). A low T value prohibits overfitting but comes at the cost of lost high-resolution features. Increasing the T value puts more weight on the experimental high-resolution data but might also result in over-interpretation. The adjustment of the regularization parameter T is especially important when running a masked 3D classification. While usually a T value of 4 is recommended, values in the range of 10-40 have proven suitable for masked classifi-

cations with smaller regions of interest requiring higher T values (Scheres, 2016). Thus, the regularization parameter T needs to be adjusted manually based on the assessment of the build-up of noise and the presence of high-resolution features. A value of $T = 40$ was found most useful for the 3D classification of the signal subtracted actomyosin particles.

Another critical parameter of not only 3D classification, but classification in general, is the number of classes K, which needs to be guessed by the user. For this reason, multiple classifications with different numbers of classes are routinely required to find a suitable value K. The optimization of the number of classes K was especially challenging in case of the actomyosin data studied within this thesis. Independent classifications of the same data asking for different numbers of classes resulted in non or only partially-overlapping results, i.e., resulting classes represented different conformational states. The reproducible discrepancy and the resemblance of the yet different states suggests an underlying continuous heterogeneity in contrast to discrete states. As the 3D classification algorithm routinely used for cryo-EM samples assumes the presence of discrete clusters, it is in general not optimal for handling data displaying continuous heterogeneity. For lack of better alternatives, it was still used for the 3D classification. To reliably map the conformational space of actomyosin, the number of classes K was manually optimized to yield the highest number of 3D classes having sufficient resolution (≤ 3.7 Å) and details for model building. Details about the processing pipeline and results of the actomyosin complex are given in the corresponding results section (Section 4.5.7).

3.3.1.8 Preparation of final maps

The overall goal of a cryo-EM processing pipeline is always the generation of one or, in case of multiple conformations, several high-resolution 3D electron density maps. Therefore, the last major processing step is usually a 3D refinement, which outputs two half maps which require further postprocessing (Figure 3.14, also see Section 2.4.4). The postprocessing routine initially estimates the resolution according to the $FSC_{0.143}$ criterion, before it filters the averaged and masked half maps to the determined resolution. In this way, only information contributing to signal is maintained while noise is reduced. In addition, the final postprocessed map is sharpened by either an automatically estimated or user provided B-factor, thereby enhancing the amplitude of high-resolution signal and effectively up-weighting the corresponding high-resolution features in the final electron density map. The concept of a single resolution value and a single B-factor accounting for the exponential drop of amplitudes toward higher frequencies is at most a rough estimate. In reality, the resolution of a map varies locally depending on the local flexibility and alignment accuracy (Figure 3.19). Equally, the required B-factor, which is tightly coupled to the resolution, is not homogeneous throughout the map. Consequently, filter-

ing a map to a single value and applying one overall B-factor results in local over- and under-filtering and sharpening (Figure 3.19). For this reason, additional strategies were utilized in this thesis to reliably map all information available. Besides standard postprocessing or postrefinement in RELION (Scheres, 2012) and SPHIRE (Moriya et al., 2017), maps were furthermore filtered to local resolution in SPHIRE (Moriya et al., 2017) and filtered according to local agreement using the LAFTER software (Ramlaul et al., 2019) (Figure 3.19). If required, the B-factor was furthermore manually adjusted to avoid fragmentation of flexible loops or ligands. In this way, high-resolution features such as side chain densities were visualized using high B-factors (strong sharpening) and low filtering (to higher resolution), while flexible regions such as the D-loop, which can adopt two conformations, required stronger filtering (to lower resolution) and only little sharping (Figure 3.19).

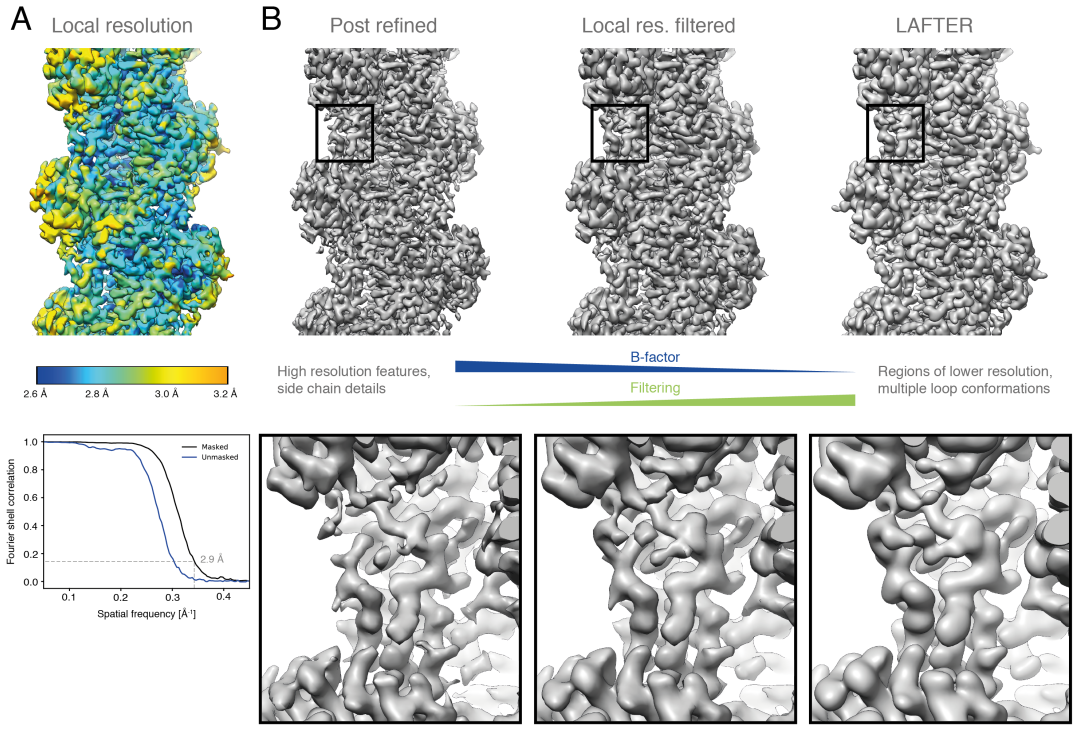

Fig. 3.19: Schematic illustrating the need for map optimization. **(A)** The resolution of the F-actin-*cis*-OJ8 structure varies locally between 2.6 Å to 3.2 Å, while the FSC-0.143 criterion reports an average resolution of 2.9 Å (bottom). **(B)** The same map either postrefined, filtered to local resolution or denoised with LAFTER is shown side by side. The two conformations of the D-loop (bottom, inset) become only visible when the sharpening and filtering is adapted. Ramps indicate the applied B-factor (high corresponds to strong sharpening) and filtering (stronger filtering corresponds to a lower resolution).

3.3.2 Atomic model building and refinement

In order to facilitate the analysis of protein-protein and protein-ligand interactions, atomic models were built and refined into the high-resolution electron density maps. Over the

course of this thesis, there were major advances in the development of model building and refinement software. Thus different software packages and strategies were used (Table 3.4). All strategies have in common, that they start from an initial reference model of the same or a homologous protein. In case of α-actin, atomic models of ADP-bound F-actin were directly available (von der Ecken et al., 2016, 2015) and were later complemented by additional atomic models of F-actin in different nucleotide states or bound to stabilizing ligands (Merino et al., 2018, Pospich et al., 2020). An initial model for *Pf* Actin 1 was created by homology modeling with MODELLER (Eswar et al., 2008, Sali and Blundell, 1993) in CHIMERA (Pettersen et al., 2004) based on a sequence alignment generated by CLUSTAL Ω (Sievers et al., 2011) and using the atomic model of F-actin (von der Ecken et al., 2016) as a reference. The resulting monomer model was flexibly fitted into the density using iMODFIT (Lopéz-Blanco and Chacón, 2013). Starting models and constraint libraries (in cif format) for non-standard ligands, including JASP and PHD, were created based on SMILES (simplified molecular input line entry specification) strings povided by the ZINC database (Irwin and Shoichet, 2005) using GRADE.globalphasing (Smart et al., 2011) or ELBOW (Moriarty et al., 2009). Course initial refinements of ligand models were performed in COOT (Debreczeni and Emsley, 2012, Emsley et al., 2010) providing the cif library, before all starting models were combined into a pentameric (F-actin) or multimeric (actomyosin) model by rigid body fitting in CHIMERA (Pettersen et al., 2004).

***Pf* Actin 1** A pentamer of *Pf* Actin 1 was initially real-space refined in PHENIX (Adams et al., 2011, Afonine et al., 2018) applying non-crystallographic symmetry (NCS) and secondary structure restraints based on the crystal structural of the globular protein (PDB 4CBU, Vahokoski et al. (2014)). Afterwards, the model was adjusted manually in COOT (Debreczeni and Emsley, 2012, Emsley et al., 2010). As the density corresponding to the D-loop was weak, the loop was refined into the density sum of the two subunits which had the best quality in this region. Still, the resolution was limited, allowing only the refinement of the protein backbone, while side chains were placed in the most likely orientation. This model was then merged with three copies of JASP and five copies of ADP (PDB 5JLF, von der Ecken et al. (2016)). The composite model was real-space refined in PHENIX (Adams et al., 2011, Afonine et al., 2018) applying protein and ligand restraints. Finally, the atomic model was refined and validated against one half map using REFMAC (Brown et al., 2015), using, besides NCS and ligand restraints, additional chain, helix and sheet restraints generated by PROSMART (Nicholls et al., 2014). To minimize model bias and avoid overrefinement, the refinement settings were iteratively optimized while displacing all atoms randomly by 0.5 Å. Final settings were chosen based on the agree-

ment of the FSC of the model against both half maps. These settings were finally used for a refinement without atom displacement against the postprocessed combined density map (also see Section 3.3.1.8). Further details on this model building and refinement strategy can be found in the methods section of the corresponding publication (Pospich et al., 2017).

Ligand-bound F-actin Atomic models of F-actin in different nucleotide states and stabilized by JASP or PHD were built and refined using ROSETTA (DiMaio et al., 2015, Fleishman et al., 2011, Song et al., 2013). ROSETTA utilizes statistical methods and local density-guided optimization to generate an energetically reasonable atomic model and has proven more powerful than less sophisticated, standard refinement approaches (DiMaio et al., 2015). ROSETTA automatically creates an approximate parameter set for ligands based on their chemical nature, assuming that their starting model is close to the energy minimum. As ROSETTA could not *per se* handle post-translational modifications, HIS73 was only methylated to HIC73 after the refinement in ROSETTA and regularized in COOT (Debreczeni and Emsley, 2012, Emsley et al., 2010). Initially, all models were adjusted manually in COOT. The before unseen open D-loop conformation was modeled by Dr. Felipe Merino using extensive rebuilding and molecular dynamics flexible fitting (MDFF) (for details see methods of (Merino et al., 2018)). When the conformation of the D-loop was mixed, i.e., both the open and the closed conformation were represented by the electron density, only the dominant state was modeled. The starting model was inputted to one to three rounds of iterative rebuilding in ROSETTA (DiMaio et al., 2015) enforcing helical symmetry and each time generating 960 models. To avoid overrefinement, models were refined against one half map, while the other one was used for the subsequent validation. After convergence assessment, the best model was finally locally refined with energy minimization and repacking in ROSETTA (Fleishman et al., 2011). When necessary, this model was adjusted manually in COOT, followed by another round of iterative rebuilding or local refinement. The modeling of the Mg^{+2}-nucleotide ligand required additional restraints. Hence, distance restraints were applied to Mg^{+2} and PO_4 and an octahedral water coordination was added manually to the magnesium for the final relaxation of the structure. Further details on the model building and refinement strategy using ROSETTA can be found in the methods section of the corresponding publications (Merino et al., 2018, Pospich et al., 2020).

OJ8-stabilized F-actin and actomyosin filaments The latest atomic models were built with ISOLDE (Croll, 2018) in CHIMERAX (Goddard et al., 2018), a real-time interactive graphical environment that utilizes molecular dynamics force fields for model building. In this way, the user can manually adjust the model to the electron density map within a

live molecular dynamics simulation. The density map itself is translated into an additional energy term within the force field, allowing the refinement against multiple maps. To reliably model both high-resolution and low-resolution features within one structure, several maps, e.g., with different B-factors applied or filtered to local resolution, were thus used for the refinement in ISOLDE. Custom residue definitions for ligands were created based on the ELBOW `--amber` output within the ISOLDE shell. Hydrogens were added prior to the first ISOLDE refinement using `addh` in CHIMERA (Pettersen et al., 2004) and adjusted manually when necessary. Only the central unique chain and residues in close contact were included in the simulation and rebuilt. Each refinement in ISOLDE was started with a ∼2-3 min all atom simulation to reduce the overall energy of the system. Afterwards, overlapping stretches of the protein were successively adjusted and refined. When necessary rotamer and secondary structure restraints were introduced. Finally, the quality of the model was assessed using the metrics provided by ISOLDE (Ramachandran plot, rotamer outlier and clash score) and outliers were individually fixed. The orientation of a few rotamers required adjustment in COOT (Debreczeni and Emsley, 2012, Emsley et al., 2010). The full pentameric complex was assembled by docking of the central, refined subunit in CHIMERA (Pettersen et al., 2004). If required, the updated F-actin pentamer was addressed to another round of refinement in ISOLDE. After ISOLDE, models were real-space refined in PHENIX (Adams et al., 2011, Afonine et al., 2018) against a sharpened density map filtered to nominal resolution ($FSC_{0.143}$, also see Section 3.3.1.8). To only relax and validate the model but prohibit large changes, local grid search, rotamer and Ramachandran restraints were deactivated and the starting model was used as a reference. Furthermore, NCS and secondary structure restraints were applied and a cif library provided for all ligands. Further details on the model building and refinement strategy utilized for OJ8-stabilized F-actin can be found in the methods section of the corresponding publication (Pospich et al., 2021).

For the rigor actomyosin complexes, a previous cryo-EM structure of aged F-actin stabilized by PHD (PDB: 6T20, Pospich et al. (2020)), or of young JASP-stabilized F-actin (PDB: 5OOD, Merino et al. (2018)) and a rigor-like crystal structure of the myosin Va-LC complex (PDB: 1OE9, Coureux et al. (2003) were used as starting models. For all other states, the atomic model of the aged rigor complex was used as a reference. Atomic models of class averages were built starting from the ISOLDE session of the average, all-particle model. PHD and JASP was replaced by single-residue initial models generated by ELBOW (Moriarty et al., 2009) and coarsely refined in COOT prior to model building in ISOLDE. Nucleotides were treated similarly. The density corresponding to the light chain of myosin was of insufficient quality for reliable model building. Hence, a rotamer-optimized crystal structure (PDB 1OE9, (Coureux et al., 2003)) was rigid body fitted into the density using CHIMERA (Pettersen et al., 2004) instead (prior to the real-space

refinement in PHENIX). Only models containing one actin and one myosin molecule were refined in ISOLDE, whereas atomic models consisting of three actin subunits and two myosin molecules were assembled from the models of the monomeric complex and real-space refined in PHENIX. Structure-based homology models of myosin (P_iR and intermediate recovery stroke state) were created with SWISS MODEL (Waterhouse et al., 2018) from a sequence alignment generated by Clustal Ω (Sievers et al., 2011).

Residues not represented by the electron density map, e.g., due to flexibility, were not included in the respective atomic model. All atomic models were assessed and validated using MOLPROBITY (Chen et al., 2010) and EMRINGER (Barad et al., 2015) statistics, which analyze the rationality of the model and its agreement with the experimental data, respectively. All models associated with a publication and corresponding electron density maps were deposited to the public PDB (protein data bank) (Burley et al., 2018) and EMDB (electron microscopy data bank) (Lawson et al., 2011), respectively (also see Table 4.1). This required changing the residue assignment of PHD from a single non-standard residue to a hepta-peptide consisting of TRP-EEP-ALA-DTH-CYS-HYP-ALA.

3.3.3 Structural analysis tools

The visualization, comparison and most of the analysis of the electron density maps and corresponding atomic models was performed in CHIMERA (Pettersen et al., 2004) using its various tools including *inter alia* matchmaker for superposition of models, morphing of maps and models, coloring by attribute and calculation of surfaces. All high-resolution images and movies were also created with CHIMERA using its Python scripting interface in case of the latter. For the representation of surfaces, atomic models were protonated in accordance to the pH of the buffer using H++ (Anandakrishnan et al., 2012). For the identification of hydrophobic interactions, models were colored by hydrophobicity inputting per-residue scores (Hessa et al., 2005). The hydrophobicity of JASP was evaluated using PLATINUM (Pyrkov et al., 2009). Couloumbic surface coloring within CHIMERA was used when analysing electrostatic interactions.

Besides visual analysis, protein-protein and protein-ligand interactions were analyzed with PDBSUM (Laskowski, 2009) and LIGPLOT$^+$ (Laskowski and Swindells, 2011), respectively. Furthermore, the contribution of individual residues to the binding energy was assessed by *in silico* alanine screenings using ROBETTA (Kortemme and Baker, 2002, Kortemme et al., 2004). Here, residues of interest are sequentially mutated to alanine and the change in free energy $\Delta\Delta G$ is reported.

Conformational changes and structural heterogeneity were characterized by principal com-

ponent analysis (PCA) using the BIO3D library (Grant et al., 2006) in R. In addition to the clustering of models, this library also supports the direct visualization of the result and exporting of trajectories along a principle component. Protein domain motion was furthermore analyzed by DYNDOM (Hayward and Lee, 2002). This online tool compares two atomic models, identifies mobile domains and hinge regions and reports their relative motion.

All analysis of data in text file format was conducted in Python. In particular, plots, e.g., of FSC curves, were created using NumPy (Harris et al., 2020) and Matplotlib (Hunter, 2007).

Purpose	**Software**	**Reference**
Data Acquisition	EPU	Thermo Fisher
On-the-fly preprocessing	TRANSPHIRE	Stabrin et al. (2020)
Drift correction + DW	MOTIONCOR2	Zheng et al. (2017)
	SUMMOVIE	Grant and Grigorieff (2015)
	UNBLUR	Grant and Grigorieff (2015)
CTF estimation	CTFFIND4	Rohou and Grigorieff (2015)
	GCTF	Zhang (2016)
Picking	EMAN2 *e2helixboxer*	Tang et al. (2007)
	SPARX *sxhelixboxer*	Behrmann et al. (2012b)
	SPHIRE STRIPER	Wagner et al. (2020)
	SPHIRE crYOLO	Wagner et al. (2020, 2019)
Particle extraction	RELION *relion_preprocess*	Scheres (2012) He and Scheres (2017)
	SPARX *sxhelixboxer*	Behrmann et al. (2012b)
	SPHIRE *sp_window*	Moriya et al. (2017)
2D classification	RELION *relion_refine*	Scheres (2012) He and Scheres (2017)
	SPHIRE *sp_isac2*	Moriya et al. (2017)
	SPHIRE *sp_isac2_gpu*	Stabrin et al. (2020)
Initial 3D model	EMAN2	Tang et al. (2007)
	SPARX	Hohn et al. (2007)
	SPHIRE	Moriya et al. (2017)
3D refinement	RELION *relion_refine*	Scheres (2012) He and Scheres (2017) Zivanov et al. (2018)
	SPHIRE *sp_meridien_alpha*	Stabrin et al. (2020)
CTF refinement	RELION *relion_ctf_refine*	Zivanov et al. (2018)
	SPHIRE *sp_ctf_refine_meridien*	Moriya et al. (2017)
Polishing	RELION *relion_motion_refine*	Zivanov et al. (2019)
Signal subtraction	SPHIRE	Moriya et al. (2017)
3D classification	RELION *relion_refine*	Scheres (2012)
Map optimization	LAFTER	Ramlaul et al. (2019)
	SPHIRE *sp_localres*	Moriya et al. (2017)
	SPHIRE *sp_filterlocal*	Moriya et al. (2017)

Table 3.3: Overview of software packages used for cryo-EM processing. To ease the recognition of software within the text all package names are written in capital letters.

Purpose	Software	Reference
Model building and refinement	CHIMERA	Pettersen et al. (2004)
	CHIMERAX	Goddard et al. (2018)
	CLUSTAL Ω	Sievers et al. (2011)
	COOT	Emsley et al. (2010)
	ELBOW	Moriarty et al. (2009)
	GRADE	Smart et al. (2011)
	iMODFIT	Lopéz-Blanco and Chacón (2013)
	ISOLDE	Croll (2018)
	MODELLER	Sali and Blundell (1993) Eswar et al. (2008)
	PHENIX	Adams et al. (2011) Afonine et al. (2018)
	PROSMART	Nicholls et al. (2014)
	REFMAC	Brown et al. (2015)
	ROSETTA	DiMaio et al. (2015) Fleishman et al. (2011) Wang et al. (2016)
	SWISS MODEL	Waterhouse et al. (2018)
Validation	EMRINGER	Barad et al. (2015)
	MOLPROBITY	Chen et al. (2010)
Databases	CSD	Groom et al. (2016)
	EMDB	Lawson et al. (2011)
	PDB	Burley et al. (2018)
	UNIPROT	The UniProt Consortium (2017)
	ZINC	Irwin and Shoichet (2005)
Analysis tools	BIO3D (R)	Grant et al. (2006)
	CHIMERA	Pettersen et al. (2004)
	DYNDOM	Hayward and Lee (2002)
	H++	Anandakrishnan et al. (2012)
	LIGPLOT$^+$	Laskowski and Swindells (2011)
	PDBSUM	Laskowski (2009)
	PLATINUM	Pyrkov et al. (2009)
	ROBETTA	Kortemme and Baker (2002) Kortemme et al. (2004)

Table 3.4: Overview of software packages used for model building and analysis. To ease the recognition of software within the text all package names are written in capital letters.

4 Results and Discussion

With the aim to unravel the structural effects of sequence variations, nucleotide hydrolysis and small molecule binding, several high-resolution structures of F-actin and an actomyosin complexes were solved by cryo-EM in this thesis (Table 4.1, also see Section 2.5). These structures are presented and discussed in detail within this chapter (Sections 4.1 to 4.5). Initially, the structure of filamentous *Pf*Actin1, an unusual actin essential for the infectivity of the malaria parasite *Plasmodium falciparum*, is described (Section 4.1). A comparison with the structure of α-actin sheds light on the structural basis of filament instability, which is caused by subtle sequence variations. Next, the structural transition of F-actin upon ATP hydrolysis is assessed by comparing four structures of F-actin in different nucleotide states (Section 4.2). Based on our structures, we propose a model of actin polymerization and aging, and also suggest a mechanism by which nucleotide-sensitive ABPs distinguish different nucleotide states of F-actin. Finally, two additional structures of JASP-bound F-actin show that JASP stabilizes F-actin by trapping a specific nucleotide state, in this way possibly interfering with the binding of nucleotide-sensitive ABPs. To further investigate the structural effect of actin inhibitors, five novel structures of PHD- and JASP-stabilized F-actin are subsequently compared (Section 4.3). These results not only reveal previously unexpected differences between the effects of JASP and PHD, but also indicate that both inhibitors stabilize natural conformations of F-actin. To facilitate the development of novel functionalized F-actin inhibitors, the molecular recognition mechanism of OJ8, a photoswitchable JASP derivate, is subsequently analyzed based on high-resolution structures of both switch states (Section 4.4). In the final section of this chapter, the structural transition of myosin bound to F-actin is characterized based on high-resolution structures, either in absence of a nucleotide, or in complex with ADP or AppNHp (Section 4.5). By comparing these new structures to previously published crystal structures of other states, we propose a detailed structural model of the myosin motor cycle. Furthermore, we identify a pronounced structural heterogeneity of myosin, which we believe is essential for the transition between distinct structural states. Finally, an additional structure of myosin bound to young JASP-stabilized F-actin is studied to shed light on the selectivity of myosin for a specific nucleotide state. This chapter eventually concludes with a comprehensive discussion of all results and an outlook (Section 4.6).

A majority of the findings of this thesis have been published in peer-reviewed journals (Merino et al., 2018, Pospich et al., 2021, 2017, 2020). The corresponding articles are referenced within each of the sections (Sections 4.1-4.4) and can be found on the journals' web pages. A summary of key information about sample preparation, vitrification and

imaging conditions is additionally given in each section. An overview of all structures resolved in this thesis and corresponding accession codes (EMDB and PDB) is given in Table 4.1.

Complex name	**Resolution**	**# EMDB**	**# PDB**	**Reference**
JASP-stabilized *Pf* Actin 1	3.8 Å	3805	5OGW	Pospich et al. (2017)
F-actin-AppNHp	3.6 Å	3838	5OOE	Merino et al. (2018)
F-actin-ADP-BeF_x	3.4 Å	3839	5OOF	Merino et al. (2018)
F-actin-ADP-P_i	3.3 Å	4259	6FHL	Merino et al. (2018)
F-actin-ADP	4.1 Å	3835	5ONV	Merino et al. (2018)
F-actin-ADP-P_i JASP	3.7 Å	3837	5OOD	Merino et al. (2018)
F-actin-ADP JASP	3.6 Å	3836	5OOC	Merino et al. (2018)
F-actin-PHD	3.3 Å	10363	6T1Y	Pospich et al. (2020)
F-actin-PHD-aged	3.7 Å	10364	6T20	Pospich et al. (2020)
F-actin-PHD-Alexa	3.6 Å	10367	6T25	Pospich et al. (2020)
F-actin-JASP-aged 1	3.7 Å	10365	6T23	Pospich et al. (2020)
F-actin-JASP-aged 2	3.1 Å	10366	6T24	Pospich et al. (2020)
F-actin-*trans*-OJ8	3.6 Å	11790	7AHQ	Pospich et al. (2021)
F-actin-*cis*-OJ8	2.9 Å	11787	7AHN	Pospich et al. (2021)
F-actin-PHD-aged + MyoVa-rigor	3.3 Å	-	-	to be published
F-actin-PHD-aged + MyoVa-ADP	3.1 Å	-	-	to be published
F-actin-PHD-aged + MyoVa-AppNHp	2.9 Å	-	-	to be published
F-actin-JASP	3.1 Å	-	-	to be published
F-actin-JASP + MyoVa-rigor	3.2 Å	-	-	to be published

Table 4.1: Overview of all cryo-EM structures resolved in this thesis. Entries are grouped by project. Due to the pronounced heterogeneity, a number of structures showing different conformations were resolved for all actomyosin states (a total of 18 structures, ranging from 3.3 Å - 3.7 Å). To keep this table concise, these structures are not included here (see Section 4.5.7 and Supplementary Figure S2 for details).

4.1 Structural basis of filament instability of *Pf* Actin

The results of this section were published as

> Pospich, S., Kumpula, E.-P., von der Ecken, J., Vahokoski, J., Kursula, I. and Raunser, S. (**2017**) Near-atomic structure of jasplakinolide-stabilized malaria parasite F-actin reveals the structural basis of filament instability. *Proceedings of the National Academy of Sciences of the United States of America*, 114(40):10636-10641

and can be accessed via

> **Online version**: https://www.pnas.org/content/114/40/10636

Pf Actin1 filaments were prepared as described in Section 3.1.3 and vitrified using the manual backside blotting procedure presented in Section 3.2.2.1. JASP-stabilized *Pf* Actin1 was kindly prepared by Dr. Julian von der Ecken. JASP is referred to as JAS in this publication. A concise overview of the sample preparation and imaging conditions is given in Table 4.2. The data set was processed using the hybrid SPA processing pipeline described in Section 3.3.1.3. A detailed description of all data processing steps is included in the methods section of the original publication.

Non-stabilized *Pf* Actin1	
Sample	$\sim$ 10 µM *Pf* Actin1
Buffer	10 mM HEPES pH 7.5, 0.2 mM $CaCl_2$, 50 mM KCl, 4mM $MgCl_2$, 1mM EGTA, 0.5 mM TCEP, 0.5 mM ATP, 0.02 % Tween 20
Vitrification	1.5 µl, 30 s incubation, R2/1 Quantifoils, manual backside blotting for 6-8 s, cryoplunger CP3
Data acquisition	Screening only, Tecnai G2 Spirit
JASP-stabilized *Pf* Actin1	
Sample	JASP-stabilized *Pf* Actin1, concentration adjusted empirically Prepared by Dr. J. von der Ecken
Buffer	10 mM HEPES pH 7.5, 0.2 mM $CaCl_2$, 50 mM KCl, 4mM $MgCl_2$, 5 mM DTT, 0.5 mM ATP, 0.04 % Tween 20
Vitrification	2 µl, 30 s incubation, C-Flats 2/1, manual backside blotting for 4 s, cryoplunger CP3
Data acquisition	Cs-corrected Titan Krios, Falcon II linear mode, 1.5 s exposure, 24 frames, total dose 110 e$Å^{-2}$, pixel size 1.14 Å, 4er spot scan, defocus range 0.8-2.7 µm

Table 4.2: Overview of sample preparation and imaging conditions of *Pf* Actin1.

4.2 Structural transition of F-actin upon ATP hydrolysis

The characterization of the structural transition of F-actin upon ATP hydrolysis was conducted in collaboration with Dr. Felipe Merino. Dr. Merino prepared and analyzed the structures of F-actin in complex with AppNHp, ADP-BeF_x and ADP, performed molecular dynamics simulations and principal component analyses, and wrote the manuscript. The structure of F-actin in complex with ADP-P_i was solved in a joint effort, while the structures of JASP-stabilized F-actin in complex with ADP and ADP-P_i were studied as part of this thesis.

The results of this section were published as

> Merino, F.*, Pospich, S.*, Funk, J., Wagner, T., T. Küllmer, F., Arndt, H.-D., Bieling, P. and Raunser, S. (**2018**) Structural transitions of F-actin upon ATP hydrolysis at near-atomic resolution revealed by cryo-EM. *Nature structural & molecular biology*, 25(6):528-537

and can be accessed via

> **Online version**: https://www.nature.com/articles/s41594-018-0074-0

F-actin in complex with ADP-P_i was prepared as described in Section 3.1.2 and vitrified using the automatic blotting procedure presented in Section 3.2.2.1. JASP-stabilized F-actin in complex with either ADP-P_i or ADP was prepared as described in Sections 3.1.1 to 3.1.2 with an extra depolymerization and polymerization cycle. While JASP-cLys was added to G-actin in both cases, the nucleotide was exchanged to ADP by replacing ATP by ADP in the dialysis buffer for the F-actin-ADP JASP sample. JASP-stabilized F-actin was vitrified using the manual blotting procedure presented in Section 3.2.2.1. A concise overview of the sample preparation and imaging conditions is given in Tables 4.3 to 4.4. Data sets were processed using the hybrid SPA processing pipeline described in Section 3.3.1.3. A detailed description of all data processing steps is included in the methods section of the original publication.

F-actin-AppNHp	
Sample	F-actin, concentration empirically adjusted ∼0.3-10 µM Prepared by Dr. F. Merino
Buffer	5 mM HEPES pH 7.5, 100 mM KCl, 2mM $MgCl_2$, 2mM NaN_3, 0.5 mM TCEP, 0.4 AppNHp, 0.02-0.04 % Tween 20
Vitrification	1.5-1.8 µl, 30-60 s incubation, R2/1 Quantifoils, manual backside blotting for 6-11 s, cryoplunger CP3
Data acquisition	Cs-corrected Titan Krios, Falcon II linear mode, 1.5 s exposure, 25 frames, total dose 110 e$Å^{-2}$, pixel size 1.14 Å, 4er spot scan, defocus range 0.5-2.6 µm
F-actin-ADP-BeF_x	
Sample	F-actin, concentration empirically adjusted ∼0.3-10 µM Prepared by Dr. F. Merino
Buffer	5 mM HEPES pH 7.5, 100 mM KCl, 2 mM $MgCl_2$, 2 mM NaN_3, 1 mM TCEP, 0.2 mM ADP, 0.2 mM BeF_2, 5 mM NaF, 0.02-0.04 % Tween 20
Vitrification	1.5-1.8 µl, 30-60 s incubation, R2/1 Quantifoils, manual backside blotting for 6-11 s, cryoplunger CP3
Data acquisition	Cs-corrected Titan Krios, Falcon II linear mode, 1.5 s exposure, 25 frames, total dose 83 e$Å^{-2}$, pixel size 1.14 Å, 4er spot scan, defocus range 0.5-2.8 µm
F-actin-ADP-P_i	
Sample	∼10 µM F-actin
Buffer	5 mM HEPES pH 7.5, 50 mM KCl, 2 mM $MgCl_2$, 2 mM NaN_3, 0.5 mM TCEP, 0.2 mM ADP, 50 mM postassium phosphate pH 7.5, 0.04 % Tween 20
Vitrification	1.5 µl, no incubation, R2/1 Quantifoils, automatic blotting for 8 s at 13 °, blot force -25, drain time 1s, Vitrobot
Data acquisition	Cs-corrected Titan Krios, Falcon III linear mode, 1.5 s exposure, 35 frames, total dose 93 e$Å^{-2}$, pixel size 1.1 Å, 4er spot scan, defocus range 0.4-3.2 µm

Table 4.3: Overview of sample preparation and imaging conditions of F-actin-AppNHp, F-actin-ADP-BeF_x and F-actin-ADP-P_i.

F-actin-ADP-P_i JASP	
Sample	∼0.35 µM F-actin and ∼0.71 µM JASP-cLys JASP-cLys was added to G-actin before polymerization
Buffer	5 mM Tris-HCl pH 7.5, 1 mM DTT, 100 mM KCl, 2mM $MgCl_2$, 0.02 % Tween 20, ∼9 % DMSO
Vitrification	1.5 µl, 30 s incubation, R2/1 Quantifoils, manual backside blotting for 9.5 s, cryoplunger CP3
Data acquisition	Cs-corrected Titan Krios, GIF quantum-energy filter, slit with 15 eV, K2 summit super-resolution mode, 15 s exposure, 75 frames, total dose 78 $eÅ^{-2}$, pixel size 1.09 Å, 4er spot scan, defocus range 0.5-3.0 µm
F-actin-ADP JASP	
Sample	∼0.6 µM F-actin and ∼ 1.4µM JASP-cLys The nucleotide was exchanged to ADP by dialysis JASP-cLys was added to G-actin before polyermization
Buffer	5 mM Tris-HCl pH 7.5, 1 mM DTT, 100 mM KCl, 2mM $MgCl_2$, 0.04 % Tween 20, 0.12 % DMSO
Vitrification	1.8 µl, 60 s incubation, R2/1 Quantifoils, manual backside blotting for 11 s, cryoplunger CP3
Data acquisition	Cs-corrected Titan Krios, Falcon II linear mode, 2.1 s exposure, 40 frames, total dose 71 $eÅ^{-2}$, pixel size 1.14 Å, 4er spot scan, defocus range 0.5-2.8 µm
F-actin-ADP	
Sample	F-actin, concentration empirically adjusted ∼0.3-10 µM Prepared by Dr. F. Merino
Buffer	5 mM HEPES pH 7.5, 100 mM KCl, 2mM $MgCl_2$, 2mM NaN_3, 1 mM TCEP, 0.2 mM ADP, 0.02-0.04 % Tween 20
Vitrification	1.5-1.8 µl, 30-60 s incubation, 2/1 C-Flats, manual backside blotting for 6-11 s, cryoplunger CP3
Data acquisition	Cs-corrected Titan Krios, Falcon II linear mode, 1.6 s exposure, 27 frames, total dose 95 $eÅ^{-2}$, pixel size 1.14 Å, 4er spot scan, defocus range 0.7-2.9 µm

Table 4.4: Overview of sample preparation and imaging conditions of F-actin-ADP, F-actin-ADP JAS and F-actin-ADP-P_i JASP.

4.3 Structural effects and functional implications of PHD and JASP

The results of this section were published as

> Pospich, S., Merino, F. and Raunser, S. (**2020**) Structural Effects and Functional Implications of Phalloidin and Jasplakinolide Binding to Actin Filaments. *Structure*, 28(4):437-449

and can be accessed via

> **Online version**: https://doi.org/10.1016/j.str.2020.01.014

JASP- and PHD-stabilized F-actin was prepared as described in Sections 3.1.1 to 3.1.2 and vitrified using either the manual or the automatic blotting procedure presented in Section 3.2.2.1. F-actin-PHD-aged was kindly prepared by Dr. Felipe Merino. To study the structural effect of the toxins, JASP and PHD were either added to G-actin during polymerization or to F-actin after overnight aging; in case of the latter, data set names contain the tag 'aged' to ease the identification. A concise overview of the sample preparation and imaging conditions is given in Tables 4.5 to 4.6. Data sets were processed using the hybrid SPA processing pipeline described in Section 3.3.1.3. A detailed description of all data processing steps is included in the methods section of the original publication.

The analysis and interpretation of this study strongly relies on our previous results on the structural transition of F-actin upon ATP hydrolysis, especially the existence of two distinct D-loop states, namely the closed and open state (also see Section 4.2). Shortly after our publication (Merino et al., 2018), another laboratory also published structures of F-actin in different nucleotide states, but did however not observe the open D-loop state (Chou and Pollard, 2019). This discrepancy naturally provoked many questions during the peer-reviewing process of this work on the effect on PHD and JASP. Thus, we included a supplementary discussion into our manuscript (Pospich et al., 2020), which, on the one hand, aims to shed light on the factors that might have let to the discrepancy, and, on the other hand, reassesses the results based on recently published new insights.

F-actin-PHD	
Sample	∼0.2 µM F-actin and ∼0.4 µM PHD PHD was added to G-actin before polymerization
Buffer	5 mM Tris-HCl pH 7.5, 1 mM DTT, 100 mM KCl, 2mM $MgCl_2$, 2 mM NaN_3, 0.02 % Tween 20, ∼0.01 % methanol
Vitrification	1.5 µl, 30 s incubation, R2/1 Quantifoils, manual backside blotting for 9 s, cryoplunger CP3
Data acquisition	Cs-corrected Titan Krios, Falcon II linear mode, 2.1 s exposure, 40 frames, total dose 71 $eÅ^{-2}$, pixel size 1.14 Å, 4er spot scan, defocus range 0.6-2.8 µm
F-actin-PHD-aged	
Sample	∼5 µM F-actin and ∼10 µM PHD PHD was added to F-actin after overnight aging Prepared by Dr. F. Merino
Buffer	5 mM Tris-HCl pH 7.5, 1 mM DTT, 100 mM KCl, 2mM $MgCl_2$, 2 mM NaN_3, 0.03 % Tween 20, ∼2.0 % methanol
Vitrification	1.8 µl, no incubation, R2/1 Quantifoils, automatic blotting for 8.5 s at 13 °, blot force -25, drain time 0.5 s, Vitrobot
Data acquisition	Cs-corrected Titan Krios, Falcon III linear mode, 1.5 s exposure, 35 frames, total dose 87 $eÅ^{-2}$, pixel size 1.12 Å, 4er spot scan, defocus range 0.7-2.8 µm
F-actin-PHD-Alexa	
Sample	∼8.4 µM F-actin and ∼16.8 µM PHD PHD was added to G-actin before polymerization
Buffer	5 mM Tris-HCl pH 7.5, 1 mM DTT, 100 mM KCl, 2mM $MgCl_2$, 2 mM NaN_3, 0.02 % Tween 20, ∼1.48 % methanol
Vitrification	1.5 µl, no incubation, R2/1 Quantifoils, automatic blotting for 6.5 s at 13 °, blot force -25, drain time 1 s, Vitrobot
Data acquisition	Cs-corrected Titan Krios, Falcon III linear mode, 1.5 s exposure, 35 frames, total dose 92 $eÅ^{-2}$, pixel size 1.12 Å, 4er spot scan, defocus range 0.4-2.6 µm

Table 4.5: Overview of sample preparation and imaging conditions of PHD-stabilized F-actin.

F-actin-JASP-aged 1	
Sample	∼7.5 µM F-actin and ∼15 µM JASP-cLys JASP was added to F-actin after overnight aging
Buffer	5 mM Tris-HCl pH 7.5, 1 mM DTT, 100 mM KCl, 2mM $MgCl_2$, 2 mM NaN_3, 0.02 % Tween 20, ∼0.5 % DMSO
Vitrification	1.5 µl, no incubation, R2/1 Quantifoils, automatic blotting for 8 s at 13 °, blot force -25, drain time 0.5 s, Vitrobot
Data acquisition	Cs-corrected Titan Krios, Falcon III linear mode, 2.1 s exposure, 35 frames, total dose 88 $eÅ^{-2}$, pixel size 1.12 Å, 4er spot scan, defocus range 1.0-3.0 µm
F-actin-JASP-aged 2	
Sample	∼5 µM F-actin and ∼10 µM JASP-cLys JASP was added to F-actin after overnight aging
Buffer	5 mM Tris-HCl pH 7.5, 1 mM DTT, 100 mM KCl, 2mM $MgCl_2$, 2 mM NaN_3, 0.02 % Tween 20, ∼0.2 % DMSO
Vitrification	3.0 µl, no incubation, R2/1 Quantifoils, automatic blotting for 9 s at 13 °, blot force -20, drain time 0 s, Vitrobot
Data acquisition	Titan Krios, GIF quantum-energy filter, slit with 15 eV, K2 summit super-resolution mode, 15 s exposure, 40 frames, total dose 78 $eÅ^{-2}$, pixel size 1.05 Å, 4er spot scan, defocus range 0.5-3.0 µm

Table 4.6: Overview of sample preparation and imaging conditions of JASP-stabilized F-actin.

4.4 Cryo-EM resolves isomeric states of F-actin photoswitch

Optojasps are photo-switchable JASP derivatives which provide direct spatiotemporal control of the actin cytoskeleton (Section 2.2.4). To characterize the molecular recognition mechanism and the effect of the optojasp photoswitch OJ8 on F-actin, high-resolution cryo-EM structures of both isomeric states were solved in this thesis. Ion-pair reversed-phase chromatography was furthermore utilized to assess the switching capability of OJ8 within the actin filament.

The results of this section were published as

> Pospich, S., Küllmer, F., Nasufović, V., Funk, J., Belyy, A., Bieling, P., Arndt, H.-D. and Raunser, S. (**2021**) Cryo-EM resolves molecular recognition of an optojasp photoswitch bound to actin filaments in both switch states. *Angewandte Chemie International Edition*, Online ahead of print.

and can be accessed via

> **Online version**: https://doi.org/10.1002/anie.202013193

OJ8-stabilized F-actin was prepared as described in Sections 3.1.1 to 3.1.2 with special care to avoid a mixture of isomeric states of OJ8. Samples were vitrified using the automatic blotting procedure presented in Section 3.2.2.1. A concise overview of the sample preparation and imaging conditions is given in Table 4.7. The F-actin-*trans*-OJ8 data set was processed using the hybrid SPA processing pipeline described in Section 3.3.1.3, while the F-actin-*cis*-OJ8 data set was processed using the helical SPHIRE pipeline presented in Section 3.3.1.4. A detailed description of all data processing steps is included in the methods section of the original publication.

F-actin-*trans*-OJ8	
Sample	∼10 µM F-actin and ∼20 µM JASP-cLys OJ8 was added to G-actin before polymerization Sample was protected from light to avoid photo-activation
Buffer	5 mM Tris-HCl pH 7.5, 1 mM DTT, 100 mM KCl, 2mM $MgCl_2$, 2 mM NaN_3, 0.02 % Tween 20, ∼0.7 % DMSO
Vitrification	1.5 µl, no incubation, R2/1 Quantifoils, automatic blotting for 7 s at 13 °, blot force -25, drain time 1 s, Vitrobot
Data acquisition	Cs-corrected Titan Krios, Falcon III linear mode, 1.5 s exposure, 35 frames, total dose 92 $eÅ^{-2}$, pixel size 0.68 Å, 4er spot scan, defocus range 0.6-3.0 µm
F-actin-*cis*-OJ8	
Sample	∼5 µM F-actin and ∼10 µM JASP-cLys OJ8 was added to G-actin before polymerization Sample was repetitively photo-activated
Buffer	5 mM Tris-HCl pH 7.5, 1 mM DTT, 100 mM KCl, 2mM $MgCl_2$, 2 mM NaN_3, 0.02 % Tween 20, ∼0.4 % DMSO
Vitrification	1.5 µl, no incubation, R2/1 Quantifoils, automatic blotting for 7.5 s at 13 °, blot force -25, drain time 1 s, Vitrobot
Data acquisition	Titan Krios, GIF quantum-energy filter, slit with 20 eV, K2 summit counting mode, 15 s exposure, 40 frames, total dose 86 $eÅ^{-2}$, pixel size 1.05 Å, 4er spot scan, defocus range 0.7-2.3 µm

Table 4.7: Overview of sample preparation and imaging conditions of OJ8-stabilized F-actin.

4.5 Structural characterization of actomyosin nucleotide states

The ATPase-driven motor cycle of myosin has been studied for decades (Figure 2.8, also see Section 2.3.2). Yet, only some structural transitions of myosin within this cycle have been resolved, hampering our understanding of the force-generation mechanism.

Today, various crystal structures of all states of myosin that are not associated with actin binding, specifically the post-rigor and pre-powerstroke (PPS) state, are available (for an overview of structures see Sweeney et al. (2020)). Additionally, myosin was successfully crystallized in a rigor-like and a putative P_i-release (P_iR) state (Llinas et al., 2015), both in absence of actin. Actin-bound states of myosin have also been studied, but required the usage of cryo-EM instead of X-ray crystallography (also see Section 2.1). While a first medium-resolution structure of the rigor state gave valuable insight into the architecture of the actomyosin complex (Behrmann et al., 2012a), the underlying molecular interactions could not be described before 2016, when the first high-resolution structure became available (von der Ecken et al., 2016). Since then, the rigor state has been solved at high-resolution ($\leq$ 4 Å) for a number of different myosins (Doran et al., 2020, Mentes et al., 2018, Risi et al., 2020, Vahokoski et al., 2020), allowing the detailed description and comparison of the actomyosin interface. States other than rigor have proven challenging to characterize structurally, primarily due to their weaker binding to F-actin. Usage of high-duty ratio myosins (myosin IB, V and VI) eventually facilitated the structural characterization of the strong-ADP state (Gurel et al., 2017, Mentes et al., 2018, Wulf et al., 2016). Yet, only one of these studies reached high-resolution (myosin IB, Mentes et al. (2018)), finally revealing the structural transition of myosin upon ADP release.

Despite these major advances, our knowledge remains restricted to transitions between unbound (post-rigor to PPS) or strongly bound states of myosin (strong-ADP to rigor). Conversely, the conformational changes associated with binding to F-actin (transition PPS to P_iR), phosphate release (P_iR to strong-ADP) and binding of ATP (rigor to post-rigor) remain elusive. Filling these gaps requires high-resolution structures of weak-binding states of myosin, such as the PPS, P_iR and post-rigor state. Moreover, additional structures of other myosins in the strong-ADP state are required to assess if the structural transition upon ADP release is conserved throughout the myosin family.

Due to structural differences between myosins, the complete motor cycle would ideally be solved for a single myosin. Myosin V and VI are promising candidates, as they are high-duty ratio myosins and have been successfully crystallized in many different states (also see Section 2.3.2). Previous medium-resolution cryo-EM studies have furthermore demonstrated that the rigor and the strong-ADP state can be prepared for both myosin V and VI (Gurel et al., 2017, Wulf et al., 2016). Although at low-resolution, the report of a pre-powerstroke transition state of myosin V (Volkmann et al., 2005) finally suggests

myosin V as the optimal protein to study weak binding states. While previous structures were limited to low- or medium-resolution, the recent developments in cryo-EM are likely to enable the reconstruction of high-resolution structures (also see Section 2.4.6).

With the aim to shed light on the structural transition of myosin, the structure of myosin Va (S1 fragment with one essential light chain, ELC) in complex with F-actin and different nucleotides was studied by cryo-EM in this thesis (also see Section 3.1). Details on the methodology and results are presented in the subsequent sections.

4.5.1 The rigor state and the actomyosin interface

Nucleotide-free myosin Va (hereafter referred to as myosin) was prepared as described in Section 3.1.4. To reduce the flexibility of filaments, which might limit the achievable resolution, aged F-actin was stabilized by phalloidin (aged PHD-F-actin) prior to cryo-EM sample preparation. Cryo-EM samples were prepared using the on-grid incubation method described in Section 3.2.2.1 and imaged using a state-of-the-art electron microscope (Supplementary Figure S1). A concise overview of the sample preparation and imaging conditions is given in Table 4.8.

F-actin-PHD-aged + Myosin-rigor	
Sample	$\sim$ 3 µM F-actin, $\sim$6 µM PHD and $\sim$ 3 µM myosin PHD was added to F-actin after overnight aging
Buffer F-actin	10 mM HEPES pH 7.5, 100 mM KCl, 2 mM $MgCl_2$, 1 mM NaN_3, 1 mM DTT, 0.02 % Tween 20, 0.39 % methanol
Buffer myosin	10 mM HEPES pH 7.5, 100 mM KCl, 2 mM $MgCl_2$, 1 mM NaN_3, 1 mM DTT, 0.02 % Tween 20
Vitrification	On-grid decoration, 3 µl F-actin, 60 s incubation, R2/1 Quantifoils, manual side blotting, 3 µl myosin, 30 s incubation, automatic blotting for 9 s, blot force -15, drain time 1 s, 13 °C, Vitrobot,
Data acquisition	Titan Krios, K2 super-resolution mode, 15 s exposure, 40 frames, total dose 79 $eÅ^{-2}$, pixel size 1.06 Å, 4er spot scan, defocus range 0.4-2.8 µm

Table 4.8: Overview of sample preparation and imaging conditions of F-actin-PHD-aged decorated with myosin in the rigor state.

Actomyosin filaments were processed using helical SPHIRE (also see Section 3.3.1.4) following a multi-step processing pipeline (for details see Supplementary Figure S2). In total, two electron density maps were reconstructed from the same set of particles. To resolve the actomyosin interface, which involves two actin molecules per myosin molecule,

the refinement was focused on the central three actin and two myosin molecules (hereafter referred to as central 3er/2er map). By subsequently subtracting all signal but the central actomyosin molecule (hereafter referred to as central 1er map), the quality of the myosin density could be further improved. In this way, an average resolution of 3.2 Å (central 3er/2er) and 3.3 Å (central 1er) was achieved (Supplementary Figures S1, S2 and S3). The local resolution indicates a gradual decrease of the resolution towards the periphery of the filament, ranging from 2.5 Å in the central actin subunit to ~5-8 Å in the light chain (LC, Supplementary Figure S3). Whereas the resolution gradient along the filament axis reflects the overall filament flexibility, the radial decrease illustrates the intrinsic flexibility of myosin, which has also been reported in previous cryo-EM studies (Mentes et al., 2018, von der Ecken et al., 2016). To account for the differences in resolution, several maps, that were optimized for either high- or low-resolution details (also see Section 3.3.1.8), were used for atomic model building (also see Section 3.3.2). In this way, a reliable atomic model of the complete actomyosin complex was generated, in which all ligands and most side chains are resolved (Figure 4.1).

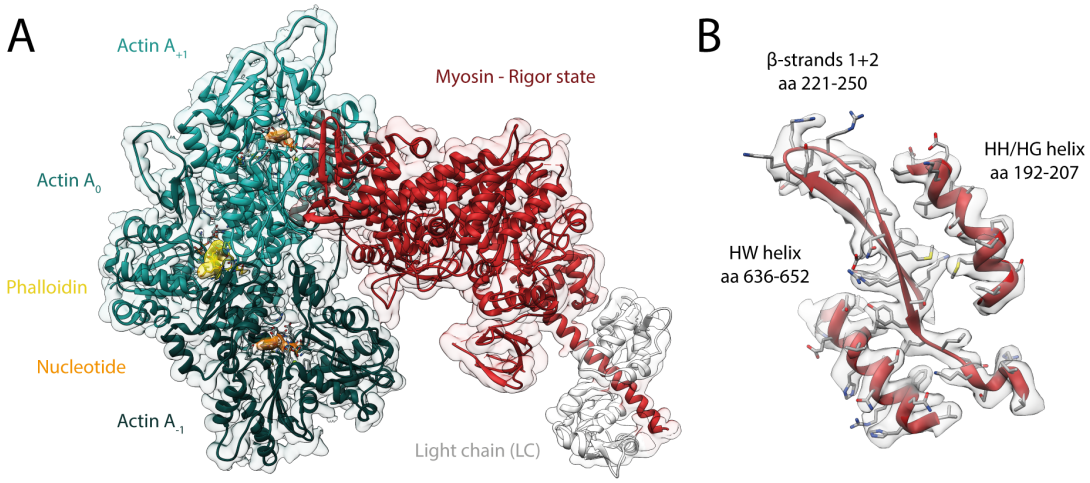

Fig. 4.1: Overview of the structure of the actomyosin complex in the rigor state. **(A)** Atomic model and LAFTER electron density map of the central myosin molecule (red, LC: white) bound to F-actin (shades of sea green, three subunits shown, A_{-1} to A_{+1}). Nucleotides and phalloidin are highlighted in orange and yellow, respectively. **(B)** Model-map agreement within a central section of myosin. Most side chains are resolved within the postrefined electron density map (gray).

Previous cryo-EM studies of the actomyosin V complex were limited to low- (Volkmann et al., 2005) and medium-resolution (Wulf et al., 2016). The structure presented in this thesis is, hence, the first to resolve the molecular details of the rigor state of myosin Va and its interactions with F-actin (Figures 4.1). It encompasses all hallmarks of the rigor state including a closed actin binding cleft, facilitating strong binding to F-actin, and a post-powerstroke lever arm orientation (Figure 4.2). Accordingly, we find the active site unoccupied and open (Supplementary Figure S4, also see Figure 4.3D).

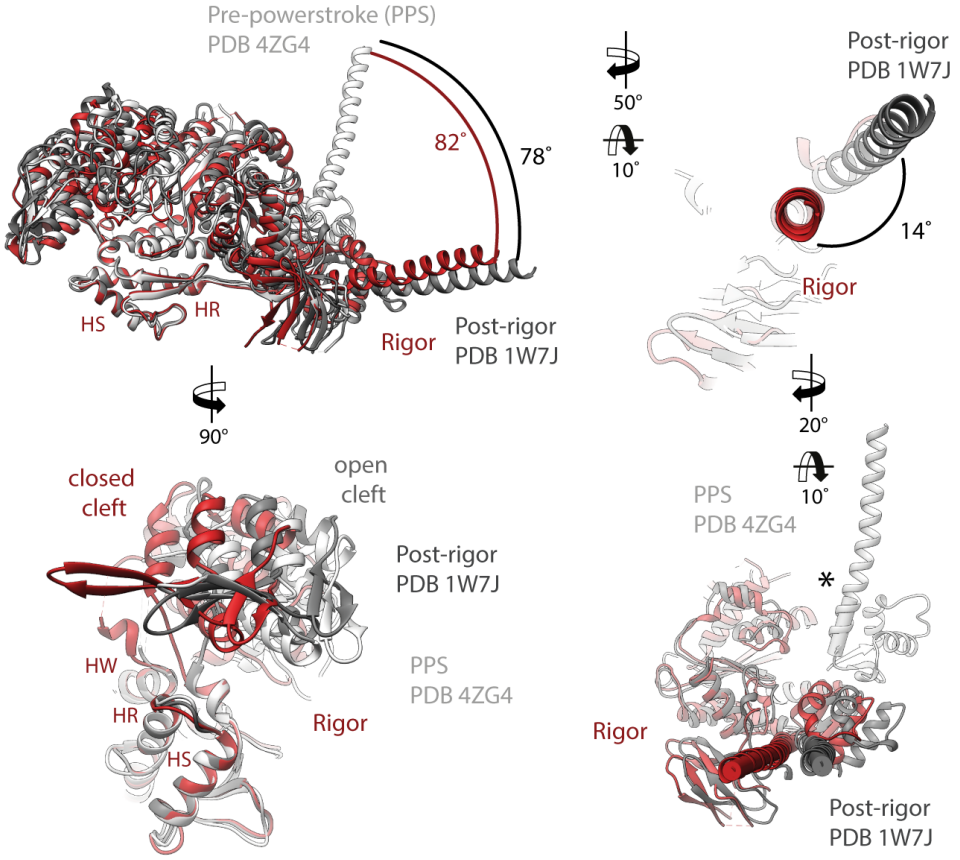

Fig. 4.2: Comparison of the rigor cryo-EM structure (red) with crystal structures of the same myosin in the post-rigor (PDB: 1W7J, Coureux et al. (2004)) and PPS state (PDB: 4ZG4, Wulf et al. (2016)) (shades of gray). A superposition of atomic models illustrates the closure of the central cleft in the rigor state and the relative rotations of the lever arm. Intriguingly, the relative swing angle is bigger for the rigor (82 °) than for the post-rigor state (78 °). The lever arm of the PPS state was computationally extended (original length indicated by asterisk). Models were superimposed based on the HW, HS and HR helices within the L50 domain.

The overall architecture of the complex is not only in good agreement with the medium-resolution reconstruction published earlier (Wulf et al., 2016), but also closely resembles the rigor-like crystal structures solved for this myosin isoform (Coureux et al., 2004, 2003). The atomic models superimpose almost perfectly, and noteworthy deviations can only be found at the F-actin binding interface and within the lever arm (Figure 4.3A-C). While the former can be readily explained by the absence of F-actin, the latter might be caused by crystal packing. The fact that two rigor-like crystal structures (PDB 1OE9, 1W7I) have the same lever arm orientation and also originate from crystals with the same space group supports this hypothesis. It is furthermore supported by a third rigor-like crystal structure (PDB 1W8J), in which the position of the lever arm, which is not completely resolved, depends on the crystal contacts (four molecules in the asymmetric unit) (Coureux et al., 2004). Assessment of the structural flexibility of myosin finally adds additional evidence, as the conformation of the rigor-like lever arm falls outside of the confor-

mational space covered by the lever arm within our rigor cryo-EM data set (Figure 4.3C). Although SO_4 and ADP are bound to the active site of the rigor-like structures, they do not alter the overall organization of the active site, but only give rise to small, isolated changes of the P-loop (Figure 4.3D). Considering this close resemblance, we can confirm that the crystallized conformation of myosin Va (Coureux et al., 2004, 2003), although in absence of actin and thus artificial, is rigor-like, as suggested earlier based on a medium-resolution cryo-EM structure (Wulf et al., 2016).

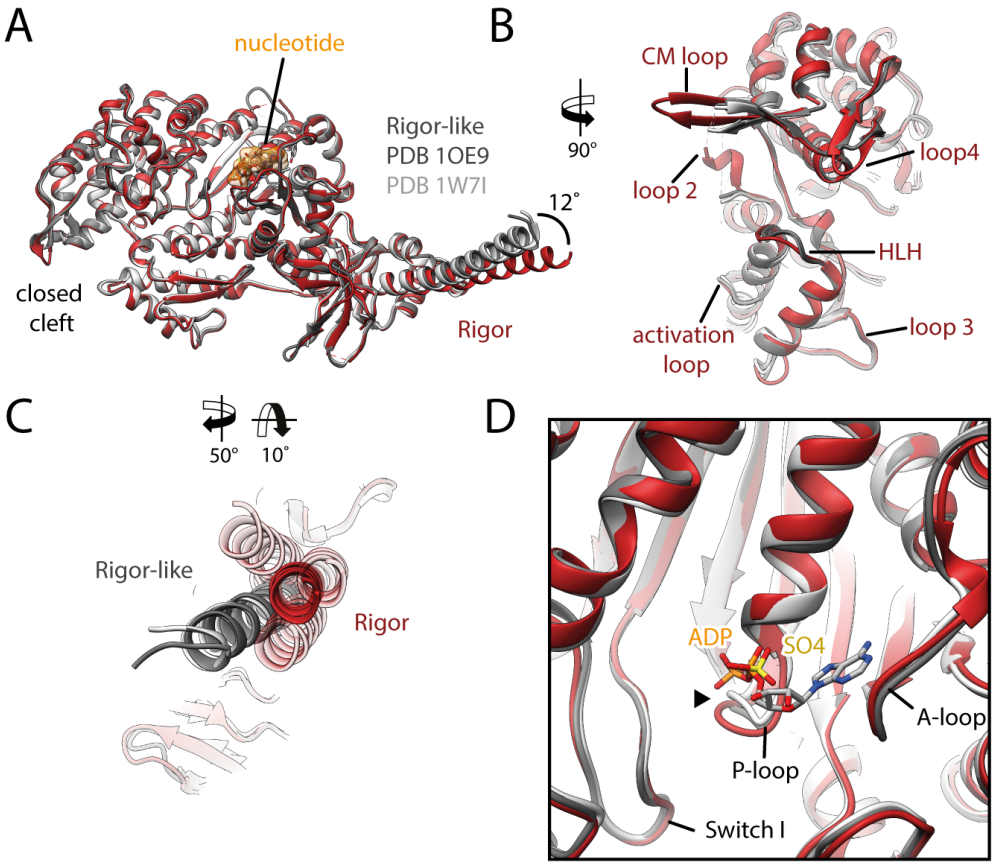

Fig. 4.3: Comparison of the rigor cryo-EM structure (red) with crystal structures of the same myosin in the rigor-like state (PDB: 1OE9, Coureux et al. (2003) and PDB: 1W7I, Coureux et al. (2004)) (shades of gray). **(A)** Superposition of the rigor state with two rigor-like crystal structures. Deviations are limited to the actin interface, in particular the CM loop, loop 4 and loop 2 **(B)**, and the lever arm **(C)**. Interestingly, the lever arm orientation seen in the rigor-like states does not superimpose with any conformation seen for the rigor complex (average: red and 3D classes: transparent red), but localizes outside of its conformational space. **(D)** The active site is open in both the rigor and rigor-like states and the SO_4 and ADP bound to the rigor-like crystal structures only give rise to small, isolated changes of the P-loop.

The actomyosin interface is comprised of six structural elements within myosin, namely the cardiomyopathy (CM) loop, loop 4, the helix-loop-helix (HLH) motif, the activation loop, loop 3 and loop 2 (Figure 4.4). The CM loop (aa 376-392) and loop 4 (aa 338-354) are both part of the U50 domain and vary in length between different myosins. In contrast

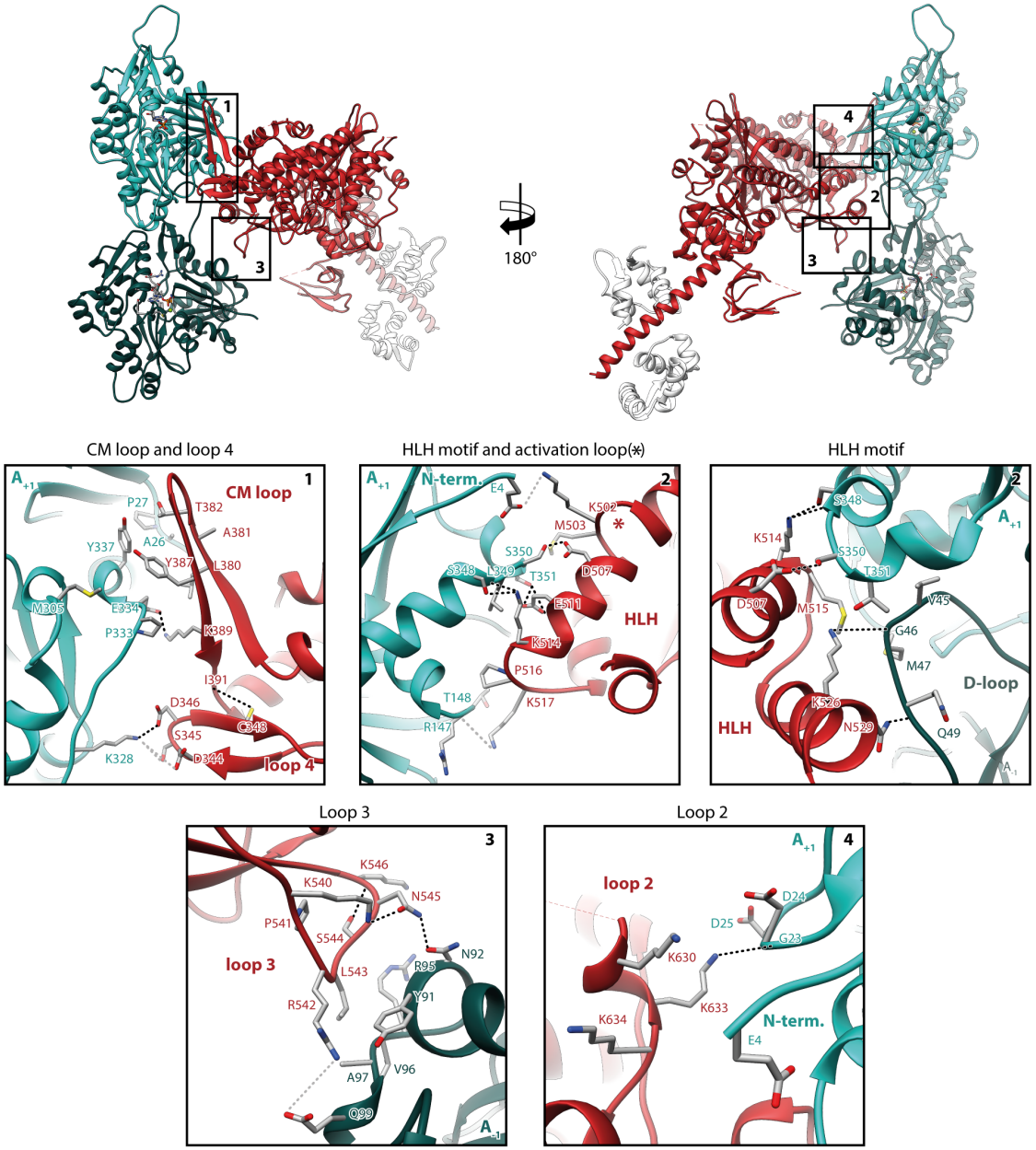

Fig. 4.4: Overview and close-up views of all interfaces of the rigor actomyosin complex. **(Top)** Front and back view of the central myosin molecule and the two actin subunits (A_{-1} and A_{+1}) it is bound to. Black boxes indicate the location of close-up views shown below. **(Bottom)** Close-up views of all actomyosin interfaces including the cardiomyopathy (CM) loop, helix-loop-helix (HLH) motif, loops 2-4 and the activation loop (highlighted by an asterisk). Side chains of key residues are displayed and labeled for both actin and myosin. Dashed lines indicate hydrogen bonds.

to other high-duty ratio myosins, such as myosin I and VI, the CM loop is short in myosin V and thus more similar to the CM loop of myosin IIC (von der Ecken et al., 2016). In accordance to its hydrophobic nature, it primarily interacts with F-actin by hydrophobic interactions between residues L380, A381, T382 and Y387 of myosin and P333, Y337, A26 and P27 in subdomains 3 and 1 of actin A_{+1} (Figure 4.4.1). An additional, highly conversed hydrogen bond (K389-E334, predicted by PDBsum, see Section

3.3.3) further stabilizes this interface. While mainly hydrophobic interactions have also been reported for other myosins, weak supporting electrostatic interactions at the tip and base of the CM loop were also described (Fujii and Namba, 2017, Gurel et al., 2017, Mentes et al., 2018, Risi et al., 2020, von der Ecken et al., 2016). In myosin V, we find only one charged residue (E385) at the tip of the CM loop and no stabilizing electrostatic interactions at its base.

The conformation of loop 4 (aa 338-354) in myosin V differs from all others reported so far. It is not only more compact, folding in a β-hairpin, but also localizes closer to the base of the CM-loop, where it gets stabilized by a non-conserved hydrogen bond between C348 and I391 (Figure 4.4.1). Loop 4 interacts electrostatically with subdomain 3 of actin A_{+1} and all residues at its tip (D344, S345 and D346) can potentially form a hydrogen bond with lysine K328. Analogous interactions have been reported for other myosins, despite the varying length and conformation of this loop (Fujii and Namba, 2017, Gurel et al., 2017, Risi et al., 2020, von der Ecken et al., 2016). Only myosin IB represents an exception, as its loop 4 is hydrophobic and has a weaker interaction potential in general (Mentes et al., 2018).

The HLH motif (aa 505-531) within the L50 domain forms extensive hydrophobic contacts with both subdomain 3 of actin A_{+1} and the D-loop of actin A_{-1} (Figure 4.4.2). Six additional hydrogen bonds (D507-S350, E511-T351, K514-S348, K517-G146, K526-G46, N529-Q49) further stabilize this contact, making it the tightest of all six binding elements. The hydrophobic nature of this interface as well as many key residues, such as E511, K517 and K526, are highly conserved within the myosin family (Mentes et al., 2018, Risi et al., 2020, von der Ecken et al., 2016). The HLH motif is also structure-wise the most similar feature among all myosins studied to date. This finding is in agreement with its proposed significance for the formation of an initial contact with F-actin and the subsequent transition from a weak to a strong binding state (Onishi et al., 2006).

A structural element that does not contribute to the binding of F-actin in all myosins is the activation loop (aa 501-504) (Gurel et al., 2017). It directly precedes the HLH-motif and is either short, as it is the case for myosin V and some myosins of class II (Doran et al., 2020, Fujii and Namba, 2017), or long as in myosin IB and myosin IIC (Mentes et al., 2018, von der Ecken et al., 2016). In myosin V, it primarily interacts electrostatically with a complementary charged patch around the N-terminus in subdomain 1 of actin A_{+1} (Figure 4.4.2). Yet, it also forms supplementary hydrophobic interactions (M503-S350). A putative hydrogen bond between lysine K502 and glutamate E5 additionally strengthens the contact. Interestingly, electrostatic interactions with the activation loop were reported to give rise to an ordering of the N-terminus of actin in some myosins (Banerjee et al., 2017, Behrmann et al., 2012a, Fujii and Namba, 2017, Mentes et al., 2018, Vahokoski

et al., 2020). Within the rigor structure of myosin V, the N-terminus is, however, not ordered, resembling the structure of F-actin in absence of myosin (Merino et al., 2018, Pospich et al., 2020).

Loop 3 (aa 532-546) belongs to the L50 domain and forms the Milligan contact (Milligan et al., 1990). It interacts both electrostatically and hydrophobically with subdomain 1 of actin A_{-1} (Figure 4.4.3). Additional hydrogen bonds stabilize not only the actomyosin interaction (R542-Q99 and N545-N92), but also the conformation of the loop itself (K540-N545 and S544-K546). The conformation of loop 3 and its interactions with F-actin vary markedly between myosins. Whereas the loop is pulled away from the actin interface forming no or only a weak contact in myosin II (Doran et al., 2020, Fujii and Namba, 2017, Risi et al., 2020, von der Ecken et al., 2016), loop 3 is large in myosin I and VI extending towards the interface, thereby facilitating a strong interaction (Gurel et al., 2017, Mentes et al., 2018). Considering the comparably strong interaction of loop 3 with F-actin in myosin V, we speculate that an intimate Milligan contact might be a general feature of high-duty ratio myosins, which need to bind tightly to F-actin to fulfill their function as cargo-transporters or molecular anchors.

The last structural element involved in the binding of actin is loop 2 (aa 593-635), which connects the U50 and L50 domain. Loop 2 is exceptionally long in myosin V and is only partially resolved in our structure (Figure 4.4.4). This is also the case for most myosin structures resolved so far (Banerjee et al., 2017, Doran et al., 2020, Risi et al., 2020, von der Ecken et al., 2016), only the short loop 2 of myosin IB could be completely resolved (Mentes et al., 2018). Within myosin V, the C-terminal part of loop 2 adopts a unique α-helical fold, facilitating a compact packing of basic residues (K630, K633, K634) (Figure 4.4.4). The resulting positively charged surface interacts electrostatically with a complementary charged patch on the surface of subdomain 1 of actin A_{+1}, near its N-terminus. Lysine K633 furthermore forms a non-conserved hydrogen bond with glycine G23. Although the length of loop 2 varies between myosins, its electrostatic nature represents a common feature (Gurel et al., 2017, Mentes et al., 2018, Vahokoski et al., 2020, von der Ecken et al., 2016).

The majority of interactions described here has been successfully predicted earlier based on low-resolution cryo-EM data (Volkmann et al., 2005). Yet, only this high-resolution structure has enabled their detailed description and uncovering of the previously unseen α-helical fold of the C-terminus of loop 2. The structure has furthermore enabled a comparison of the actomyosin interface of myosin V with the ones reported for other myosins (Banerjee et al., 2017, Doran et al., 2020, Gurel et al., 2017, Mentes et al., 2018, Risi et al., 2020, Vahokoski et al., 2020, von der Ecken et al., 2016). Our results support that all myosins utilize a common set of structural elements with conserved hydrophobic or

electrostatic properties to bind to F-actin. However, the precise nature of individual interactions and contributing residues varies significantly (Mentes et al., 2018, Robert-Paganin et al., 2020). This is mostly due to varying loop lengths, which are thought to tune the kinetic properties of the motor. Based on the comparison of the different actomyosin interfaces, we suggest that tighter interactions can be found in high-duty ratio myosins. The binding interface of myosin V, for example, is composed of all six potential interaction sites and thereby establishes a maximum of contacts. In addition, intimate Milligan contacts have been exclusively described for high-duty ratio myosins, suggesting that this contact is key for a high binding affinity.

Despite the intriguing similarity of the actomyosin interface, the overall structure of myosins from distinct classes differs markedly. A superposition of all rigor-state cryo-EM structures with an resolved lever arm shows pronounced conformational differences, which ultimately give rise to lever arm orientations deviating by as much as 54 ° (Figure 4.5A). These variations again highlight the necessity to solve the complete motor cycle for a single myosin isoform to finally understand the structural transitions underlying force production (also see Section 2.3.2).

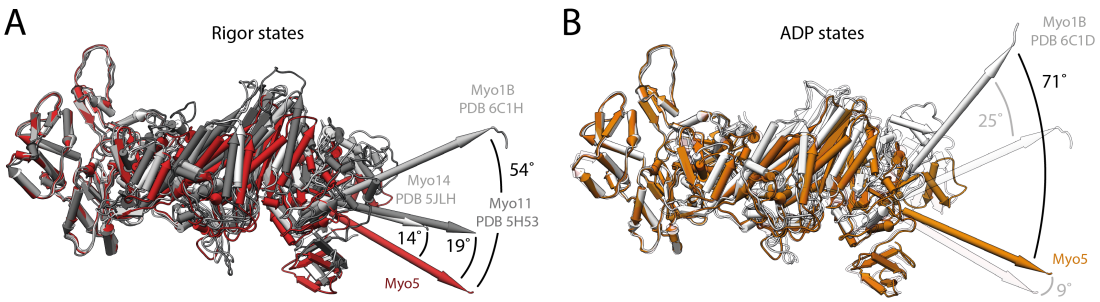

Fig. 4.5: Comparison of atomic models of the rigor and ADP states of different actomyosin complexes solved by cryo-EM. **(A)** Superposition of the rigor states of Myo5 (from this thesis, red), Myo11 (PDB: 5H53, Fujii and Namba (2017)), Myo14 (PDB: 5JLH, von der Ecken et al. (2016)) and Myo1B (PDB: 6C1H, Mentes et al. (2018)) (shades of grey), illustrating strongly varying conformations and lever arm orientations. **(B)** Superposition of the strong-ADP states of Myo5 (from this thesis, orange, see next Section) and Myo1B (PDB: 6C1D, Mentes et al. (2018), light grey). Corresponding rigor states of these two myosins are shown as transparent. The difference in the orientation of the lever arm is even more pronounced in the ADP state, increasing from a relative rotation of 54 ° to 71 °. Only structures with modeled lever arm were included in this comparison and aligned on the central actin subunit.

4.5.2 The strong-ADP state

Myosin in the ADP state was prepared as described in Section 3.1.4. Cryo-EM samples were prepared and imaged in analogy to the rigor state (Supplementary Figure S5). A concise overview of the sample preparation and imaging conditions is given in Table 4.9.

Processing of the data set using the pipeline already established for the rigor complex (Supplementary Figure S2) enabled the reconstruction of the ADP complex to a resolution of 3.0 Å (central 3er/2er) and 3.1 Å (central 1er, Supplementary Figures S2, S3 and S5). The high-resolution of this structure allows the clear identification of Mg^{2+}-ADP in the active site (Figure 4.6, Supplementary Figure S4) as well as analysis of its coordination (Figure 4.6B-C).

F-actin-PHD-aged + Myosin-ADP	
Sample	∼ 3 µM F-actin, ∼6 µM PHD and ∼ 4 µM myosin PHD was added to F-actin after overnight aging
Buffer F-actin	10 mM HEPES pH 7.5, 100 mM KCl, 2 mM $MgCl_2$, 1 mM NaN_3, 1 mM DTT, 0.02 % Tween 20, 0.42 % methanol
Buffer myosin	10 mM HEPES pH 7.5, 100 mM KCl, 22 mM $MgCl_2$, 1 mM NaN_3, 1 mM DTT, 2 mM ADP, 0.02 % Tween 20
Vitrification	On-grid decoration, 3 µl F-actin, 60 s incubation, R2/1 Quantifoils, manual side blotting, 3 µl myosin, 30 s incubation, automatic blotting for 9 s, blot force -15, drain time 0 s, 13 °C, Vitrobot,
Data acquisition	Titan Krios, K2 super-resolution mode, 15 s exposure, 40 frames, total dose 82 $eÅ^{-2}$, pixel size 1.06 Å, 4er spot scan, defocus range 0.3-3.2 µm

Table 4.9: Overview of sample preparation and imaging conditions of F-actin-PHD-aged decorated with myosin bound to ADP.

The active site of myosin is composed of three loops, which connect the central transducer β-sheet with the upper 50 kDa (U50), lower 50 kDa (L50) and N-terminal domain of myosin (also see Figure 2.7). However, only two of these loops, namely the P-loop and switch I, are involved in the coordination of ADP (Figure 4.6B). The P-loop (aa 164-168, highlighted in pastel yellow in all figures of the active site) localizes to the center of the active site and coordinates both the β-phosphate of ADP and the Mg^{2+} ion by hydrogen bonds (predicted by PDBSUM, see Section 3.3.3). Additional hydrogen bonds furthermore connect the nucleotide to the HF helix (aa 169-183) trailing the P-loop (Figure 4.6B). These interactions are representative for the Walker-A nucleotide binding motif (Walker et al., 1982), which is not only found in myosin, but also in other molecular motors and G-proteins (Figure 4.7, also see Section 2.3.1). Switch I (aa 208-220, highlighted in pastel blue) does not directly interact with ADP, but forms a hydrogen bond with the Mg^{2+} ion and thereby indirectly contributes to the coordination of the β-phosphate (Figure 4.6C). The last key loop, switch II (aa 439-448, pastel green), does not form any contacts with Mg^{2+}-ADP, in agreement with its proposed role in ATP hydrolysis and the

subsequent release of the inorganic phosphate (Sweeney et al., 2020). The conformation of switch II is, nevertheless, directly coupled to the architecture of the active site, as it forms a hydrogen bond with the HF helix (D437-T170).

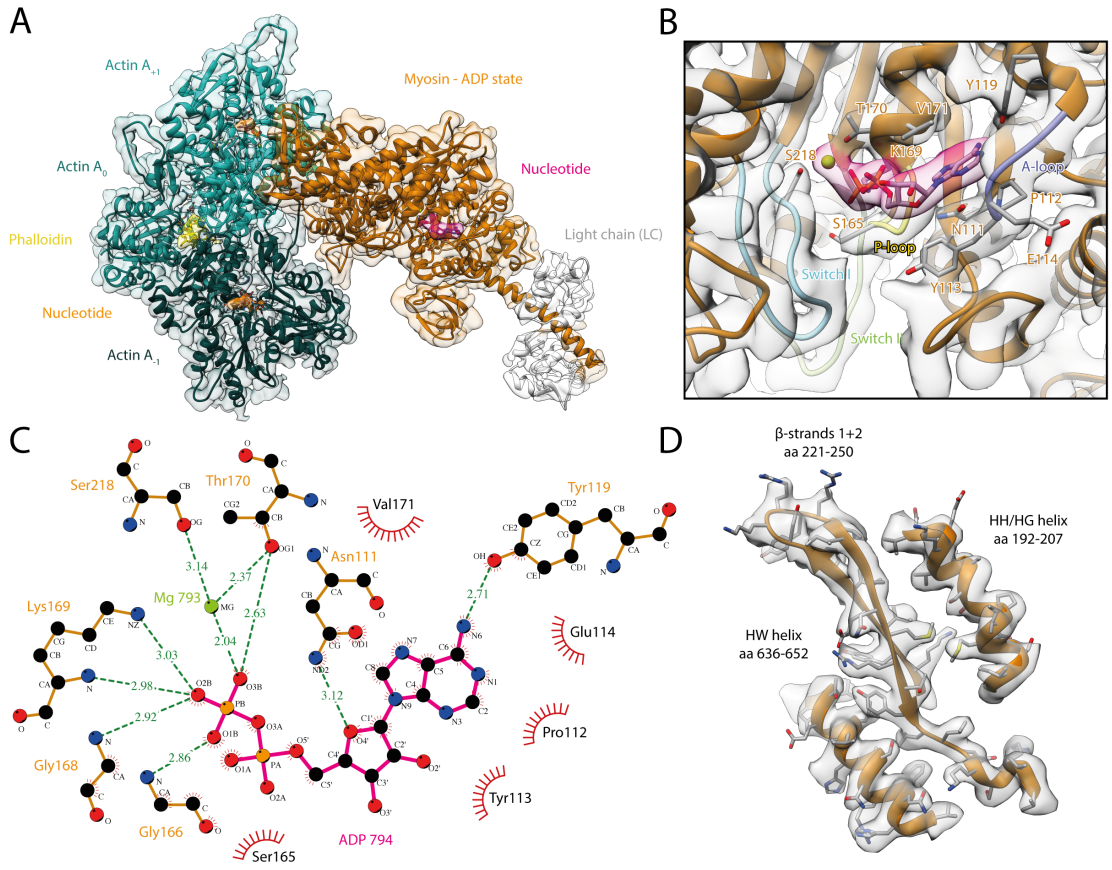

Fig. 4.6: Overview of the structure and active site of the actomyosin complex bound to ADP. **(A)** Atomic model and LAFTER electron density map of the central myosin molecule (orange, LC: white) bound to F-actin (shades of sea green, three subunits shown, A_{-1} to A_{+1}). Nucleotides and phalloidin are highlighted in orange, pink and yellow, respectively. **(B)** Close-up view of the myosin active site consisting of the P-loop (yellow, 164-168), switch I (blue, aa 208-220), switch II (green, aa 439-448) and the A-loop (purple, aa 111-116). Only side chains involved in the binding of ADP are displayed. Also see Supplementary Figure S4. **(C)** 2D protein-ligand interaction diagram illustrating the coordination of ADP by hydrogen bonds (dashed green lines) and hydrophobic interactions (red rays). **(D)** Illustration of the model-map agreement within a central section of myosin. Most side chains are resolved by the postrefined electron density map (transparent gray).

While the P-loop and switch I primarily interact with the β-phosphate of ADP, a hitherto unnamed loop (aa 111-116, pastel purple) stabilizes the adenosine moiety by hydrophobic interactions and a single hydrogen bond. Due to its association with the adenosine, it will hereafter be referred to as A-loop (adenosine-binding loop). Finally, a tyrosine (Y119) trailing the A-loop, forms another hydrogen bond with the adenosine completing the coordination of ADP.

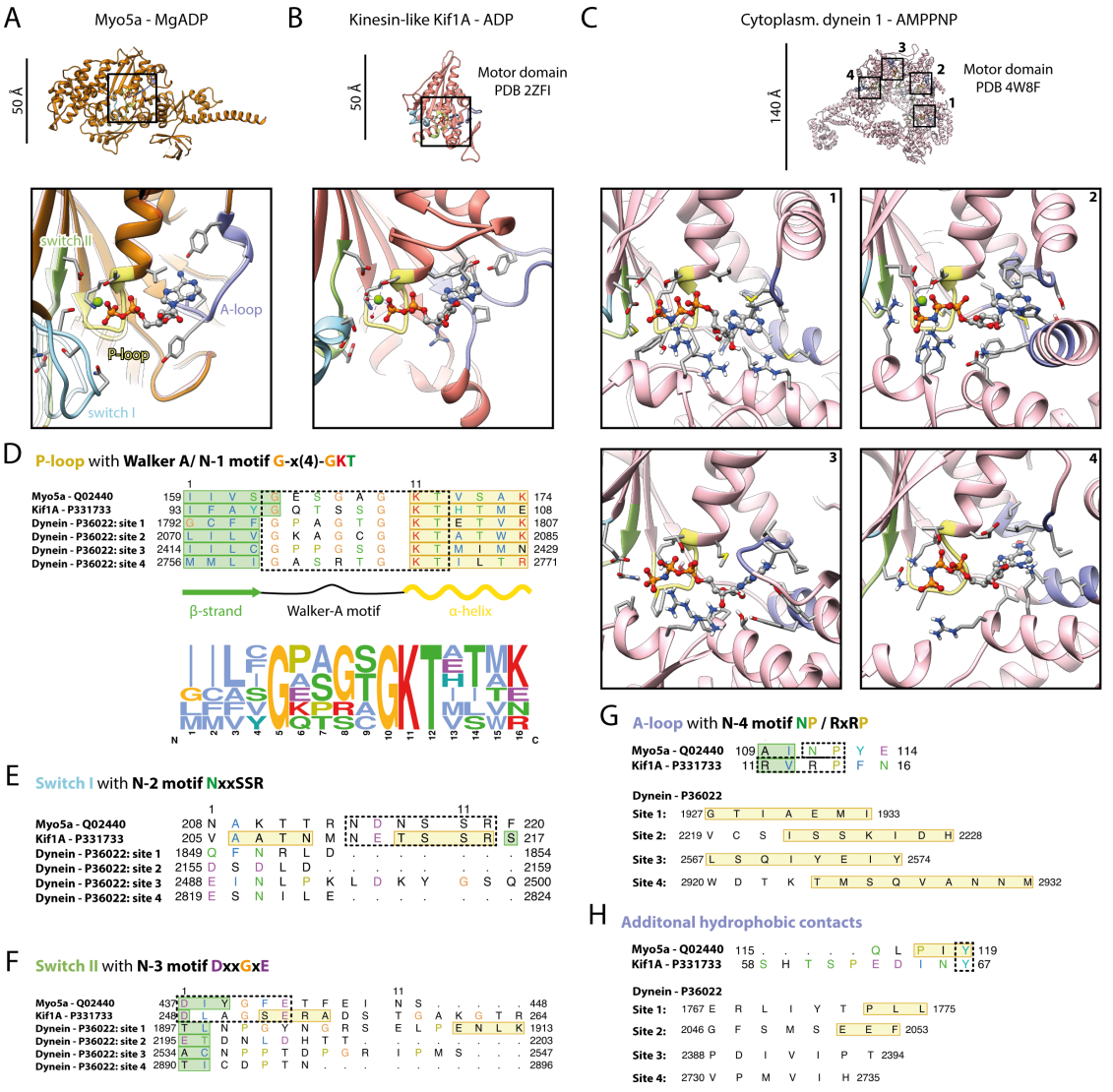

Fig. 4.7: Comparison of the active site and sequence of myosin Va (ADP state: orange, rigor state: transparent), kinesin-like Kif1A (PDB: 2ZFI, Nitta et al. (2008), salmon) and dynein 1 (PDB: 4W8F, Bhabha et al. (2014), light pink). **(A-C)** Overview of each motor structure with scale bar **(top)**. The active sites are highlighted by black boxes and shown as close-up inserts **(bottom)**. Conserved nucletide-coordinating loops are the P-loop (yellow), switch I (blue) and switch II (green). The adenosine is additionally coordinated by hydrophic loops (purple). **(D-H)** Structure-based sequence alignments with highlighted motifs (dashed boxes) and secondary structure elements (α-helix: yellow, β-strand: green). **(D)** All three motors share a common Walker A/ N-1 motif located in the P-loop. Myosin and kinesin moreover share N-2, N-3 and N-4 motifs in their **(E)** switch I, **(F)** switch II and **(G)** A-loops. **(H)** Finally, a tyrosine additionally stabilizes the adenosine in both myosin Va and kinesin-like Kif1A.

A comparison of the coordination of ADP with that of weakly-bound ADP in the rigor-like state of myosin V (Coureux et al., 2004) reveals a distinct, for the strong-ADP state specific coordination (Figure 4.8A), as suggested earlier based on medium-resolution cryo-EM data (Wulf et al., 2016). This finding is in good agreement with the coordination of ADP in the sole other high-resolution structure of the strong-ADP state of myosin IB (Mentes et al., 2018). In particular, the position and orientation of Mg^{2+}-ADP relative to

the HF helix is almost identical to that found in myosin IB (Mentes et al., 2018). This

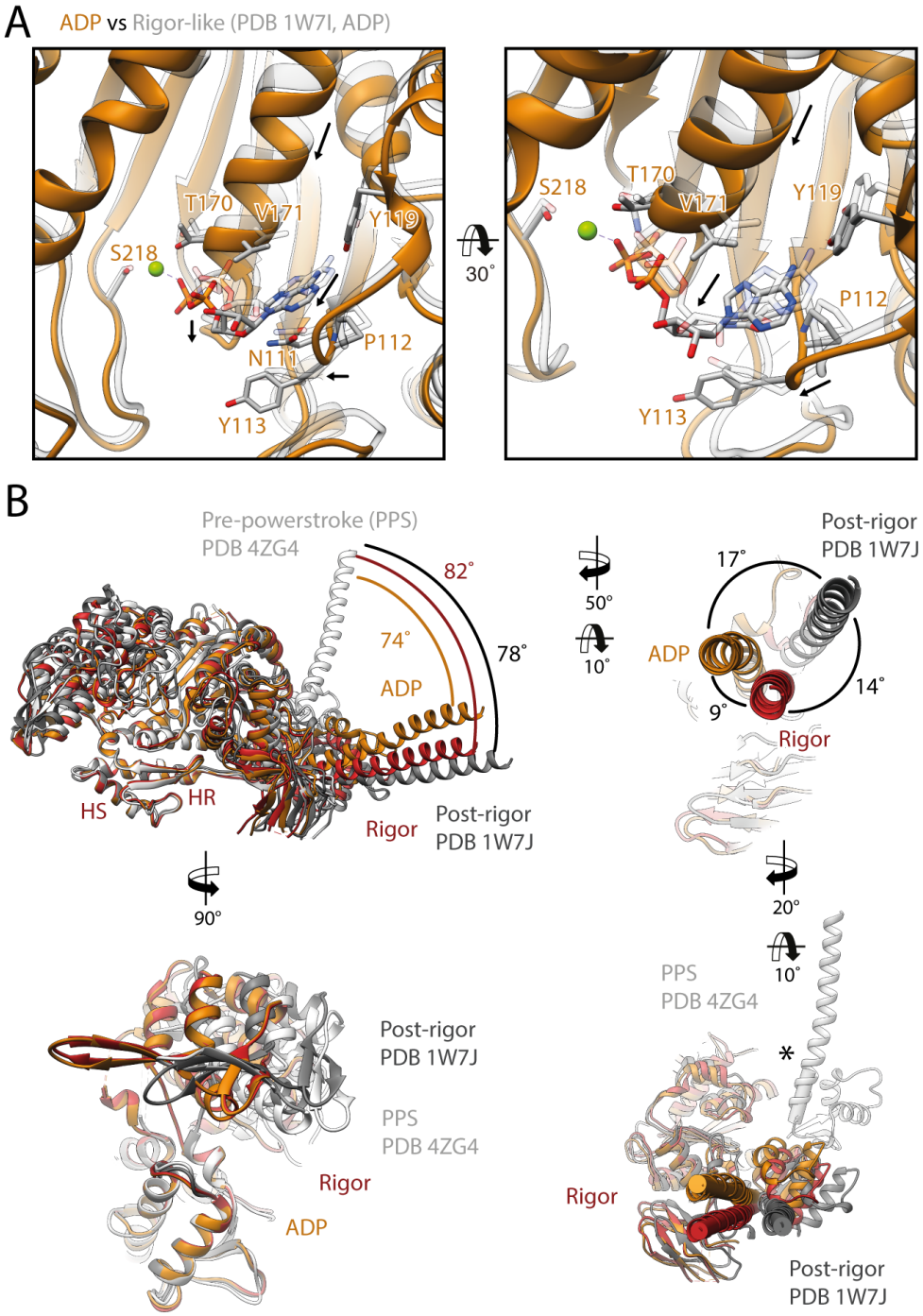

Fig. 4.8: Comparison of the cryo-EM structures of myosin Va in the rigor (red) and strong-ADP state (orange) with crystal structures of the same myosin in the rigor-like (PDB: 1OE9, Coureux et al. (2003) and PDB: 1W7I, Coureux et al. (2004)), post-rigor (PDB: 1W7J, Coureux et al. (2004)) and PPS state (PDB: 4ZG4, Wulf et al. (2016)) (shades of gray). **(A)** Superposition of the strong-ADP and ADP-bound rigor-like state (PDB: 1W7I) illustrating that the coordination of ADP in the strong-ADP state differs markedly from the one in the rigor-like state, giving rise to considerable allosteric rearrangements (indicated by black arrows). **(B)** Superposition of the strong-ADP, rigor, post-rigor (dark gray) and PPS (light gray) states illustrating the closure of the central cleft in actin-bound states and the relative rotations of the lever arm. Same views as in Figure 4.3, but including the strong-ADP cryo-EM structure.

goes along with a close resemblance of the binding interface formed by the P-loop, HF helix and the A-loop. The position of switch I, however, differs markedly between the two structures. In myosin IB switch I localizes closer to the nucleotide and converter domain, shifting by 2-3 Å relative to switch I in myosin Va. This suggests that, although the general architecture of the active site is conserved among myosins, small local reorganizations occur and possibly account for the different kinetics within the myosin family. The functional and structural versatility compatible with a conserved active site is well illustrated by the molecular motors myosin, kinesin and dynein (Figure 4.7). While all three motors rely on the same structural core, they use it to power highly divergent processes (see Section 2.3.1).

The overall structure of the ADP state superimposes well with a previously published medium-resolution structure of the same complex (Wulf et al., 2016). It furthermore encompasses all hallmarks of the strong-ADP state including a closed actin binding cleft, giving rise to an actomyosin interface indistinguishable from the rigor-state (Supplementary Figure S6), and a post-powerstroke lever arm orientation (Figures 4.6A and 4.8B). The lever arm position differs, however, from the post-powerstroke orientation found in the rigor state by 9 °, in agreement with a previously reported rotation of 9.5 ° (Wulf et al., 2016). A similar, yet larger swing of the lever arm upon ADP release was reported for myosin IB (25 °) and myosin VI (30 °) (Gurel et al., 2017, Mentes et al., 2018). A comparison of our structure with myosin IB (Mentes et al., 2018) illustrates that differences in the overall conformation give rise to the different lever arm orientations (Figure 4.5). Against this background, the question arises if the structural transition upon ADP release and thus the mechanism of mechanochemical coupling also differs between myosins.

4.5.3 Structural transition upon ADP release

The rigor state directly follows the strong-ADP state within the myosin motor cycle (Figure 2.8). A comparison of the high-resolution structures of these two states thus allows the detailed description of the structural transition of myosin Va upon Mg^{2+}-ADP release (Figure 4.9).

A superposition of the two structures illustrates that the actomyosin interface is highly conserved and hence not affected by the structural transition of myosin (Figure 4.9A, Supplementary Figure S6). Structural rearrangements at the active site are instead transmitted to the N-terminal and converter domain of myosin, ultimately giving rise to a minor lever arm swing (Figure 4.9). A close-up view of the active site reveals how the loss of the nucleotide is transmitted to distant domains (Figure 4.9B). The release of Mg^{2+}- ADP results in the reorganization of the nucleotide binding cleft. Here, switch I slightly

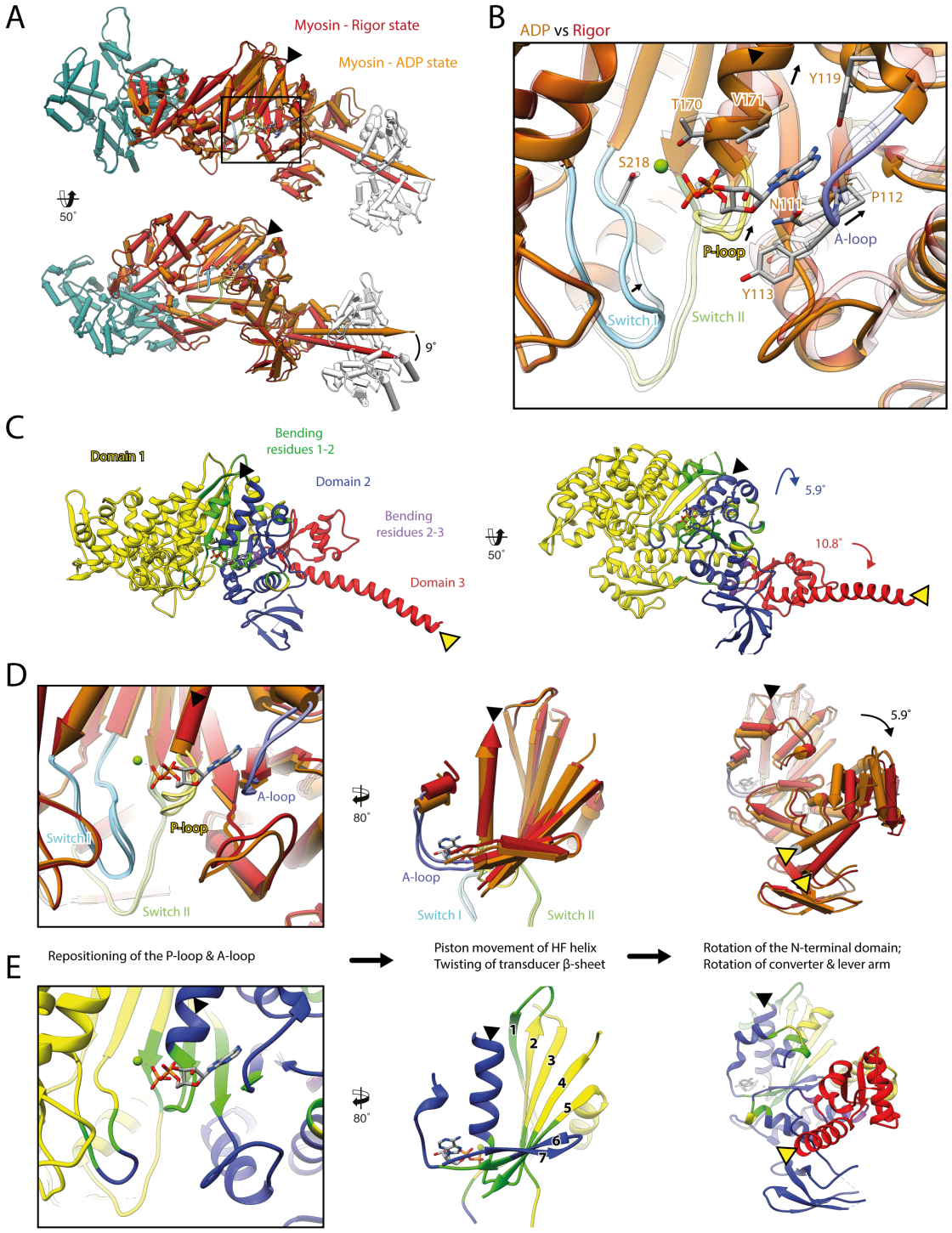

Fig. 4.9: Illustration of the structural transition of myosin upon Mg^{2+}-ADP release. **(A)** Superposition of the strong-ADP (orange) and rigor (red) structures illustrating that changes of the active site (black box) are not transmitted to the actomyosin interface, but to the N-terminal and converter domain. **(B)** Close-up view of the active site showing the structural rearrangements (indicated by black arrows) upon Mg^{2+}-ADP release. The rigor structure is shown as transparent. **(C)** Illustration of domain movements between the two states (predicted by the DynDom software). **(D)** Scheme illustrating the transmission of structural changes from the active site to the lever arm. **(E)** Same views as in D), but colored by DynDom domains, also see C). The HF helix and lever arm is highlighted by a black and yellow arrowhead, respectively.

moves into the now unoccupied pocket, while switch II remains unchanged. This movement is, however, not transmitted to neighboring structural elements and hence not critical. Conversely, both the P-loop (aa 164-168) and the A-loop (aa 111-116) shift outwards considerably thereby opening the active site (Figure 4.9B). The upwards movement of the P-loop is directly coupled to a piston movement of the HF helix (aa 169-183), which is incompatible with a Mg^{2+}-coordinating hydrogen bond with switch II (T170-D437) (Mentes et al., 2018). While it is tempting to speculate that the loss of Mg^{2+} triggers this structural transition, the rearrangement could also proceed the release. After ADP release, a new network of hydrogen bonds stabilizes the rigor conformation of the active site. Lysine K169 (HF helix), which has previously coordinated the β-phosphate of ADP, forms hydrogen bonds with aspartate D437 and isoleucine I438 (switch II) in the absence of ADP. Because of this, the coupling of the central transducer β-sheet to the U50 and N-terminal domains differs between the strong-ADP and the rigor state.

The HF helix packs close to the transducer β-strands 3 and 4 as well as the N-terminal domain (Figure 4.9). In doing so, it directly transmits the structural rearrangements of the active site to these structural elements. Specifically, it gives rise to a twisting of the transducer and a rotation of the N-terminal domain (Figure 4.9D-E). The transducer and N-terminal domain are also directly coupled to the A-loop, which coordinates the adenosine moiety in the strong-ADP state (Figure 4.6). When ADP is lost, destabilization of the A-loop allows it to shift laterally (Figure 4.9D-E). In this way, the A-loop can follow or possibly even promote the twisting of the transducer and rotation of the N-terminal domain, which are both directly connected to it (Figure 4.9D-E). Based on the rearrangement of the A-loop, we propose that the nucleotide state of myosin is transmitted to the periphery by the P-loop and the A-loop and that their mutual interplay defines the orientation of the N-terminal domain. Small shifts at the active site ($\sim$1-2 Å) thereby get amplified to a significant rotation of the N-terminal domain as well as the converter domain coupled to it, ultimately giving rise to a lever arm swing of $\sim$9 ° (Figure 4.9).

The domain motions associated with the release of Mg^{2+}-ADP were furthermore analyzed using DynDom (Hayward and Lee, 2002) (see Section 3.3.3). The algorithm identified three distinct domains which rotate relative to each other during the strong-ADP to rigor transition (Figure 4.9C). The first and largest domain covers almost the complete U50 and L50 domains (shown in yellow, 452 residues). It hardly changes between the states with an overall RMSD of $\sim$0.5 Å. This result is in good agreement with our structural analysis, indicating that structural changes are not transmitted toward the actomyosin interface. The second domain (shown in blue, 181 residues) encompasses the N-terminal domain including the SH1 and SH2 helices. Upon ADP release, it rotates counterclockwise by $\sim$6 ° relative to domain 1 (Figure 4.9C). To allow this rotation, a number of structural elements (shown in green), including the P-loop as well as parts of the A-loop

and the central transducer β-sheet, need to bend. Interestingly, switch I itself contains a hinge region, allowing its tip to follow the rotation of domain 2 (Figure 4.9E). Again, this is in good agreement with the structural analysis, which did not only identify the structural elements acting as hinge regions, but also the overall rotation of the N-terminal domain. The third domain (shown in red, 93 residues), however, did not become apparent in this analysis. It is composed of the converter domain including the lever arm and rotates by $\sim$11 $^\circ$ relative to domain 2 (Figure 4.9C). The hinge region of this domain (shown in purple) is small, involving only two residues in the N-terminal and four residues in the converter domain. The semi-independent rotation of this domain is possibly due to its coupling to both the N-terminal domain and the relay helix (U50 domain) (Figures 4.9 and 2.7). The conformation of the relay helix does not significantly differ between the strong-ADP and the rigor state. A rigid-body rotation of the N-terminal and converter domain might therefore result in a clash with this helix or alternatively loss of critical stabilizing interactions. By instead rotating semi-independently, the converter domain can maintain its interactions with the N-terminal domain and the relay helix.

The results of the structural and domain analysis can be combined into one model describing the mechanochemical coupling that give rise to the structural transition of myosin upon ADP release (Figure 4.9D). The P-loop, HF helix and A-loop are key for the coordination of Mg^{2+}-ADP in the strong-ADP state. Loss of the nucleotide breaks the interaction network stabilizing their conformation. As a result, the P-loop and A-loop move out of the nucleotide cleft. The HF helix, furthermore, follows the movement of the P-loop performing a piston movement. The conformation of all these structural elements is directly coupled to the one of the central transducer β-sheet. Specifically, their rearrangements cause twisting of the transducer, which eventually gives rise to a rotation of the complete N-terminal domain by $\sim$6 $^\circ$. The converter, which is directly connected to the N-terminal domain (Figure 2.7), finally undergoes an additional rotation of $\sim$11 $^\circ$ causing a small lever arm swing.

Similar structural transitions were reported for myosin IB, V and VI based on either medium- or high-resolution cryo-EM data (Gurel et al., 2017, Mentes et al., 2018, Wulf et al., 2016). These include not only the rotation of the N-terminal and converter domain, but also its coupling to the active site via the transducer, HF helix and the P-loop. In case of myosin IB, even an analogous remodeling of hydrogen bonds due to the piston movement of the HF helix was described (Mentes et al., 2018). Furthermore, all studies conclude that the cleft closure and the actomyosin interface is, if at all, only subtly altered (Gurel et al., 2017, Mentes et al., 2018, Wulf et al., 2016). All these commonalities suggest that the structural transition of myosin upon ADP release as well as the underlying mechanism of mechanochemical coupling is generally conserved. Some of the details reported for the transition, however, differ from what we found for myosin Va.

First, the role of the A-loop in the mechanochemical coupling has not been recognized before, although it is also involved in the binding of ADP in other myosins. Specifically, only one study described an ancillary movement of this loop upon ADP release (Gurel et al., 2017). Second, a partial unwinding of the relay helix (aa 449-479) was described for myosin IB and VI (Gurel et al., 2017, Mentes et al., 2018). Conversely, we find a conserved relay helix conformation in myosin V. This difference could arise from the significantly larger lever arm swings of myosin IB and VI upon ADP release (25 ° and 30 °) compared to myosin V (9 °) (Gurel et al., 2017, Mentes et al., 2018). Not only do the swings differ, but also the lever arm positions within the same state. For example, the lever arm orientations in the rigor and the strong-ADP state of myosin V and myosin IB deviate by 54 ° and 71 °, respectively (Supplementary Figure 4.5). Based on this, it stands to reason that unwinding of the relay helix is a prerequisite for large swings. The extent of the swing could, furthermore, tune the force-sensitivity of myosin. It is well known that the lifetime of the strong-ADP state is prolonged under load (Kovács et al., 2007, Laakso et al., 2008, Takagi et al., 2006, Veigel et al., 2005). In this way, early detachment is prevented, increasing the processivity and anchoring potential of myosin. Structural data suggest that mechanical loads block the transition to the rigor state by inhibiting the lever arm swing associated with ADP release (Mentes et al., 2018). It is reasonable to assume that bigger lever swings are more easily stalled by load than smaller ones. The large lever swing of myosin IB, consequently, would make it more force-sensitive than myosin V. This hypothesis is supported by biochemical studies reporting an almost 40-fold stronger force-sensitivity of myosin IB compared to myosin V (Laakso et al., 2008, Veigel et al., 2005). Whether this hypothesis also holds true for other myosins remains to be investigated.

4.5.4 The AppNHp state

All weak-binding states of myosin are linked to the presence of a γ-phosphate in the active site, either in form of ATP (post-rigor state) or as inorganic phosphate (P_i) after hydrolysis (PPS and P_iR state). As ATP hydrolysis and phosphate release are fast in myosin, the lifetime of these states is generally too short to allow sample preparation for cryo-EM. One potential way to overcome this obstacle is the usage of non-hydrolyzable ATP analogs. A number of different analogs is available commercially, mimicking not only ATP but also ADP-P_i transition states (Bagshaw, 2001). If an analog is suitable to mimic a certain nucleotide state, and whether it resembles ATP or rather a transition state, strongly depends on the protein.

AppNHp, also known as AMP-PNP, is a common ATP analog, in which a nitrogen replaces the oxygen in between the β- and γ-phosphate. In contrast to other analogs,

AppNHp is not hydrolyzed by myosin within a range of temperatures (4 °C to 25 °C) (Yengo et al., 2002). Crystal structures of myosin II furthermore show that AppNHp is coordinated similarly to ATP (Bauer et al., 2000, Gulick et al., 1997) with only minor changes in the network of hydrogen bonds, which likely give rise to the altered binding affinities reported (Yengo et al., 2002). While biochemical studies suggest that AppNHp stabilizes an intermediate state between strong and weak actin binding, the nature of this state is unclear. Low-resolution cryo-EM studies of myosin V bound to AppNHp reported a mixture of states within the same actomyosin filament (Volkmann et al., 2005). Specifically, a conformation with a primed lever arm (pre-powerstroke) was found alongside to a relaxed lever arm state (post-powerstroke), indicating that AppNHp is also suitable to trap a pre-powerstroke transition state. This state was suggested to represent a posthydrolysis ADP-P_i state, such as the P_iR state (Llinas et al., 2015, Volkmann et al., 2005). In line with the report of two distinct states, kinetic data suggest that AppNHp can stabilize myosin V in two different states in dependence of the incubation temperature (personal communication with Prof. Dr. Lee Sweeney). Incubation at 4 °C will likely give rise to a post-rigor state, while myosin can possibly explore both the PPS or P_iR and the post-rigor state at higher temperatures (25 °C). Consequently, AppNHp might facilitate the structural characterization of the beginning and the end of the powerstroke (also see Figure 2.8).

To exploit the potential of AppNHp, aged PHD-stabilized F-actin was decorated with AppNHp-bound myosin, prepared as described in Sections 3.1.4-3.1.4, either at 4 °C or at 25 °C (see Section 3.2.2.1 for details). In agreement with a weaker binding affinity, the concentration of myosin had to be significantly increased to fully decorate the actin filaments (∼10-13 µM instead of ∼3-4 µM for the rigor and strong-ADP state), despite a reduced ionic strength of the buffer. Except for the incubation temperature, cryo-EM samples were prepared in analogy to the rigor state and imaged similarly (Supplementary Figures S7-S8). In particular, both AppNHp data sets were collected within one session; thus, identical microscope settings were used. A concise overview of the sample preparation and imaging conditions is given in Table 4.10.

The 4 °C and 25 °C data sets were processed independently using the established processing pipeline described for the rigor state (Supplementary Figure S2). The actomyosin complexes were resolved to 3.0 Å (central 3er/2er and central 1er, 4 °C) and 3.1 Å (central 3er/2er and central 1er, 25 °C), respectively (Supplementary Figures S3, S7 and S8). Surprisingly, the two electron density maps were found to superimpose perfectly (Supplementary Figure S9). Similarly, 3D classes, which were computed to assess the structural heterogeneity of myosin and to identify a potential mixture of structural states, indicated a similar degree of freedom by mapping into the same conformational space (Supplementary Figure S9B). Hence, we conclude that myosin adopts the same state in both our

AppNHp data sets. While we cannot exclude that AppNHp is generally associated with only one state independent of the incubation temperature, it is likely that the temperature drop during the plunging process overwrote the effect of the incubation temperature. In this way, both samples have possibly experienced a similar, low effective temperature, giving rise to the same conformational state.

F-actin-PHD-aged + Myosin-AppNHp-4 °C	
Sample	∼ 4 µM F-actin, ∼8 µM PHD and ∼13 µM myosin PHD was added to F-actin after overnight aging
Buffer F-actin	10 mM HEPES pH 7.5, 100 mM KCl, 2 mM $MgCl_2$, 1 mM NaN_3, 1 mM DTT, 0.02 % Tween 20, 0.6 % methanol
Buffer myosin	10 mM HEPES pH 7.5, 13 mM KCl, 6 mM $MgCl_2$, 1 mM NaN_3, 1 mM DTT, 5 mM AppNHp, 0.02 % Tween 20
Vitrification	On-grid decoration, 3 µl F-actin, 60 s incubation, R2/1 Quantifoils, manual side blotting, 3 µl myosin, 60 s incubation, automatic blotting for 9 s, blot force -25, drain time 1 s, 4 °C, Vitrobot
Data acquisition	Cs-corrected Titan Krios, GIF quantum-energy filter, slit with 20 eV, K2 super-resolution mode, 15 s exposure, 40 frames, total dose 81 $eÅ^{-2}$, pixel size 1.10 Å, 4er spot scan, defocus range 0.5-2.8 µm
F-actin-PHD-aged + Myosin-AppNHp-25 °C	
Sample	∼ 6 µM F-actin, ∼12 µM PHD and ∼ 10 µM myosin PHD was added to F-actin after overnight aging
Buffer F-actin	10 mM HEPES pH 7.5, 10 mM KCl, 2 mM $MgCl_2$, 1 mM NaN_3, 1 mM DTT, 0.02 % Tween 20, 0.9 % methanol
Buffer myosin	10 mM HEPES pH 7.5, 10 mM KCl, 6 mM $MgCl_2$, 1 mM NaN_3, 1 mM DTT, 5 mM AppNHp, 0.02 % Tween 20
Vitrification	On-grid decoration, 3 µl F-actin, 60 s incubation, R2/1 Quantifoils, manual side blotting, 3 µl myosin, 30 s incubation, automatic blotting for 9 s, blot force -25, drain time 0 s, 25 °C, Vitrobot
Data acquisition	Cs-corrected Titan Krios, GIF quantum-energy filter, slit with 20 eV, K2 super-resolution mode, 15 s exposure, 40 frames, total dose 81 $eÅ^{-2}$, pixel size 1.10 Å, 4er spot scan, defocus range 0.8-3.0 µm

Table 4.10: Overview of sample preparation and imaging conditions of F-actin-PHD-aged decorated with myosin bound to AppNHp at 4 °C and 25 °C.

With the aim to improve the overall resolution, the two data sets were subsequently combined and re-refined. The resulting electron density map does not only closely resemble the maps calculated for the independent data sets (Supplementary Figure S9), but is also

of superior quality and resolution - 2.9 Å for the central 3er/2er and central 1er map (Figure 4.10, Supplementary Figures S10 and S3). For this reason, atomic models were only build and analyzed for the combined AppNHp data set.

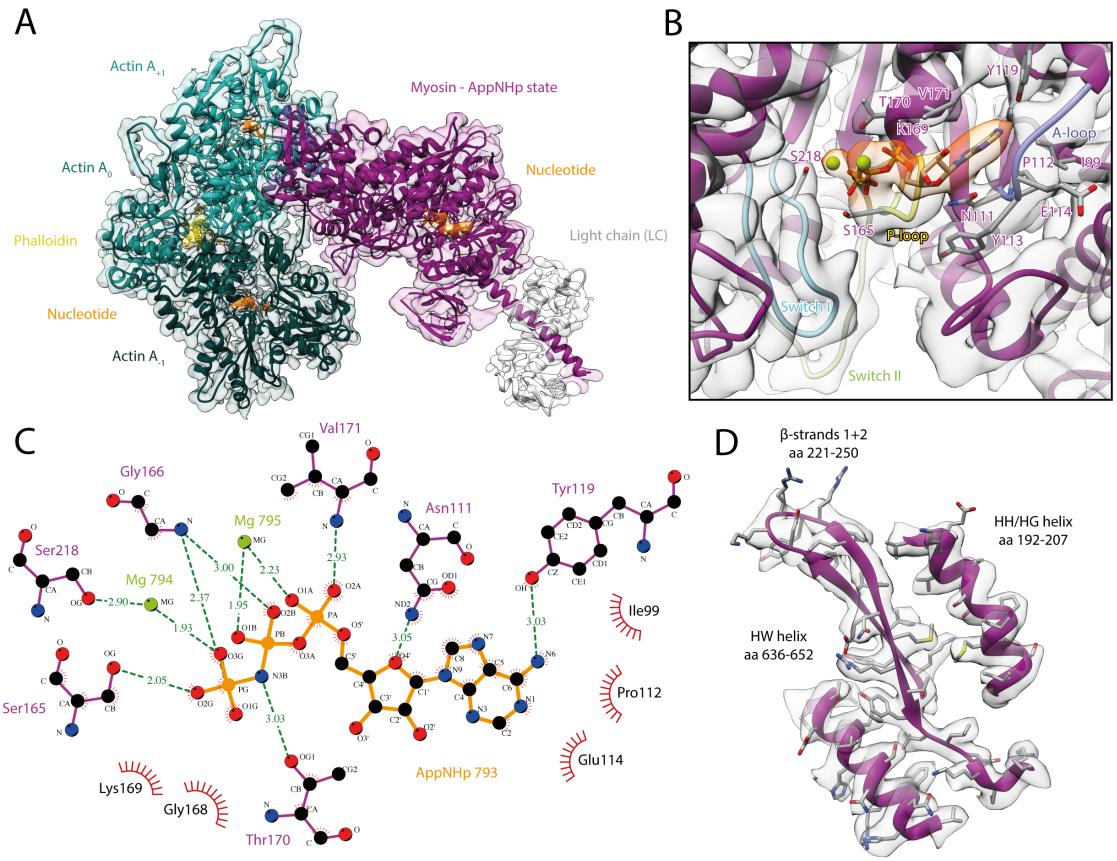

Fig. 4.10: Overview of the structure and active site of the actomyosin complex bound to AppNHp. **(A)** Atomic model and LAFTER electron density map of the central myosin molecule (purple, LC: white) bound to F-actin (shades of sea green, three subunits shown, A_{-1} to A_{+1}). Nucleotides and phalloidin are highlighted in orange and yellow, respectively. **(B)** Close-up view of the myosin active site consisting of the P-loop (yellow, 164-168), switch I (blue, aa 208-220), switch II (green, aa 439-448) and the A-loop (purple, aa 111-116). Only side chains involved in the binding of AppNHp are displayed. Also see Supplementary Figure S4. **(C)** 2D protein-ligand interaction diagram illustrating the coordination of AppNHp by hydrogen bonds (dashed green lines) and hydrophobic interactions (red rays). **(D)** Illustration of the model-map agreement within a central section of myosin. Most side chains are resolved by the postrefined electron density map (transparent gray).

The high resolution of the electron density map allowed a reliable modeling of actin and myosin including all ligands (Figure 4.10). Besides the Mg^{2+}-ADP and PHD molecules bound to F-actin, AppNHp in the active site of myosin could be clearly identified (Figure 4.10A-B, Supplementary Figure S4). The strength of the corresponding electron density indicates a high to complete saturation of myosin with AppNHp. Interestingly, it also suggests the presence of two ions, which likely both correspond to Mg^{2+} based on the size of the density and the buffer composition. While one ion localizes to approximately the position Mg^{2+} takes in the active site of the strong-ADP state (close to the

γ-phosphate of AppNHp), the other one resides in between the α- and β-phosphate of AppNHp (Figure 4.10B, Supplementary Figure S4). Although the presence of a second ion is unexpected, it is reasonable considering the coordination of AppNHp in the active site (Figure 4.10C). Similar to ADP, AppNHp is coordinated by a network of hydrogen bonds and additional hydrophobic interactions with the P-loop, switch I and A-loop (predicted by PDBSum). The nature of interactions and involved residues however differ, possibly due to the difference in the size of the two nucleotides (also see Figure 4.6C).

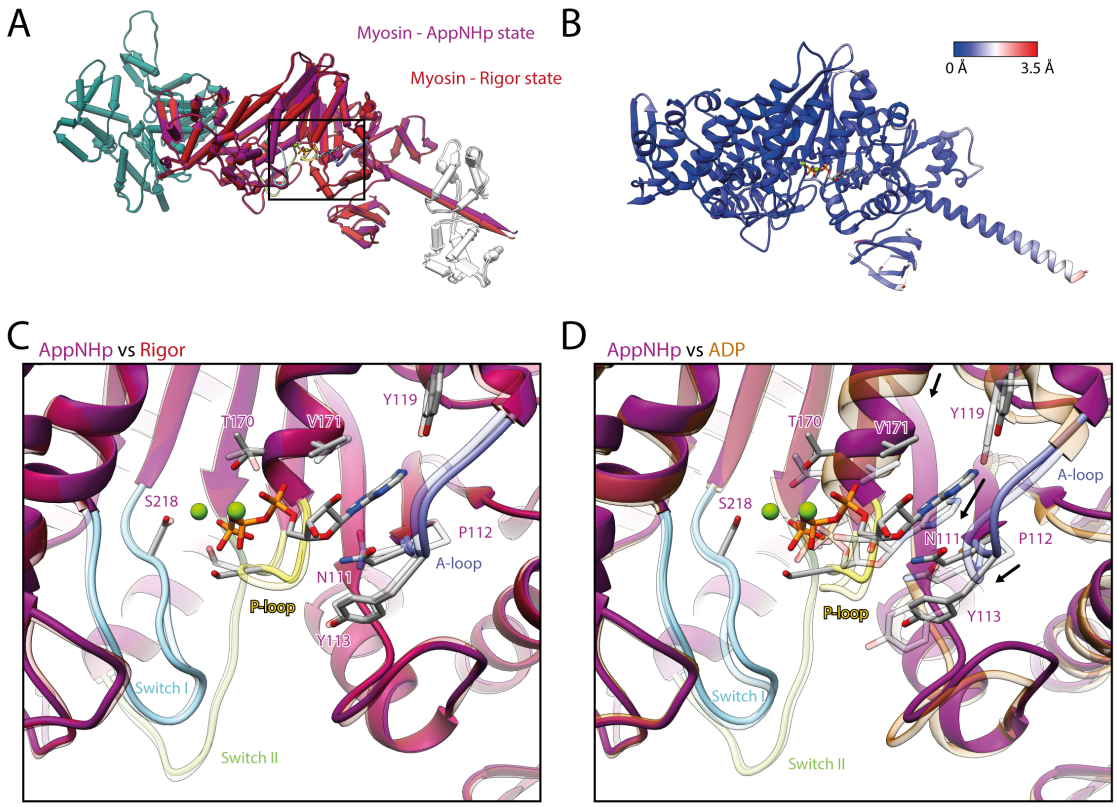

Fig. 4.11: Comparison of the AppNHp structure with the rigor and strong-ADP state. **(A)** Superposition of the atomic models of the rigor state (red) and the AppNHp state (purple), illustrating their close resemblance. **(B)** The root mean square deviation (RMSD) of the backbones of these two structures is remarkably low, with higher values localizing exclusively to regions of lower local resolution. **(C)** Comparison of the active sites of the AppNHp state (purple) and rigor state (transparent red), showing that only small, local changes are associated with the binding of AppNHp. **(D)** The active sites of the AppNHp state (purple) and the strong-ADP state (transparent orange), in contrast, differ markedly including the relative position of the nucleotide. Structural rearrangements due to the binding of ADP are indicated by black arrows. The binding of a nucleotide is consequently not directly linked to a conformational change, but requires a specific coordination. For color code see Figure 4.10.

A comparison of the AppNHp structure with the rigor structure reveals a remarkable similarity (Figure 4.11A-B). The two atomic models superimpose almost perfectly and only small deviations can be found in regions of lower local resolution, such as the lever arm and SH3-like domain (also see Supplementary Figure S3). As these differences can be

readily explained by modeling inaccuracies, we conclude that myosin bound to AppNHp adopts a conformation resembling the rigor state within both our data sets. In line with this, we find a highly conserved actomyosin interface in the AppNHp structure (Supplementary Figure S6).

In contrast to our results, a mixture of pre- and post-powerstroke states was reported for AppNHp bound actomyosin filaments based on a low-resolution cryo-EM study of myosin V (Volkmann et al., 2005). A comparison of the sample preparation protocols reveals only minor differences. In particular, myosin was incubated for 30 min with 1 mM Mg^{2+}-AppNHp in a buffer containing 10 mM imidazole (pH 7.4), 10 mM NaCl, 1 mM $MgCl_2$, 1 mM EGTA, 1 mM DTT and 1 mM NaN_3, before it was used to decorate F-actin on the grid (Volkmann et al., 2005). In this thesis, myosin was only briefly incubated with Mg^{2+}-AppNHp (5 mM AppNHp and 4 mM $MgCl_2$) directly before on-grid decoration of actin (see Sections 3.1.4 and 3.2.2.1). Considering that myosin cannot hydrolyze AppNHp (Yengo et al., 2002) and that we find myosin saturated with AppNHp in our cryo-EM structure, it is yet very unlikely that these differences in preparation give rise to the presence or absence of a pre-powerstroke state. As the resolution of the previous study ($\geq$40 Å) does neither allow the identification of the bound nucleotide nor the analysis of the active site, the structural basis of this discrepancy will probably remain elusive.

The compatibility of the rigor conformation with a bound ATP analog, specifically the presence of a γ-phosphate, is at first puzzling, but becomes evident when comparing the active sites of the rigor, strong-ADP and AppNHp bound state (Figure 4.11C-D). Overall, the active site of the AppNHp structure closely resembles that of the rigor state. Only small local changes, including an upwards movement of the P-loop (residues 164-168) and a lateral shift of the adenosine loop (residues 111-116), are associated with AppNHp binding and do not alter the overall conformation of myosin (Figure 4.11C). In particular, the interaction of lysine K169 with switch I, which specifically stabilizes the rigor conformation (Coureux et al., 2004), is maintained. It is thereby in contrast to the strong-ADP state, where K169 binds the β-phosphate of ADP (Figure 4.6). Generally, the active site of the strong-ADP state differs markedly from those of the AppNHp and rigor states (Figure 4.11D, also see Section 4.5.3). Binding of a nucleotide is consequently not directly linked to a conformational change. Instead, the specific coordination associated with strong nucleotide binding likely initiates the structural rearrangements. A rigor-like crystal structure with ADP weakly-bound to its active site supports this conclusion (Coureux et al., 2004). In this structure, the ADP is coordinated and positioned almost identically to the AppNHp in our cryo-EM structure (Figure 4.12A). This illustrates that a structural transition of the active site towards the strong-ADP conformation is not required for ADP binding (Figures 4.12A, also see Section 4.5.3). Instead, ADP can also bind weakly to the active site of the rigor conformation. Due to the absence of Mg^{2+} in the rigor-like crystal

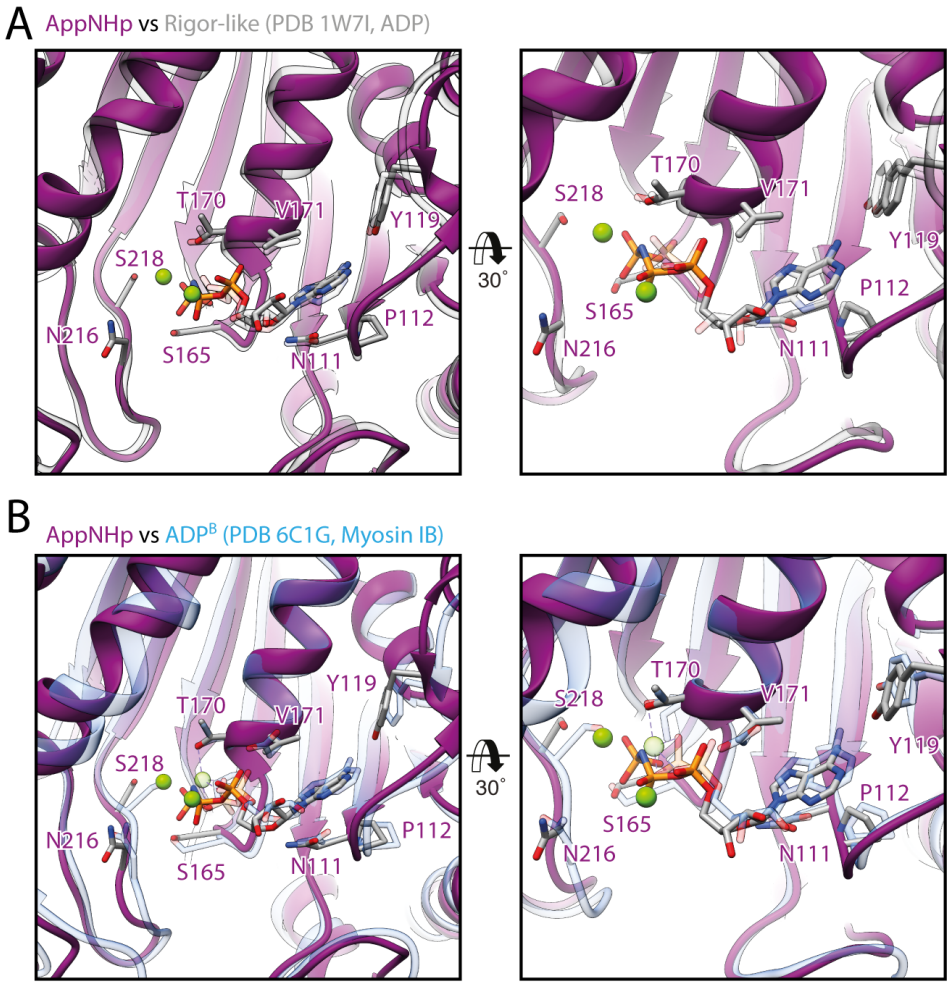

Fig. 4.12: Comparison of the active site of myosin Va bound to AppNHp with the one of ADP-bound rigor-like myosin Va (PDB 17WI, Coureux et al. (2004)) **(A)** and ADP-bound myosin IB in a strong-ADP to rigor transition state (PDB 6C1G, Mentes et al. (2018)) **(B)**. A superposition of atomic models on the HF helix reveals a close resemblance suggesting that the conformation of the active site is characteristic for weak nucleotide binding in general.

structure, loss of Mg^{2+} coordination was suggested to be essential for weak ADP binding (Coureux et al., 2004). The presence of Mg^{2+} in our AppNHp structure and its close resemblance with the crystal structure, however, indicate that the binding strength, i.e., weak or strong, does not solely dependent on Mg^{2+}. Furthermore, weak binding was proposed to be limited to ADP, as the presence of a γ-phosphate would be incompatible with the rigor state (Coureux et al., 2004). Although it is possible that AppNHp can bind in a way that is inaccessible for ATP, for example, because of a higher conformational flexibility of the P-N-P bond, our data suggest that weak binding is also available for ATP. As the aforementioned crystal structure was achieved by soaking pre-formed rigor-like crystals with ADP (Coureux et al., 2004), it is unclear whether this coordination is artificial or represents a possibly short-lived intermediate state within the myosin motor cycle, e.g., during the strong-ADP to rigor transition. A recent cryo-EM study of myosin IB reported

two distinct structural states of myosin bound to ADP (Mentes et al., 2018). While one represents the strong-ADP state, the other is reminiscent of the rigor state. Interestingly, not only does the coordination of ADP within these two states differ from one another, but resembles the one observed in the strong-ADP state and the AppNHp state of myosin V, respectively (Figure 4.12B). The fact that the two ADP states of myosin IB were found in the same cryo-EM sample (Mentes et al., 2018) suggests that the coordination associated with weak-binding of ADP is not artificial but of biological relevance. In particular, the associated structure possibly represent an intermediate along the strong-ADP to rigor transition (Coureux et al., 2004, Mentes et al., 2018). Based on these results, we suggest that AppNHp also gives rise to an intermediate state, which likely localizes between the rigor and the post-rigor state and has a characteristic weak nucleotide binding affinity due to the conformation of the active site. Additional evidence for the genuineness of the AppNHp coordination and the associated myosin structure comes from the way it was prepared. Specifically, myosin was incubated with AppNHp prior to the decoration of F-actin within this thesis (see Section 3.2.2.1) making it unlikely that the rigor state had already formed when the nucleotide bound.

Do our results indicate that AppNHp is a poor ATP analog when it comes to myosin? Biochemical evidence and a previous low-resolution cryo-EM study both suggest that AppNHp is well suited to study weak-binding transition states (Volkmann et al., 2005, Yengo et al., 2002). Although we find a conformation similar to the rigor state for our AppNHp-bound myosin, the high myosin concentration required to fully decorate actin filaments indicates a lower binding affinity (also see Section 3.2.2.1). Based on this, we therefore hypothesize that AppNHp can give rise to different structural states, similar to ADP in myosin IB (Mentes et al., 2018). Differences in the binding affinity for F-actin likely select one state, namely the rigor to post-rigor transition state with AppNHp weakly-bound, over the other(s). Alternatively, or complementarily, AppNHp might cause a fast structural transition resulting in the direct detachment of myosin from actin. In this case, one would only find the transition state bound to F-actin, while myosin in the post-transition state, potentially the post-rigor state, appears unbound in the background of cryo-EM micrographs. In agreement with this assumption, we find a significant amount of unbound myosin in the background of our AppNHp data sets (Figure 4.13A). Finally, we therefore propose that the AppNHp structure represents a transition state between the rigor and the post-rigor state, hereafter referred to as post-rigor transition (PRT) state, in which ATP has already bound weakly, but the structural changes giving rise to detachment from F-actin have not yet been triggered.

To test this hypothesis, we aimed to solve a 3D structure of the background myosin using standard single-particle analysis. Unfortunately, myosin shows a strongly preferred orientation within the amorphous ice layer, impeding all 3D reconstruction attempts (Fig-

ure 4.13B, also see Section 2.4.4). The preparation of new cryo-EM samples is, consequently, indispensable to answer this question. Overcoming the orientation problem will probably require the usage of grids with an additional continuous support layer. While this can solve the orientation problem by reducing interactions with the air-water interface (also see Section 3.2), it simultaneously makes the preparation of grids allowing a high-resolution reconstruction more difficult. This is because additional layers generally reduce the image contrast, which is already weak for myosin due to its rather low molecular weight ($\sim$ 110 kDa). Hence, extensive optimization going beyond the scope of this thesis is required to elucidate if AppNHp-bound myosin in the absence of F-actin adopts the post-rigor state.

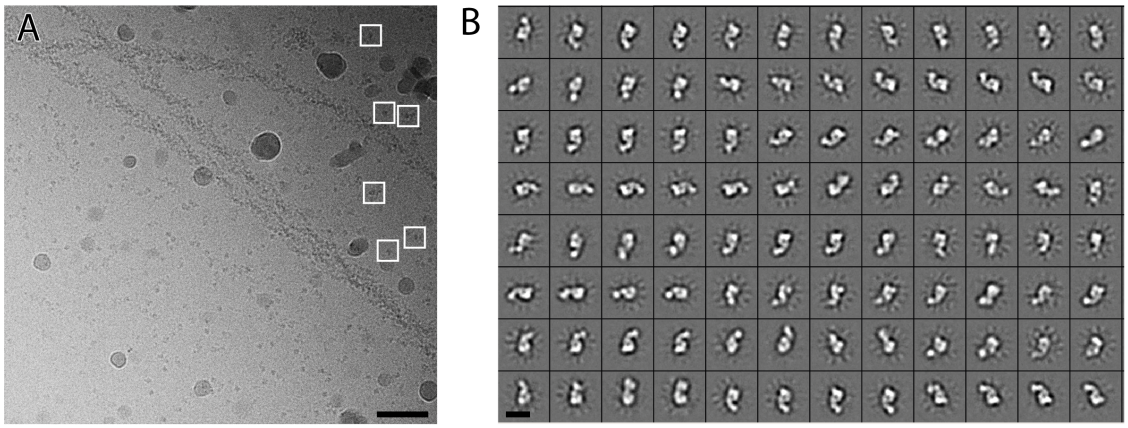

Fig. 4.13: Appearance and preferred orientation of single-particle myosin. **(A)** Representative, contrast-enhanced micrograph of the AppNHp data set (4 °C) with many unbound myosin molecules in the background. Particle boxes (white) are shown for a few particles to highlight their size. Scale bar 500 Å. **(B)** Representative 2D class averages of myosin illustrating its strongly preferred orientation to a single side-view. Scale bar 100 Å.

4.5.5 Myosin-induced structural changes of F-actin

Several studies have reported structural changes of F-actin due to binding of myosin (Behrmann et al., 2012a, Gurel et al., 2017, von der Ecken et al., 2016, Wulf et al., 2016). These include subtle changes, such as shifting of the D-loop and the H-plug by $\sim$1-2 Å (Behrmann et al., 2012a, Gurel et al., 2017, von der Ecken et al., 2016), but also ordering of the N-terminus, which is directly linked to the nucleotide-binding pocket of actin (Banerjee et al., 2017, Behrmann et al., 2012a, Fujii and Namba, 2017, Mentes et al., 2018, Vahokoski et al., 2020, von der Ecken et al., 2016). The conformation of F-actin was, moreover, reported to depend on the state of myosin (Gurel et al., 2017, Wulf et al., 2016). Myosin V, for instance, was shown to alter the twist of F-actin in a nucleotide state dependent manner (Wulf et al., 2016). To further characterize the myosin-induced structural transition of F-actin, the structure of F-actin in the rigor actomyosin complex was

compared to a model of undecorated, aged PHD-stabilized F-actin (PDB: 6T20, Pospich et al. (2020)). The comparison reveals only subtle differences mapping primarily to the D-loop and loops that are known for their flexibility (Figure 4.14, also see Pospich et al. (2020)). The most prominent alteration within the D-loop is glutamine Q49, which moves away from the actomyosin interface by ∼2 Å to enable the formation of a hydrogen bond with N529 in the HLH motif of myosin (Figure 4.14, also see Figure 4.4). An opposite movement was reported for the D-loop of myosin IIC, which orients towards the myosin interface (von der Ecken et al., 2016). The exact structural rearrangements of the D-loop within F-actin thus likely depend on the myosin isoform.

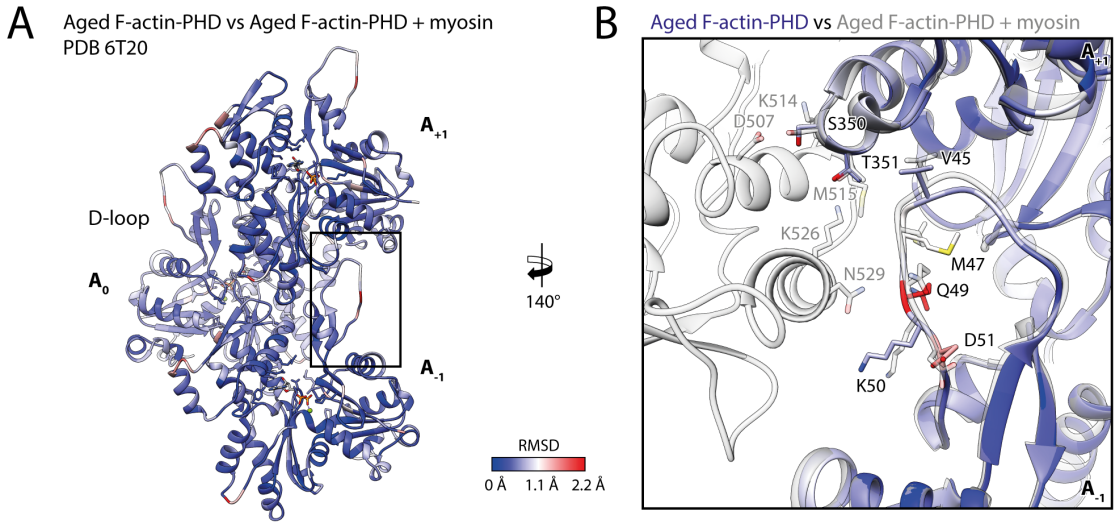

Fig. 4.14: Illustration of the structural similarity of aged PHD-stabilized F-actin in absence and presence of myosin. **(A)** Atomic model of aged F-actin-PHD (PDB: 6T20, Pospich et al. (2020), three subunits shown, A_{-1} to A_{+1}) color-coded by the root mean square deviation (RMSD) of this structure with the one of aged F-actin-PHD decorated with myosin (rigor). **(B)** Close-up view of the D-loop interface. The atomic model of the actomyosin complex is superimposed (transparent gray), illustrating that the changes associated with myosin binding are small. Subunits were aligned individually to account for errors in the calibration of the pixel size.

Interestingly, our data do not indicate any alterations of F-actin linked to the state of myosin. The structure of aged PHD-stabilized F-actin within the presented rigor, strong-ADP and AppNHp-bound post-rigor transition state actomyosin complexes is highly similar. Not only do the actomyosin interfaces superimpose almost perfectly (Supplementary Figure S6), but all inter- and intrastrand interactions are also maintained, suggesting a conserved overall structure of F-actin. The helical symmetry of all structures, furthermore, does not significantly deviate from one another and from undecorated aged F-actin-PHD (Supplementary Figure S11). Minor differences in both the rise (∼0.2 Å) and twist (∼0.3 °) can be readily explained by errors in the pixel sizes of the respective data sets. Inaccuracies in the fitting of atomic models, required to determine the symmetry parameters, can furthermore give rise to small deviations.

The conserved symmetry we observe is in contrast to a previously reported additional twist of 0.8 ° and 0.5 ° for the rigor and strong-ADP state of myosin Va, respectively (Wulf et al., 2016). As PHD was also used to stabilize actin filaments in this study, it does not offer an explanation for the discrepancy. The most likely cause is therefore the helical refinement strategy used to process the 8 Å actomyosin data (Wulf et al., 2016). Although processing was performed with caution and processing of subsets supported the altered symmetry, helical refinement strategies are in general more prone to over-refinement, which may remain concealed at medium-resolution (also see Section 2.4.5). The fact that no change of symmetry was reported for the rigor and strong-ADP states of mysoin IB and VI supports this suggestion (Gurel et al., 2017, Mentes et al., 2018).

Overall, we only find minor structural rearrangements of F-actin upon myosin binding, which do not affect the symmetry of actin or its internal interactions. Simultaneously, we notice an increase in the local resolution of F-actin in the actomyosin complex compared to bare F-actin (Supplementary Figure S3). While this can be solely due to an improved alignment accuracy, it could also reflect a reduced flexibility of F-actin due to myosin binding. In line with this, myosin has been reported to structurally stabilize F-actin (Gurel et al., 2017, von der Ecken et al., 2016).

4.5.6 Nucleotide sensitivity and conformational selection

Myosin V was reported to be sensitive to the nucleotide state of F-actin (Zimmermann et al., 2015). Increased run lengths and landing rates on young F-actin indicate a preference for the structural state associated with ATP/ADP-P_i. As young actin can be primarily found at the barbed end, toward which myosin V walks, this preference is thought to promote its processivity. Interestingly, myosin V was not only shown to distinguish ADP and ADP-P_i F-actin, but also young and aged F-actin stabilized by PHD (Zimmermann et al., 2015). The former gave rise to run lengths resembling those for ADP-P_i actin, thereby suggesting that young PHD-stabilized F-actin can be used to mimic the short-lived ADP-P_i state (Zimmermann et al., 2015). Later cryo-EM structures of young and old PHD-stabilized F-actin showed that the two mainly differ in their conformation of the D-loop C-terminus interface (Pospich et al., 2020) (Section 4.3). Considering that myosin directly interacts with this interface (Figure 4.4), it is tempting to speculate that myosin reads the age of F-actin from the conformation of the D-loop. A similar mechanism was suggested for coronin, based on molecular modeling and TIRF microscopy data (Merino et al., 2018) (Section 4.2).

With the aim to reveal the structural basis of the nucleotide preference of myosin Va, actomyosin filaments consisting of young F-actin and myosin in the rigor state were prepared as described in Section 3.1.4. Specifically, F-actin was trapped in a young, ADP-P_i-bound

state using JASP (see Section 3.1.2). While PHD is also suitable to trap the open D-loop state, its effect is weaker than that of JASP, which stabilizes the open state irrespective of the nucleotide state (Pospich et al., 2020) (Section 4.3). Cryo-EM samples of the actomyosin complex as well as young JASP-stabilized F-actin alone were prepared and imaged in analogy to the rigor state (Supplementary Figure S12). A concise overview of the sample preparation and imaging conditions is given in Table 4.11.

F-actin-JASP	
Sample	∼ 3 µM F-actin and ∼6 µM PHD JASP was added to G-actin before polymerization No extra JASP was added after resuspension of the pellet
Buffer F-actin	10 mM HEPES pH 7.5, 100 mM KCl, 2 mM $MgCl_2$, 1 mM NaN_3, 1 mM DTT, 0.02 % Tween 20
Vitrification	3 µl, no incubation, R2/1 Quantifoils, automatic blotting for 9 s, blot force -15, drain time 0 s, 13 °C, Vitrobot
Data acquisition	Cs-corrected Titan Krios, GIF quantum-energy filter, slit with 20 eV, K2 super-resolution mode, 15 s exposure, 40 frames, total dose 80 eÅ^{-2}, pixel size 1.10 Å, 4er spot scan, defocus range 0.3-2.8 µm
F-actin-JASP + Myosin-rigor	
Sample	∼ 3 µM F-actin, ∼6 µM JASP and ∼ 3.5 µM myosin JASP was added to G-actin before polymerization No extra JASP was added after resuspension of the pellet
Buffer F-actin	10 mM HEPES pH 7.5, 10 mM KCl, 2 mM $MgCl_2$, 1 mM NaN_3, 1 mM DTT, 0.02 % Tween 20
Buffer myosin	10 mM HEPES pH 7.5, 10 mM KCl, 6 mM $MgCl_2$, 1 mM NaN_3, 1 mM DTT, 0.02 % Tween 20
Vitrification	On-grid decoration, 3 µl F-actin, 60 s incubation, R2/1 Quantifoils, manual side blotting, 3 µl myosin, 30 s incubation, automatic blotting for 9 s, blot force -15, drain time 0 s, 1325 °C, Vitrobot
Data acquisition	Cs-corrected Titan Krios, GIF quantum-energy filter, slit with 20 eV, K2 super-resolution mode, 15 s exposure, 40 frames, total dose 80 eÅ^{-2}, pixel size 1.10 Å, 4er spot scan, defocus range 0.6-3.0 µm

Table 4.11: Overview of sample preparation and imaging conditions of bare F-actin-JASP and F-actin-JASP decorated with myosin in the rigor state.

Processing of the actin-only data set yielded a 3.1 Å (central 3er/2er) resolution reconstruction (Figure 4.15, Supplementary Figures S2, S12 and S13). In accordance with our previous structures, we find clear density for not only Mg^{2+}-ADP, but also inorganic

phosphate within the active site (Supplementary Figure S4, also see Sections 4.2 and 4.3). The D-loop C-terminus interface furthermore primarily adopts the expected open conformation, which is defined by an outwards bend D-loop and an extended C-terminus (Figures 4.15 and 4.17A). These hallmarks confirm that we have successfully trapped the desired young state of F-actin.

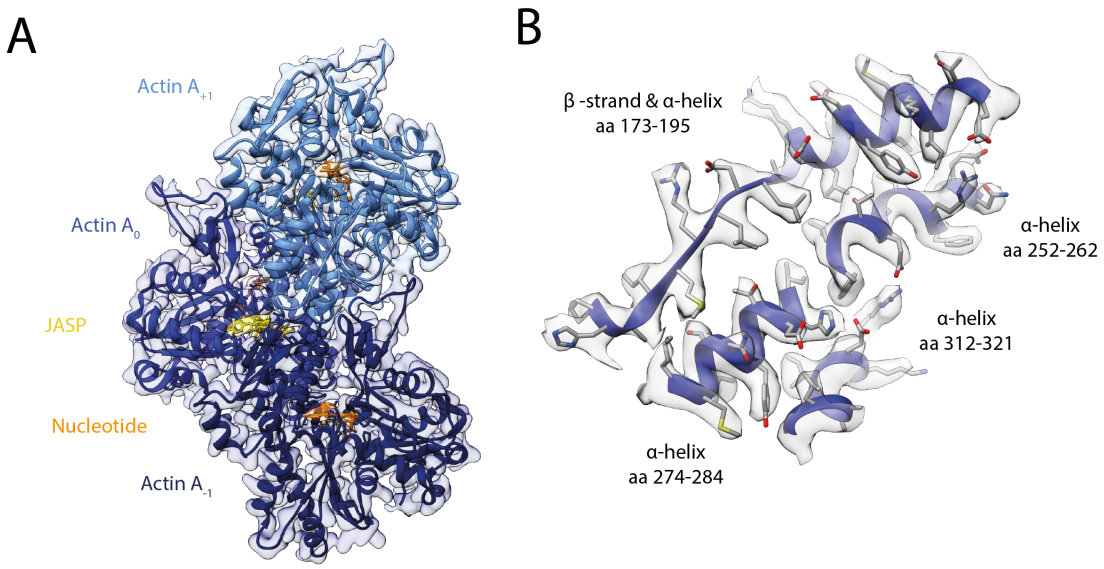

Fig. 4.15: Overview of the structure of young JASP-stabilized F-actin. **(A)** Atomic model and LAFTER electron density map of the central three actin subunits (shades of blue, A_{-1} to A_{+1}). The D-loop primarily adopts the open conformation typical for JASP-stabilized F-actin. Nucleotides and JASP are highlighted in orange and yellow, respectively. **(D)** Illustration of the model-map agreement within a central section of actin. Most side chains are resolved by the postrefined electron density map (transparent gray).

We next solved the structure of the young actomyosin complex to 3.2 Å (central 3er/2er and 1er) using the processing pipeline established for the rigor state (Figure 4.16, Supplementary Figures S2, S12 and S13). In line with the reference structure of F-actin, there is clear density for inorganic phosphate within the active site of F-actin (Supplementary Figure S4). Intriguingly, we simultaneously find an exclusively closed conformation of the D-loop C-terminus interface with a characteristic α-helical C-terminus (Figure 4.16, 4.17B). This is in stark contrast to the open D-loop state of the reference structure (Figure 4.17A-B). As the same F-actin sample was used to prepare the actin-only and actomyosin cryo-EM grids and they were furthermore vitrified within an hour, the altered conformation cannot be due to differences in the sample preparation. We therefore conclude that myosin changes the conformation of F-actin. Specifically, it overrides the effect of JASP, which stabilizes the open D-loop state, and instead selects the closed D-loop conformation (Figure 4.17A-B). A superposition of the atomic models indicates that the open D-loop conformation would not clash with myosin and is thus theoretically compatible with myosin binding (Figure 4.17C). The packing of the actomyosin

interface is, however, more compact for the closed D-loop conformation (Figure 4.17D). Consequently, the closed conformation is possibly selected due to its superior shape complementarity to myosin, eventually facilitating tighter interactions.

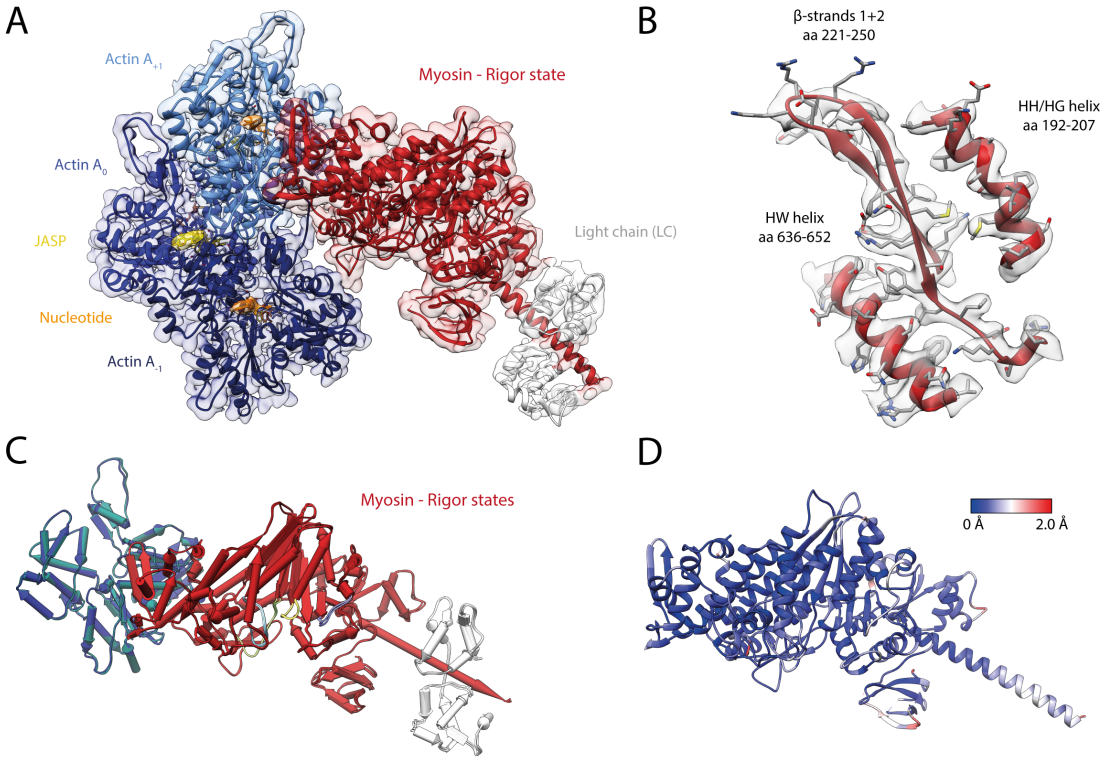

Fig. 4.16: Overview of the structure of the young rigor actomyosin complex. **(A)** Atomic model and LAFTER electron density map of the central myosin molecule (red, LC: white) bound to young JASP-stabilized F-actin (shades of blue, three subunits shown, A_{-1} to A_{+1}). The D-loop solely adopts a closed conformation, despite the presence of JASP. Nucleotides and JASP are highlighted in orange and yellow, respectively. **(B)** Model-map agreement within a central section of myosin. Most side chains are resolved within the postrefined electron density map (gray). **(C-D)** Superposition and color-coded root mean square deviation (RMSD) of the young and old (actin in sea green) rigor actomyosin complex, illustrating their structural identity. Residues with increased RMSD solely localize to regions of lower local resolution and can therefore be explained by modeling inaccuracies.

The structure of myosin in the young rigor complex is basically identical to the one found in the aged rigor complex (Figure 4.16C-D). Only minor differences (RMSD $\leq$ 2 Å) are present in regions of lower local resolution, which can be readily explained by modeling inaccuracies (Figure 4.16D, Supplementary Figure S13). Interestingly, binding of myosin to young JASP-stabilized F-actin solely affects the conformation of the D-loop C-terminus interface (Figure 4.18A-B). The transition to the closed D-loop state requires a large, but isolated shift ($\sim$ 9 Å) of the D-loop tip and the last few residues of the C-terminus. The conformation adapted in this way closely resembles the one of PHD-stabilized F-actin within the aged rigor actomyosin complex (Figures 4.18C-D and 4.1). Based on this result, we propose that myosin specifically selects the closed D-loop state representative

for aged, ADP-bound F-actin. In doing so, it can override the structural effects of both JASP and the P_i bound to the active site. The similarity of the young and aged actomyosin complexes furthermore suggests that the formation of the closed D-loop - HLH motif interface is critical for the high-binding affinity of the rigor state.

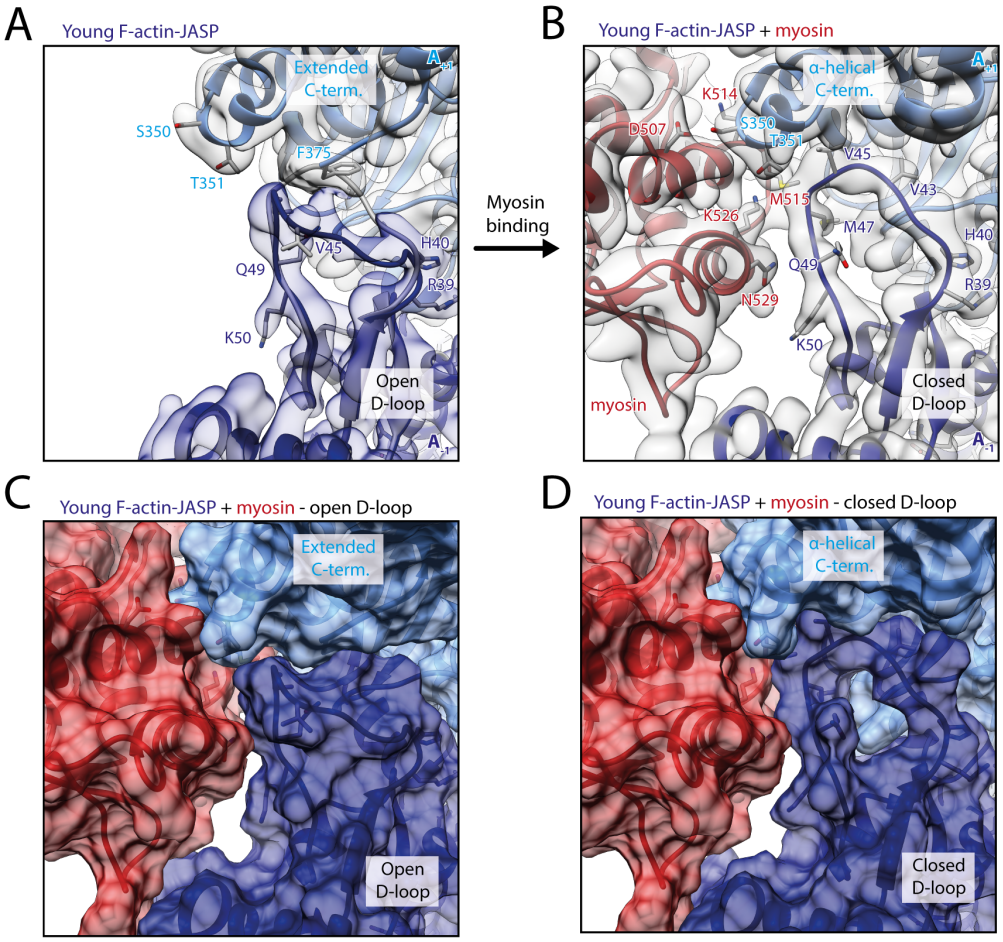

Fig. 4.17: Structural transition of young JASP-stabilized F-actin upon myosin binding. **(A)** Before myosin binding, the D-loop primarily adopts the open conformation and the C-terminus is extended. A superimposed atomic model (gray) highlights a minor density corresponding to the closed D-loop. **(B)** Binding of myosin (red) causes a structural transition to the closed D-loop conformation, which comes with an α-helical C-terminus. **(C)** Surface representation of young JASP-stabilized F-actin (open D-loop, as shown in A) illustrating that the open D-loop conformation would not clash with myosin (computationally docked). **(D)** Surface representation of the young actomyosin complex (closed D-loop, as shown in B).

While the structure of the young actomyosin complex reveals for the first time that myosin selects a specific conformation of F-actin, it unfortunately does not provide a structural explanation for the nucleotide-sensitivity of myosin V (Zimmermann et al., 2015). On the contrary, it even suggests that myosin overrides the nucleotide state of F-actin. The two studies do, however, not generally contradict each other. The open D-loop conformation, which we attribute to the young ADP-P_i state of F-actin, could, for example, promote

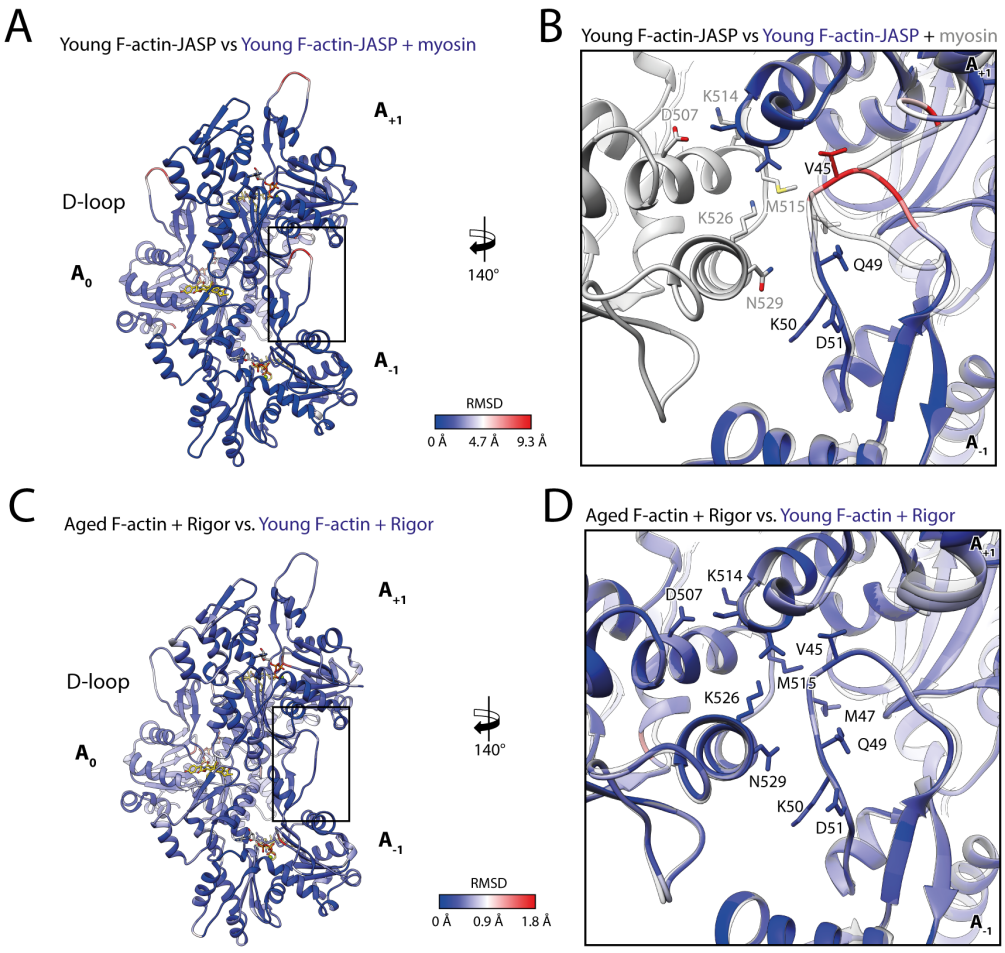

Fig. 4.18: Structural transition of young JASP-stabilized F-actin upon myosin binding. **(A-B)** Root mean square deviation (RMSD) of young F-actin-JASP before and after myosin binding illustrating a major rearrangement of the D-loop and C-terminus. **(C-D)** RMSD highlighting the similarity of myosin-bound, aged F-actin-PHD and young F-actin-JASP. Subunits were aligned individually to account for errors in the calibration of the pixel size.

the formation of an initial contact with myosin. Alternatively, the structural plasticity associated with the open state, rather than the conformation itself, might be beneficial for the binding process. Once initial contacts are established, the subsequent transition from a weak- to a strong-binding state, potentially causes a structural transition of F-actin, eventually locking it in the closed D-loop conformation. This theory is in line with a number of biochemical and biophysical studies suggesting that a structural rearrangement of F-actin and its structural plasticity are critical for proper myosin activity (Anson et al., 1995, Drummond et al., 1990, Kim et al., 2002, Nishikawa et al., 2002, Noguchi et al., 2012, Oztug Durer et al., 2011, Prochniewicz et al., 2010, Prochniewicz and Thomas, 2001). Moreover, both the D-loop C-terminus interface and the HLH motif were predicted to contribute to the initial binding interface (Gurel et al., 2017, Lehman et al., 2013, Risi et al., 2017, Robert-Paganin et al., 2020). Although appealing, this theory can ultimately only be tested by high-resolution structures of weak-binding states.

Our results offer a structural explanation for the quenching of pyrene fluorescence upon myosin binding. Pyrene conjugated to cysteine 374 in the C-terminus of F-actin is a widely used tool to report not only actin kinetics, but also myosin binding (Kouyama and Mihashi, 1981). While closure of the actin binding cleft of myosin is thought to cause fluorescence quenching, the exact timing and the structural basis have not been uncovered yet (Llinas et al., 2015, Robert-Paganin et al., 2020). A recent cryo-EM structure has revealed that pyrene wedges itself between the tip of the D-loop and the hydrophobic groove surrounding it (Chou and Pollard, 2020). In doing so, it displaces the D-loop, pushing it partially out of its pocket. Although its a minor rearrangement, it results in a significantly decreased myosin binding affinity (Taylor, 1991). Quenching of pyrene fluorescence due to the binding of myosin was suggested to be caused by conformational changes that expose the pyrene to the solvent (Chou and Pollard, 2020). If myosin would bind to pyrene-labeled F-actin without altering its structure, it would possibly make the environment of pyrene more hydrophobic, as the HLH-motif is strongly hydrophobic and the contact tight (also see Figure 4.17D). An increase in hydrophobicity, however, would increase the fluorescence, as is the case for actin polymerization (Taylor, 1991). Because of this, a myosin-induced change of the pyrene position is highly plausible. Based on our structural data, we suggest that the pyrene-induced D-loop conformation interferes with the mechanism by which myosin selects the closed D-loop and thereby lowers the binding affinity. Furthermore, we propose that myosin pushes pyrene out of its binding pocket upon its transition to a strong-binding state, thereby quenching its fluorescence. Whether the selection of the closed D-loop state is a prerequisite for the formation of a high-affinity actomyosin interface and if this is also the case for myosins other than myosin Va remains to be investigated.

Finally, the conformational selection we observe for myosin might have implications for the actin cytoskeleton in general. Specifically, myosin could possibly tune the aging process and remodeling of actin filaments by altering their conformation. On the one hand, phosphate release could be fostered by the myosin-induced ADP-like state of F-actin, thereby promoting the aging of actin filaments (Merino et al., 2018). On the other hand, the conformational change of F-actin might additionally affect its interactions with nucleotide sensitive ABPs such as coronin (Cai et al., 2007a, Ge et al., 2014, Merino et al., 2018) and cofilin (Blanchoin et al., 2000, Muhlrad et al., 2006, Suarez et al., 2011). While these proteins cannot bind simultaneously to myosin due to the overlap of their binding sites, it is possible that the myosin-induced closed D-loop state is also maintained once myosin has detached. In this way, it could directly affect the binding of ABPs and hence the remodeling of the actin cytoskeleton. In particular, the myosin-induced closed D-loop state might promote the depolymerization of actin subunits that myosin has already passed on its way to the barbed end. Thereby, recycling of actin subunits and hence the elonga-

tion of actin filaments might be accelerated, facilitating a faster end-to-end cargo transport by myosin. Biochemical studies will be required to test the effect of myosin on both the aging and remodeling of actin filaments.

4.5.7 Pronounced structural heterogeneity

A careful inspection of the electron density maps of all actomyosin complexes reveals a consistently lower map quality of the U50 domain. In particular, the U50 domain is less well resolved than regions within the L50 and N-terminal domain in its proximity, suggesting that a flexibility of this particular domain rather than the complete myosin is causative for the lower resolution. Interestingly, structural flexibility of the U50 domain was also reported for the first medium-resolution cryo-EM structure of the rigor actomyosin complex (Behrmann et al., 2012a). To assess the flexibility of myosin, signal subtracted particles of all four data sets were 3D classified without alignment (Supplementary Figure S2, also see Section 3.3.1.7). The resulting 3D class averages were not reproducible; rather, they strongly depended on the number of classes computed. Furthermore, the mapped conformations only partially overlapped, indicating convergence to different local minima. We therefore conclude that the heterogeneity of myosin in our samples is continuous, in contrast to the discrete conformations reported for myosin IB (Mentes et al., 2018). 3D classification algorithms are generally not well suited to map continuous motion, as they expect a certain number of discrete clusters. For this reason, a neural network based software dedicated to the modeling of continuous distributions recently became available (Zhong et al., 2020a,b). Unfortunately, it proved unsuitable for the processing of our actomyosin data, as it does not support masking and was thus strongly affected by residual densities of the signal subtraction process. For the lack of better alternatives, standard 3D classification was therefore used to map the structural heterogeneity of myosin. The number of classes was manually optimized to yield the highest number of 3D class averages with sufficient detail for atomic modeling ($\leq$3.7 Å). Ultimately, a total of 18 3D classes with resolutions ranging from 3.3 Å to 3.7 Å were reconstructed and modeled for the four independent data sets (aged rigor, ADP, AppNHp and young rigor, see Supplementary Figures S1, S2, S5, S10 and S12 for details).

A superposition of the atomic models of the 3D class averages and the average structure (central 1er) illustrates the conformational heterogeneity of myosin (Figures 4.19A and 4.20A). Interestingly, actin is highly conserved in all structures and states, indicating that

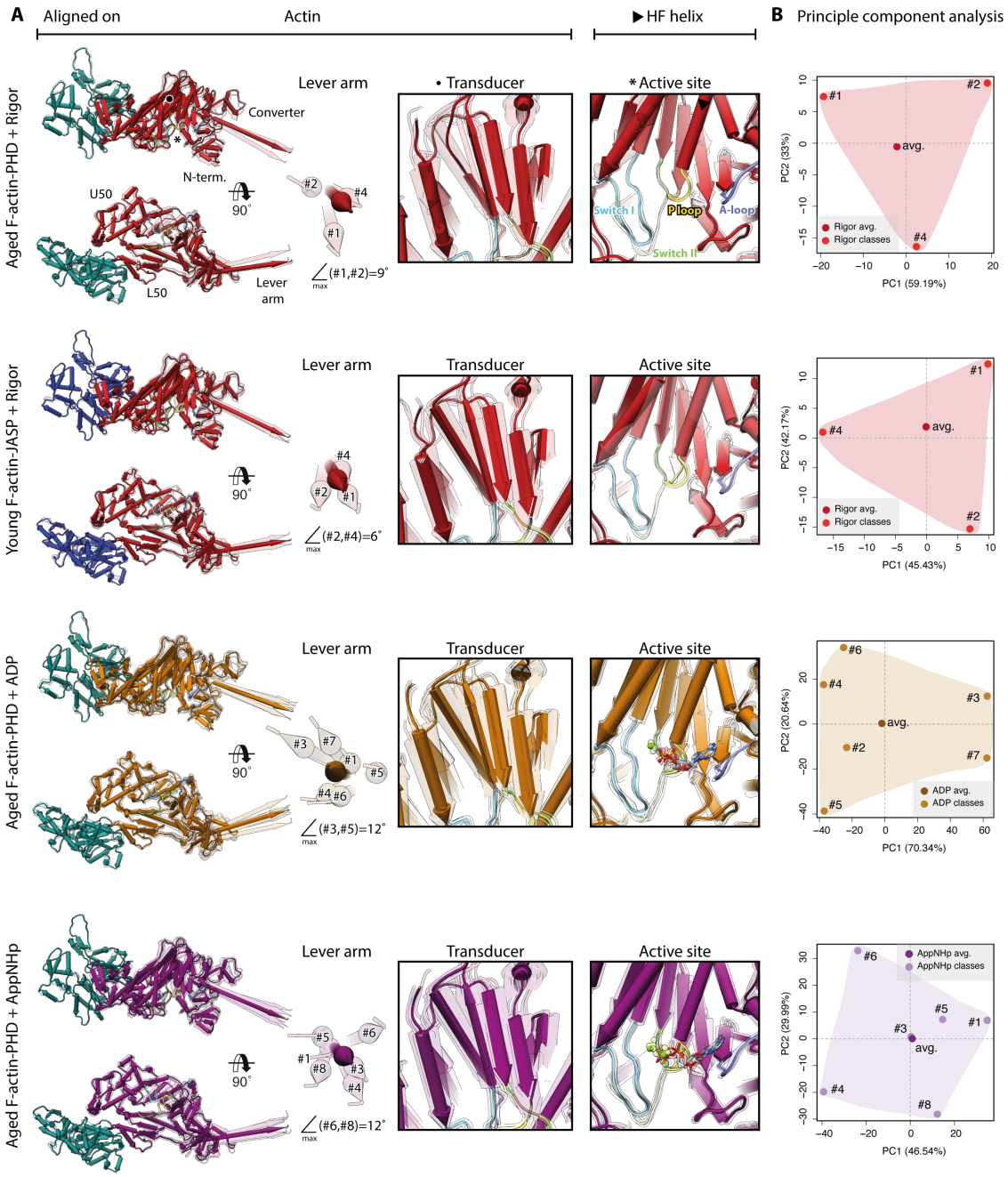

Fig. 4.19: Conformational flexibility of myosin in the rigor (red), strong-ADP (orange) and AppNHp-bound post-rigor transition state (purple). Actin is colored by its age (aged PHD-stabilized: sea green, young JASP-stabilized: blue). **(A)** Superposition of atomic models (average: opaque, 3D classes: transparent) for each state based on either the actin subunit or the HF helix (indicated by black arrow head). Pivoting of the U50 domain causes shifting and twisting of the transducer and eventually a rotation of the N-terminal and converter domain, giving rise to an altered lever arm orientation. The extent of this change depends on the nucleotide state. Inserts show either the transducer β-sheet (black dot) or the active site (asterisk), which is highly conserved within 3D classes. **(B)** Mapping of the average and 3D class average models into the first two principal components of a principal component analysis (PCA), illustrating the overall conformational space covered. Classes are labeled by their number (#1-#8, also see Supplementary Figure S2). For a comparison of conformational extremes see Figure 4.20.

the conformational heterogeneity does not significantly alter the actomyosin interface and thereby the actin filament. In line with this, we find the actomyosin interface well resolved and maintained in all nucleotide states studied in this thesis (Supplementary Figure S6). The L50 domain and especially the HLH-motif, which forms the tightest and largest contact with actin, hardly change between classes. This is in good agreement with the conservation of the HLH-motif within the myosin superfamily and its central role in the binding of actin (also see Section 4.5.1). Conversely, all other domains exhibit conformational flexibility (Figures 4.19A and 4.20A). First and foremost, the U50 domain pivots, thereby moving toward or away from the actin interface. In doing so, it surprisingly does not affect the actomyosin interface, as the changes are absorbed by loops connecting the CM-loop and loop 4 to the U50 domain. A similar rotation of the U50 domain was reported for the medium-resolution rigor structure of myosin IE (Behrmann et al., 2012a), suggesting that the flexibility of this domain is a general feature of myosin. While pivoting of the U50 domain results in slight variations of the cleft opening, it does not affect the conformation of the active site linked to it (Figures 4.19A and 4.20A). Instead, it causes twisting and shifting of the central transducer β-sheet, which is in turn coupled to a rotation of the N-terminal domain and eventually the converter domain. In this way, pivoting of the U50 domain gives rise to different lever arm positions within the 3D classes of a single data set (Figures 4.19A and 4.20A). Generally, this coupling closely resembles the one described for the structural transition upon ADP release (Section 4.5.3). Yet, it seems uncoupled from the active site and the identity of the nucleotide, as we do not find any significant variations in the active site of the 3D classes. Specifically, we do not find evidence for the presence of a nucleotide in the rigor data, mixture of nucleotides in the AppNHp structures or partial release of either Mg^{2+} or ADP in the strong-ADP state. While we cannot exclude that this is due to limitations of the 3D classification algorithm (Pospich and Raunser, 2018), the close resemblance of the active site indicates that the conformational heterogeneity is indeed not directly linked to the nucleotide. Along these lines, a crystal structure with a partially re-primed lever arm without any changes at the active site has been reported for myosin VI (Blanc et al., 2018). Whereas the nucleotide likely does not give rise to the different conformations, it still has an effect on the extent of the flexibility. In particular, we find stronger heterogeneity in the ADP and AppNHp data sets, resulting in a more pronounced alteration of the lever arm position.

The lever arm orientations within the data sets differ by as much as 9 ° in the rigor state and 12 ° in the strong-ADP and the AppNHp-bound post-rigor transition (PRT) states (Figures 4.19A and 4.20A). The extent is intriguing, considering that the lever arm swing associated with ADP-release amounts to only 9 ° for this myosin (Sections 4.5.2-4.5.3). However, not only does the lever arm move in one dimension (the one of the lever arm swing upon ADP-release), but in two dimensions resulting in a distribution of

lever arm conformations around the position within the average structure (Figures 4.19A and 4.20A). A similar movement of the lever arm, i.e., perpendicular to its normal swing direction, due to a flexibility of the converter domain was also reported for myosin IE (Behrmann et al., 2012a).

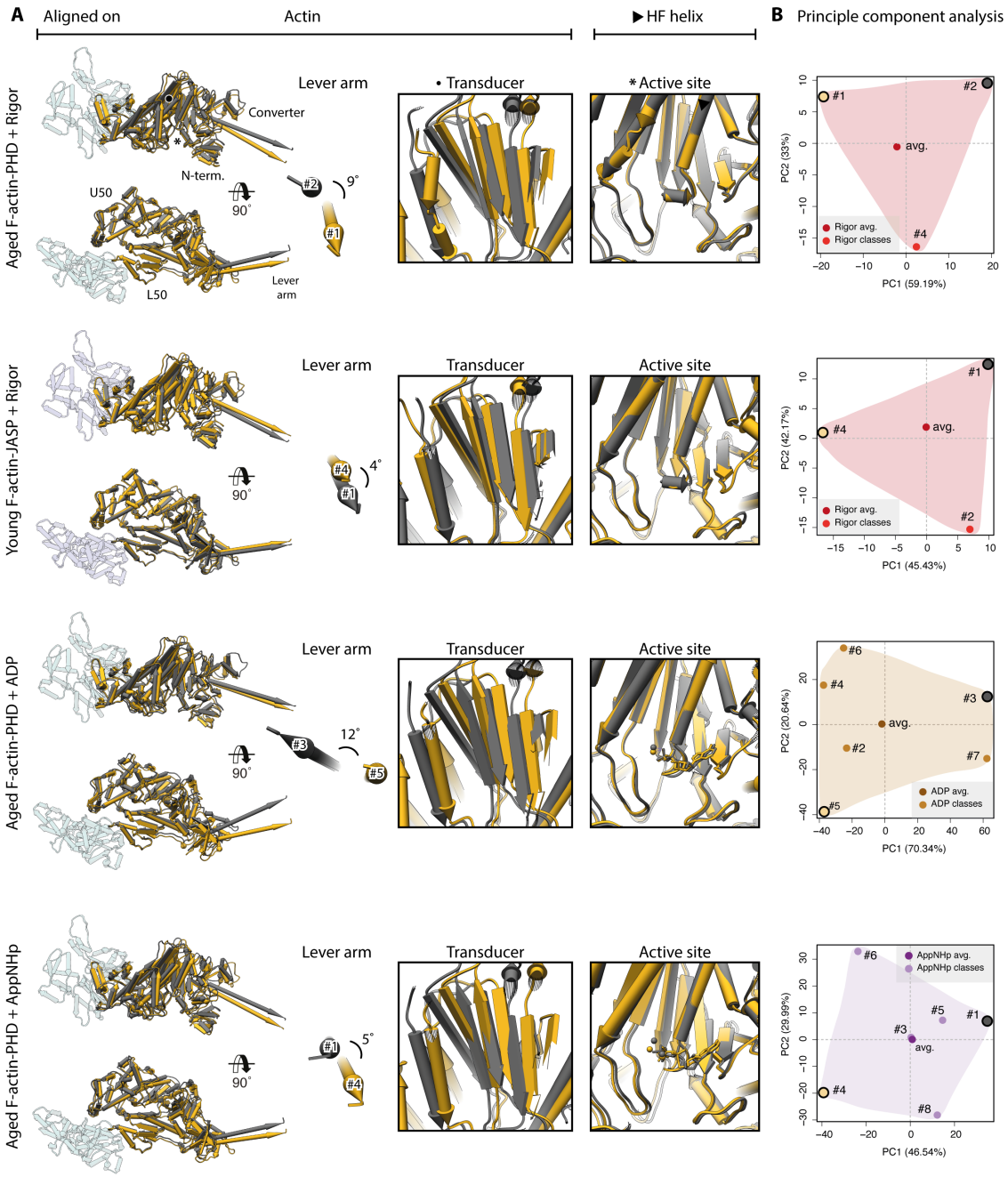

Fig. 4.20: Extreme conformations of myosin in the rigor, strong-ADP and AppNHp-bound post-rigor transition state. **(A)** Same views as in Figure 4.19A but displaying only the extreme structures along the first principal component (yellow and gray). **(B)** Mapping of the average and 3D class models into the first two principal components as shown in Figure 4.19B. The localization of the extreme structures shown in (A) are additionally highlighted (yellow and gray dots).

Not only does the average structure localize to the center of the lever arm distribution, but also represents the average conformation of all other sites of the protein. Consequently, we conclude that the individual 3D classes represent sampling points within the 3D conformational space spanned by the continuous flexibility of myosin. Accordingly, we find the average structure at approximately the center of the cluster mapped onto the first two principal components (PCs) as computed in a principal component analysis (PCA) of all structures of one state (see Section 3.3.3 of methods). The PCA furthermore confirms that both actin and the HLH-motif are highly conserved, as most of their residues were identified as the stable core shared by all structures.

To impartially compare the conformations of the different nucleotide states of myosin, PCA of all models, including averages and 3D classes of the aged rigor, strong-ADP and PRT (AppNHp) states and the young rigor state, was performed (Figure 4.21). In agreement with their structural similarity, the average structures of the PRT state (AppNHp), the aged rigor state and young rigor state localize close to each other along the first three PCs, which account for ∼88 % of the total variations within the data set (Figure 4.21A). Interestingly, the corresponding conformational spaces spanned by all models of these data set (indicated by colored polygons) also co-localize well. Only the conformational space of the PRT state (AppNHp) is significantly larger, in line with the larger extent of conformational changes, e.g., the lever arm swing, observed for this state (Figure 4.21 and 4.19-4.20). This indicates that, although similar to the rigor state, the AppNHp-bound PRT state is not identical to the nucleotide-free rigor state. It furthermore suggests that myosin can possibly adopt different conformations when bound to AppNHp, supporting our hypothesis that AppNHp can give rise to different structural states (Section 4.5.4). The conformational space of the PRT state is, however, extended towards the strong-ADP state (Figure 4.21), and thereby does not provide any evidence for a pre-powerstroke transition state.

In accordance to its distinct conformation, the strong-ADP average structure does not map close to any of the other averages (Figure 4.21A). The large conformational space it covers does additionally not overlap with any other within the first and second PC space. Mapping of the second and third PC, however, reveals a partial overlap with the PRT state conformational space and a minor intersection with the one of the young rigor state (Figure 4.21A). The former is in good agreement with the larger extent of flexibility seen in both the strong-ADP and the AppNHp-bound PRT state (Figure 4.19-4.20).

A comparison of the lever arm positions of all models reflects the result of the PCA (Figure 4.21B). In particular, the average lever arm positions of the rigor and PRT states are alike, while the strong-ADP state differs markedly. In addition, the 2D spaces spanned by the lever arms of each data set relate in a way similar to the conformational spaces in

the PCA. This is not surprising, considering that the first and third PCs map well-defined motions of the lever arm (Figure 4.21B). Along the first PC, the lever arm rotates resulting in a diagonal displacement, whereas the third PC describes an arc movement of the lever arm (Figure 4.21B).

The conformational changes mapped on each PC are well illustrated by both their trajetories and the extreme structures, i.e., the structures localizing to both ends of each PC (Figure 4.21C-D). The motion along the first PC corresponds to pivoting of the U50 domain towards actin and a rotation of the N-terminal and converter domain coupled to it. In this way, these rearrangements cause most of the lever arm movement observed in all structures (Figure 4.21B). Interestingly, the HF helix performs a piston-like movement, resembling the one during the strong-ADP to rigor transition (see Section 4.5.3). Whereas the first PC accounts for $\sim$53 % of the overall variation within the data, the second and third PC only make up $\sim$19 % and $\sim$16 %, respectively. On the first glance, the movement along the second PC resembles the one along the first PC, as it affects the same structural elements (U50, N-terminal and converter domain). Yet, they move in another direction, which is almost perpendicular to the one along the first PC. Specifically, the U50 domain pivots towards the central transducer β-sheet, thereby causing it to shift laterally (Figure 4.21C-D and 4.19-4.20). Thereupon, the N-terminal and converter domains tilt toward the active site, giving rise to a small lever arm displacement. The third PC maps a rotation of the N-terminal and converter domains around the transducer, which acts as a hinge region (Figure 4.21C-D). As this movement is neither associated with the U50 domain nor with the active site, it possibly accounts for the internal flexibility of the transducer β-sheet.

The movements along the PCs, especially the first one, are reminiscent of the structural transition of myosin upon ADP release (Section 4.5.3). The fact that the average structures of the rigor and the strong-ADP state localize to a diagonal in the 2D space spanned by the first and second PC illustrates that the structural transition upon ADP release is indeed composed of conformational changes described by these two PCs (Figure 4.21A). This consequently also indicates that the structural heterogeneity as well as the transition of myosin rely on the same principal mechanism of conformational coupling. In contrast to the other two PCs, movements along the third PC are not related to the strong-ADP to rigor transition. The average structures of all states cluster around the origin of the PC3 axis, thereby indicating that this PC primarily represents variations apparent in the structures of the 3D classes (Figure 4.21A). This is in good agreement with our suggestion that this PC accounts for the internal flexibility of the transducer β-sheet.

Whether the structural heterogeneity we report here is a general feature of the myosin family or a hallmark of myosin V cannot be deduced from our data. Yet, conformational

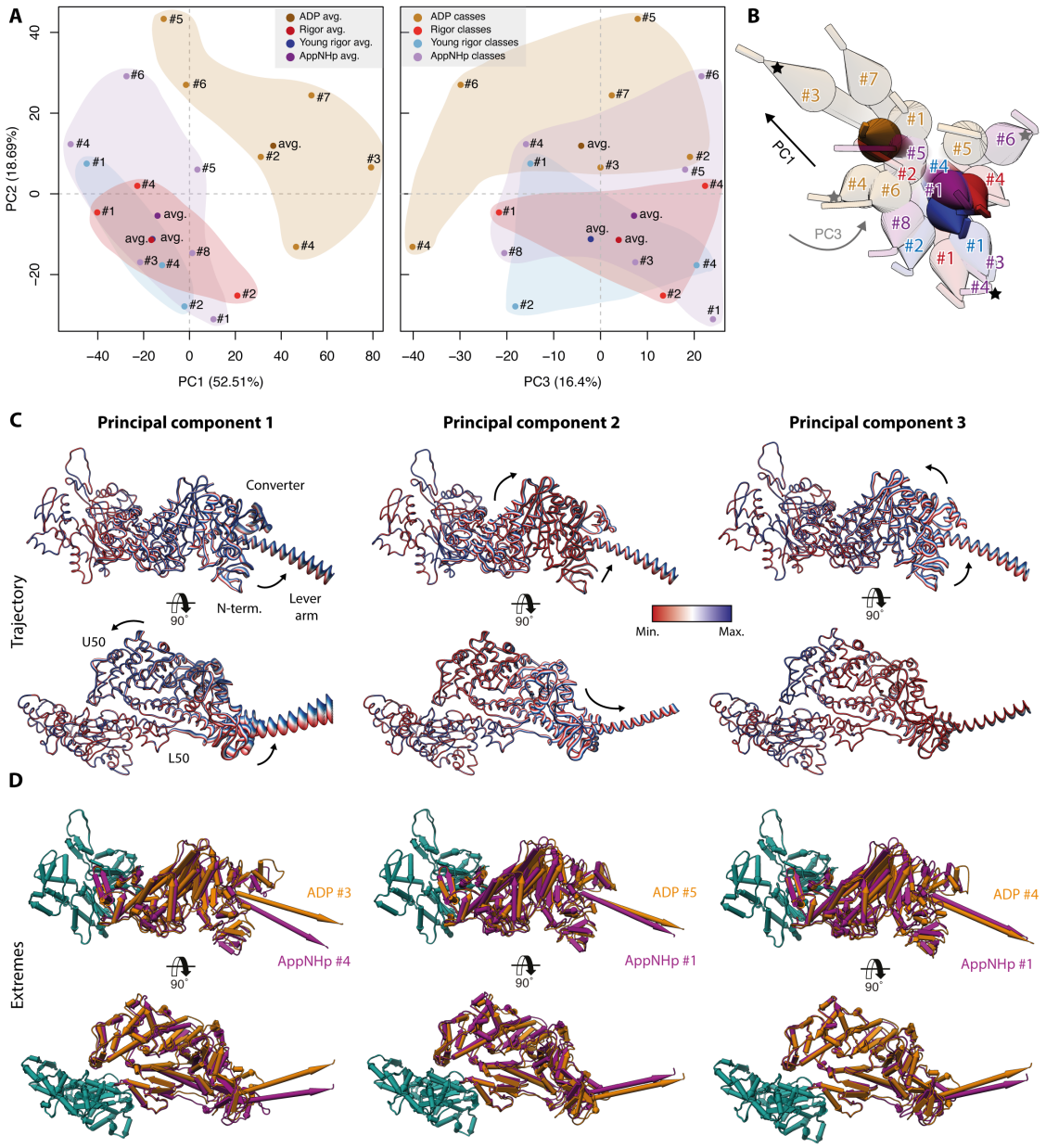

Fig. 4.21: PCA of all myosin structures. **(A)** Mapping of atomic models into the first and second as well as the second and third principal component. Data points are colored by the state of myosin (aged rigor: red, aged strong-ADP: orange/brown, aged AppNHp-bound PRT: purple and young rigor: blue, average structure: opaque, 3D classes: transparent) and conformational spaces indicated by correspondingly colored 2D polygons. **(B)** Superposition of all lever arm positions. Changes along the first and third principal component are highlighted by a black and gray arrow, respectively (extremes marked with asterisks). **(C)** Color-coded trajectories along the first, second and third principal component (red minimum, blue maximum). Arrows indicate the mapped conformational changes. **(D)** Same views as in (C) but showing the extreme structures along each principal component. For color code see Figure 4.19.

flexibility has also been reported for other myosins (Behrmann, 2012, Behrmann et al., 2012a, Mentes et al., 2018). An early medium-resolution cryo-EM study of myosin IE identified several conformational states within a rigor data set (Behrmann, 2012, Behrmann et al., 2012a). Eigenanalysis revealed a pronounced flexibility of the U50, N-terminal and

converter domain, reminiscent of the heterogeneity we observe for myosin Va. As a similar variability of the converter domain is apparent in prepower-stroke crystal structures of myosin IE (Kollmar et al., 2002), the flexibility of the converter domain was suggested to be an intrinsic property of myosin IE (Behrmann, 2012, Behrmann et al., 2012a). Further evidence that the tightly bound rigor state is not rigid comes from biochemical experiments on myosin II (Klein et al., 2008). Site-directed spin labeling indicated a mixture of structural states in the rigor as well as the pre- and posthydrolysis state of myosin. In particular, both open and closed cleft conformations were detected in the rigor actomyosin complex, indicating that the coupling between the nucleotide and structural state is not rigid (Klein et al., 2008). This is not only in good agreement with the overall conformational heterogeneity we observe for myosin Va, but also with our conclusion that binding of a nucleotide does not dictate a discrete structural state (also see Section 4.5.4). In line with this, two distinct states were reported for myosin IB bound to Mg^{2+}-ADP (Mentes et al., 2018). Specifically, differences in the coordination of Mg^{2+}-ADP give rise to either the strong-ADP state or a conformation similar to the rigor state (also see Section 4.5.4). Apart from these two conformations, 3D classifications of signal subtracted particles did not indicate any conformational flexibility in the rigor and strong-ADP state of myosin IB (Mentes et al., 2018). While myosin IB might differ from myosin IE and Va with regard to its rigidity, it is also possible that the processing strategy was not suitable to detect small, continuous changes. On the one hand, the two distinct states in the ADP data set have likely dominated the classification and thereby concealed any flexibility. On the other hand, an extremely low regularization parameter of $T = 2$ ($T = 10 - 40$ suggested by the developers of the software) was used for the classifications, which is likely too conservative to focus on small changes in signal subtracted particles (also see Section 3.3.1.7). The sensitivity of this parameter is representative for the difficulties characteristic for the 3D classification of actomyosin. Generally, it is necessary to isolate a single asymmetric subunit, e.g., the central actomyosin molecule, to analyze the structural heterogeneity. Signal subtraction, which is most suitable method to do so, has only recently been developed and was thus not available in all cryo-EM studies (Bai et al., 2015). Additionally, the separation of especially continuous conformations requires rather large data sets consisting of several hundred thousands of particles. Data sets of this size have only become feasible in the last few years thanks to advances in both software and hardware (also see Section 2.4.6). Lastly, the potential of available 3D classification algorithms is generally limited (Pospich and Raunser, 2018). While changes in multi-protein complexes can usually be determined well, the detection of flexibility within single domains or even smaller structural elements remains challenging. Because of all these reasons, it is quite possible that an existing structural heterogeneity could not be identified for myosin IB as well as other myosins. Considering the described flexibility of myosin IE and II (Behrmann,

2012, Behrmann et al., 2012a, Klein et al., 2008), we therefore speculate that structural heterogeneity is not limited to myosin Va, but a general feature of the myosin superfamily. Future structural and biochemical studies of different myosins will likely bring new insights into the structural flexibility of myosin and its biological function.

Taken together, our data show a pronounced structural heterogeneity of myosin, which originates from several semi-independent conformational changes. Interestingly, the predominant changes and their coupling are reminiscent of the structural changes upon ADP release. We therefore conclude that the structural flexibility we observe is not artificial, but probably of biological relevance for the structural transition of myosin throughout its motor cycle. In particular, we propose that myosin does not adopt a single, distinct conformation, but a thermodynamic ensemble of conformations. The associated conformational flexibility possibly promotes the transition of myosin between structural states, by giving rise to intermediate conformations which are more likely to bind ATP, hydrolyze it or release hydrolysis products, such as P_i and Mg^{2+}-ADP. Once the binding, hydrolysis or release process is initiated, changes at the active site likely trigger a cascade of fast conformational changes, which ultimately result in the structural transition of myosin. The altered "ground" structure and energy finally defines the conformational space of this new state. This model also offers an explanation how applying force to the lever arm might inhibit ADP release. External forces likely restrain the lever arm position and thereby the overall flexibility of myosin. In this way, intermediate conformations promoting the release of Mg^{2+}-ADP might no longer be accessible, i.e., fall outside of the conformational space. A recently published crystal structure of a recovery stroke intermediate and molecular dynamics (MD) simulations of myosin VI support our model (Blanc et al., 2018). The structure illustrates that the lever arm can partially re-prime, while the active site remains open and thereby unchanged from the post-rigor conformation. This in combination with the MD results indicates that the recovery stroke is mostly driven by thermal fluctuations and that the new conformation only eventually gets stabilized by closing of switch II (Blanc et al., 2018). Hence, these findings support our conclusions and collectively suggest that the coupling of the active site and the lever arm is not rigid and potentially of a statistical nature rather than purely mechanic (Blanc et al., 2018). As most insights of the myosin motor cycle come from crystal structures of discrete states, the potential role of thermodynamic fluctuations has hardly received any attention. Future experiments testing the energetic and dynamic landscape of myosin are therefore required to assess if the force-generation by myosin is a thermodynamically-driven process.

4.5.8 Combined structural model of the myosin motor cycle

To fully understand the structural basis of force generation, all states along the myosin motor cycle need to be resolved to high-resolution. The presented cryo-EM structures of myosin Va in the strong-ADP, rigor and AppNHp-bound post-rigor transition (PRT) state represent a major step towards this goal. Structures of the post-rigor (PDB 1W7J, myosin Va, Coureux et al. (2004)) and PPS state (PDB 4ZGW, myosin Vc, Wulf et al. (2016)) have been successfully solved by X-ray crystallography before. Hence, only two states, which are accessible by crystallography, namely the phosphate release (P_iR) and the intermediate recovery stroke states (subsequently referred to as intermediate state), have not been solved for myosin V yet. To fill these gaps, homology models of the two states were computed using Swiss Model (Waterhouse et al., 2018) starting from the crystal structures of myosin VI (P_iR state: PDB 4PJM, Llinas et al. (2015); Intermediate state: PDB 5O2I, Blanc et al. (2018)) and a sequence alignment generated by Clustal Ω (Sievers et al., 2011). Unfortunately, the validity of the resulting homology models is limited, as myosin Va and myosin VI only share ~38 % of their sequence and furthermore have opposite directionality (also see Section 2.3). Yet, the general mechanism and the structural core of both myosins is very similar. Replacement of the unusual lever arm of myosin VI by a conventional one, for example, reverses its directionality making it a "standard" plus-end motor (Bryant et al., 2007, Park et al., 2007). Therefore, changes at the active site of myosin VI are likely representative for all myosins, while their coupling to the periphery and especially to the converter domain and lever arm is unique. Consequently, the computed homology models can only partially fill the structural gaps in the motor cycle of myosin V and their limitations have to be taken into account during any analysis (Figure 4.22). However, even when disregarding the homology models of the P_iR and intermediate state, our three new actin-bound structures make the motor cycle of myosin V the currently most complete cycle available. A comparison of sequential states within the cycle therefore does not only allow a molecular description of key transitions of myosin (Figures 4.23-4.29), but also the proposal of a unified structural model of force generation.

Myosin undergoes complex, multi-domain rearrangements during its motor cycle. Choosing an appropriate reference system for the comparison of structures is consequently critical for the reliable description of structural changes. Due to the high conservation of the L50 domain and especially the HLH motif in all states bound strongly to F-actin, we chose to superimpose all atomic models on the HR (aa 493-514), HS (aa 520-531) and HW helices (aa 635-653) within this domain (Figures 4.23B). While overall structural changes become apparent using this reference, the partially large domain movements make a comparison of the active sites challenging. For this reason, models were imposed on the HF

helix (aa 169-190, trailing the P-loop) when comparing the active sites instead (Figure 4.23B). The comparisons made in this way reveal the conformational changes at both the active site and the actin binding interface, and furthermore indicate how these are coupled

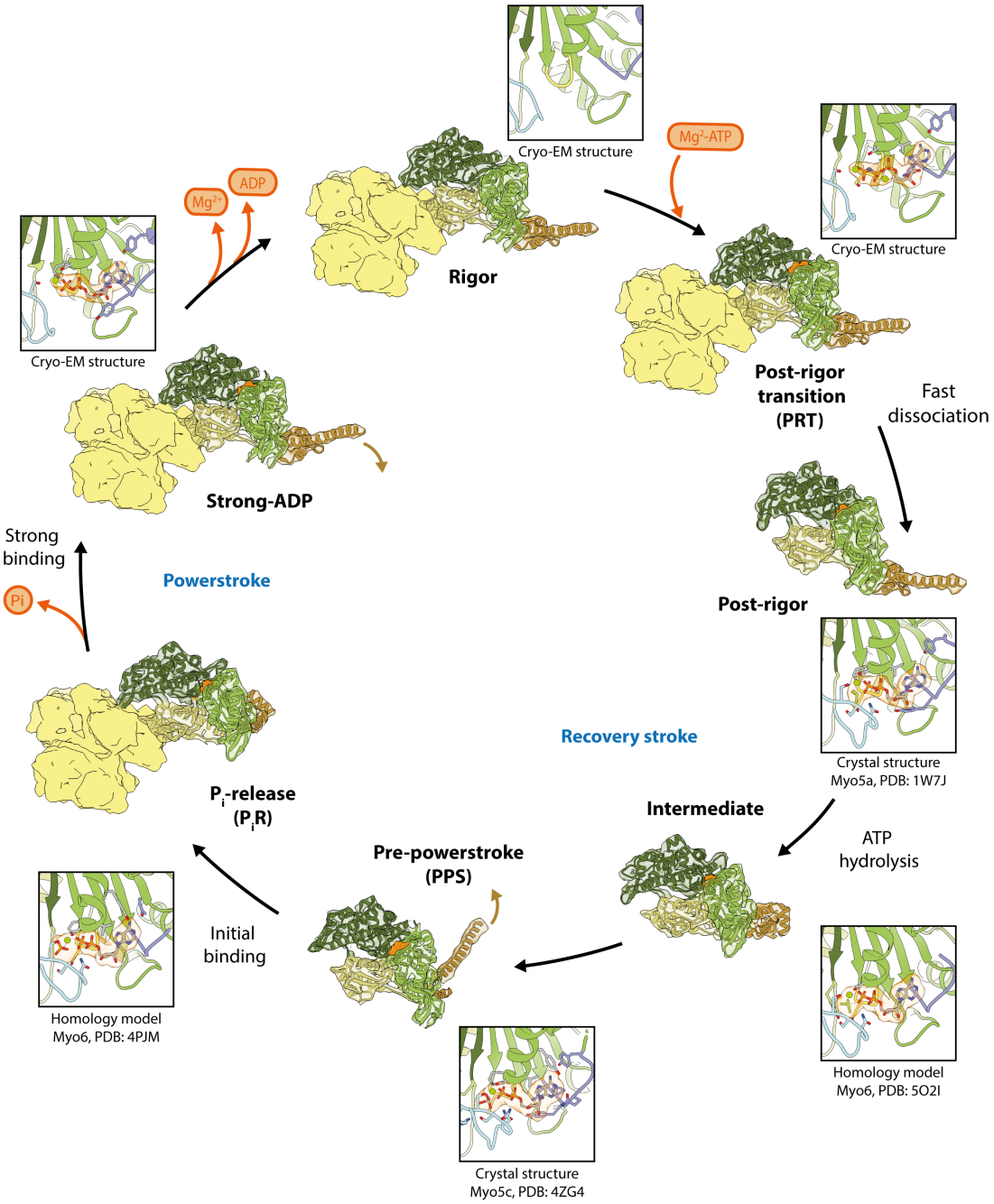

Fig. 4.22: Compilation of all states within the motor cycle of myosin V that have been resolved to high-resolution up to date. The strong-ADP, rigor and PRT state were solved by cryo-EM within this thesis. Crystal structures of myosin Va and Vc have revealed the post-rigor and PPS state, respectively (Coureux et al., 2004, Wulf et al., 2016). The putative intermediate and PiR release states are homology models based on myosin VI crystal structures (Blanc et al., 2018, Llinas et al., 2015). Inserts show the active site of each state, highlighting the nucleotide (orange) and its coordination by the P-loop, switch I, switch II and the A-loop. PDB accession codes are stated below each insert. Densities were simulated from atomic models. For color-code see Figure 2.8 and Supplementary Figure S4.

to the lever arm. An additional, unbiased analysis of domain movements using DynDom (Hayward and Lee, 2002) finally complements the results (only for non-homology models, Figure 4.25). In the following, the conformational changes associated with the structural transition of myosin V along its motor cycle are described individually.

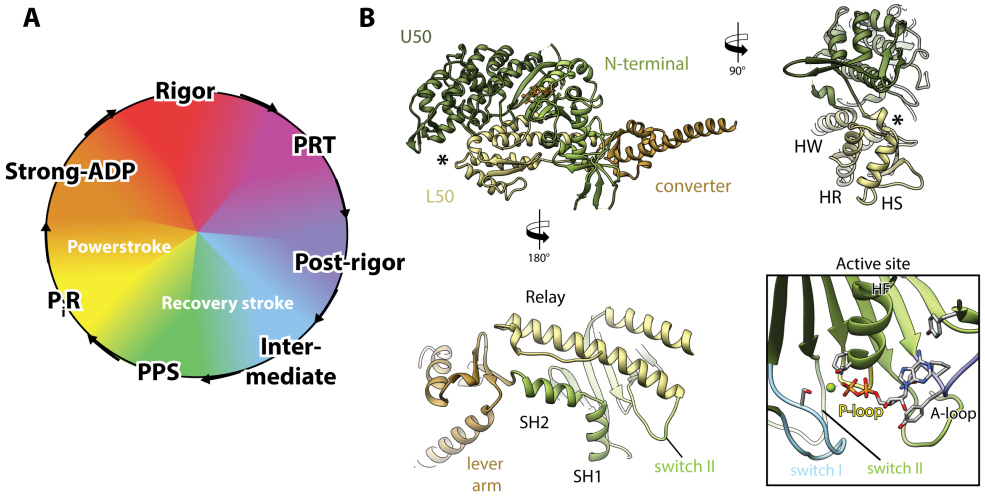

Fig. 4.23: Legend for the illustration of the conformational changes of myosin V during its transition between key structural states shown in Figures 4.24 to 4.29. **(A)** Pictogram of the myosin motor cycle highlighting the rainbow color-scheme used for the depiction of structural states (rigor: red, PRT: purple, post-rigor: slate blue, intermediate: light blue, PPS: green, P_iR: yellow, strong-ADP: orange). **(B)** Color-coded legend of myosin highlighting domains and key structural elements. See Figure 2.8 for an explanation of the color-code.

Rigor to PRT transition In absence of a nucleotide, myosin remains strongly bound to F-actin in the rigor state. ATP binding eventually triggers a cascade of conformational changes, which ultimately result in the detachment from the actin filament (also see Section 3.1.4). Our new AppNHp-bound PRT state structure indicates that ATP binding does not directly trigger the transition to the post-rigor state and thereby loss of affinity for F-actin. Instead, it suggests that ATP initially binds weakly to myosin. By doing so, it gives rise to only small changes of the P-loop and switch I, which are not communicated to other structural elements and thus do not alter the conformation of myosin (Figure 4.24). Specifically, the interactions between the P-loop and switch I (E164&S165-N21) as well as the P-loop and switch II (K169-D437) typical for the rigor state (Coureux et al., 2004) are maintained in the PRT state and prevent high-affinity binding of AppNHp (Yengo et al., 2002). In addition, switch II is still in position to directly interact with the SH1 helix and thereby stabilizes the rigor conformation of the lever arm. The actin binding cleft of myosin remains closed, facilitating strong binding to F-actin. This finding is in contrast to a previous suggestion that the γ-phosphate would act as a wedge inhibiting closure of the major cleft and thereby strong binding to actin (Llinas et al., 2015).

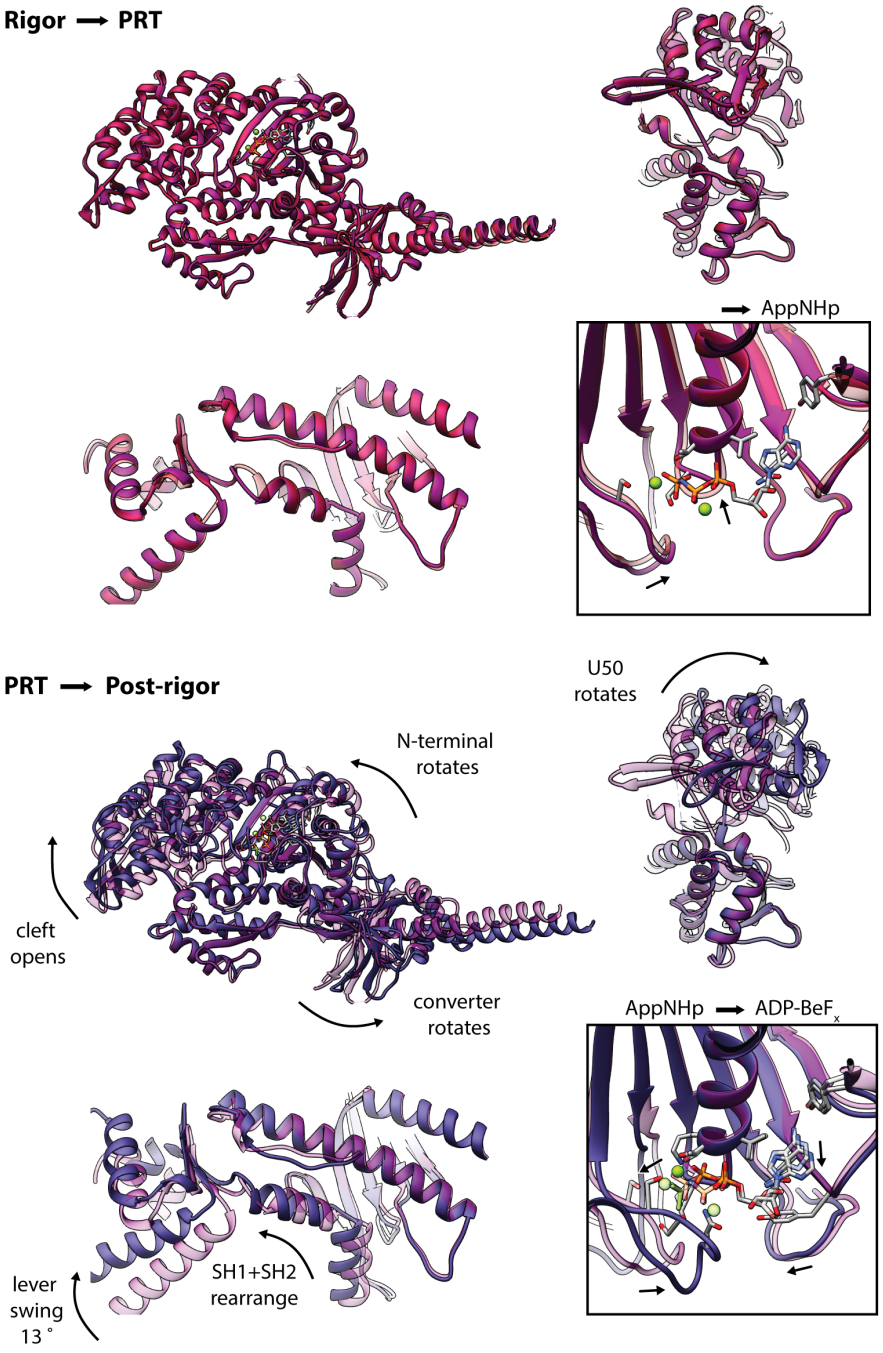

Fig. 4.24: Illustration of the conformational changes of myosin V during its transition between key structural states (Rigor to PRT and PRT to Post-Rigor). Superposition of atomic models of successive structural states along the myosin motor cycle. Models were either aligned on the HR, HS and HW helices (overall conformation) or on the HF helix (active site). The precursor structure is shown as transparent. Major conformational changes are highlighted by black arrows. Structures are shown according to their sequence in the motor cycle from top to bottom and are continued in Figures 4.26 to 4.29. See Figure 4.23 for color code and a legend of key structural elements.

Our AppNHp-bound structure generally indicates that the rigid coupling of all four domains is likely preserved upon initial weak binding of ATP. It thereby highlights that ATP binding alone does not dictate the post-rigor state. Considering this and taking into

account that the post-rigor conformation is incompatible with actin binding, it is questionable whether a theoretical weakly-bound post-rigor state exists (Sweeney and Holzbaur, 2018, Walklate et al., 2016). Instead, myosin might adopt the PRT state as long as it remains bound to F-actin and only eventually transitions to the post-rigor conformation when it has already started to detach, for example, due to thermal fluctuations (also see Section 4.5.7).

PRT to post-rigor transition The transition from weak to strong binding of ATP likely triggers the structural transition to the post-rigor state. A comparison of our structure of the AppNHp-bound PRT state with the post-rigor crystal structure (PDB 1W7J, bound to ADP-BeF_x, Coureux et al. (2004)) reveals that strong binding requires a re-positioning of the nucleotide. Specifically, it sightly rotates around the α-phosphate, so that the purine moiety moves downwards, while the β-phosphate positions closer to the P-loop (Figure 4.24). The phosphate analog BeF_x is furthermore located closer to switch I than the γ-phosphate of AppNHp and the Mg^{2+} ion has shifted towards the β-phosphate to allow binding to both BeF_x and this phosphate. Interestingly, the position of BeF_x is almost identical to the one of VO_4 and close to that of P_i found in crystal structures of other states (Blanc et al., 2018, Coureux et al., 2004, Llinas et al., 2015, Wulf et al., 2016). This indicates that ADP-BeF_x possibly mimics a hydrolysis transition state (ADP-P_i) rather than ATP. Re-positioning of the nucleotide gives, on the one hand, rise to subtle adjustments of the P-loop and the A-loop as well as a small rotation of the N-terminal domain ($\sim$10 °, Figure 4.25). On the other hand, it is accompanied by striking changes of switch I and switch II, which have moved to coordinate the BeF_x (Figure 4.24). In this way, the interaction network of the P-loop, switch I and switch II, which has previously stabilized the rigor state, is broken. As the different nucleotide identity (AppNHp versus ADP-BeF_x) might affect the architecture of the active site, it would be preferable to compare the PRT structure to a post-rigor structure bound to AppNHp or ATP. While such structures are unfortunately not available, a comparison with other crystal structures reveals that the observed changes of switch I and switch II are characteristic for the post-rigor state (Coureux et al., 2004, Fisher et al., 1995).

Switch I and switch II are directly coupled to the U50, L50 and N-terminal domains. Hence, their movements give rise to a number of major structural rearrangements (Figure 4.24), which are facilitated by sliding on hydrophobic patches (Coureux et al., 2004). First, the central transducer β-sheet, which connects all domains to the active site, is distorted. Second, the actin binding cleft opens due to a rotation of the U50 relative to the L50 domain ($\sim$18 °, Figure 4.25) causing the detachment of myosin. Finally, the interface of the relay and the SH1 and SH2 helices is remodeled resulting in a rotation of the converter domain, which culminates in a lever arm swing of $\sim$13 ° almost perpendicular

to the powerstroke direction.

In accordance, the unbiased analysis of domain motions identified a total of four domains which approximately represent the four structural domains of myosin (U50, L50, N-terminal and converter) (Figure 4.25). All four perform semi-independent rotations that result in an overall re-arrangement of domains and the formation of new contacts, for example, between switch I and the P-loop. Interestingly, the identified hinge regions, including the relay and the SH2 helix, the transducer, switch II, the strut and finally loop 1 and loop 2, are well known for their importance in the structural transition of myosin as well as for tuning its kinetic constants (Robert-Paganin et al., 2020). Mutations of loop 1, which connects the U50 domain to the HF helix, for example, affect the rate of phosphate and ADP release (Sweeney et al., 1998).

Post-rigor to intermediate transition Once myosin has detached, another structural transition gives rise to ATP hydrolysis and the recovery stroke, which leaves the lever arm in a primed position (also see Section 3.1.4). The intermediate state is thought to represent a transition state during the recovery stroke and thus possibly indicates how it is initiated (Blanc et al., 2018). A comparison of the post-rigor crystal structure (PDB 1W7J, bound to ADP-BeF_x, Coureux et al. (2004)) with the homology model of the intermediate state (bound to ADP-BeF_x) reveals a close resemblance of the active sites suggesting that the observed conformational changes are meaningful (Figure 4.26). In particular, we observe a small shift of switch II while the rest of the active site, including the position of the nucleotide, basically remains unchanged. Only the purine moiety of ADP slightly shifts upwards. This movement is however reversed in the following transition to the PPS state (Figure 4.26). Thus, it is likely due to a slightly different coordination of ADP in myosin VI. Notably, switch II movement is accompanied by a rearrangement of the interface between the relay helix and helices SH1 and SH2, giving rise to a partially primed converter and lever arm position. Whereas the new conformation of this interface is PPS-like in case of myosin VI (Blanc et al., 2018), it is closer to the post-rigor state of myosin V, highlighting the limitation of this homology model. In addition, we find a rotation of the U50 domain resulting in the partial closure of the actin bindin cleft. Considering that this rotation is opposed to the one taking place during the transition to the PPS state (Figure 4.26), this cleft organization is likely a specific feature of myosin VI rather than a general feature of the recovery stroke. Although the homology model cannot reveal the molecular coupling of this structural transition, the similarity of the active site and the L50 domain still indicates that the recovery strokes of myosin V and VI probably take place in a similar manner. In particular, they are both likely initiated by thermal fluctuations rather than closing of switch II (Blanc et al., 2018).

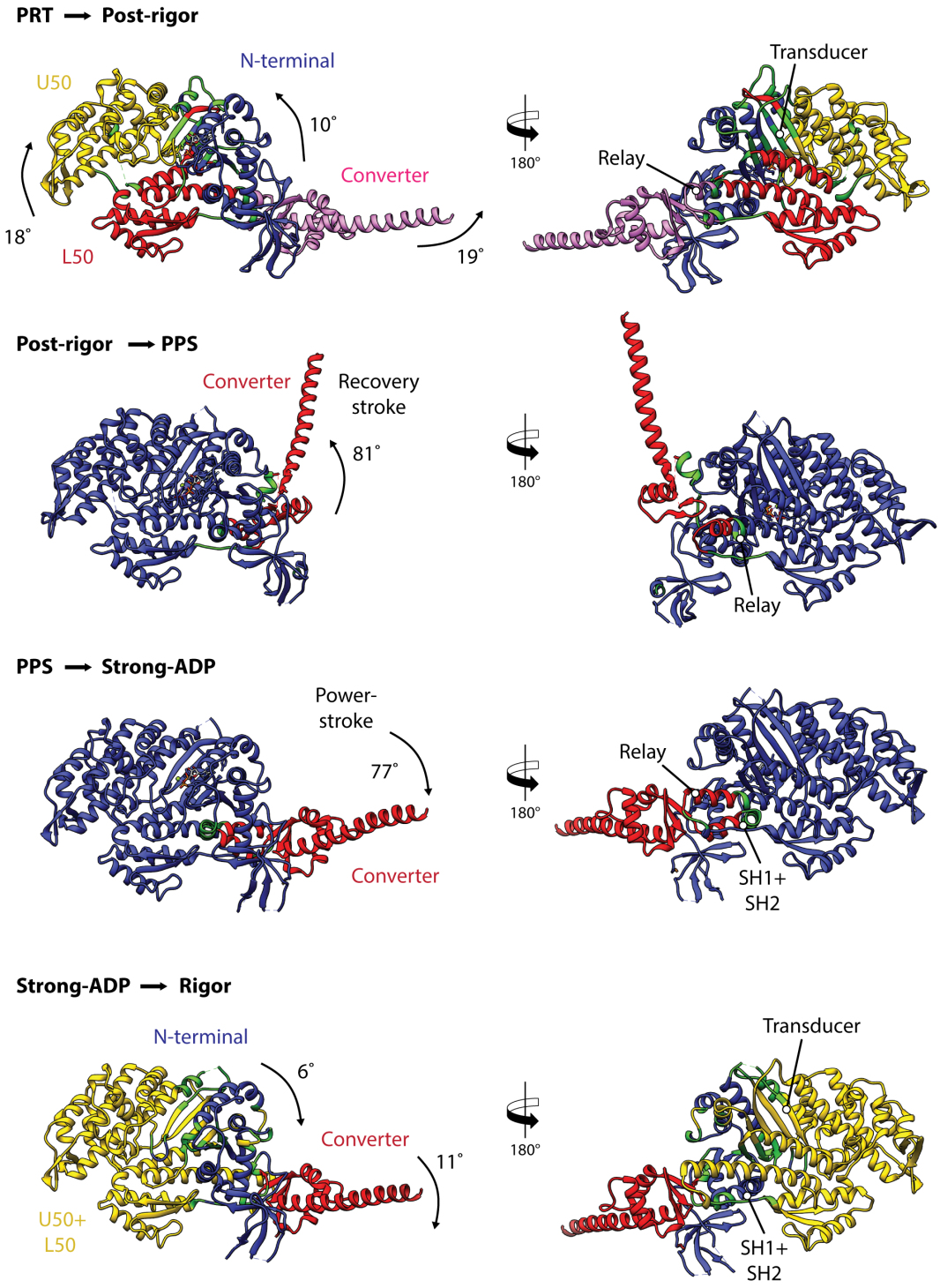

Fig. 4.25: Illustration of the conformational changes of myosin V during its transition between key structural states. Depiction of the domain movements identified by DynDom. Structures are shown according to their sequence in the motor cycle from top to bottom. For simplification only the atomic model of the post-transition state is shown. Hinge regions and bending residues are shown in green, while domains are shown in yellow, red, blue and pink, respectively. Only key structural elements are labeled. See Figure 4.23 for a detailed legend.

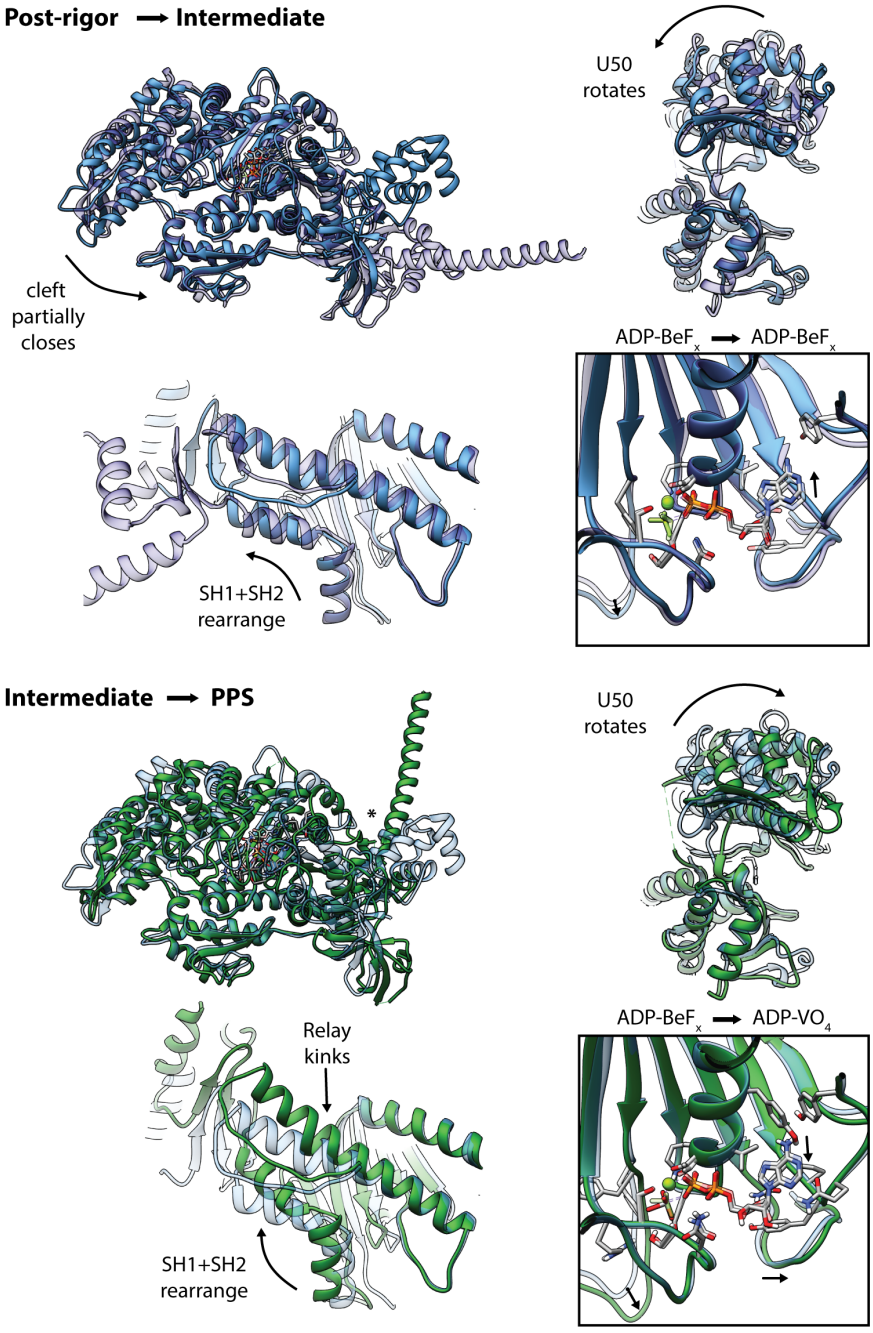

Fig. 4.26: Illustration of the conformational changes of myosin V during its transition between key structural states (Post-rigor to Intermediate and Intermediate to PPS). Superposition of atomic models of successive structural states along the myosin motor cycle; continuation of Figure 4.24. The shown transitions involve a homology model (intermediate state); the implications of this comparison are thus limited. The precursor structure is shown as transparent. The lever arm of the PPS state was computationally elongated (original length indicated by asterisk). Structures are shown according to their sequence in the motor cycle from top to bottom and are continued in Figures 4.27 to 4.29. See Figure 4.23 for legend.

Intermediate to PPS transition The completion of the recovery stroke requires large conformational changes which are well illustrated by a comparison of the intermediate state homology model and the PPS crystal structure (PDB 4ZG4, bound to ADP-VO_4,

Wulf et al. (2016)) (Figure 4.26). In particular, switch II moves towards VO_4 and thereby closes the active site. By doing so, it establishes a geometry promoting hydrolysis involving the formation of a hydrogen bond with VO_4 (G459) and a salt bridge with switch I (E461-R205) (Blanc et al., 2018). Apart from this, the active site organization and localization of the nucleotide remains mostly unchanged with VO_4 taking the position of BeF_x. We only observe a small rotation of the N-terminal domain and a downward shifting of the purine moiety of ADP. The latter is however likely not meaningful as discussed in the previous paragraph. The dominant shift of switch II is coupled to twisting of the transducer β-sheet and kinking of the relay helix. The remodeled interface of this helix with the N-terminal domain and especially the SH1 and SH2 helices results in a major rotation of the converter domain. In the course of this, the lever arm performs the recovery stroke.

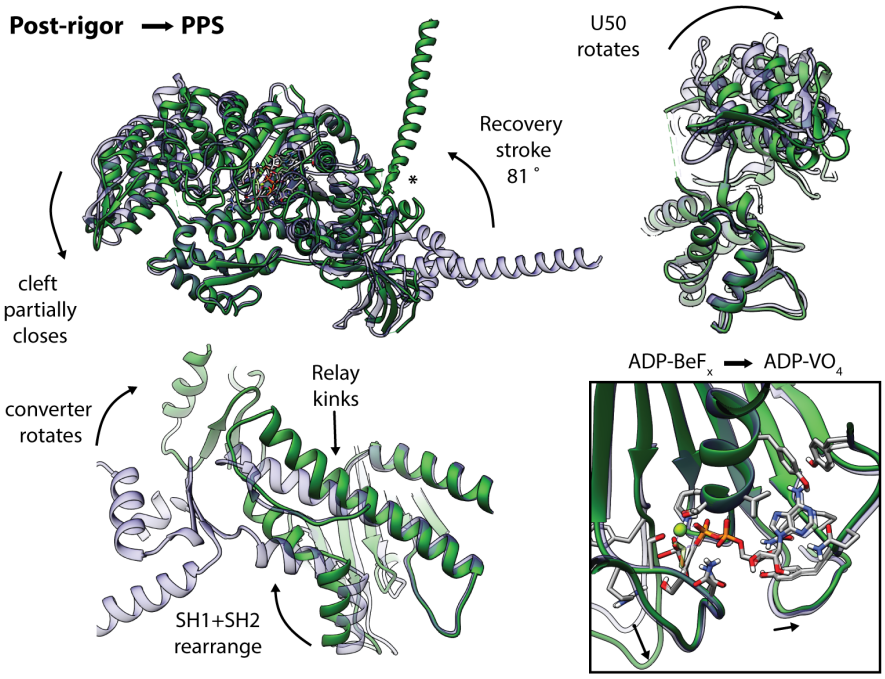

Fig. 4.27: Illustration of the conformational changes of myosin V during its transition between key structural states (Post-rigor to PPS). Superposition of atomic models of successive structural states along the myosin motor cycle; continuation of Figures 4.24 to 4.26. The precursor structure is shown as transparent. The lever arm of the PPS state was computationally elongated (original length indicated by asterisk). Structures are shown according to their sequence in the motor cycle from top to bottom and are continued in Figures 4.28 to 4.29. See Figure 4.23 for legend.

Post-rigor to PPS transition As the validity of the intermediate state homology model is limited, we have also directly compared the post-rigor (PDB 1W7J, bound to ADP-BeF_x, Coureux et al. (2004)) and the PPS state (PDB 4ZG4, bound to ADP-VO_4, Wulf et al. (2016)) (Figure 4.27). The apparent conformational changes are reminiscent of those identified based on the comparison with the intermediate state. Specifically, we find

a similar small rotation of the N-terminal domain and a closure of switch II, while the rest of the active site, even the orientation of side chains, remains conserved. The absolute shift of switch II is, however, larger in the post-rigor to PPS transition, as switch II adopts an in between position in the intermediate state. The transducer is twisted and the relay helix is kinked to avoid a clash with the SH1 helix (Coureux et al., 2004). In this way, a new interface between the relay helix and the SH1 and SH2 helices is formed resulting in a rotation of the converter domain. This in turn gives rise to the recovery stroke consisting of a lever arm rotation of $\sim$81 $^\circ$ toward its primed position. While the nature of all these conformational changes also became apparent in the comparison of the intermediate and the PPS state, we find an additional rotation of the U50 domain causing a partial cleft closure in this comparison, which probably has remained concealed before due to the limitations of the homology model. This change was also not recognized in the computational analysis of domain motions, which only shows a rotation of the converter domain around the kink in the relay helix (Figure 4.25).

Intriguingly, the changes at the active site as well as the overall domain movements associated with the recovery stroke are small compared to the ones upon detachment from F-actin in the post-rigor state (Figures 4.24 and 4.25). In particular, the recovery stroke is primarily coupled to closing of switch II, while changes of both switch I and switch II give rise to a reorganization of basically all domains in the post-rigor state. Yet, this domain rearrangement is only associated to a small swing of the lever arm, in contrast to the large $\sim$81 $^\circ$ rotation during the recovery stroke. This opposition highlights, on the one hand, the complexity of the mechanochemical coupling within myosin, which facilitates semi-independent motions of the single domains. On the other hand, it showcases the pronounced effect of actin binding on the overall structure of myosin. Finally, it indicates a rigid mechanical coupling of the actin binding site to the other domains, in contrast to the suggested statistical coupling of the active site and the lever arm (Blanc et al., 2018).

PPS to P_iR transition Initial weak binding of the PPS state to F-actin is thought to trigger the transition to the P_iR state, which likely precedes the powerstroke (Llinas et al., 2015, Robert-Paganin et al., 2020). Although the validity of the homology model of the P_iR state (bound to ADP-P_i) is limited because of the aforementioned reasons, a comparison with the preceding PPS and succeeding strong-ADP state illustrates that the P_iR model indeed represents an in between conformation (Figure 4.28). This is in line with mutational studies showing that myosin II, V and VI use the same mechanism to release P_i from their active site (Llinas et al., 2015). The active sites of the PPS and P_iR structures are almost identical with P_i taking the position previously occupied by VO_4. Only switch II moves out of the active site and thereby opens an exit tunnel for the phosphate. Coupled to the shift of switch II is a rotation of the U50 domain, which results in a

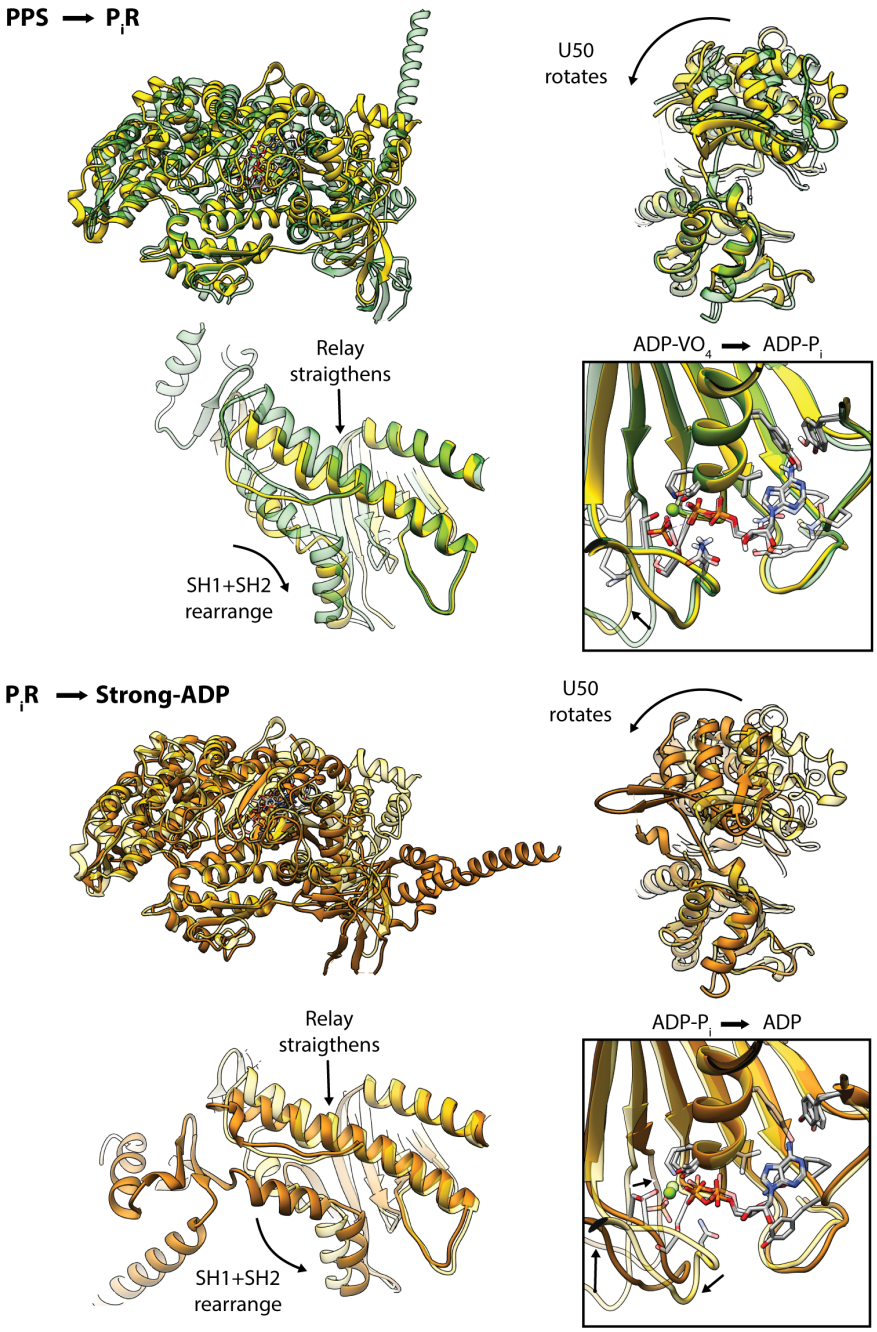

Fig. 4.28: Illustration of the conformational changes of myosin V during its transition between key structural states (PPS to P_iR and P_iR to Strong-ADP). Superposition of atomic models of successive structural states along the myosin motor cycle; continuation of Figures 4.24 to 4.27. The shown transitions involve a homology model (P_iR state); the implications of this comparison are thus limited. The precursor structure is shown as transparent. The lever arm of the PPS state was computationally elongated (original length indicated by asterisk). Structures are shown according to their sequence in the motor cycle from top to bottom and are continued in Figure 4.29. See Figure 4.23 for legend.

partial closure of the actin binding cleft. While the extent of this rotation likely depends on the myosin isoform, it is thought to be essential for actin binding as the open conformation seen in the PPS state does not allow a stereo-specific contact (Llinas et al., 2015). Opening

of the P_i exit tunnel, moreover, causes partial straightening of the relay helix and the formation of a new interface with the SH1 and SH2 helices and the N-terminal domain. Although this remodeling partially reverts the conformational changes giving rise to the PPS state, it was reported to alter the transducer β-sheet as well as the converter domain only minimally, in this way leaving the lever arm in its primed position. Because of the overall conservation of the conformation, P_i can re-enter the active site and cause re-isomerization to the PPS state in absence of load (Llinas et al., 2015). Interestingly, a second phosphate binding site consisting of S153, T197, S203 and E461 was identified at the mouth of the exit tunnel, were P_i possibly remains bound until the powerstroke has completed (Llinas et al., 2015).

P_iR to strong-ADP transition While the P_iR state possibly represents the first force-generating state with a considerable binding affinity for F-actin, complete closure of the actin binding cleft is necessary to achieve the high binding affinity required to keep myosin from detaching during the powerstroke (Llinas et al., 2015, Robert-Paganin et al., 2020). Based on the crystal structure of the P_iR state, release of P_i from the active site was suggested to trigger both cleft closure and the powerstroke (Llinas et al., 2015). A comparison of the P_iR homology model with our cryo-EM structure of the strong-ADP state reveals the underlying structural changes of this key transition (Figure 4.28). Loss of P_i, on the one hand, results in a slight re-positioning of the α- and β-phosphates as well as the Mg^{2+} ion towards the P-loop. On the other hand, both switch I and switch II change their position as their conformation is no longer stabilized by interactions with P_i. In particular, switch I shifts downward to coordinate the Mg^{2+} ion, while switch II moves closer to the P-loop thereby facilitating the formation of two new hydrogen bonds (Y439-G164, D437-T170, also see Section 4.5.2). The concerted movement of both switches is directly coupled to the closure of the actin binding cleft as well as the powerstroke. Specifically, the changes give rise to a distortion of the transducer β-sheet and eventually a major rotation of the U50 domain relative to the L50 domain resulting in the closure of the actin binding cleft. Simultaneously, the relay helix fully straightens and the SH1 and SH2 helices rearrange to form a interface reminiscent of the rigor conformation. As a consequence, the converter domain performs a large rotation which gives rise to the force-producing lever arm swing known as powerstroke.

PPS to strong-ADP transition To verify the conformational changes identified based on the P_iR homology model, we have also directly compared the PPS crystal structure (PDB 4ZG4, bound to ADP-VO_4, Wulf et al. (2016)) and the strong-ADP state cryo-EM structure (Figure 4.29). The overall conformational changes are very similar endorsing the validity of the P_iR homology model. The rearrangements at the active site are basically

identical to the ones described before. Only the absolute shift of switch II is different, as it adopts an altered conformation in the P_iR state to allow phosphate release. Apart from this, we find an analogous transducer distortion and rotation of the U50 domain, which gives rise to closure of the actin binding cleft. Finally, this comparison also supports the straightening of the relay helix and the rearrangement of the SH1 and SH2 helices relative to it. While all of these hallmarks were readily identified based on the homology model, an additional rotation of the N-terminal domain, which probably also supports the lever arm swing, has remained concealed. This is not unexpected, as the homology model is based on a crystal structure of myosin VI, which does not share its domain coupling with myosin V. Based on these results, we suggest that straightening of the relay helix and the rotation of the N-terminal domain, which is possibly caused by the rearrangement of the SH1 and SH2 helices, induce the rotation of the converter domain in a concerted fashion. As a consequence, the lever arm performs the force-generating powerstroke which is characterized by a $\sim$77 $^\circ$ rotation. This result is in good agreement with the computational analysis of domain motions, which also indicates a $\sim$77 $^\circ$ rotation of the converter domain around the relay and SH2 helices (Figure 4.25). Interestingly, a smaller rotation of 58 $^\circ$ has been proposed earlier based on a medium-resolution cryo-EM structure of the strong-ADP state (Wulf et al., 2016). As the same PPS crystal structure was used to calculate the angle of the lever swing, the discrepancy might be due to the limited resolution ($\sim$7-9 Å), which has possibly hampered the modeling of the lever arm. This is, however, contradicted by the fact that the angle of the lever swing associated with ADP release, which was computed based on the same cryo-EM structure, matches our high-resolution results perfectly (also see Section 4.5.2). The difference might therefore rather originate from the way the rotation angle was measured, than the resolution itself.

Surprisingly, the computational domain analysis did not detect the closure of the actin binding cleft, despite the large rotation of the U50 domain associated with it (Figure 4.25). The analysis of the PRT to post-rigor transition has demonstrated that the software is able to detect cleft opening and therefore theoretically also cleft closure (Figure 4.25). That the closure was yet not identified, indicates that the underlying motions can possibly not be described by semi-independent domain movements and consequently might be less concerted than the ones of the post-rigor transition. One possible explanation for this observation could be that the six actin binding elements (HLH motif, activation loop, CM loop, loop 2, loop 3 and loop 4, also see Section 4.5.1) cause local deformations that partially uncouple the domain motions.

The domains and hinge regions identified are reminiscent of the ones found for the post-rigor to PPS transition (Figure 4.25). Additionally, the motions of the converter domain are opposite, so that the rotation of the lever arm is almost completely reversed. Based on this, we conclude that the recovery stroke and the powerstroke likely rely on the same

coupling mechanism, which is in particular characterized by the kinking and straightening of the relay helix.

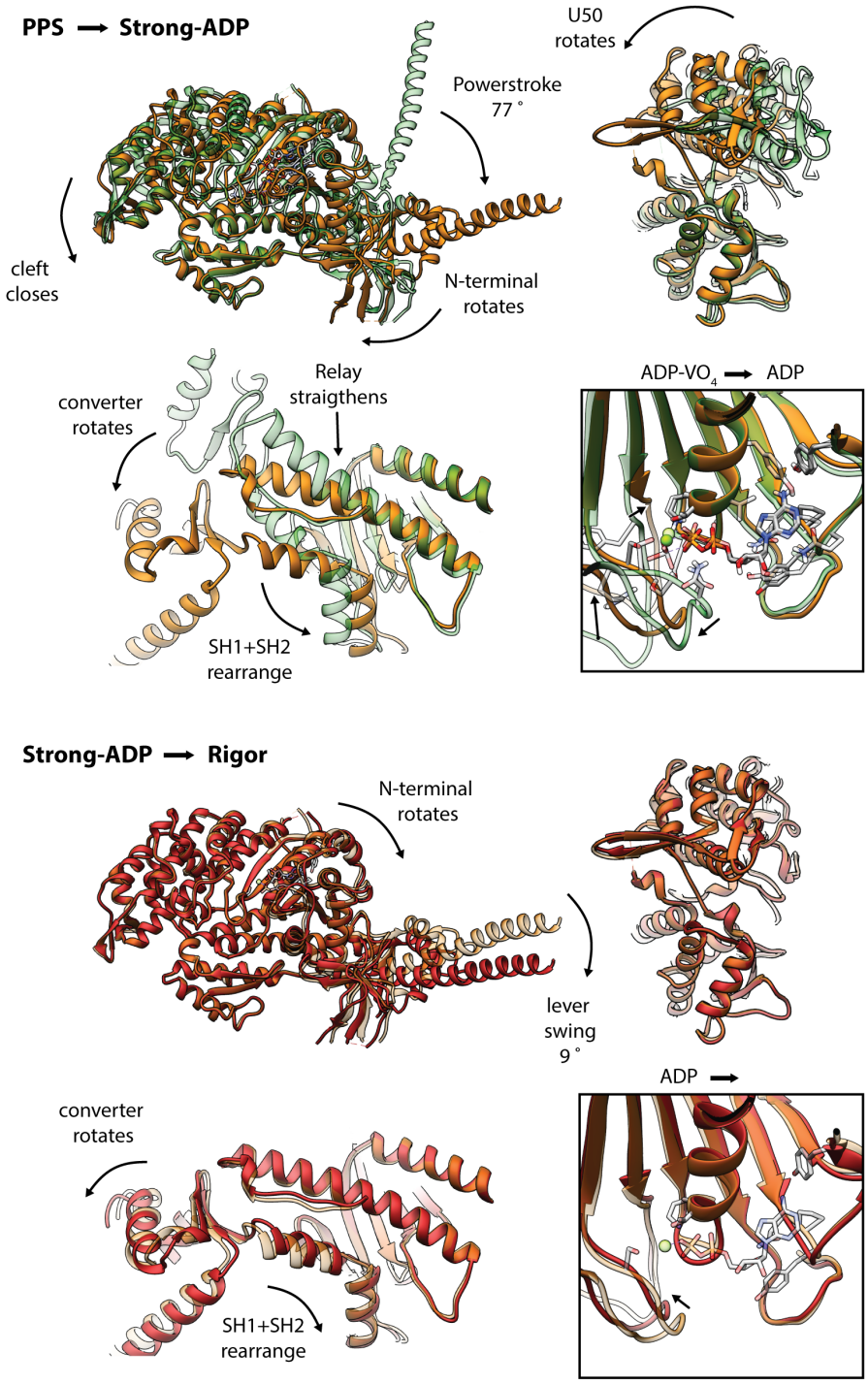

Fig. 4.29: Illustration of the conformational changes of myosin V during its transition between key structural states (PPS to Strong-ADP and Strong-ADP to Rigor). Superposition of atomic models of successive structural states along the myosin motor cycle; continuation of Figures 4.24 to 4.28. The precursor structure is shown as transparent. The lever arm of the PPS state was computationally elongated (original length indicated by asterisk). Structures are shown according to their sequence in the motor cycle from top to bottom. See Figure 4.23 for legend.

Strong-ADP to rigor transition In absence of load, myosin will soon transition to the rigor state, which has the highest binding affinity for F-actin. This transition is likely triggered by the sequential release of Mg^{2+} and ADP, and gives rise to another minor lever arm swing (also see Section 3.1.4 and detailed discussion of the strong-ADP to rigor transition in Section 4.5.2). Loss of Mg^{2+}-ADP primarily causes re-positioning of the A-loop and the P-loop (Figure 4.29). While the first causes a small rotation of the N-terminal domain (∼6 °, Figure 4.25), the latter results in a piston movement of the HF helix as well as twisting of the transducer β-sheet (also see Figure 4.9). In this way, the interface between the U50 and L50 domains and the N-terminal domain gets remodeled. This is well illustrated by the shift of switch I, which is connected to the U50 domain, relative to the HF helix (Figure 4.29). The resulting rigor conformation of the active site is stabilized by hydrogen bonds between the P-loop and switch I (E164&S165-N21) as well as the P-loop and switch II (K169-D437).

Interestingly, the changes at the active site do not alter the position of either the L50 or the U50 domain and thus also do not affect cleft closure (Figure 4.29). This finding is in contrast to the previous suggestion that sequential product release, i.e., P_i and Mg^{2+}-ADP, would be coupled to three distinct degrees of cleft closure according to the increase of the binding affinity of the corresponding states (Llinas et al., 2015). Our results indicate that the higher binding affinity of the rigor state is not due to alterations of the actin binding interface, which is well conserved in all three actin-bound states solved in this thesis (Supplementary Figure S6). Based on our heterogeneity analysis (see Section 4.5.7) we suggest that the difference in binding affinity is instead due to the different degrees of structural flexibility. By being significantly more flexible, the strong-ADP state is possibly more likely to detach from F-actin than the rigor state (also see Figure 4.21).

The rotation of the N-terminal domain, although small, results in a rearrangement of the SH1 and SH2 helices relative to the relay helix and ultimately a rotation of the converter domain. As a consequence, the lever arm rotates by ∼9 °, finally releasing all the energy that was stored in the protein structure during the recovery stroke. These conformational changes as well as the key role of the N-terminal domain are well reflected by the result of the computational domain motion analysis (Figure 4.25). It thereby confirms that the ADP release is communicated to the lever arm by the N-terminal domain, in contrast to the relay helix dependent coupling in case of the recovery stroke and the powerstroke.

Summary and Implications The sequential comparison of all resolved states along the motor cycle of myosin V has revealed the molecular details of each transition. Despite the complexity of the structural changes, a few structural elements stand out by acting as key role players. One of these is switch II, which undergoes major rearrangements during both the recovery stroke and powerstroke (Figures 4.23-4.29). In particular, it closes the active

site to accomplish a hydrolysis competent geometry in the PPS state and adopts an open conformation when P_i is released. Based on the two marked conformations of switch II, the PPS and post-rigor state were initially referred to as closed and open state, respectively (Geeves and Holmes, 1999). Furthermore, the conformation of switch II was assumed to dictate the lever arm position, i.e., closed=primed, open=relaxed (Reubold et al., 2003). This designation and assumption are, however, too simplistic as switch II adopts several distinct conformations throughout the motor cycle, which are not necessarily coupled to a lever arm re-orientation (Coureux et al., 2004, Llinas et al., 2015). The most striking example of a switch II movement, which does not affect the lever arm, can possibly be found in the P_iR state. Here, switch II shifts by 4 Å to open an exit tunnel for P_i without significantly altering the lever arm position (Llinas et al., 2015). This illustrates that switch II movements are not rigidly coupled to the lever arm in a simple mechanical manner. Instead, the interplay of switch II and other key structural elements, such as switch I and the transducer β-sheet, likely defines the lever arm orientation. In line with this, we observe a small lever arm swing upon ADP release which is not associated to a movement of switch II (Figures 4.29). Additional high-resolution structures of, for example, myosin V in the P_iR or intermediate state as well as of states which have not been solved yet will be required to finally unravel the intricate mechanism controlling the lever arm.

The interplay of switch I and switch II probably also defines the relative position of the U50 and L50 domains and thus opening and closure of the actin binding cleft. This coupling also explains why strong nucleotide binding and strong binding to F-actin are reciprocal (Coureux et al., 2004). Closure of the actin binding cleft results in large shifts of both switch I and switch II, which consequently can no longer tightly coordinate the nucleotide (Figure 4.29).

Another key structural element is the central transducer β-sheet. It connects all domains to the active site and undergoes various deformations, mostly twisting and shifting, when the active site rearranges during the myosin motor cycle. The plasticity of the transducer was suggested to define the kinetic constants of myosin. In particular, mutations within neighboring regulatory elements, such as loop 1, were suggested to either facilitate or retard the distortion of the transducer and thereby affect the release of phosphate and ADP (Coureux et al., 2004, Sweeney et al., 1998). In line with this, we find distortions of the transducer in basically all structural transitions. While the transducer was previously suggested to primarily couple the active site and the actin binding interface (Coureux et al., 2003), our analysis suggests that the transducer also transmits changes to the N-terminal and thereby the converter domain. We have additionally identified a considerable structural flexibility of the transducer, which transmits to adjacent domains (Section 4.5.7). We hence propose that the transducer acts as a central adjustment screw, which can tune

the relative orientation of all surrounding domains.

The last key structural element is the relay helix. Not only does it undergo major conformational changes itself, i.e., kinking and straightening, but its interaction with the N-terminal domain, especially the SH1 and the SH2 helices, defines the orientation of the converter domain and hence the lever arm (Figures 4.24-4.29). Interestingly, we find two alternative mechanisms by which this interface is remodeled during the motor cycle. When myosin is detached from actin, rearrangements of switch I and switch II are transmitted to the L50 domain and ultimately the relay helix. In the PPS state for instance, the relay helix adopts a kinked conformation to avoid a clash with the SH1 helix (Coureux et al., 2004). After the recovery stroke, the kinked conformation is maintained until strong binding to F-actin eventually triggers straightening of the relay helix and thereby the powerstroke (Figure 4.29). When myosin is bound to F-actin and P_i has left the active site, switch I and switch II hardly change their position. The remodeling of the relay helix interface upon ADP release consequently has another structural basis (Figure 4.29). Here, loss of the nucleotide gives rise to a small rotation of the N-terminal domain, which results in a re-positioning of the SH1 and SH2 helices and thereby a small lever arm swing. The changes at the active site that lead to this rearrangement are surprisingly subtle compared to the large rearrangements of switch I and II in case of the other coupling pathway.

Our results finally do not only indicate two alternative mechanisms that control the lever arm position, but also a pronounced flexibility of its orientation (Section 4.5.7). In particular, we find that thermal flexibility of the transducer and N-terminal domain give rise to a number of different lever arm conformations within the same nucleotide state (also see Figure 4.21). The direction of the lever swing is thereby not restricted to the direction of the recovery and powerstroke, but is two dimensional. The underlying plasticity might allow myosin to maintain its overall conformation under load.

Lastly, our data give insights into the nature of the coupling mechanisms within myosin. There are two major sites, namely the actin binding cleft and the active site, which are allosterically coupled to the overall conformation of myosin (Robert-Paganin et al., 2020). Based on our structural analysis and the observed pronounced flexibility (see Section 4.5.7), we propose a rigid mechanical coupling of the actin binding cleft, while the active site coupling is looser and of statistical nature. The latter was already suggested earlier based on MD simulations of the intermediate recovery stroke state (Blanc et al., 2018). The simulations in particular implied that the recovery stroke is initially driven by thermal fluctuations and only eventually gets stabilized by closure of the active site. It thereby also indicates that the recovery stroke is partially uncoupled from the ATPase activity of myosin (Blanc et al., 2018). This finding is in stark contrast to previously proposed models assuming a rigid mechanical coupling of the active site (Fischer et al.,

2005). Our data on the structural heterogeneity of myosin now provide further evidence for a statistical coupling. The fact that myosin can adopt a conformation close to the one of the rigor state, while ADP is still strongly bound to its active site, indicates that ADP release is not triggering the structural rearrangement. Instead, it is likely that thermal fluctuations initiate the transition to the rigor state and that release of ADP only eventually takes place (also see Section 4.5.7). Additional evidence for the non-rigid coupling of the active site finally comes from the PRT state structure with weakly-bound nucleotide (Section 4.5.4). Especially the compatibility of a bound ATP analog (AppNHp) with a conformation similar to the rigor questions a rigid mechanical coupling. If the coupling would be purely mechanical, ATP binding would directly trigger the transition to the post-rigor state and hence detachment from F-actin. By binding weakly to myosin, AppNHp does however not trigger any transition. Assuming that weak binding is also accessible for ATP, this indicates that thermal fluctuations are required to initiate the transition from weak to strong ATP binding and consequently the formation of the post-rigor state.

In contrast to the statistical coupling of the active site, our data suggest that the closure of the actin binding cleft is rigidly and mechanically coupled to the rest of the protein. Cleft closure due to strong actin binding causes a pronounced rearrangement of the active site, which renders it incapable for high-affinity nucleotide binding (specifically P_i) (Figure 4.29). A comparable rearrangement was neither observed in structures with an open cleft, nor in our analysis of the structural flexibility. Furthermore, the conformational change is basically reversed when myosin detaches from actin (Figures 4.24-4.29), suggesting that actin binding acts as an "on/off" switch for strong ATP/ADP-P_i binding. In this way, actin binding directly promotes the release of hydrolysis products and hence force production. Additional high-resolution structures of in particular weak-binding states, that illustrate how actin activates myosin, will be required to test this hypothesis.

4.5.9 Summary and Conclusions

The three high-resolution cryo-EM structures of myosin Va in the strong-ADP, rigor and AppNHp-bound PRT state presented in this thesis have provided a range of new insights into the structural basis of force generation. First, they have revealed the molecular details of the actomyosin interface of myosin Va for the first time (Section 4.5.1). Myosin Va binds to actin not only by the HLH motif, the CM loop, loop 4 and loop 2, but also by the activation loop and loop 3. By doing so, it forms a maximum of contacts in agreement with its characteristic high binding affinity. A comparison with the rigor state of other myosins shows that loop 2, although not completely resolved, adopts a unique α-helical fold. The comparison furthermore suggests that a tight Milligan contact (loop 3) (Milligan et al., 1990) might be a specific feature of high-duty ratio myosins. Second,

our structures have allowed the description of the structural transition of myosin Va upon ADP release for the first time (Sections 4.5.2-4.5.3). Since only one structure of the strong-ADP state was solved to high-resolution before (myosin IB) (Mentes et al., 2018), it was not clear if the described conformational changes are universal. A comparison with our structure of the strong-ADP state has now shown that the general effect of ADP release is conserved, that the resulting overall conformation and lever arm swing, however, depends on the myosin isoform. The structure of myosin bound to AppNHp finally has revealed a previously unexpected state reminiscent of the rigor state (Section 4.5.4). Specifically, it was anticipated that the presence of a γ-phosphate is incompatible with the rigor conformation (Llinas et al., 2015). Our structure now demonstrates that AppNHp and probably also ATP can bind weakly to myosin in the rigor conformation without considerably altering it. We have therefore concluded that binding of a nucleotide does not dictate the structural state of myosin. Instead, a high-affinity coordination of ATP has to be established to trigger the transition to the post-rigor state and hence detachment from F-actin. Based on the lower affinity of AppNHp-bound myosin and previously published results, we have finally proposed that our structure represents a transition state between the rigor and post-rigor state, which we named post-rigor transition (PRT) state and which probably replaces the theoretical weakly-bound post-rigor state (Sweeney and Holzbaur, 2018, Walklate et al., 2016). An earlier cryo-EM study of myosin IB moreover indicates that a conformation close to the rigor is possibly also adopted during the strong-ADP to rigor transition (Mentes et al., 2018). Conformations similar to the rigor state might consequently serve as transition states facilitating strong actin-binding in general. Interestingly, our data also provide evidence that AppNHp can give rise to different structural states as suggested earlier (Volkmann et al., 2005, Yengo et al., 2002). In particular, AppNHp might promote the detachment from F-actin due to a transition to the post-rigor state (Section 4.5.4). Future cryo-EM studies will be required to reveal the structure of myosin bound to AppNHp in absence of F-actin.

With the aim to elucidate the structural basis of nucleotide sensitivity, we have also solved the rigor state of myosin Va bound to F-actin stabilized in the young ADP-P_i state. Surprisingly, we find that myosin specifically selects the closed D-loop conformation and by doing so overrides the effect of JASP (Section 4.5.6). While myosin-induced changes of F-actin have also been described earlier (Behrmann et al., 2012a, Gurel et al., 2017, von der Ecken et al., 2016, Wulf et al., 2016), they are small compared to the one we describe here. In accordance with this, we find only minor changes of the structure of PHD-stabilized aged F-actin upon myosin binding (Section 4.5.5). The fact that strongly-bound myosin Va stabilizes the closed D-loop state, which is typical for aged F-actin, although it preferentially binds to young F-actin (Zimmermann et al., 2015) suggests that the young, open D-loop conformation of F-actin promotes the initial weak-binding of

myosin. Even though we could not reveal how myosin selects the nucleotide state of actin, our results still have some interesting implications. On the one hand, the conformational selection of the closed D-loop offers an explanation how closure of the actin binding cleft causes quenching of pyrene fluorescence (Section 4.5.5). On the other hand, myosin might promote filament aging and thereby affect the binding of other nucleotide-sensitive binding partners. By doing so, it might ultimately even affect the remodeling of the actin cytoskeleton, a possibility that has not been recognized before.

Our analysis of the structural heterogeneity has revealed a pronounced flexibility of myosin within all states we have studied (Section 4.5.7). We have in particular identified conformational changes that give rise to a lever arm swing as large as the one upon ADP release. A principal component analysis of all 3D classes and average structures has furthermore illustrated that myosin covers a considerable conformational space. While the location and extent of this space is nucleotide dependent, the relative position of the spaces indicates that the transition between the strong-ADP, rigor and AppNHp-bound PRT state is driven by thermal fluctuations. We have therefore proposed that the structure of myosin in a specific nucleotide state is not rigid, but highly dynamic. In this way, myosin eventually adopts a short-lived intermediate state that promotes the binding or release of a nucleotide and thereby the transition towards the next structural state along its motor cycle (Section 4.5.7). This proposal is in good agreement with a previous study suggesting a statistical, i.e., thermodynamical, coupling of the active site and the lever arm (Blanc et al., 2018). It moreover offers an explanation for the different binding affinities of the strong-ADP and rigor state, which is not due to distinct degrees of cleft closure as suggested earlier (Llinas et al., 2015)

The three new cryo-EM structures of myosin Va have finally allowed us to assemble the currently most complete structural model of the myosin motor cycle (Section 4.5.8). Comparisons of subsequent states within this cycle have revealed the molecular details of the structural transitions essential for force production. While these are highly complex and their coupling still not fully understood, we were able to identify key structural elements, such as switch II, switch I, the transducer and the relay helix, and describe their role in the mechanochemical coupling. We have furthermore shown that the conformation of the relay-SH1-SH2 helix interface defines the position of the lever arm and that two alternative pathways transmit changes from the nucleotide pocket to this site. When myosin is detached from F-actin, concerted changes of switch I and switch II give rise to kinking or straightening of the relay helix. Strong binding to actin fixes both switches in their position. Because of this, loss of ADP is instead communicated via a rotation of the N-terminal domain including the SH1 and SH2 helices. Based on the observed structural changes, we have lastly proposed a rigid mechanical coupling of the actin binding cleft to the rest of the protein. It is thereby in contrast to the possibly statistical coupling of the

active site.

Whilst the results of this thesis represent major contributions to the structural understanding of actomyosin, many key questions remain unanswered. For instance, we still lack knowledge about how actin binding activates myosin and how ATP binding triggers detachment of myosin. Only high-resolution structures of weak-binding states will eventually provide answers to these questions. Yet, they are intrinsically difficult to trap, as illustrated in this thesis (see Section 4.5.4). Another aspect we could not shed light on in this study is the nucleotide sensitivity of myosin V. Future studies will hopefully further characterize this feature and eventually reveal its structural basis. Additional experiments are also required to validate the specific selection of the closed D-loop state of F-actin and to test if myosin in this way affects the remodeling of the cytoskeleton. The structural flexibility finally represents another interesting characteristic of myosin, which has hardly been recognized and studied before. We have now provided evidence that thermodynamic fluctuations might be essential for the force generation process. Testing of this hypothesis will require additional high-resolution cryo-EM structures of (acto)myosin as well as biochemical and computational studies characterizing the dynamics of myosin.

4.6 Comprehensive discussion and outlook

My aim for this doctoral thesis was to shed light on the structure-function relationship of actin and myosin. Therefore, I planned to solve a number of high-resolution cryo-EM structures of actin alone and in complex with myosin. Specifically, I wanted to characterize a distinct actin from *Plasmodium* as well as actin and myosin in different nucleotide states or bound to small-molecule inhibitors (see Section 2.5).

The results presented in Sections 4.1 to 4.5 illustrate the successful implementation of my intent. Furthermore, they show how the 19 high-resolution cryo-EM structures I have solved during this thesis project (partially in collaboration with Dr. Felipe Merino) have revealed answers to many of the unanswered research questions of the field (also see Section 2.5). A comprehensive discussion of all results and an outlook is given in this section. In particular, it initially discusses how methodological advances in cryo-EM have promoted the structural characterization of F-actin and actomyosin (Section 4.6.1). In addition, it outlines my own contributions to recent software developments, which have paved the way for future cryo-EM studies. Finally, it gives a general perspective for the structure determination of F-actin complexes and indicates future trends. Subsequently, my results on F-actin and actomyosin as well as their implications are briefly summarized and put into the context of the current state of research (Sections 4.6.2 and 4.6.3). In this framework, open research questions are identified and experiments suggested that can potentially provide answers to these.

4.6.1 Impact of recent advances in cryo-EM

A number of major advances in both hardware and software have resulted in a "resolution revolution" in the field of cryo-EM (Kühlbrandt, 2014) (see Section 2.4.6). The development has, however, not stalled at that point, but has continuously progressed since 2014 and ultimately enabled the reconstruction of ∼1.2 Å cryo-EM structures (Nakane et al., 2020, Yip et al., 2020). Recent advances have also greatly promoted the structural characterization of F-actin and actomyosin (Bradshaw and Paul, 2019). First, the achievable resolution has considerably increased. This trend is well illustrated by the four, sequentially solved cryo-EM structure of *Plasmodium falciparum* F-actin 1. The resolution of the first cryo-EM structure solved in 2014 was limited to ∼25 Å (Vahokoski et al., 2014). The usage of a direct electron detector instead of a CCD camera, contributed for the most part to the improved resolution of ∼8 Å I attained in my master thesis project preceding this doctoral thesis (Pospich, 2015). Within my doctoral project, I aimed for an even higher resolution and therefore used a state-of-the-art microscope, which facilitates automated data acquisition, and maximum-likelihood processing software (Section 4.1). By

doing so, I was able to reconstruct a near-atomic resolution structure at 3.8 Å, which has revealed the molecular details of *Pf* Actin1 for the first time (Pospich et al., 2017). Lately, advanced processing strategies, such as particle polishing and per-particle CTF refinement (also see Section 3.3.1.5), improved the achievable resolution even further, giving rise to a 2.6 Å cryo-EM structure (Vahokoski et al., 2020). The impact of recent advances is not limited to the resolution, but also extends to the time and effort required to solve a cryo-EM structure. While solving two high-resolution structures within one doctoral thesis project represented an outstanding performance in 2016 (von der Ecken, 2016), I was able to solve a total of 19 high-resolution structures during my thesis project (partially in collaboration, see Section 4). This is primarily due to the automation of many laborious tasks, in particular data acquisition and preprocessing (also see Sections 3.2.2.3 and 3.3.1.1). In addition, the computational infrastructure and software packages available today are by far superior to the ones in 2016, making the computational reconstruction faster. Simultaneously, the size of a standard cryo-EM data set has increased dramatically from ∼1,000-2,000 micrographs depicting ∼100,000 particles in 2014 (von der Ecken et al., 2015), to ten thousands of micrographs and millions of particles (Stabrin et al., 2020). While this development benefits the achievable resolution, it also requires careful data handling, fast software, sophisticated automation and ultimately an optimized processing strategy. During my doctoral project I actively contributed to the development of novel software dedicated to both automation and the 3D refinement of helical samples. On the one hand, I was involved in the conceptualization and testing of helical SPHIRE, a processing pipeline for helical samples . The resulting 3D refinement program `sp_meridien_alpha.py` could successfully replace the previously used hybrid processing strategy in RELION, achieving high-resolution for both F-actin and actomyosin (also see Sections 3.3.1.3-3.3.1.4 and 4.4 -4.5). On the other hand, I supported the development of TranSPHIRE (Stabrin et al., 2020). This package does not only allow automated on-the-fly preprocessing and optimization of cryo-EM data, but also the reconstruction of a first 3D structure while the data acquisition is still running (Section 3.3.1.1). Starting from these two software tools, I successfully established a processing pipeline for both actin and actomyosin filaments (Sections 3.3 and 4.5). As the pipeline is also applicable to other F-actin complexes, it directly promotes future cryo-EM studies.

In general, cryo-EM has become more accessible within the last five years, as the field and its methodology has become well established. For example, most modern software packages come with a user-friendly graphical interface and thus no longer require scripting. Furthermore, many companies have specialized on cryo-EM products and offer not only devices for sample preparation and imaging, but also pre-installed GPU-boxes for processing. In this way, also smaller labs that cannot afford a computer cluster can nowadays solve cryo-EM structures. Pioneering studies have finally introduced key protocols

for the sample preparation and processing of F-actin and actomyosin (Behrmann et al., 2012a, von der Ecken et al., 2016, 2015), and thereby paved the way for subsequent cryo-EM studies. A combination of all these factors has eventually promoted the structural characterization of various F-actin complexes (Banerjee et al., 2017, Belyy et al., 2020, Chou and Pollard, 2019, 2020, Das et al., 2020, Doran et al., 2020, Fujii and Namba, 2017, Galkin et al., 2015, Grintsevich et al., 2017, Gurel et al., 2017, Huehn et al., 2018, 2020, Iwamoto et al., 2018, Kumari et al., 2020, Mei et al., 2020, Mentes et al., 2018, Merino et al., 2018, Oda et al., 2020, Pospich et al., 2021, 2017, 2020, Ren et al., 2019, Risi et al., 2020, Shaaban et al., 2020, Tanaka et al., 2018, Vahokoski et al., 2020, Wulf et al., 2016, Xu et al., 2020, Yamada et al., 2020, Zimmet et al., 2020).

Cryo-EM is not only an optimal tool for the structural characterization of F-actin in complex with ABPs, but also has great potential for structure-based drug design (Merino and Raunser, 2016a, Pospich and Raunser, 2018). That cryo-EM is suitable to resolve small molecules and their interactions with F-actin was initially proven by the structures of JASP- and PHD-stabilized F-actin I have solved within this thesis project (Section 4.1-4.3) (Merino et al., 2018, Pospich et al., 2017, 2020) as well as the structures of F-actin in complex with PHD or lifeact solved by others (Belyy et al., 2020, Das et al., 2020, Iwamoto et al., 2018, Kumari et al., 2020, Mentes et al., 2018). The final proof that cryo-EM allows structure-based drug design comes from the structures of F-actin bound to optojasp presented in this thesis (Section 4.4) (Pospich et al., 2021). In particular, they illustrate that cryo-EM can resolve the isomeric states of a photoswitch and thus a complex, non-rigid small molecule. This result does not only serve as a proof of principle, but also represents a starting point for the rational design of actin inhibitors. Optojasps, for instance, could develop into a powerful biochemical tool. On the one hand, they would facilitate future studies of actin and its binding partners. On the other hand, they could also promote the characterization of cellular processes that are not directly related to actin by providing an optical control of the cell cycle. Finally, actin inhibitors can potentially also serve as drugs. Many disease related processes rely on actin filaments. Actin 1 of the human malaria parasite *Plasmodium falciparum* studied in this thesis, for instance, is an attractive drug target as it is directly linked to the pathology of the parasite (Section 4.1). Altogether, cryo-EM will likely play a major role in the structure-based design of drugs in the near future. As many proteins have been previously inaccessible, due to their reluctance to crystallize, this could be a breakthrough in medicinal biochemistry.

Taken together, cryo-EM has provided the most part of our structural knowledge of F-actin, actomyosin and ABPs. Although many key structures have already been solved in the last years, numerous key role players of the actin cytoskeleton and muscle contraction remain uncharacterized. For instance, we are still lacking high-resolution structures of capping protein and formin, which bind to the ends of F-actin. But also the structures of the

pointed and barbed end of F-actin remain to be revealed. Hence, the potential of cryo-EM has not yet been exhausted, but this method will also be of central relevance for structural studies of actin complexes in the future. Nonetheless, single-particle cryo-EM in its current implementation has some limitations. In particular, it struggles with highly heterogeneous as well as small protein complexes. This is mostly due to an insufficient contrast, which in turn requires more powerful processing algorithms. As a result, it is currently not possible to study, for example, sub-stochiometrically bound small ligands or nucleotide gradients. This would however be necessary to fully understand the aging process and cooperativity of actin filaments and thereby ultimately the structural basis of cytomotility (Pospich and Raunser, 2018). Future advances in cryo-EM will hopefully address and eventually overcome these limitations.

Another severe limitation of single-particle cryo-EM is the requirement to purify the protein complex of interest. By doing so, the protein is not only taken out of its crowded cellular environment, but is also separated from numerous interacting proteins that modulate its structure and function. The sarcomere, the smallest contractile subunit of the muscle, is an archetypical example of a complex multi-protein system. While F-actin and myosin alone are sufficient to generate force, only the interplay of both proteins with various regulatory proteins facilitates the concerted action required for muscle contraction (Huxley, 2004). Hence, cryo-EM studies of actomyosin, although of utmost importance for understanding the structural basis of force-generation, can never reveal the molecular details of muscle contraction. For this purpose, native sarcomeres need to be structurally characterized, which is only possible by cryo-ET in combination with sub-tomogram averaging (also see Section 2.1). Whilst this method is not as established as single-particle cryo-EM yet, recent advances have culminated in ∼3-4 Å resolution structures (Dick et al., 2020, Schur et al., 2016, Turoňová et al., 2017). In addition, latest studies have showcased the great potential of cryo-ET for structural studies of the cytoskeleton and muscle (Burbaum et al., 2020, Chakraborty et al., 2020b, Fäßler et al., 2020, Martins et al., 2021, Oda and Yanagisawa, 2020, Paul et al., 2020, Song et al., 2020, Wang et al., 2020). In summary, these results promise a bright future for cryo-ET in general, but especially for research dedicated to actin-based systems (reviewed in (Bradshaw and Paul, 2019, Chakraborty et al., 2020a)). In addition, future developments will likely further promote cryo-ET and give rise to a revolution similar to the one of cryo-EM (see Section 2.4.6). Cryo-ET therefore will possibly evolve from a supplementary method to a real alternative to high-resolution single-particle cryo-EM and eventually might even replace it as the standard method for studying F-actin complexes.

4.6.2 Deciphering the structure-function relationship of actin

Actin is a structural protein that fulfills a multitude of essential functions within eukaryotic cells. In its filamentous form it serves, for instance, as a track for the molecular motor myosin, thereby enabling key processes such as cargo transport and muscle contraction. F-actin does however not only act as a rigid scaffold, but is highly dynamic within the cytoskeleton (see Section 2.2). This is on the one hand due to a multitude of protein-protein interactions. On the other hand, the structure-function relationship of actin is additionally tuned by its ATPase activity. Here, polymerization triggers ATP hydrolysis and the subsequent release of inorganic phosphate eventually results in a destabilization of the filament (Section 2.2.1). The associated structural states of F-actin are thought to be sensed by nucleotide-sensitive ABPs, such as coronin and cofilin, which in this way facilitate the directed remodeling of the actin cytoskeleton (see Sections 2.2.1-2.2.2).

Although actin has been extensively studied since its discovery in 1942 (Straub, 1942), it was not before 1990 that the first crystal structure of G-actin was published (Kabsch et al., 1990). While this structure elucidated the overall architecture of actin, it could not reveal the structural basis of actin filaments. It took in fact another ∼20 years, until X-ray fiber diffraction and subsequently cryo-EM unveiled the molecular details of F-actin at high-resolution (Oda et al., 2009, von der Ecken et al., 2015) (also see Section 2.2.1). While these results represent a milestone of the actin research, they could only partially elucidate the structure-function relationship of actin. In particular, the structural effect of ATP hydrolysis and phosphate release as well as the mechanism by which ABPs read the nucleotide state of F-actin has remained elusive. Furthermore, there was no structural knowledge about how the stability of actin filaments is altered by, for example, sequence variations or drug-like small molecules. Shedding light on these aspects was the main focus of the presented thesis project, which thereby directly follows on the previous cryo-EM work on F-actin performed in the Raunser lab (von der Ecken et al., 2015).

Within this thesis project, I have solved a total of 14 high-resolution structures of F-actin (partially in collaboration with Dr. Felipe Merino, see Section 4) to assess the structural effect of ATP hydrolysis, sequence variations and binding of PHD and JASP. The structures in their entirety show that conformational changes within F-actin are generally subtle. Consequently, not only is the sequence of actin highly conserved (Gunning et al., 2015), but also its overall filament architecture. Interestingly, the conservation also extends to the actin-like proteins found in archaea and bacteria, which form double-stranded filaments reminiscent of F-actin (recently reviewed in Pospich and Raunser (2018). Despite their subtlety, small changes in the sequence can nevertheless have a dramatic effect on the filament stability. The structure of *Pf*Actin1, for example, indicates that the unusual instability of this actin, which makes the usage of JASP for structural studies

indispensable, originates from a substitution of a mere eight residues at key interfaces (Section 4.1) (Pospich et al., 2017). A similar sensitivity to small alterations has been reported for the actin-like proteins MamK and MreB, which lose their polymerization capability due to a single point mutation (Löwe et al., 2016, van den Ent et al., 2014). This suggests that the sensitivity of actin to small changes has evolved early and possibly represents a key mechanism for tuning its function.

The structural changes associated with the nucleotide state of F-actin are also surprisingly small. We found that ATP hydrolysis and the subsequent release of phosphate primarily alter the conformation of the D-loop C-terminus interface (Section 4.2) (Merino et al., 2018). In particular, our structures have for the first time revealed a second conformation of this interface, which we refer to as the open D-loop state. In contrast to the closed D-loop state, which is characteristic for ADP-bound F-actin (Galkin et al., 2015, von der Ecken et al., 2015), the D-loop is bent outward with respect to the filament axis. In addition, the C-terminal tail no longer adopts an α-helical fold, but extends into a hydrophobic pocket, where it directly interacts with the D-loop (Section 4.2). Interestingly, the D-loop C-terminus interface is part of the binding interface of many nucleotide-sensitive ABPs and also myosin. Based on this and additional experiments probing the binding affinity of coronin-1B, we have therefore proposed that ABPs possibly read the nucleotide state of F-actin from this interface (Section 4.2) (Merino et al., 2018).

Intriguingly, an independent cryo-EM study of F-actin in different nucleotide states did not observe the open D-loop conformation (for details see 4.2) (Pospich et al., 2020). This discrepancy was, on the one hand, suggested to be linked to the identity of the divalent metal ion in the active site, i.e., Ca^{2+} or Mg^{2+}. On the other hand, it might be due to the nucleotide states studied. First, the density for the open D-loop conformation was strongest in our structure of ADP-BeF_x-F-actin and this state was not included in the competing study. Second, we have shown that AppNHp is a suboptimal ATP analog when it comes to F-actin, as it likely gives rise to a mixture of states in dependence of its purity (see Section 4.2). While there is increasing evidence for the existence of the open D-loop state, both from our lab as well as independent work (Kumari et al., 2020, Pospich et al., 2020, Ren et al., 2019), additional high-resolution structures as well as functional experiments are required to clarify if the open D-loop state is indeed a hallmark of the triphosphate state of F-actin. Ideally, one would solve the structure of the short-lived ATP state. One option to achieve this would be the usage of other, possibly photo-caged ATP analogs (see Bagshaw (2001) for an overview of available analogs). Alternatively, one could try to render F-actin hydrolysis incompetent by point mutations. Further experiments are also needed to test if the D-loop conformation is indeed how ABPs sense the nucleotide state of F-actin; or if they rather sense the reported nucleotide-dependent structural plasticity (also see Sections 4.2) (Chou and Pollard, 2019, Merino et al., 2018).

For this purpose, TIRF fluorescence microscopy is especially well-suited as illustrated in this thesis (Section 4.2). Mutational and labeling approaches have moreover the potential to bring valuable insights.

This thesis has finally also revealed the structural effect of PHD and JASP on F-actin for the first time (Sections 4.2-4.4) (Merino et al., 2018, Pospich et al., 2020). The presented cryo-EM structures have not only allowed the detailed description of the respective binding sites, but also illustrate that PHD and JASP stabilize F-actin by strengthening both the intrastrand and interstrand contacts. Surprisingly, we found that the two toxins trap the open D-loop state and the inorganic phosphate inside the active site when added to ATP-G-actin during the polymerization. Additional experiments furthermore showed that JASP generally stabilizes the open state and promotes rebinding of phosphate, even when added to ADP-G-actin or to aged filaments. Conversely, addition of PHD to aged filaments does not give rise to the open D-loop, but stabilizes the closed conformation typical for ADP-F-actin (Section 4.3). These results demonstrate that JASP and PHD do not have the same effect on F-actin, despite their chemical similarity and shared binding site. They furthermore indicate that the toxins can be deliberately used to mimic a specific nucleotide state of F-actin, what is in line with the results of a previous study assessing the nucleotide-sensitivity of myosin (Zimmermann et al., 2015). While this highlights the great potential of JASP and PHD, it simultaneously indicates that JASP- and PHD-based actin labels likely interfere with the binding of accessory proteins. They should consequently be used with caution or, if applicable, be replaced by less invasive labels (also see Section 4.3). By characterizing a photoswitchable optojasp, this thesis has finally laid the foundation for future structure-based design efforts of functional JASP analogs (Section 4.4) (Pospich et al., 2021). These do not only represent promising tools for biochemical research, but can also serve as a starting point for the development of a medical drug (Section 4.4) (Pospich et al., 2021).

Overall, this thesis has contributed greatly to our structural understanding of actin and its remodeling by ABPs. It illustrates that the cytoskeleton is a highly sophisticated, intricate system, which is tuned by a number of small "adjustment screws", i.e., ATP hydrolysis and protein-protein interactions. While additional cryo-EM structure of F-actin complexes brought further valuable insights into the structure-function relationship of actin (Belyy et al., 2020, Chou and Pollard, 2019, 2020, Das et al., 2020, Grintsevich et al., 2017, Huehn et al., 2018, 2020, Iwamoto et al., 2018, Kumari et al., 2020, Mei et al., 2020, Mentes et al., 2018, Ren et al., 2019, Shaaban et al., 2020, Tanaka et al., 2018, Vahokoski et al., 2020, Xu et al., 2020, Zimmet et al., 2020), it is still not fully understood. On the one hand, the resolutions that have been achieved so far ($\geq$2.6 Å) were not sufficient to fully resolve the coordination of the nucleotide including water molecules. This would, however, be necessary to finally identify the molecular details of ATP hydrolysis

and phosphate release as well as their coupling to the surface of the actin filament. On the other hand, structural studies were so far mostly limited to isolated, reconstituted protein complexes. Finally, F-actin usually has to be completely decorated with an ABP or saturated with a ligand to allow high-resolution, what is in stark contrast to native conditions. While this "reductionist approach" (Asano et al., 2016) has allowed the reconstruction of high-resolution structures by cryo-EM, it is unsuitable to study actin in its native environment. It consequently can also not elucidate how the interplay of ABPs affects the overall structure of F-actin. Cryo-ET has the potential to fill this gap and might even completely replace cryo-EM in the long term (also see Section 4.6.1). Finally, the development of novel methods is required to ultimately understand the structural transition of F-actin upon ATP hydrolysis. Native actin filaments are, in contrast to the reconstituted filaments studied by cryo-EM, highly dynamic and encompass a nucleotide gradient. Resolving this gradient and the structural changes associated with it requires either highly sophisticated 3D sorting strategies or a high-resolution imaging technique that does not rely on averaging (Pospich and Raunser, 2018). Such methods would also facilitate the identification of long-range effects caused by, for example, sub-stoichiometric binding of ABPs or small molecule ligands. Taken together, all these open research questions illustrate that actin remains a highly interesting protein to study.

4.6.3 Revealing the structural basis of force generation by myosin

The motor protein myosin is a key role player in a plethora of essential cellular processes (see Section 2.3). The mechanism by which it generates the force that *inter alia* drives muscle contraction has been studied for decades. Initially, myosin was primarily studied by biochemical experiments, which have brought great insights into the diversity and kinetics of the myosin family. With the publication of the first crystal structure of myosin in 1993 (Rayment et al., 1993b), efforts were increasingly focused on its structural characterization. While these culminated in a number of crystal structures of different myosins and structural states, it was not before 2012 that the first medium-resolution cryo-EM structure of the actomyosin complex was solved (Behrmann et al., 2012a) (recently reviewed in Sweeney et al. (2020) and Robert-Paganin et al. (2020)). In a pioneering study, the same lab later published the first high-resolution structure of the actomyosin rigor complex (von der Ecken et al., 2016). Despite these breakthroughs, the structural basis of force generation has still not been fully revealed. Structures of all key states along the motor cycle are required to unravel how ATP hydrolysis and actin binding regulate myosin. Recent cryo-EM structures of different myosins have furthermore shown that it is vital to solve the complete motor cycle for a single myosin isoform, as the domain coupling differs within the myosin family (see Section 3.1.4).

This thesis project directly connects to the previous cryo-EM work performed in the Raunser lab (Behrmann et al., 2012a, von der Ecken et al., 2016). The main focus was on the structural characterization of the actin-bound states of myosin Va to ultimately assemble a structural model of the complete motor cycle. Although AppNHp unfortunately did not give rise to a weak-binding state (see Section 4.5.4), this work still allowed the assembly of the currently most complete structural cycle. In particular, I was able to solve high-resolution structures of the strong-ADP, the rigor and a AppNHp-bound post-rigor transition state (Sections 4.5.1-4.5.4). Based on these, I could not only describe the structural transition upon ADP release in detail, but also identify structural elements and coupling mechanisms that are key for the transition along the motor cycle in general (Section 4.5.8). My work has furthermore revealed two features of myosin, namely its structural flexibility and its ability to specifically select the closed D-loop state of F-actin (Sections 4.5.5-4.5.7), which were previously hardly or not recognized at all. These findings have a number of possible implications, for example, for the driving force of the motor cycle and the remodeling of the cytoskeleton, which need to be tested by future studies (for details see Section 4.5.9). While the results of this thesis represent a considerable contribution to the characterization of the structure-function relationship of myosin (discussed in detail in Section 4.5.9), further investigations are required to finally reveal the intricate details of force generation. Today, there is a particularly great need for structural data on weak-binding states (Schröder, 2020). Only one crystal structure of myosin VI in the putative P_iR state (Llinas et al., 2015) has so far given some insight into how actin possibly activates phosphate release and thereby the progression of the motor cycle. Although crystal structures of other myosins in this state would already be of great interest, cryo-EM structure of actomyosin illustrating the release of phosphate would be invaluable. Similarly, only cryo-EM can reveal how ATP binding results in detachment from F-actin. According to their nature, weak-binding states are intrinsically difficult to structurally characterize, as discussed and illustrated in this thesis (see Sections 3.1.4 and 4.5.4). Even though AppNHp presented a promising and elegant way to trap a short-lived weak-binding state of myosin Va, it eventually gave rise to a strongly-bound state reminiscent of the rigor state, which likely represents a transition state between the rigor and post-rigor state (Section 4.5.4). Other methods are hence required to trap myosin in a weakly-bound state. One option would be the usage of other, possibly photo-caged, ATP/ADP-P_i analogs (see Bagshaw (2001) for an overview of available analogs). Alternatively, point mutations could be introduced into the active site with the aim to inhibit the structural transition of myosin. A less invasive strategy would be the usage of small molecules that specifically stabilize short-lived states. A potential candidate could be omecamtiv mercarbil (OM), a drug that enhances force generation in the heart (Malik et al., 2011, Robert-Paganin et al., 2020). OM binds to a pocket which is only available

when the lever arm is in a primed position (Planelles-Herrero et al., 2017). It thereby inhibits the powerstroke, while facilitating phosphate release (Planelles-Herrero et al., 2017, Rohde et al., 2017, Woody et al., 2018). Consequently, OM could potentially be used to stabilize both the weakly-bound PPS and the P_iR state of myosin (Malik et al., 2011, Planelles-Herrero et al., 2017). Finally, weak-binding states could possibly also be studied using time-resolved cryo-EM (Frank, 2017). Here, two liquid samples are sprayed onto the surface of a grid which is already halfway through its plunging path. By doing so, the two samples, i.e., protein and nucleotide in solution, are only in contact for ∼10-1000 ms before the vitrification stops the reaction (Lu et al., 2009).

New insights would probably also come from cryo-EM structures of myosin alone. Although all major states that are not associated with actin binding have already been solved by X-ray crystallography, crystal packing is likely to camouflage any structural flexibility. In addition, many structures have been obtained by soaking pre-formed crystals with nucleotides, what can potentially result in artificial conformations.

In addition to high-resolution structures of previously unresolved states, data on the dynamics and structural flexibility of myosin are required to understand its transition between known states. Cryo-EM in combination with 3D classification can directly provide information about the conformational space of myosin, as demonstrated in this thesis (Section 4.5.7). Future developments facilitating the collection of larger data sets and the analysis of continuous structural heterogeneity will likely further increase the potential of cryo-EM. Molecular dynamics simulations are moreover a powerful tool, which will surely contribute greatly to our understanding of the myosin motor cycle. Finally, valuable dynamic and energetic data can also be achieved by biochemical experiments using, for example, spin labels (Klein et al., 2008)

While the characterization of the myosin motor domain is already highly complex, it must not be forgotten that it represents a strongly simplified system. Myosin Va for instance does not only have a long tail which encompasses the cargo binding domain, but is also dimeric (see Section 2.3). Studies of the motor domain can consequently only give insight into the structural basis of force generation, but not in its regulation by the tail domain or the second myosin. For this purpose, the complete, ideally native complex needs to be characterized. Two recent independent studies have demonstrated that cryo-EM is also suitable to study the structure of dimeric myosin (Scarff et al., 2020, Yang et al., 2020), thereby indicating a potential direction for future research efforts. An additional simplification comes from the need to saturate F-actin with myosin to reach high-resolution. Even in muscle, where many myosin heads bind simultaneously to an actin filament, the majority of actin subunits remains unoccupied (Goody et al., 1985, Wang et al., 2020). In its cellular environment myosin is furthermore regulated by various other proteins.

Within the muscle, for example, tropomyosin and troponin directly regulate the activity of myosin (Huxley, 2004). Finally, studies of the isolated motor domain completely disregard the effect of load on the structure and kinetics of myosin. All these aspects illustrate that myosin is embedded in a intricate interaction network and that its full understanding requires the structural characterization of myosin *in situ* by, for example, cryo-ET (also see Section 4.6.1).

References

Adams, P. D., Afonine, P. V., Bunkóczi, G. et al. (**2011**). The Phenix software for automated determination of macromolecular structures. *Methods*, 55(1):94–106.

Afonine, P. V., Poon, B. K., Read, R. J., Sobolev, O. V., Terwilliger, T. C., Urzhumtsev, A. and Adams, P. D. (**2018**). Real-space refinement in PHENIX for cryo-EM and crystallography. *Acta crystallographica. Section D, Structural biology*, 74(Pt 6):531–544.

Amann, K. J. and Pollard, T. D. (**2001**). The Arp2/3 complex nucleates actin filament branches from the sides of pre-existing filaments. *Nature cell biology*, 3(3):306–310.

Anandakrishnan, R., Aguilar, B. and Onufriev, A. V. (**2012**). H++ 3.0: automating pK prediction and the preparation of biomolecular structures for atomistic molecular modeling and simulations. *Nucleic Acids Research*, 40(W1):W537–W541.

Anderson, A. C. (**2003**). The process of structure-based drug design. *Chemistry & biology*, 10(9):787–797.

Angrisano, F., Delves, M. J., Sturm, A., Mollard, V., McFadden, G. I., Sinden, R. E. and Baum, J. (**2012**a). A GFP-actin reporter line to explore microfilament dynamics across the malaria parasite lifecycle. *Molecular and biochemical parasitology*, 182(1-2):93–96.

Angrisano, F., Riglar, D. T., Sturm, A. et al. (**2012**b). Spatial localisation of actin filaments across developmental stages of the malaria parasite. *PloS one*, 7(2):e32188.

Anson, M., Drummond, D. R., Geeves, M. A., Hennessey, E. S., Ritchie, M. D. and Sparrow, J. C. (**1995**). Actomyosin kinetics and in vitro motility of wild-type Drosophila actin and the effects of two mutations in the Act88F gene. *Biophysical journal*, 68(5):1991–2003.

Archenzo (**2005**). Amanita phalloides. Piacenzaś mountains. GNU Free Documentation License and Creative Commons License. Website: https://commons.wikimedia.org/wiki/File:Amanita_phalloides_1.JPG. Accessed 11.12.2020.

Asakura, S. (**1961**). The interaction between G-actin and ATP. *Archives of biochemistry and biophysics*, 92(1):140–149.

Asano, S., Engel, B. D. and Baumeister, W. (**2016**). In Situ Cryo-Electron Tomography: A Post-Reductionist Approach to Structural Biology. *Journal of Molecular Biology*, 428(2 Pt A):332–343.

Bagshaw, C. (**2001**). ATP analogues at a glance. *Journal of cell science*, 114(Pt 3):459–460.

Bagshaw, C. R. and Trentham, D. R. (**1974**). The characterization of myosin-product complexes and of product-release steps during the magnesium ion-dependent adenosine triphosphatase reaction. *The Biochemical journal*, 141(2):331–349.

Bai, X.-C., Rajendra, E., Yang, G., Shi, Y. and Scheres, S. H. (**2015**). Sampling the conformational space of the catalytic subunit of human γ-secretase. *eLife*, 4:e11182.

Banerjee, C., Hu, Z., Huang, Z., Anthony Warrington, J., Taylor, D. W., Trybus, K. M., Lowey, S. and Taylor, K. A. (**2017**). The Structure of the Actin-Smooth Muscle Myosin Motor Domain Complex in the Rigor State. *Journal of structural biology*, 200(3):325–333.

Barad, B. A., Echols, N., Wang, R. Y.-R., Cheng, Y., DiMaio, F., Adams, P. D. and Fraser, J. S. (**2015**). EMRinger: side chain-directed model and map validation for 3D cryo-electron microscopy. *Nature methods*, 12(10):943–946.

Barden, J. A., Miki, M., Hambly, B. D. and Dos Remedios, C. G. (**1987**). Localization of the phalloidin and nucleotide-binding sites on actin. *European journal of biochemistry / FEBS*, 162(3):583–588.

Bauer, C. B., Holden, H. M., Thoden, J. B., Smith, R. and Rayment, I. (**2000**). X-ray structures of the apo and MgATP-bound states of Dictyostelium discoideum myosin motor domain. *Journal of Biological Chemistry*, 275(49):38494–38499.

Behrmann, E. (**2012**). *Structure of the Actin/Tropomyosin/Myosin Rigor Complex as Revealed by Cryo-Electrin Microscopy*. Ph.D. thesis, Technische Universität Dortmund.

Behrmann, E., Müller, M., Penczek, P. A., Mannherz, H. G., Manstein, D. J. and Raunser, S. (**2012**a). Structure of the rigor actin-tropomyosin-myosin complex. *Cell*, 150(2):327–338.

Behrmann, E., Tao, G., Stokes, D. L., Egelman, E. H., Raunser, S. and Penczek, P. A. (**2012**b). Real-space processing of helical filaments in SPARX. *Journal of structural biology*, 177(2):302–313.

Belmont, L. D., Patterson, G. M. and Drubin, D. G. (**1999**). New actin mutants allow further characterization of the nucleotide binding cleft and drug binding sites. *Journal of cell science*, 112 (Pt 9):1325–1336.

Belyy, A., Merino, F., Sitsel, O. and Raunser, S. (**2020**). Structure of the Lifeact-F-actin complex. *PLoS biology*, 18(11):e3000925.

Bernecky, C., Herzog, F., Baumeister, W., Plitzko, J. M. and Cramer, P. (**2016**). Structure of transcribing mammalian RNA polymerase II. *Nature*, 529(7587):551–554.

Bhabha, G., Cheng, H.-C., Zhang, N., Moeller, A., Liao, M., Speir, J. A., Cheng, Y. and Vale, R. D. (**2014**). Allosteric communication in the dynein motor domain. *Cell*, 159(4):857–868.

Bhargav, S. P., Vahokoski, J., Kumpula, E.-P. and Kursula, I. (**2013**). Crystallization and preliminary structural characterization of the two actin isoforms of the malaria parasite. *Acta crystallographica. Section F, Structural biology and crystallization communications*, 69(Pt 10):1171–1176.

Blanc, F., Isabet, T., Benisty, H., Sweeney, H. L., Cecchini, M. and Houdusse, A. (**2018**). An intermediate along the recovery stroke of myosin VI revealed by X-ray crystallography and molecular dynamics. *Proceedings of the National Academy of Sciences of the United States of America*, 115(24):6213–6218.

Blanchoin, L. and Pollard, T. D. (**2002**). Hydrolysis of ATP by polymerized actin depends on the bound divalent cation but not profilin. *Biochemistry*, 41(2):597–602.

Blanchoin, L., Pollard, T. D. and Mullins, R. D. (**2000**). Interactions of ADF/cofilin, Arp2/3 complex, capping protein and profilin in remodeling of branched actin filament networks. *Current biology*, 10(20):1273–1282.

Booth, D. S., Avila-Sakar, A. and Cheng, Y. (**2011**). Visualizing proteins and macromolecular complexes by negative stain EM: from grid preparation to image acquisition. *Journal of visualized experiments*, (58):3227.

Borowiak, M., Küllmer, F., Gegenfurtner, F. et al. (**2020**). Optical Manipulation of F-Actin with Photoswitchable Small Molecules. *Journal of the American Chemical Society*, 142(20):9240–9249.

Borowiak, M., Nahaboo, W., Reynders, M. et al. (**2015**). Photoswitchable Inhibitors of Microtubule Dynamics Optically Control Mitosis and Cell Death. *Cell*, 162(2):403–411.

Bracewell, R. N. (**1956**). Strip Integration in Radio Astronomy. *Australian Journal of Physics*, 9:198.

Bradshaw, M. and Paul, D. M. (**2019**). After the revolution: how is Cryo-EM contributing to muscle research? *Journal of muscle research and cell motility*, 40(2):93–98.

Brilot, A. F., Chen, J. Z., Cheng, A. et al. (**2012**). Beam-induced motion of vitrified specimen on holey carbon film. *Journal of structural biology*, 177(3):630–637.

Brown, A., Long, F., Nicholls, R. A., Toots, J., Emsley, P. and Murshudov, G. (**2015**). Tools for macromolecular model building and refinement into electron cryo-microscopy reconstructions. *Acta crystallographica. Section D, Biological crystallography*, 71(Pt 1):136–153.

Bryant, Z., Altman, D. and Spudich, J. A. (**2007**). The power stroke of myosin VI and the basis of reverse directionality. *Proceedings of the National Academy of Sciences of the United States of America*, 104(3):772–777.

Bubb, M. R., Spector, I., Beyer, B. B. and Fosen, K. M. (**2000**). Effects of jasplakinolide on the kinetics of actin polymerization. An explanation for certain in vivo observations. *The Journal of biological chemistry*, 275(7):5163–5170.

Burbaum, L., Schneider, J., Scholze, S., Böttcher, R. T., Baumeister, W., Schwille, P., Plitzko, J. M. and Jasnin, M. (**2020**). Molecular-scale visualization of sarcomere contraction within native cardiomyocytes. *bioRxiv*.

Burley, S. K., Berman, H. M., Bhikadiya, C. et al. (**2018**). RCSB Protein Data Bank: biological macromolecular structures enabling research and education in fundamental biology, biomedicine, biotechnology and energy. *Nucleic Acids Research*, 47(D1):D464–D474.

Cai, L., Makhov, A. M. and Bear, J. E. (**2007**a). F-actin binding is essential for coronin 1B function in vivo. *Journal of cell science*, 120(Pt 10):1779–1790.

Cai, L., Marshall, T. W., Uetrecht, A. C., Schafer, D. A. and Bear, J. E. (**2007**b). Coronin 1B coordinates Arp2/3 complex and cofilin activities at the leading edge. *Cell*, 128(5):915–929.

Carlier, M. F. and Pantaloni, D. (**1986**). Direct evidence for ADP-inorganic phosphate-F-actin as the major intermediate in ATP-actin polymerization. Rate of dissociation of inorganic phosphate from actin filaments. *Biochemistry*, 25(24):7789–7792.

Carlier, M. F. and Pantaloni, D. (**1988**). Binding of phosphate to F-ADP-actin and role of F-ADP-Pi-actin in ATP-actin polymerization. *Journal of Biological Chemistry*, 263(2):817–825.

CDC (**1970**). Centers of Disease Control and Prevention - Public Health Image Library ID:4162, *Helminthosporium*. Public domain, free of any copyright. Website: https://phil.cdc.gov/Details.aspx?pid=4162. Accessed 11.12.2020.

Cecchini, M., Alexeev, Y. and Karplus, M. (**2010**). Pi release from myosin: a simulation analysis of possible pathways. *Structure*, 18(4):458–470.

Chakraborty, S., Jasnin, M. and Baumeister, W. (**2020**a). Three-dimensional organization of the cytoskeleton: a cryo-electron tomography perspective. *Protein science*, 29(6):1302–1320.

Chakraborty, S., Mahamid, J. and Baumeister, W. (**2020**b). Cryoelectron Tomography Reveals Nanoscale Organization of the Cytoskeleton and Its Relation to Microtubule Curvature Inside Cells. *Structure*, 28(9):991–1003.e4.

Chem Sim 2001 (**2020**). Skeletal formula of phalloidin, a bicyclic heptapeptide produced by the death cap mushroom Amanita phalloides. Public domain, free of any copyright. Website: https://commons.wikimedia.org/wiki/File:Skeletal_formula_of_phalloidin.svg. Accessed 11.12.2020.

Chen, J., Noble, A. J., Kang, J. Y. and Darst, S. A. (**2019**). Eliminating effects of particle adsorption to the air/water interface in single-particle cryo-electron microscopy: Bacterial RNA polymerase and CHAPSO. *Journal of structural biology: X*, 1:100005.

Chen, V. B., Arendall, W. B., Headd, J. J. et al. (**2010**). MolProbity: all-atom structure validation for macromolecular crystallography. *Acta crystallographica. Section D, Biological crystallography*, 66(Pt 1):12–21.

Cho, C. and Vale, R. D. (**2012**). The mechanism of dynein motility: insight from crystal structures of the motor domain. *Biochimica et biophysica acta*, 1823(1):182–191.

Chou, S. Z. and Pollard, T. D. (**2019**). Mechanism of actin polymerization revealed by cryo-EM structures of actin filaments with three different bound nucleotides. *Proceedings of the National Academy of Sciences of the United States of America*, 116(10):4265–4274.

Chou, S. Z. and Pollard, T. D. (**2020**). Cryo-electron microscopy structures of pyrene-labeled ADP-Pi- and ADP-actin filaments. *Nature communications*, 11(1):5897–9.

Coluccio, L. M., editor (**2020**). *Myosins. A Superfamily of Molecular Motors*, volume 1239 of *Advances in Experimental Medicine and Biology*. Springer International Publishing, 2nd edition.

Cooke, R. and Murdoch, L. (**1973**). Interaction of actin with analogs of adenosine triphosphate. *Biochemistry*, 12(20):3927–3932.

Cooper, J. A. (**1987**). Effects of cytochalasin and phalloidin on actin. *The Journal of cell biology*, 105(4):1473–1478.

Coureux, P.-D., Sweeney, H. L. and Houdusse, A. (**2004**). Three myosin V structures delineate essential features of chemo-mechanical transduction. *The EMBO journal*, 23(23):4527–4537.

Coureux, P.-D., Wells, A. L., Ménétrey, J., Yengo, C. M., Morris, C. A., Sweeney, H. L. and Houdusse, A. (**2003**). A structural state of the myosin V motor without bound nucleotide. *Nature*, 425(6956):419–423.

Crews, P. (**2019**a). *Jaspis splendens*. Research group website. Reprinted with permission from author. Website: https://crewslab.sites.ucsc.edu/sponges/. Accessed 11.12.2020.

Crews, P. (**2019**b). *Jasplakinolide*. Research group website. Reprinted with permission from author. Website: https://crewslab.sites.ucsc.edu/. Accessed 11.12.2020.

Crews, P., Manes, L. V. and Boehler, M. (**1986**). Jasplakinolide, a cyclodepsipeptide from the marine sponge, *Jaspis* SP. *Tetrahedron Letters*, 27(25):2797–2800.

Croll, T. I. (**2018**). ISOLDE: a physically realistic environment for model building into low-resolution electron-density maps. *Acta crystallographica. Section D, Structural biology*, 74(Pt 6):519–530.

Curry, S. (**2015**). Structural Biology: A Century-long Journey into an Unseen World. *Interdisciplinary science reviews : ISR*, 40(3):308–328.

Dancker, P. and Hess, L. (**1990**). Phalloidin reduces the release of inorganic phosphate during actin polymerization. *Biochimica et biophysica acta*, 1035(2):197–200.

Dancker, P., Löw, I., Hasselbach, W. and Wieland, T. (**1975**). Interaction of actin with phalloidin: polymerization and stabilization of F-actin. *Biochimica et biophysica acta*, 400(2):407–414.

Danev, R. and Baumeister, W. (**2016**). Cryo-EM single particle analysis with the Volta phase plate. *eLife*, 5:e13046.

Danev, R., Buijsse, B., Khoshouei, M., Plitzko, J. M. and Baumeister, W. (**2014**). Volta potential phase plate for in-focus phase contrast transmission electron microscopy. *Proceedings of the National Academy of Sciences of the United States of America*, 111(44):15635–15640.

Das, S., Ge, P., Oztug Durer, Z. A., Grintsevich, E. E., Zhou, Z. H. and Reisler, E. (**2020**). D-loop Dynamics and Near-Atomic-Resolution Cryo-EM Structure of Phalloidin-Bound F-Actin. *Structure*, 28(5):586–593.e3.

De Rosier, D. J. (**1997**). Electron cryomicroscopy. Who needs crystals anyway? *Nature*, 386(6620):26–27.

Debreczeni, J. É. and Emsley, P. (**2012**). Handling ligands with Coot. *Acta crystallographica. Section D, Biological crystallography*, 68(Pt 4):425–430.

Dick, R. A., Xu, C., Morado, D. R. et al. (**2020**). Structures of immature EIAV Gag lattices reveal a conserved role for IP6 in lentivirus assembly. *PLoS pathogens*, 16(1):e1008277.

DiMaio, F., Song, Y., Li, X. et al. (**2015**). Atomic-accuracy models from 4.5-Å cryo-electron microscopy data with density-guided iterative local refinement. *Nature methods*, 12(4):361–365.

D'Imprima, E., Floris, D., Joppe, M., Sánchez, R., Grininger, M. and Kühlbrandt, W. (**2019**). Protein denaturation at the air-water interface and how to prevent it. *eLife*, 8:e42747.

Dobrowolski, J. M., Niesman, I. R. and Sibley, L. D. (**1997**). Actin in the parasite Toxoplasma gondii is encoded by a single copy gene, ACT1 and exists primarily in a globular form. *Cell motility and the cytoskeleton*, 37(3):253–262.

Dominguez, R. and Holmes, K. C. (**2011**). Actin structure and function. *Annual review of biophysics*, 40(1):169–186.

Doran, M. H., Pavadai, E., Rynkiewicz, M. J. et al. (**2020**). Cryo-EM and Molecular Docking Shows Myosin Loop 4 Contacts Actin and Tropomyosin on Thin Filaments. *Biophysical journal*, 119(4):821–830.

Drewry, L. L. and Sibley, L. D. (**2015**). Toxoplasma Actin Is Required for Efficient Host Cell Invasion. *mBio*, 6(3):e00557.

Drubin, D. G., Jones, H. D. and Wertman, K. F. (**1993**). Actin structure and function: roles in mitochondrial organization and morphogenesis in budding yeast and identification of the phalloidin-binding site. *Molecular biology of the cell*, 4(12):1277–1294.

Drummond, D. R., Peckham, M., Sparrow, J. C. and White, D. C. (**1990**). Alteration in crossbridge kinetics caused by mutations in actin. *Nature*, 348(6300):440–442.

Dubochet, J. (**2011**). Cryo-EM-the first thirty years. *Journal of microscopy*, 245(3):221–224.

Dubochet, J., Adrian, M., Chang, J. J., Homo, J. C., Lepault, J., McDowall, A. W. and Schultz, P. (**1988**). Cryo-electron microscopy of vitrified specimens. *Quarterly reviews of biophysics*, 21(2):129–228.

Edgar181 (**2010**). Chemical structure of cytochalasin D. Public domain, free of any copyright. Website: https://en.wikipedia.org/wiki/File:Cytochalasin_D.png. Accessed 11.12.2020.

Edgar181 (**2015**). Chemical structure of latrunculin A. Public domain, free of any copyright. Website: https://commons.wikimedia.org/wiki/File:Latrunculin_A_structure.svg. Accessed 11.12.2020.

Egelman, E. H. (**2000**). A robust algorithm for the reconstruction of helical filaments using single-particle methods. *Ultramicroscopy*, 85(4):225–234.

Egelman, E. H. (**2007**a). Single-particle reconstruction from EM images of helical filaments. *Current opinion in structural biology*, 17(5):556–561.

Egelman, E. H. (**2007**b). The iterative helical real space reconstruction method: surmounting the problems posed by real polymers. *Journal of structural biology*, 157(1):83–94.

Egelman, E. H. (**2014**). Ambiguities in helical reconstruction. *eLife*, 3:e04969.

Egelman, E. H., Francis, N. and DeRosier, D. J. (**1982**). F-actin is a helix with a random variable twist. *Nature*, 298(5870):131–135.

Egerton, R. F., editor (**2005**). *Physical Principles of Electron Microscopy - An Introduction to TEM, SEM and AEM*. Springer, 1st edition.

Emsley, P., Lohkamp, B., Scott, W. G. and Cowtan, K. (**2010**). Features and development of Coot. *Acta crystallographica. Section D, Biological crystallography*, 66(Pt 4):486–501.

Erickson, H. P. (**2001**). Cytoskeleton. Evolution in bacteria. *Nature*, 413(6851):30.

Estes, J. E., Selden, L. A. and Gershman, L. C. (**1981**). Mechanism of action of phalloidin on the polymerization of muscle actin. *Biochemistry*, 20(4):708–712.

Eswar, N., Eramian, D., Webb, B., Shen, M.-Y. and Sali, A. (**2008**). Protein structure modeling with MODELLER. *Methods in molecular biology*, 426:145–159.

Faruqi, A. R. and Henderson, R. (**2007**). Electronic detectors for electron microscopy. *Current opinion in structural biology*, 17(5):549–555.

Fäßler, F., Dimchev, G., Hodirnau, V.-V., Wan, W. and Schur, F. K. M. (**2020**). Cryo-electron tomography structure of Arp2/3 complex in cells reveals new insights into the branch junction. *Nature communications*, 11(1):6437–10.

Faulstich, H., Schäfer, A. J. and Weckauf, M. (**1977**). The dissociation of the phalloidin-actin complex. *Hoppe-Seyler's Zeitschrift für physiologische Chemie*, 358(2):181–184.

Fenteany, G. and Zhu, S. (**2003**). Small-molecule inhibitors of actin dynamics and cell motility. *Current topics in medicinal chemistry*, 3(6):593–616.

Firtel, R. A. (**1981**). Multigene families encoding actin and tubulin. *Cell*, 24(1):6–7.

Fischer, S., Windshügel, B., Horak, D., Holmes, K. C. and Smith, J. C. (**2005**). Structural mechanism of the recovery stroke in the myosin molecular motor. *Proceedings of the National Academy of Sciences of the United States of America*, 102(19):6873–6878.

Fisher, A. J., Smith, C. A., Thoden, J. B., Smith, R., Sutoh, K., Holden, H. M. and Rayment, I. (**1995**). X-ray structures of the myosin motor domain of Dictyostelium discoideum complexed with MgADP·BeF_x and MgADP·AlF4$^-$. *Biochemistry*, 34(28):8960–8972.

Fleishman, S. J., Leaver-Fay, A., Corn, J. E. et al. (**2011**). RosettaScripts: a scripting language interface to the Rosetta macromolecular modeling suite. *PloS one*, 6(6):e20161.

Frank, J. (**1973**). The envelope of electron microscopic transfer functions for partially coherent illumination. *Optik*, 38:519–539.

Frank, J. (**2005**). *Three-Dimensional Electron Microscopy of Macromolecular Assemblies. Visualization of Biological Molecules in Their Native State*. Oxford University Press Inc.

Frank, J. (**2017**). Time-resolved cryo-electron microscopy: Recent progress. *Journal of structural biology*, 200(3):303–306.

Fujii, T., Iwane, A. H., Yanagida, T. and Namba, K. (**2010**). Direct visualization of secondary structures of F-actin by electron cryomicroscopy. *Nature*, 467(7316):724–728.

Fujii, T. and Namba, K. (**2017**). Structure of actomyosin rigour complex at 5.2 Å resolution and insights into the ATPase cycle mechanism. *Nature communications*, 8:13969.

Funk, J., Merino, F., Venkova, L. et al. (**2019**). Profilin and formin constitute a pacemaker system for robust actin filament growth. *eLife*, 8:e50963.

Galkin, V. E., Orlova, A. and Egelman, E. H. (**2012**). Actin filaments as tension sensors. *Current biology*, 22(3):R96–101.

Galkin, V. E., Orlova, A., Schröder, G. F. and Egelman, E. H. (**2010**). Structural polymorphism in F-actin. *Nature structural & molecular biology*, 17(11):1318–1323.

Galkin, V. E., Orlova, A., Vos, M. R., Schröder, G. F. and Egelman, E. H. (**2015**). Near-atomic resolution for one state of F-actin. *Structure*, 23(1):173–182.

Gao, M., Berghaus, M., von der Ecken, J., Raunser, S. and Winter, R. (**2015**). Condensation agents determine the temperature-pressure stability of F-actin bundles. *Angewandte Chemie (International ed. in English)*, 54(38):11088–11092.

Ge, P., Durer, Z. A. O., Kudryashov, D., Zhou, Z. H. and Reisler, E. (**2014**). Cryo-EM reveals different coronin binding modes for ADP– and ADP–BeFx actin filaments. *Nature structural & molecular biology*, 21(12):1075–1081.

Geeves, M. A. and Holmes, K. C. (**1999**). Structural mechanism of muscle contraction. *Annual review of biochemistry*, 68(1):687–728.

Gemperlein, K., Zaburannyi, N., Garcia, R., La Clair, J. and Müller, R. (**2018**). Metabolic and Biosynthetic Diversity in Marine Myxobacteria. *Marine Drugs*, 16(9):314–16.

Glaeser, R. M. (**2013**). Invited review article: Methods for imaging weak-phase objects in electron microscopy. *The Review of scientific instruments*, 84(11):111101.

Glaeser, R. M. (**2018**). PROTEINS, INTERFACES, AND CRYO-EM GRIDS. *Current opinion in colloid & interface science*, 34:1–8.

Glaeser, R. M. (**2019**). How Good Can Single-Particle Cryo-EM Become? What Remains Before It Approaches Its Physical Limits? *Annual review of biophysics*, 48(1):45–61.

Glaeser, R. M., Hagen, W. J. H., Han, B.-G., Henderson, R., McMullan, G. and Russo, C. J. (**2021**). Defocus-dependent Thon-ring fading. *Ultramicroscopy*, 222:113213.

Glaeser, R. M. and Hall, R. J. (**2011**). Reaching the information limit in cryo-EM of biological macromolecules: experimental aspects. *Biophysical journal*, 100(10):2331–2337.

Goddard, T. D., Huang, C. C., Meng, E. C., Pettersen, E. F., Couch, G. S., Morris, J. H. and Ferrin, T. E. (**2018**). UCSF ChimeraX: Meeting modern challenges in visualization and analysis. *Protein science*, 27(1):14–25.

Goddette, D. W. and Frieden, C. (**1986**). The kinetics of cytochalasin D binding to monomeric actin. *Journal of Biological Chemistry*, 261(34):15970–15973.

Goody, R. S., Hofmann, W. and Mannherz, G. H. (**1977**). The binding constant of ATP to myosin S1 fragment. *European journal of biochemistry / FEBS*, 78(2):317–324.

Goody, R. S., Reedy, M. C., Hofmann, W., Holmes, K. C. and Reedy, M. K. (**1985**). Binding of myosin subfragment 1 to glycerinated insect flight muscle in the rigor state. *Biophysical journal*, 47(2 Pt 1):151–169.

Grant, B. J., Rodrigues, A. P. C., ElSawy, K. M., McCammon, J. A. and Caves, L. S. D. (**2006**). Bio3d: an R package for the comparative analysis of protein structures. *Bioinformatics*, 22(21):2695–2696.

Grant, T. and Grigorieff, N. (**2015**). Measuring the optimal exposure for single particle cryo-EM using a 2.6 Å reconstruction of rotavirus VP6. *eLife*, 4:e06980.

Greenberg, M. J., Arpağ, G., Tüzel, E. and Ostap, E. M. (**2016**). A Perspective on the Role of Myosins as Mechanosensors. *Biophysical journal*, 110(12):2568–2576.

Gringer (**2009**). Diagram outlining the internal components of a basic TEM system. GNU Free Documentation License and Creative Commons License. Website: https://commons.wikimedia.org/wiki/File:Scheme_TEM_en.svg. Accessed 21.11.2020.

Grintsevich, E. E., Ge, P., Sawaya, M. R., Yesilyurt, H. G., Terman, J. R., Zhou, Z. H. and Reisler, E. (**2017**). Catastrophic disassembly of actin filaments via Mical-mediated oxidation. *Nature communications*, 8(1):2183.

Groom, C. R., Bruno, I. J., Lightfoot, M. P. and Ward, S. C. (**2016**). The Cambridge Structural Database. *Acta crystallographica. Section B*, 72(Pt. 2):171–179.

Gulick, A. M., Bauer, C. B., Thoden, J. B. and Rayment, I. (**1997**). X-ray structures of the MgADP, MgATPgammaS, and MgAMPPNP complexes of the Dictyostelium discoideum myosin motor domain. *Biochemistry*, 36(39):11619–11628.

Gunning, P. W., Ghoshdastider, U., Whitaker, S., Popp, D. and Robinson, R. C. (**2015**). The evolution of compositionally and functionally distinct actin filaments. *Journal of cell science*, 128(11):2009–2019.

Gurel, P. S., Kim, L. Y., Ruijgrok, P. V., Omabegho, T., Bryant, Z. and Alushin, G. M. (**2017**). Cryo-EM structures reveal specialization at the myosin VI-actin interface and a mechanism of force sensitivity. *eLife*, 6:e31125.

Hagen, W. J. H., Wan, W. and Briggs, J. A. G. (**2016**). Implementation of a cryo-electron tomography tilt-scheme optimized for high resolution subtomogram averaging. *Journal of structural biology*, 197(2):191–198.

Hanson, J. and Huxley, H. E. (**1953**). Structural basis of the cross-striations in muscle. *Nature*, 172(4377):530–532.

Harris, C. R., Millman, K. J., van der Walt, S. J. et al. (**2020**). Array programming with NumPy. *Nature*, 585(7825):357–362.

Hartman, M. A., Finan, D., Sivaramakrishnan, S. and Spudich, J. A. (**2011**). Principles of unconventional myosin function and targeting. *Annual review of cell and developmental biology*, 27(1):133–155.

Hayward, S. and Lee, R. A. (**2002**). Improvements in the analysis of domain motions in proteins from conformational change: DynDom version 1.50. *Journal of molecular graphics & modelling*, 21(3):181–183.

He, S. and Scheres, S. H. W. (**2017**). Helical reconstruction in RELION. *Journal of structural biology*, 198(3):163–176.

Henderson, R. (**1995**). The potential and limitations of neutrons, electrons and X-rays for atomic resolution microscopy of unstained biological molecules. *Quarterly reviews of biophysics*, 28(2):171–193.

Henderson, R., Sali, A., Baker, M. L. et al. (**2012**). Outcome of the first electron microscopy validation task force meeting. *Structure*, 20(2):205–214.

Hertzog, M. and Carlier, M.-F. (**2005**). Functional characterization of proteins regulating actin assembly. *Current protocols in cell biology*, Chapter 13(1):Unit 13.6–13.6.23.

Hessa, T., Kim, H., Bihlmaier, K. et al. (**2005**). Recognition of transmembrane helices by the endoplasmic reticulum translocon. *Nature*, 433(7024):377–381.

Hliscs, M., Millet, C., Dixon, M. W., Sidén-Kiamos, I., McMillan, P. and Tilley, L. (**2015**). Organization and function of an actin cytoskeleton in Plasmodium falciparum gametocytes. *Cellular microbiology*, 17(2):207–225.

Hodge, T. and Cope, M. J. (**2000**). A myosin family tree. *Journal of cell science*, 113 Pt 19:3353–3354.

Hohn, M., Tang, G., Goodyear, G. et al. (**2007**). SPARX, a new environment for Cryo-EM image processing. *Journal of structural biology*, 157(1):47–55.

Holmes, K. C. (**1997**). The swinging lever-arm hypothesis of muscle contraction. *Current biology*, 7(2):R112–8.

Holmes, K. C., Popp, D., Gebhard, W. and Kabsch, W. (**1990**). Atomic model of the actin filament. *Nature*, 347(6288):44–49.

Houdusse, A., Kalabokis, V. N., Himmel, D., Szent-Györgyi, A. G. and Cohen, C. (**1999**). Atomic structure of scallop myosin subfragment S1 complexed with MgADP: a novel conformation of the myosin head. *Cell*, 97(4):459–470.

Houdusse, A. and Sweeney, H. L. (**2016**). How Myosin Generates Force on Actin Filaments. *Trends in biochemical sciences*, 41(12):989–997.

Huehn, A., Cao, W., Elam, W. A., Liu, X., De La Cruz, E. M. and Sindelar, C. V. (**2018**). The actin filament twist changes abruptly at boundaries between bare and cofilin-decorated segments. *The Journal of biological chemistry*, 293(15):5377–5383.

Huehn, A. R., Bibeau, J. P., Schramm, A. C., Cao, W., De La Cruz, E. M. and Sindelar, C. V. (**2020**). Structures of cofilin-induced structural changes reveal local and asymmetric perturbations of actin filaments. *Proceedings of the National Academy of Sciences of the United States of America*, 117(3):1478–1484.

Hunter, J. D. (**2007**). Matplotlib: A 2D graphics environment. *Computing in Science & Engineering*, 9(3):90–95.

Huxley, A. F. and Niedergerke, R. (**1954**). Structural changes in muscle during contraction; interference microscopy of living muscle fibres. *Nature*, 173(4412):971–973.

Huxley, H. E. (**2004**). Fifty years of muscle and the sliding filament hypothesis. *European journal of biochemistry / FEBS*, 271(8):1403–1415.

Ilari, A. and Savino, C. (**2008**). Protein structure determination by x-ray crystallography. *Methods in molecular biology*, 452:63–87.

Irwin, J. J. and Shoichet, B. K. (**2005**). ZINC–a free database of commercially available compounds for virtual screening. *Journal of chemical information and modeling*, 45(1):177–182.

Isambert, H., Venier, P., Maggs, A. C., Fattoum, A., Kassab, R., Pantaloni, D. and Carlier, M. F. (**1995**). Flexibility of actin filaments derived from thermal fluctuations. Effect of bound nucleotide, phalloidin, and muscle regulatory proteins. *Journal of Biological Chemistry*, 270(19):11437–11444.

Iwamoto, D. V., Huehn, A., Simon, B., Huet-Calderwood, C., Baldassarre, M., Sindelar, C. V. and Calderwood, D. A. (**2018**). Structural basis of the filamin A actin-binding domain interaction with F-actin. *Nature structural & molecular biology*, 25(10):918–927.

Jin, L., Milazzo, A.-C., Kleinfelder, S. et al. (**2008**). Applications of direct detection device in transmission electron microscopy. *Journal of structural biology*, 161(3):352–358.

Kabsch, W., Mannherz, H. G., Suck, D., Pai, E. F. and Holmes, K. C. (**1990**). Atomic structure of the actin:DNase I complex. *Nature*, 347(6288):37–44.

Kardos, R., Vig, A., Orbán, J., Hild, G., Nyitrai, M. and Lorinczy, D. (**2007**). The effect of jasplakinolide on the thermodynamic properties of ADP.BeF(x) bound actin filaments. *Thermochimica acta*, 463(1-2):77–80.

Katagiri, K. and Matsuura, S. (**1971**). Antitumor activity of cytochalasin D. *The Journal of antibiotics*, 24(10):722–723.

Keeley, A. and Soldati, D. (**2004**). The glideosome: a molecular machine powering motility and host-cell invasion by Apicomplexa. *Trends in cell biology*, 14(10):528–532.

Khoshouei, M., Radjainia, M., Phillips, A. J., Gerrard, J. A., Mitra, A. K., Plitzko, J. M., Baumeister, W. and Danev, R. (**2016**). Volta phase plate cryo-EM of the small protein complex Prx3. *Nature communications*, 7:10534.

Kikkawa, M., Sablin, E. P., Okada, Y., Yajima, H., Fletterick, R. J. and Hirokawa, N. (**2001**). Switch-based mechanism of kinesin motors. *Nature*, 411(6836):439–445.

Kim, E., Bobkova, E., Hegyi, G., Muhlrad, A. and Reisler, E. (**2002**). Actin cross-linking and inhibition of the actomyosin motor. *Biochemistry*, 41(1):86–93.

Klein, J. C., Burr, A. R., Svensson, B., Kennedy, D. J., Allingham, J., Titus, M. A., Rayment, I. and Thomas, D. D. (**2008**). Actin-binding cleft closure in myosin II probed by site-directed spin labeling and pulsed EPR. *Proceedings of the National Academy of Sciences of the United States of America*, 105(35):12867–12872.

Kollmar, M., Dürrwang, U., Kliche, W., Manstein, D. J. and Kull, F. J. (**2002**). Crystal structure of the motor domain of a class-I myosin. *The EMBO journal*, 21(11):2517–2525.

Kortemme, T. and Baker, D. (**2002**). A simple physical model for binding energy hot spots in protein-protein complexes. *Proceedings of the National Academy of Sciences of the United States of America*, 99(22):14116–14121.

Kortemme, T., Kim, D. E. and Baker, D. (**2004**). Computational alanine scanning of protein-protein interfaces. *Science's STKE*, 2004(219):pl2.

Koubassova, N. A. and Tsaturyan, A. K. (**2011**). Molecular mechanism of actin-myosin motor in muscle. *Biochemistry. Biokhimiia*, 76(13):1484–1506.

Kouyama, T. and Mihashi, K. (**1981**). Fluorimetry study of N-(1-pyrenyl)iodoacetamide-labelled F-actin. Local structural change of actin protomer both on polymerization and on binding of heavy meromyosin. *European journal of biochemistry / FEBS*, 114(1):33–38.

Kovács, M., Thirumurugan, K., Knight, P. J. and Sellers, J. R. (**2007**). Load-dependent mechanism of nonmuscle myosin 2. *Proceedings of the National Academy of Sciences of the United States of America*, 104(24):9994–9999.

Kovar, D. R. and Pollard, T. D. (**2004**). Insertional assembly of actin filament barbed ends in association with formins produces piconewton forces. *Proceedings of the National Academy of Sciences of the United States of America*, 101(41):14725–14730.

Kudryashev, M., Lepper, S., Baumeister, W., Cyrklaff, M. and Frischknecht, F. (**2010**). Geometric constrains for detecting short actin filaments by cryogenic electron tomography. *PMC biophysics*, 3(1):6.

Kudryashov, D. S., Grintsevich, E. E., Rubenstein, P. A. and Reisler, E. (**2010**). A nucleotide state-sensing region on actin. *The Journal of biological chemistry*, 285(33):25591–25601.

Kudryashov, D. S. and Reisler, E. (**2013**). ATP and ADP actin states. *Biopolymers*, 99(4):245–256.

Kudryashov, D. S., Sawaya, M. R., Adisetiyo, H., Norcross, T., Hegyi, G., Reisler, E. and Yeates, T. O. (**2005**). The crystal structure of a cross-linked actin dimer suggests a detailed molecular interface in F-actin. *Proceedings of the National Academy of Sciences of the United States of America*, 102(37):13105–13110.

Kühlbrandt, W. (**2014**). Biochemistry. The resolution revolution. *Science*, 343(6178):1443–1444.

Kuhlman, B. and Bradley, P. (**2019**). Advances in protein structure prediction and design. *Nature reviews. Molecular cell biology*, 20(11):681–697.

Kull, F. J. and Endow, S. A. (**2013**). Force generation by kinesin and myosin cytoskeletal motor proteins. *Journal of cell science*, 126(Pt 1):9–19.

Kumari, A., Kesarwani, S., Javoor, M. G., Vinothkumar, K. R. and Sirajuddin, M. (**2020**). Structural insights into actin filament recognition by commonly used cellular actin markers. *The EMBO journal*, 39(14):e104006.

Kumpula, E.-P. and Kursula, I. (**2015**). Towards a molecular understanding of the apicomplexan actin motor: on a road to novel targets for malaria remedies? *Acta crystallographica. Section F, Structural biology communications*, 71(Pt 5):500–513.

Laakso, J. M., Lewis, J. H., Shuman, H. and Ostap, E. M. (**2008**). Myosin I can act as a molecular force sensor. *Science*, 321(5885):133–136.

Lander, E. S., Linton, L. M., Birren, B. et al. (**2001**). Initial sequencing and analysis of the human genome. *Nature*, 409(6822):860–921.

Laskowski, R. A. (**2009**). PDBsum new things. *Nucleic Acids Research*, 37:D355–9.

Laskowski, R. A. and Swindells, M. B. (**2011**). LigPlot+: multiple ligand-protein interaction diagrams for drug discovery. *Journal of chemical information and modeling*, 51(10):2778–2786.

Lawson, C. L., Baker, M. L., Best, C. et al. (**2011**). EMDataBank.org: unified data resource for CryoEM. *Nucleic Acids Research*, 39:D456–64.

Lawson, J. D., Pate, E., Rayment, I. and Yount, R. G. (**2004**). Molecular dynamics analysis of structural factors influencing back door pi release in myosin. *Biophysical journal*, 86(6):3794–3803.

Lehman, W., Orzechowski, M., Li, X. E., Fischer, S. and Raunser, S. (**2013**). Gestalt-binding of tropomyosin on actin during thin filament activation. *Journal of muscle research and cell motility*, 34(3-4):155–163.

Leidenfrost, J. G. (**1796**). *De aquae communis nonnullis qualitatibus tractatus*. Hermann Ovenius, reprint H. W. Cramer.

Leidreiter, F., Roderer, D., Meusch, D., Gatsogiannis, C., Benz, R. and Raunser, S. (**2019**). Common architecture of Tc toxins from human and insect pathogenic bacteria. *Science advances*, 5(10):eaax6497.

Lengsfeld, A. M., Löw, I., Wieland, T., Dancker, P. and Hasselbach, W. (**1974**). Interaction of phalloidin with actin. *Proceedings of the National Academy of Sciences of the United States of America*, 71(7):2803–2807.

Li, X., Mooney, P., Zheng, S., Booth, C. R., Braunfeld, M. B., Gubbens, S., Agard, D. A. and Cheng, Y. (**2013**). Electron counting and beam-induced motion correction enable near-atomic-resolution single-particle cryo-EM. *Nature methods*, 10(6):584–590.

Llinas, P., Isabet, T., Song, L. et al. (**2015**). How actin initiates the motor activity of Myosin. *Developmental cell*, 33(4):401–412.

Lodish, H., Berk, A., Zipursky, S. L., Matsudaira, P., Baltimore, D. and Darnell, J. (**2000**). *Molecular Cell Biology*. W. H. Freeman, New York, 4th edition.

Lopéz-Blanco, J. R. and Chacón, P. (**2013**). iMODFIT: efficient and robust flexible fitting based on vibrational analysis in internal coordinates. *Journal of structural biology*, 184(2):261–270.

Lorenz, M., Popp, D. and Holmes, K. C. (**1993**). Refinement of the F-actin model against X-ray fiber diffraction data by the use of a directed mutation algorithm. *Journal of Molecular Biology*, 234(3):826–836.

Löwe, J., He, S., Scheres, S. H. W. and Savva, C. G. (**2016**). X-ray and cryo-EM structures of monomeric and filamentous actin-like protein MamK reveal changes associated with polymerization. *Proceedings of the National Academy of Sciences of the United States of America*, 113(47):13396–13401.

Lu, Z., Shaikh, T. R., Barnard, D. et al. (**2009**). Monolithic microfluidic mixing-spraying devices for time-resolved cryo-electron microscopy. *Journal of structural biology*, 168(3):388–395.

Lukinavičius, G., Reymond, L., D'Este, E. et al. (**2014**). Fluorogenic probes for live-cell imaging of the cytoskeleton. *Nature methods*, 11(7):731–733.

Lymn, R. W. and Taylor, E. W. (**1971**). Mechanism of adenosine triphosphate hydrolysis by actomyosin. *Biochemistry*, 10(25):4617–4624.

Lynen, F. and Wieland, U. (**1938**). Über die Giftstoffe des Knollenblätterpilzes. IV. *Justus Liebig's Annalen der Chemie*, 533(1):93–117.

Malik, F. I., Hartman, J. J., Elias, K. A. et al. (**2011**). Cardiac myosin activation: a potential therapeutic approach for systolic heart failure. *Science*, 331(6023):1439–1443.

Marko, M., Hsieh, C., Moberlychan, W., Mannella, C. A. and Frank, J. (**2006**). Focused ion beam milling of vitreous water: prospects for an alternative to cryo-ultramicrotomy of frozen-hydrated biological samples. *Journal of microscopy*, 222(Pt 1):42–47.

Martins, B., Sorrentino, S., Chung, W.-L., Tatli, M., Medalia, O. and Eibauer, M. (**2021**). Unveiling the polarity of actin filaments by cryo-electron tomography. *Structure*. doi: 10.1016/j.str.2020.12.014.

Marvin, D. A. and Nave, C. (**1982**). *X-ray Fiber Diffraction*. Springer, pp. 3–44.

McGough, A., Pope, B., Chiu, W. and Weeds, A. (**1997**). Cofilin Changes the Twist of F-Actin: Implications for Actin Filament Dynamics and Cellular Function. *The Journal of cell biology*, 138(4):771–781.

McPherson, A. and Gavira, J. A. (**2014**). Introduction to protein crystallization. *Acta crystallographica. Section F, Structural biology communications*, 70(Pt 1):2–20.

Mei, L., Espinosa de Los Reyes, S., Reynolds, M. J., Leicher, R., Liu, S. and Alushin, G. M. (**2020**). Molecular mechanism for direct actin force-sensing by α-catenin. *eLife*, 9:e62514.

Melak, M., Plessner, M. and Grosse, R. (**2017**). Actin visualization at a glance. *Journal of cell science*, 130(3):525–530.

Ménétrey, J., Bahloul, A., Wells, A. L., Yengo, C. M., Morris, C. A., Sweeney, H. L. and Houdusse, A. (**2005**). The structure of the myosin VI motor reveals the mechanism of directionality reversal. *Nature*, 435(7043):779–785.

Mentes, A., Huehn, A., Liu, X., Zwolak, A., Dominguez, R., Shuman, H., Ostap, E. M. and Sindelar, C. V. (**2018**). High-resolution cryo-EM structures of actin-bound myosin states reveal the mechanism of myosin force sensing. *Proceedings of the National Academy of Sciences of the United States of America*, 115(6):1292–1297.

Merino, F., Pospich, S., Funk, J., Wagner, T., Küllmer, F., Arndt, H.-D., Bieling, P. and Raunser, S. (**2018**). Structural transitions of F-actin upon ATP hydrolysis at near-atomic resolution revealed by cryo-EM. *Nature structural & molecular biology*, 25(6):528–537.

Merino, F., Pospich, S. and Raunser, S. (**2019**). Towards a structural understanding of the remodeling of the actin cytoskeleton. *Seminars in cell & developmental biology*, 102:51–64.

Merino, F. and Raunser, S. (**2016**a). Cryo-EM as a tool for structure-based drug development. *Angewandte Chemie*, 56(11):2846–2860.

Merino, F. and Raunser, S. (**2016**b). The mother of all actins? *eLife*, 5:e23354.

Milligan, R. A., Whittaker, M. and Safer, D. (**1990**). Molecular structure of F-actin and location of surface binding sites. *Nature*, 348(6298):217–221.

Milroy, L.-G., Rizzo, S., Calderon, A. et al. (**2012**). Selective chemical imaging of static actin in live cells. *Journal of the American Chemical Society*, 134(20):8480–8486.

Mio, K. and Sato, C. (**2018**). Lipid environment of membrane proteins in cryo-EM based structural analysis. *Biophysical Reviews*, 10(2):307–316.

Mizuno, Y., Makioka, A., Kawazu, S.-i., Kano, S., Kawai, S., Akaki, M., Aikawa, M. and Ohtomo, H. (**2002**). Effect of jasplakinolide on the growth, invasion, and actin cytoskeleton of Plasmodium falciparum. *Parasitology research*, 88(9):844–848.

Moore, P. and De Rosier, D. J. (**1970**). Reconstruction of three-dimensional images from electron micrographs of structures with helical symmetry. *Journal of Molecular Biology*, 52(2):355–369.

Moriarty, N. W., Grosse Kunstleve, R. W. and Adams, P. D. (**2009**). electronic Ligand Builder and Optimization Workbench (eLBOW): a tool for ligand coordinate and restraint generation. *Acta crystallographica. Section D, Biological crystallography*, 65(Pt 10):1074–1080.

Moriya, T., Saur, M., Stabrin, M. et al. (**2017**). High-resolution Single Particle Analysis from Electron Cryo-microscopy Images Using SPHIRE. *Journal of visualized experiments*, (123):e55448.

Muhlrad, A., Pavlov, D., Peyser, Y. M. and Reisler, E. (**2006**). Inorganic phosphate regulates the binding of cofilin to actin filaments. *The FEBS journal*, 273(7):1488–1496.

Nakane, T., Kimanius, D., Lindahl, E. and Scheres, S. H. (**2018**). Characterisation of molecular motions in cryo-EM single-particle data by multi-body refinement in RELION. *eLife*, 7:e36861.

Nakane, T., Kotecha, A., Sente, A. et al. (**2020**). Single-particle cryo-EM at atomic resolution. *Nature*, 587(7832):152–156.

Needham, J., Kleinzeller, A., Miall, M., Dainty, M., Needham, D. M. and Lawrence, A. S. C. (**1942**). IS MUSCLE CONTRACTION ESSENTIALLY AN ENZYME-SUBSTRATE COMBINATION? *Nature*, 150:46–49.

Nesmelov, Y. E., Agafonov, R. V., Burr, A. R., Weber, R. T. and Thomas, D. D. (**2008**). Structure and dynamics of the force-generating domain of myosin probed by multifrequency electron paramagnetic resonance. *Biophysical journal*, 95(1):247–256.

Nicholls, R. A., Fischer, M., McNicholas, S. and Murshudov, G. N. (**2014**). Conformation-independent structural comparison of macromolecules with ProSMART. *Acta crystallographica. Section D, Biological crystallography*, 70(Pt 9):2487–2499.

Nishikawa, S., Homma, K., Komori, Y. et al. (**2002**). Class VI myosin moves processively along actin filaments backward with large steps. *Biochemical and biophysical research communications*, 290(1):311–317.

Nitta, R., Okada, Y. and Hirokawa, N. (**2008**). Structural model for strain-dependent microtubule activation of Mg-ADP release from kinesin. *Nature structural & molecular biology*, 15(10):1067–1075.

Noguchi, T. Q. P., Komori, T., Umeki, N. et al. (**2012**). G146V mutation at the hinge region of actin reveals a myosin class-specific requirement of actin conformations for motility. *The Journal of biological chemistry*, 287(29):24339–24345.

Nyquist, H. (**1928**). Certain Topics in Telegraph Transmission Theory. *Transactions of the American Institute of Electrical Engineers*, 47(2):617–644.

Oda, T., Aihara, T. and Wakabayashi, K. (**2016**). Early nucleation events in the polymerization of actin, probed by time-resolved small-angle x-ray scattering. *Scientific reports*, 6:34539–13.

Oda, T., Iwasa, M., Aihara, T., Maéda, Y. and Narita, A. (**2009**). The nature of the globular- to fibrous-actin transition. *Nature*, 457(7228):441–445.

Oda, T., Namba, K. and Maéda, Y. (**2005**). Position and orientation of phalloidin in F-actin determined by X-ray fiber diffraction analysis. *Biophysical journal*, 88(4):2727–2736.

Oda, T. and Yanagisawa, H. (**2020**). Cryo-electron tomography of cardiac myofibrils reveals a 3D lattice spring within the Z-discs. *Communications biology*, 3(1):585–9.

Oda, T., Yanagisawa, H. and Wakabayashi, T. (**2020**). Cryo-EM structures of cardiac thin filaments reveal the 3D architecture of troponin. *Journal of structural biology*, 209(3):107450.

Olshina, M. A., Angrisano, F., Marapana, D. S. et al. (**2015**). Plasmodium falciparum coronin organizes arrays of parallel actin filaments potentially guiding directional motility in invasive malaria parasites. *Malaria journal*, 14:280.

Onishi, H., Mikhailenko, S. V. and Morales, M. F. (**2006**). Toward understanding actin activation of myosin ATPase: the role of myosin surface loops. *Proceedings of the National Academy of Sciences of the United States of America*, 103(16):6136–6141.

Orlova, E. V. and Saibil, H. R. (**2011**). Structural analysis of macromolecular assemblies by electron microscopy. *Chemical reviews*, 111(12):7710–7748.

Oztug Durer, Z. A., Diraviyam, K., Sept, D., Kudryashov, D. S. and Reisler, E. (**2010**). F-actin structure destabilization and DNase I binding loop: fluctuations mutational cross-linking and electron microscopy analysis of loop states and effects on F-actin. *Journal of Molecular Biology*, 395(3):544–557.

Oztug Durer, Z. A., Kamal, J. K. A., Benchaar, S., Chance, M. R. and Reisler, E. (**2011**). Myosin binding surface on actin probed by hydroxyl radical footprinting and site-directed labels. *Journal of Molecular Biology*, 414(2):204–216.

Oztug Durer, Z. A., Kudryashov, D. S., Sawaya, M. R., Altenbach, C., Hubbell, W. and Reisler, E. (**2012**). Structural states and dynamics of the D-loop in actin. *Biophysical journal*, 103(5):930–939.

Pardee, J. D. and Spudich, J. A. (**1982**). Purification of muscle actin. *Methods in enzymology*, 85 Pt B:164–181.

Park, H., Li, A., Chen, L.-Q., Houdusse, A., Selvin, P. R. and Sweeney, H. L. (**2007**). The unique insert at the end of the myosin VI motor is the sole determinant of directionality. *Proceedings of the National Academy of Sciences of the United States of America*, 104(3):778–783.

Paul, D. M., Mantell, J., Borucu, U., Coombs, J., Surridge, K. J., Squire, J. M., Verkade, P. and Dodding, M. P. (**2020**). In situ cryo-electron tomography reveals filamentous actin within the microtubule lumen. *The Journal of cell biology*, 219(9):e201911154.

Penczek, P. A. (**2010**a). Image restoration in cryo-electron microscopy. *Methods in enzymology*, 482:35–72.

Penczek, P. A. (**2010**b). Resolution measures in molecular electron microscopy. *Methods in enzymology*, 482:73–100.

Penczek, P. A. (**2020**). Reliable cryo-EM resolution estimation with modified Fourier shell correlation. *International Union of Crystallography Journal*, 7(Pt 6):995–1008.

Pettersen, E. F., Goddard, T. D., Huang, C. C., Couch, G. S., Greenblatt, D. M., Meng, E. C. and Ferrin, T. E. (**2004**). UCSF Chimera–a visualization system for exploratory research and analysis. *Journal of computational chemistry*, 25(13):1605–1612.

Planelles-Herrero, V. J., Hartman, J. J., Robert-Paganin, J., Malik, F. I. and Houdusse, A. (**2017**). Mechanistic and structural basis for activation of cardiac myosin force production by omecamtiv mecarbil. *Nature communications*, 8(1):190.

Pollack, A. (**2020**). *Fruiting bodies of a myxobacterium on a decaying coastal Oak in Marin County.* Instagram, personal account @marin_mushrooms. Reprinted with permission from author. Website: https://www.instagram.com/p/B8SDRohJ57H/. Accessed 11.12.2020.

Pollard, T. D. (**1986**). Rate Constants for the Reactions of ATP- and ADP-Actin with the Ends of Actin Filaments. *The Journal of cell biology*, 103(6 Pt 2):2747–2754.

Pollard, T. D. (**2016**). Actin and Actin-Binding Proteins. *Cold Spring Harbor Perspectives in Biology*, 8(8):a018226.

Pollard, T. D. and Borisy, G. G. (**2003**). Cellular motility driven by assembly and disassembly of actin filaments. *Cell*, 112(4):453–465.

Pollard, T. D. and Cooper, J. A. (**2009**). Actin, a central player in cell shape and movement. *Science*, 326(5957):1208–1212.

Pospich, S. (**2015**). *Strukturaufklärung der Aktinisoformen von Plasmodium mittels Transmissionselektronenmikroskopie*. Master's thesis, Technische Universität Dortmund.

Pospich, S., Küllmer, F., Nasufovic, V., Funk, J., Belyy, A., Bieling, P., Arndt, H.-D. and Raunser, S. (**2021**). Cryo-EM resolves molecular recognition of an optojasp photoswitch bound to actin filaments in both switch states. *Angewandte Chemie (International ed. in English)*. doi: 10.1002/anie.202013193.

Pospich, S., Kumpula, E.-P., von der Ecken, J., Vahokoski, J., Kursula, I. and Raunser, S. (**2017**). Near-atomic structure of jasplakinolide-stabilized malaria parasite F-actin reveals the structural basis of filament instability. *Proceedings of the National Academy of Sciences of the United States of America*, 114(40):10636–10641.

Pospich, S., Merino, F. and Raunser, S. (**2020**). Structural Effects and Functional Implications of Phalloidin and Jasplakinolide Binding to Actin Filaments. *Structure*, 28(4):437–449.e5.

Pospich, S. and Raunser, S. (**2017**). The molecular basis of Alzheimer's plaques. *Science*, 358(6359):45–46.

Pospich, S. and Raunser, S. (**2018**). Single particle cryo-EM-an optimal tool to study cytoskeletal proteins. *Current opinion in structural biology*, 52:16–24.

Prochniewicz, E., Chin, H. F., Henn, A., Hannemann, D. E., Olivares, A. O., Thomas, D. D. and De La Cruz, E. M. (**2010**). Myosin isoform determines the conformational dynamics and cooperativity of actin filaments in the strongly bound actomyosin complex. *Journal of Molecular Biology*, 396(3):501–509.

Prochniewicz, E. and Thomas, D. D. (**2001**). Site-specific mutations in the myosin binding sites of actin affect structural transitions that control myosin binding. *Biochemistry*, 40(46):13933–13940.

Pyrkov, T. V., Chugunov, A. O., Krylov, N. A., Nolde, D. E. and Efremov, R. G. (**2009**). PLATINUM: a web tool for analysis of hydrophobic/hydrophilic organization of biomolecular complexes. *Bioinformatics*, 25(9):1201–1202.

Qu, Z., Fujita-Becker, S., Ballweber, E., Ince, S., Herrmann, C., Schröder, R. R. and Mannherz, H. G. (**2018**). Interaction of isolated cross-linked short actin oligomers with the skeletal muscle myosin motor domain. *The FEBS journal*, 285(9):1715–1729.

Ramlaul, K., Palmer, C. M. and Aylett, C. H. S. (**2019**). A Local Agreement Filtering Algorithm for Transmission EM Reconstructions. *Journal of structural biology*, 205(1):30–40.

Rayment, I., Holden, H. M., Whittaker, M., Yohn, C. B., Lorenz, M., Holmes, K. C. and Milligan, R. A. (**1993**a). Structure of the actin-myosin complex and its implications for muscle contraction. *Science*, 261(5117):58–65.

Rayment, I., Rypniewski, W. R., Schmidt-Bäse, K. et al. (**1993**b). Three-dimensional structure of myosin subfragment-1: a molecular motor. *Science*, 261(5117):50–58.

Reece, J. B. R., Urry, L. A., Cain, M. L., Wasserman, S. A., Minorsky, P. V. and Jackson, R. B. (**2011**). *Campbell Biology*. Pearson, 9th edition.

Reedy, M. K., Holmes, K. C. and Tregear, R. T. (**1965**). Induced changes in orientation of the cross-bridges of glycerinated insect flight muscle. *Nature*, 207(5003):1276–1280.

Reimer, L. and Kohl, H. (**2008**). *Transmission Electron Microscopy - Physics of Image Dormation*. Springer series on optical sciences 36. Springer, 5th edition.

Ren, Z., Zhang, Y., Zhang, Y., He, Y., Du, P., Wang, Z., Sun, F. and Ren, H. (**2019**). Cryo-EM Structure of Actin Filaments from Zea mays Pollen. *The Plant Cell*, 31(12):2855–2867.

Reubold, T. F., Eschenburg, S., Becker, A., Kull, F. J. and Manstein, D. J. (**2003**). A structural model for actin-induced nucleotide release in myosin. *Nature structural biology*, 10(10):826–830.

Rigort, A., Bäuerlein, F. J. B., Villa, E., Eibauer, M., Laugks, T., Baumeister, W. and Plitzko, J. M. (**2012**). Focused ion beam micromachining of eukaryotic cells for cryoelectron tomography. *Proceedings of the National Academy of Sciences of the United States of America*, 109(12):4449–4454.

Risi, C., Eisner, J., Belknap, B., Heeley, D. H., White, H. D., Schröder, G. F. and Galkin, V. E. (**2017**). Ca^{2+}-induced movement of tropomyosin on native cardiac thin filaments revealed by cryoelectron microscopy. *Proceedings of the National Academy of Sciences of the United States of America*, 114(26):6782–6787.

Risi, C., Schäfer, L. U., Belknap, B., Pepper, I., White, H. D., Schröder, G. F. and Galkin, V. E. (**2020**). High-Resolution Cryo-EM Structure of the Cardiac Actomyosin Complex. *Structure*, 29(1):50–60.e4.

Robenek, H. (**1995**). *Mikroskopie in Forschung und Praxis*. GIT Verlag GmbH, Darmstadt.

Robert-Paganin, J., Pylypenko, O., Kikuti, C., Sweeney, H. L. and Houdusse, A. (**2020**). Force Generation by Myosin Motors: A Structural Perspective. *Chemical reviews*, 120(1):5–35.

Robert-Paganin, J., Robblee, J. P., Auguin, D. et al. (**2019**). Plasmodium myosin A drives parasite invasion by an atypical force generating mechanism. *Nature communications*, 10(1):3286.

Rohde, J. A., Thomas, D. D. and Muretta, J. M. (**2017**). Heart failure drug changes the mechanoenzymology of the cardiac myosin powerstroke. *Proceedings of the National Academy of Sciences of the United States of America*, 114(10):E1796–E1804.

Rohou, A. and Grigorieff, N. (**2015**). CTFFIND4: Fast and accurate defocus estimation from electron micrographs. *Journal of structural biology*, 192(2):216–221.

Rosenthal, P. B. and Henderson, R. (**2003**). Optimal determination of particle orientation, absolute hand, and contrast loss in single-particle electron cryomicroscopy. *Journal of Molecular Biology*, 333(4):721–745.

Rould, M. A., Wan, Q., Joel, P. B., Lowey, S. and Trybus, K. M. (**2006**). Crystal structures of expressed non-polymerizable monomeric actin in the ADP and ATP states. *Journal of Biological Chemistry*, 281(42):31909–31919.

Ruskin, R. S., Yu, Z. and Grigorieff, N. (**2013**). Quantitative characterization of electron detectors for transmission electron microscopy. *Journal of structural biology*, 184(3):385–393.

Russo, C. J. and Passmore, L. A. (**2016**). Progress towards an optimal specimen support for electron cryomicroscopy. *Current opinion in structural biology*, 37:81–89.

Sablin, E. P., Kull, F. J., Cooke, R., Vale, R. D. and Fletterick, R. J. (**1996**). Crystal structure of the motor domain of the kinesin-related motor ncd. *Nature*, 380(6574):555–559.

Sali, A. and Blundell, T. L. (**1993**). Comparative protein modelling by satisfaction of spatial restraints. *Journal of Molecular Biology*, 234(3):779–815.

Sawaya, M. R., Kudryashov, D. S., Pashkov, I., Adisetiyo, H., Reisler, E. and Yeates, T. O. (**2008**). Multiple crystal structures of actin dimers and their implications for interactions in the actin filament. *Acta crystallographica. Section D, Biological crystallography*, 64(Pt 4):454–465.

Scarff, C. A., Carrington, G., Casas-Mao, D., Chalovich, J. M., Knight, P. J., Ranson, N. A. and Peckham, M. (**2020**). Structure of the shutdown state of myosin-2. *Nature*, 588(7838):515–520.

Scarff, C. A., Fuller, M. J. G., Thompson, R. F. and Iadanza, M. G. (**2018**). Variations on Negative Stain Electron Microscopy Methods: Tools for Tackling Challenging Systems. *Journal of visualized experiments*, (132):57199.

Scheres, S. H. W. (**2012**). RELION: implementation of a Bayesian approach to cryo-EM structure determination. *Journal of structural biology*, 180(3):519–530.

Scheres, S. H. W. (**2016**). Processing of Structurally Heterogeneous Cryo-EM Data in RELION. *Methods in enzymology*, 579:125–157.

Scherzer, O. (**1949**). The theoretical resolution limit of the electron microscope. *Journal of Applied Physics*, 20:20–29.

Schmitz, S., Grainger, M., Howell, S., Calder, L. J., Gaeb, M., Pinder, J. C., Holder, A. A. and Veigel, C. (**2005**). Malaria parasite actin filaments are very short. *Journal of Molecular Biology*, 349(1):113–125.

Schmitz, S., Schaap, I. A. T., Kleinjung, J. et al. (**2010**). Malaria parasite actin polymerization and filament structure. *The Journal of biological chemistry*, 285(47):36577–36585.

Schröder, R. R. (**2020**). The Structure of Acto-Myosin. *Advances in experimental medicine and biology*, 1239:41–59.

Schur, F. K. M., Obr, M., Hagen, W. J. H. et al. (**2016**). An atomic model of HIV-1 capsid-SP1 reveals structures regulating assembly and maturation. *Science*, 353(6298):506–508.

Sellers, J. R. (**2000**). Myosins: a diverse superfamily. *Biochimica et biophysica acta*, 1496(1):3–22.

Shaaban, M., Chowdhury, S. and Nolen, B. J. (**2020**). Cryo-EM reveals the transition of Arp2/3 complex from inactive to nucleation-competent state. *Nature structural & molecular biology*, 27(11):1009–1016.

Shuman, H., Greenberg, M. J., Zwolak, A., Lin, T., Sindelar, C. V., Dominguez, R. and Ostap, E. M. (**2014**). A vertebrate myosin-I structure reveals unique insights into myosin mechanochemical tuning. *Proceedings of the National Academy of Sciences of the United States of America*, 111(6):2116–2121.

Sidén-Kiamos, I., Louis, C. and Matuschewski, K. (**2012**). Evidence for filamentous actin in ookinetes of a malarial parasite. *Molecular and biochemical parasitology*, 181(2):186–189.

Sievers, F., Wilm, A., Dineen, D. et al. (**2011**). Fast, scalable generation of high-quality protein multiple sequence alignments using Clustal Omega. *Molecular systems biology*, 7:539.

Sigworth, F. J., Doerschuk, P. C., Carazo, J. M. and Scheres, S. H. W. (**2010**). An introduction to maximum-likelihood methods in cryo-EM. *Methods in enzymology*, 482:263–294.

Skillman, K. M., Diraviyam, K., Khan, A., Tang, K., Sept, D. and Sibley, L. D. (**2011**). Evolutionarily divergent, unstable filamentous actin is essential for gliding motility in apicomplexan parasites. *PLoS pathogens*, 7(10):e1002280.

Škopić, M. K., Götte, K., Gramse, C., Dieter, M., Pospich, S., Raunser, S., Weberskirch, R. and Brunschweiger, A. (**2019**). Micellar Brønsted Acid Mediated Synthesis of DNA-Tagged Heterocycles. *Journal of the American Chemical Society*, 141(26):10546–10555.

Smart, O. S., Womack, T. O., Flensburg, C., Keller, P., Sharff, A., Paciorek, W., Vonrhein, C. and Bricogne, G. (**2011**). Grade Web Server version v1.103. Website: http://grade.globalphasing.org.

Smith, C. A. and Rayment, I. (**1996**). X-ray structure of the magnesium(II).ADP.vanadate complex of the Dictyostelium discoideum myosin motor domain to 1.9 Å resolution. *Biochemistry*, 35(17):5404–5417.

Smith, M. F. and Langmore, J. P. (**1992**). Quantitation of Molecular Densities by Cryo-electron Microscopy. *Journal of Molecular Biology*, 226(3):763–774.

Song, J., Patterson, R., Metlagel, Z. et al. (**2020**). A cryo-tomography-based volumetric model of the actin core of mouse vestibular hair cell stereocilia lacking plastin 1. *Journal of structural biology*, 210(1):107461.

Song, Y., DiMaio, F., Wang, R. Y.-R., Kim, D., Miles, C., Brunette, T., Thompson, J. and Baker, D. (**2013**). High-resolution comparative modeling with RosettaCM. *Structure*, 21(10):1735–1742.

Sorzano, C. O. S., Vargas, J., Otón, J. et al. (**2017**). A review of resolution measures and related aspects in 3D Electron Microscopy. *Progress in biophysics and molecular biology*, 124:1–30.

Spector, I., Shochet, N. R., Kashman, Y. and Groweiss, A. (**1983**). Latrunculins: novel marine toxins that disrupt microfilament organization in cultured cells. *Science*, 219(4584):493–495.

Stabrin, M., Schoenfeld, F., Wagner, T., Pospich, S., Gatsogiannis, C. and Raunser, S. (**2020**). TranSPHIRE: automated and feedback-optimized on-the-fly processing for cryo-EM. *Nature communications*, 11(1):5716.

Steinmetz, M. O., Stoffler, D., Müller, S. A. et al. (**1998**). Evaluating atomic models of F-actin with an undecagold-tagged phalloidin derivative. *Journal of Molecular Biology*, 276(1):1–6.

Stenoien, D. L. and Brady, S. T. (**1999**). *Molecular Motors: Kinesin, Dynein and Myosin*. Basic Neurochemistry: Molecular, Cellular and Medical Aspects. Lippincott-Raven, Philadelphia, 6th edition.

Straub, F. B. (**1942**). Actin. *Stud. Inst. Med. Chem. Univ. Szeged*, II:3–15.

Straub, F. B. and Feuer, G. (**1989**). Adenosinetriphosphate. The functional group of actin. 1950. *Biochimica et biophysica acta*, 1000:180–195.

Suarez, C., Roland, J., Boujemaa-Paterski, R. et al. (**2011**). Cofilin tunes the nucleotide state of actin filaments and severs at bare and decorated segment boundaries. *Current biology*, 21(10):862–868.

Sun, M., Rose, M. B., Ananthanarayanan, S. K., Jacobs, D. J. and Yengo, C. M. (**2008**). Characterization of the pre-force-generation state in the actomyosin cross-bridge cycle. *Proceedings of the National Academy of Sciences of the United States of America*, 105(25):8631–8636.

Sun, S., Han, Y., Paramasivam, S. et al. (**2012**). Solid-state NMR spectroscopy of protein complexes. *Methods in molecular biology*, 831:303–331.

Svitkina, T. (**2018**). The Actin Cytoskeleton and Actin-Based Motility. *Cold Spring Harbor Perspectives in Biology*, 10(1):a018267.

Sweeney, H. L. and Holzbaur, E. L. F. (**2018**). Motor Proteins. *Cold Spring Harbor Perspectives in Biology*, 10(5):a021931.

Sweeney, H. L., Houdusse, A. and Robert-Paganin, J. (**2020**). Myosin Structures. *Advances in experimental medicine and biology*, 1239:7–19.

Sweeney, H. L., Rosenfeld, S. S., Brown, F., Faust, L., Smith, J., Xing, J., Stein, L. A. and Sellers, J. R. (**1998**). Kinetic tuning of myosin via a flexible loop adjacent to the nucleotide binding pocket. *Journal of Biological Chemistry*, 273(11):6262–6270.

Takagi, Y., Homsher, E. E., Goldman, Y. E. and Shuman, H. (**2006**). Force generation in single conventional actomyosin complexes under high dynamic load. *Biophysical journal*, 90(4):1295–1307.

Tan, Y. Z., Baldwin, P. R., Davis, J. H., Williamson, J. R., Potter, C. S., Carragher, B. and Lyumkis, D. (**2017**). Addressing preferred specimen orientation in single-particle cryo-EM through tilting. *Nature methods*, 14(8):793–796.

Tanaka, K., Takeda, S., Mitsuoka, K., Oda, T., Kimura-Sakiyama, C., Maéda, Y. and Narita, A. (**2018**). Structural basis for cofilin binding and actin filament disassembly. *Nature communications*, 9(1):1860.

Tang, G., Peng, L., Baldwin, P. R., Mann, D. S., Jiang, W., Rees, I. and Ludtke, S. J. (**2007**). EMAN2: an extensible image processing suite for electron microscopy. *Journal of structural biology*, 157(1):38–46.

Tannert, R., Milroy, L.-G., Ellinger, B., Hu, T.-S., Arndt, H.-D. and Waldmann, H. (**2010**). Synthesis and structure-activity correlation of natural-product inspired cyclodepsipeptides stabilizing F-actin. *Journal of the American Chemical Society*, 132(9):3063–3077.

Taylor, E. W. (**1991**). Kinetic studies on the association and dissociation of myosin subfragment 1 and actin. *Journal of Biological Chemistry*, 266(1):294–302.

The Nobel Foundation (**1986**). The Nobel Prize in Physics. Nobel Media AB. Website: https://www.nobelprize.org/prizes/chemistry/2017/summary/. Accessed 23.11.2020.

The Nobel Foundation (**2017**). The Nobel Prize in Chemistry. Nobel Media AB. Website: https://www.nobelprize.org/prizes/chemistry/2017/summary/. Accessed 23.11.2020.

The UniProt Consortium (**2017**). UniProt: the universal protein knowledgebase. *Nucleic Acids Research*, 45(D1):D158–D169.

Thompson, A. R., Naber, N., Wilson, C., Cooke, R. and Thomas, D. D. (**2008**). Structural dynamics of the actomyosin complex probed by a bifunctional spin label that cross-links SH1 and SH2. *Biophysical journal*, 95(11):5238–5246.

Thon, F. (**1971**). *Phase contrast transfer function. Electron Microscopy in Material Sciences*. Academic Press, London.

Turoňová, B., Schur, F. K. M., Wan, W. and Briggs, J. A. G. (**2017**). Efficient 3D-CTF correction for cryo-electron tomography using NovaCTF improves subtomogram averaging resolution to 3.4 Å. *Journal of structural biology*, 199(3):187–195.

Vahokoski, J., Bhargav, S. P., Desfosses, A. et al. (**2014**). Structural differences explain diverse functions of Plasmodium actins. *PLoS pathogens*, 10(4):e1004091.

Vahokoski, J., Calder, L. J., Lopez, A. J., Molloy, J. E., Rosenthal, P. B. and Kursula, I. (**2020**). High-resolution structures of malaria parasite actomyosin and actin filaments. *bioRxiv*.

Vale, R. V. (**1996**). Switches, Latches, and Amplifiers: Common Themes of G Proteins and Molecular Motors. *The Journal of cell biology*, 135(2):291–302.

van den Ent, F., Izoré, T., Bharat, T. A., Johnson, C. M. and Löwe, J. (**2014**). Bacterial actin MreB forms antiparallel double filaments. *eLife*, 3:e02634.

van Heel, M. (**2020**). Information: to Harvest, to Have and to Hold *. *arXiv*.

van Heel, M. and Schatz, M. (**2017**). Reassessing the Revolution's Resolutions. *bioRxiv*.

Vanderwee, M. A., Humphrey, S. M., Gavin, J. B. and Armiger, L. C. (**1981**). Changes in the contractile state, fine structure and metabolism of cardiac muscle cells during the development of rigor mortis. *Virchows Archiv. B, Cell pathology including molecular pathology*, 35(2):159–167.

Vasenin, A. (**2010**). Toxic *Negombata magnifica* sponge at Shaab el Erg reef (Red Sea, Egypt). Creative Commons License. Website: https://de.wikipedia.org/wiki/Datei:Negombata_magnifica_at_Shaab_el_Erg.JPG. Accessed 11.12.2020.

Veigel, C., Schmitz, S., Wang, F. and Sellers, J. R. (**2005**). Load-dependent kinetics of myosin-V can explain its high processivity. *Nature cell biology*, 7(9):861–869.

Vig, A., Ohmacht, R., Jámbor, É., Bugyi, B., Nyitrai, M. and Hild, G. (**2011**). The effect of toxins on inorganic phosphate release during actin polymerization. *European biophysics journal*, 40(5):619–626.

Visegrády, B., Lorinczy, D., Hild, G., Somogyi, B. and Nyitrai, M. (**2004**). The effect of phalloidin and jasplakinolide on the flexibility and thermal stability of actin filaments. *FEBS letters*, 565(1-3):163–166.

Visegrády, B., Lorinczy, D., Hild, G., Somogyi, B. and Nyitrai, M. (**2005**). A simple model for the cooperative stabilisation of actin filaments by phalloidin and jasplakinolide. *FEBS letters*, 579(1):6–10.

Volkmann, N., Liu, H., Hazelwood, L., Krementsova, E. B., Lowey, S., Trybus, K. M. and Hanein, D. (**2005**). The structural basis of myosin V processive movement as revealed by electron cryomicroscopy. *Molecular cell*, 19(5):595–605.

von der Ecken, J. (**2016**). *Atomic insights into muscle contraction by transmission electron cryomicroscopy*. Ph.D. thesis, Technische Universität Dortmund.

von der Ecken, J., Heissler, S. M., Pathan-Chhatbar, S., Manstein, D. J. and Raunser, S. (**2016**). Cryo-EM structure of a human cytoplasmic actomyosin complex at near-atomic resolution. *Nature*, 534(7609):724–728.

von der Ecken, J., Müller, M., Lehman, W., Manstein, D. J., Penczek, P. A. and Raunser, S. (**2015**). Structure of the F-actin–tropomyosin complex. *Nature*, 519(7541):114–117.

Wade, R. and Frank, J. (**1977**). Electron microscopic transfer functions for partially coherent axial illumination and chromatic defocus spread. *Optik*, 49:81–92.

Wagner, T., Lusnig, L., Pospich, S., Stabrin, M., Schönfeld, F. and Raunser, S. (**2020**). Two particle-picking procedures for filamentous proteins: SPHIRE-crYOLO filament mode and SPHIRE-STRIPER. *Acta crystallographica. Section D, Structural biology*, 76(Pt 7):613–620.

Wagner, T., Merino, F., Stabrin, M. et al. (**2019**). SPHIRE-crYOLO is a fast and accurate fully automated particle picker for cryo-EM. *Communications biology*, 2:218.

Walker, J. E., Saraste, M., Runswick, M. J. and Gay, N. J. (**1982**). Distantly related sequences in the alpha- and beta-subunits of ATP synthase, myosin, kinases and other ATP-requiring enzymes and a common nucleotide binding fold. *The EMBO journal*, 1(8):945–951.

Walklate, J., Ujfalusi, Z. and Geeves, M. A. (**2016**). Myosin isoforms and the mechanochemical cross-bridge cycle. *The Journal of experimental biology*, 219(Pt 2):168–174.

Wang, L. and Sigworth, F. J. (**2006**). Cryo-EM and single particles. *Physiology*, 21:13–18.

Wang, R. Y.-R., Song, Y., Barad, B. A., Cheng, Y., Fraser, J. S. and DiMaio, F. (**2016**). Automated structure refinement of macromolecular assemblies from cryo-EM maps using Rosetta. *eLife*, 5:e17219.

Wang, S., Crevenna, A. H., Ugur, I. et al. (**2019**). Actin stabilizing compounds show specific biological effects due to their binding mode. *Scientific reports*, 9(1):9731.

Wang, Z., Grange, M., Wagner, T., Kho, A. L., Gautel, M. and Raunser, S. (**2020**). Molecular plasticity of the native mouse skeletal sarcomere revealed by cryo-ET. *bioRxiv*.

Waterhouse, A., Bertoni, M., Bienert, S. et al. (**2018**). SWISS-MODEL: homology modelling of protein structures and complexes. *Nucleic Acids Research*, 46(W1):W296–W303.

Webb, S. E., Fowler, R. E., O'Shaughnessy, C., Pinder, J. C., Dluzewski, A. R., Gratzer, W. B., Bannister, L. H. and Mitchell, G. H. (**1996**). Contractile protein system in the asexual stages of the malaria parasite Plasmodium falciparum. *Parasitology*, 112(Pt 5):451–457.

Wells, A. L., Lin, A. W., Chen, L. Q. et al. (**1999**). Myosin VI is an actin-based motor that moves backwards. *Nature*, 401(6752):505–508.

Wesseling, J. G., Smits, M. A. and Schoenmakers, J. G. (**1988**). Extremely diverged actin proteins in Plasmodium falciparum. *Molecular and biochemical parasitology*, 30(2):143–153.

Wesseling, J. G., Snijders, P. J., van Someren, P., Jansen, J., Smits, M. A. and Schoenmakers, J. G. (**1989**). Stage-specific expression and genomic organization of the actin genes of the malaria parasite Plasmodium falciparum. *Molecular and biochemical parasitology*, 35(2):167–176.

Wieland, T. and Govindan, V. M. (**1974**). Phallotoxins bind to actins. *FEBS letters*, 46(1):351–353.

Williams, D. B. and Carter, C. B. (**2009**). *Transmission Electron Microscopy - Part 1: Basics*. Springer, 2nd edition.

Woody, M. S., Greenberg, M. J., Barua, B., Winkelmann, D. A., Goldman, Y. E. and Ostap, E. M. (**2018**). Positive cardiac inotrope omecamtiv mecarbil activates muscle despite suppressing the myosin working stroke. *Nature communications*, 9(1):3838.

World Health Organization (**2020**). *World malaria report 2020: 20 years of global progress and challenges.* Geneva: World Health Organization;.

Wulf, S. F., Ropars, V., Fujita-Becker, S. et al. (**2016**). Force-producing ADP state of myosin bound to actin. *Proceedings of the National Academy of Sciences of the United States of America*, 113(13):E1844–52.

Wüthrich, K. (**1990**). Protein structure determination in solution by NMR spectroscopy. *The Journal of biological chemistry*, 265(36):22059–22062.

Xu, X.-P., Pokutta, S., Torres, M., Swift, M. F., Hanein, D., Volkmann, N. and Weis, W. I. (**2020**). Structural basis of αE-catenin-F-actin catch bond behavior. *eLife*, 9:e60878.

Yamada, Y., Namba, K. and Fujii, T. (**2020**). Cardiac muscle thin filament structures reveal calcium regulatory mechanism. *Nature communications*, 11(1):153.

Yang, S., Tiwari, P., Lee, K. H., Sato, O., Ikebe, M., Padrón, R. and Craig, R. (**2020**). Cryo-EM structure of the inhibited (10S) form of myosin II. *Nature*, 588(7838):521–525.

Yang, Y., Gourinath, S., Kovács, M. et al. (**2007**). Rigor-like structures from muscle myosins reveal key mechanical elements in the transduction pathways of this allosteric motor. *Structure*, 15(5):553–564.

Yang, Z., Fang, J., Chittuluru, J., Asturias, F. J. and Penczek, P. A. (**2012**). Iterative stable alignment and clustering of 2D transmission electron microscope images. *Structure*, 20(2):237–247.

Yarmola, E. G., Somasundaram, T., Boring, T. A., Spector, I. and Bubb, M. R. (**2000**). Actin-latrunculin A structure and function. Differential modulation of actin-binding protein function by latrunculin A. *Journal of Biological Chemistry*, 275(36):28120–28127.

Yengo, C. M., De La Cruz, E. M., Safer, D., Ostap, E. M. and Sweeney, H. L. (**2002**). Kinetic characterization of the weak binding states of myosin V. *Biochemistry*, 41(26):8508–8517.

Yildiz, A., Forkey, J. N., McKinney, S. A., Ha, T., Goldman, Y. E. and Selvin, P. R. (**2003**). Myosin V walks hand-over-hand: single fluorophore imaging with 1.5-nm localization. *Science*, 300(5628):2061–2065.

Yip, K. M., Fischer, N., Paknia, E., Chari, A. and Stark, H. (**2020**). Breaking the next Cryo-EM resolution barrier – Atomic resolution determination of proteins! *bioRxiv*.

Yount, R. G., Lawson, D. and Rayment, I. (**1995**). Is myosin a "back door" enzyme? *Biophysical journal*, 68(4 Suppl):44S–47S; discussion 47S–49S.

Zhang, K. (**2016**). Gctf: Real-time CTF determination and correction. *Journal of structural biology*, 193(1):1–12.

Zheng, S. Q., Palovcak, E., Armache, J.-P., Verba, K. A., Cheng, Y. and Agard, D. A. (**2017**). MotionCor2: anisotropic correction of beam-induced motion for improved cryo-electron microscopy. *Nature methods*, 14(4):331–332.

Zhong, E. D., Bepler, T., Berger, B. and Davis, J. H. (**2020**a). CryoDRGN: Reconstruction of heterogeneous structures from cryo-electron micrographs using neural networks. *bioRxiv*.

Zhong, E. D., Bepler, T., Davis, J. H. and Berger, B. (**2020**b). Reconstructing continous distributions of 3D protein structure from cryo-EM images. *arXiv*.

Zimmermann, D., Santos, A., Kovar, D. R. and Rock, R. S. (**2015**). Actin age orchestrates myosin-5 and myosin-6 run lengths. *Current biology*, 25(15):2057–2062.

Zimmet, A., Van Eeuwen, T., Boczkowska, M., Rebowski, G., Murakami, K. and Dominguez, R. (**2020**). Cryo-EM structure of NPF-bound human Arp2/3 complex and activation mechanism. *Science advances*, 6(23):eaaz7651.

Zivanov, J., Nakane, T., Forsberg, B. O., Kimanius, D., Hagen, W. J., Lindahl, E. and Scheres, S. H. (**2018**). New tools for automated high-resolution cryo-EM structure determination in RELION-3. *eLife*, 7:e42166.

Zivanov, J., Nakane, T. and Scheres, S. H. W. (**2019**). A Bayesian approach to beam-induced motion correction in cryo-EM single-particle analysis. *International Union of Crystallography Journal*, 6(Pt 1):5–17.

Zivanov, J., Nakane, T. and Scheres, S. H. W. (**2020**). Estimation of high-order aberrations and anisotropic magnification from cryo-EM data sets in RELION-3.1. *International Union of Crystallography Journal*, 7(Pt 2):253–267.

Publications

1. Pospich, S., Küllmer, F., Nasufovic, V., Funk, J., Belyy, A., Bieling, P., Arndt, H.-D. and Raunser, S. (**2021**). Cryo-EM resolves molecular recognition of an optojasp photoswitch bound to actin filaments in both switch states. *Angewandte Chemie (International ed. in English)*. doi: 10.1002/anie.202013193

2. Stabrin, M., Schoenfeld, F., Wagner, T., Pospich, S., Gatsogiannis, C. and Raunser, S. (**2020**). TranSPHIRE: automated and feedback-optimized on-the-fly processing for cryo-EM. *Nature communications*, 11(1):5716

3. Wagner, T., Lusnig, L., Pospich, S., Stabrin, M., Schönfeld, F. and Raunser, S. (**2020**). Two particle-picking procedures for filamentous proteins: SPHIRE-crYOLO filament mode and SPHIRE-STRIPER. *Acta crystallographica. Section D, Structural biology*, 76(Pt 7):613–620

4. Pospich, S., Merino, F. and Raunser, S. (**2020**). Structural Effects and Functional Implications of Phalloidin and Jasplakinolide Binding to Actin Filaments. *Structure*, 28(4):437–449.e5

5. Merino, F., Pospich, S. and Raunser, S. (**2019**). Towards a structural understanding of the remodeling of the actin cytoskeleton. *Seminars in cell & developmental biology*, 102:51–64

6. Škopić, M. K., Götte, K., Gramse, C., Dieter, M., Pospich, S., Raunser, S., Weberskirch, R. and Brunschweiger, A. (**2019**). Micellar Brønsted Acid Mediated Synthesis of DNA-Tagged Heterocycles. *Journal of the American Chemical Society*, 141(26):10546–10555

7. Pospich, S. and Raunser, S. (**2018**). Single particle cryo-EM-an optimal tool to study cytoskeletal proteins. *Current opinion in structural biology*, 52:16–24

8. Merino, F., Pospich, S., Funk, J., Wagner, T., Küllmer, F., Arndt, H.-D., Bieling, P. and Raunser, S. (**2018**). Structural transitions of F-actin upon ATP hydrolysis at near-atomic resolution revealed by cryo-EM. *Nature structural & molecular biology*, 25(6):528–537
Shared first authorship: Merino, F. and Pospich, S.

9. Pospich, S. and Raunser, S. (**2017**). The molecular basis of Alzheimer's plaques. *Science*, 358(6359):45–46

10. Pospich, S., Kumpula, E.-P., von der Ecken, J., Vahokoski, J., Kursula, I. and Raunser, S. (**2017**). Near-atomic structure of jasplakinolide-stabilized malaria parasite F-actin reveals the structural basis of filament instability. *Proceedings of the National Academy of Sciences of the United States of America*, 114(40):10636–10641

Conference contributions

Jul 2019 Active participation
69th Lindau Nobel Laureate Meeting dedicated to Physics

Mar 2019 Short talk and poster presentation
'Structural transitions of F-actin at near- atomic resolution - Effects of jasplakinolide and phalloidin'
16th Alpbach Motors Workshop, 'Myosin & muscle, and other motors'

Nov 2018 Chair and poster presentation
'Structure of F-actin from Plasmodium falciparum'
7th IMPRS-CMB Student Symposium, 'Unravelling cellular intricacies'

Sep 2018 Talk and poster presentation
'Species specific features of F-actin and its structural transition upon ATP hydrolysis characterized by cryo-EM'
7th Murnau Conference - New Frontiers in Structural Biology

Sep 2017 Short talk and poster presentation
'Cryo-EM structure of JAS-stabilized F-actin from malaria parasite reveals structural basis of filament instability'
Internat. Herbsttagung der Gesellschaft für Biochemie und Molekularbiologie

Jun 2017 Poster presentation
'Cryo-EM structure of JAS-stabilized F-actin from malaria parasite reveals structural basis of filament instability'
Gordon Research Conference - Three Dimensional Electron Microscopy

Oct 2016 Poster presentation
'Structure of F-actin from Plasmodium falciparum'
6th IMPRS-CMB Student Symposium, 'Interactions on all levels'

Mar 2016 Poster presentation
'Structure of F-actin from Plasmodium falciparum'
15th Alpbach Motors Workshop, 'Myosin & muscle, and other motors'

Acknowledgments

First and foremost, I would like to thank Prof. Dr. Stefan Raunser and Prof. Dr. Metin Tolan for jointly enabling me to conduct this interdisciplinary dissertation at the Max Planck Institute of Molecular Physiology. Prof. Raunser has not only given me the opportunity to learn the strings of structural biology and the associated “new world“, but has also supported me throughout my thesis, thereby promoting the successful completion of many interesting research projects. In particular, I would like to thank him for his continuous trust, even beyond the time of my doctorate. Thanks are also due to Prof. Dr. Tolan for his willingness to supervise an external thesis project as well as his continuous interest in my work.

My thanks also go to many dear colleagues, who supported me during my time at the MPI, not only professionally, but also as friends. Especially, the “actin team“ consisting of Dr. Felipe Merino, Dr. Alexander Belyy and Dr. Julian von der Ecken, but also our in-house software developers Markus Stabrin, Dr. Thorsten Wagner and Dr. Tapu Shaikh contributed to the successful completion of my work. I would also like to thank Dr. Oliver Hofnagel, Dr. Daniel Prumbaum, Nathalie Bleimling, Sandra Bergbrede and Karin Vogel-Bachmayr for their constant support at the microscopes and in the lab. Furthermore, I want to thank Prof. Dr. Christos Gatsogiannis and Prof. Dr Roger Goody for their interest in my work and many useful suggestions. For their open office door and the friendly atmosphere, my thanks go to the Hernandez team, which made me feel more than welcome. Big thanks for proofreading go to “Eric“ Zhexin Wang, Dr. Sebastian Tacke, Dr. Alexander Belyy, Dr. Evelyn Schubert, Pascal Lill, Dr. Tapu Shaikh and Markus Stabrin. Finally, I would like to thank all my colleagues in Department 3 for their open ear and readiness to help. Over the years many of you have become real friends, who have sweetened my everyday life and also helped me through difficult times.

I would also like to thank the IMPRS for their commitment and especially Christa Hornemann, who always stood by me with a good advice. Eventually, I want to thank the *Studienstiftung des deutschen Volkes* for the financial and idealistic support of my doctorate.

Moreover, my thanks go to my collaborators coming from the labs of Prof. Dr. Inari Kursula, Dr. Peter Bieling, Prof. Dr. Hans-Dieter Arndt, Dr. Andreas Brunschweiger, Prof. Dr. Anne Houdusse and Prof. Dr. Lee Sweeney, who contributed greatly to the success of my thesis research projects.

Zum Abschluss möchte ich mich herzlich bei meiner Familie und meinem Freund bedanken. Danke für eure Unterstützung, euer Verständis und euren Glauben an mich! Und nicht zuletzt, Danke für viele “late night cooking sessions“ und die unzähligen “custom-demand scripte“.

5 Appendix

5.1 Supplementary information

5.1.1 Structural characterization of actomyosin nucleotide states

The following section includes supplementary items such as figures and tables supporting the analysis and discussion of the actomyosin structures presented in this thesis.

	Central 3er/2er	Central 1er (subtracted)	Class 1	Class 2	Class 4
Microscopy					
Microscope	Titan Krios (Cs 2.7 mm)				
Voltage [kV]	300				
Camera	K2 (super resolution)				
Energy filter slit width [eV]	20				
Pixel size [Å]	1.06				
Total electron dose [e/Å^2]	79				
Exposure time [s]	15				
Frames per movie	40				
Final electron dose [e/Å^2]	79, Dose weighted				
Defocus range [µm]	0.5 – 3.0				
Number of images[a]	2,304 (3,623)				
3-D refinement statistics					
Number of helical segments	299,784	299,784	94,077	102,818	81,757
Resolution [Å]	3.2	3.3	3.5	3.5	3.6
Map sharpening factor [Å^2]	-81	-80	-89	-89	-87
Atomic model statistics					
Non-hydrogen atoms	23,288	10,148	10,139	10,139	10,139
Cross correlation masked	0.83	0.86	0.83	0.82	0.81
Molprobity score	1.28	1.18	1.24	1.25	1.31
Clashscore	5.25	3.97	4.66	4.81	5.75
EMRinger score[b]	3.14 / 3.39	3.41 / 3.10	2.97 / 3.00	3.53 / 3.00	3.01 / 3.06
Bond RMSD [Å]	0.005	0.014	0.005	0.005	0.005
Angle RMSD [°]	0.84	1.14	0.80	0.84	0.82
Rotamer outliers [%]	0.04	0.00	0.00	0.00	0.00
Ramachandran favored [%]	99.86	99.84	99.60	99.76	99.76
Ramachandran outliers [%]	0.00	0.00	0.00	0.00	0.00
CaBLAM outliers [%]	0.8	0.9	0.9	0.9	0.8

[a]In parenthesis is the initial number of images
[b]Values correspond to score against the post refined map used for real space refinement / a map filtered to local resolution

Figure S1: Data collection, refinement and model building statistics of the rigor actomyosin complex, consisting of aged F-actin-PHD and myosin in the rigor state. The central 3er/2er and central 1er maps represent average structures of a complex consisting of three actins and two myosins (central 3er/2er) or one actomyosin molecule (central 1er), respectively. The class maps are calculated from subsets identified by 3D classification. See Supplementary Figure S2 for details.

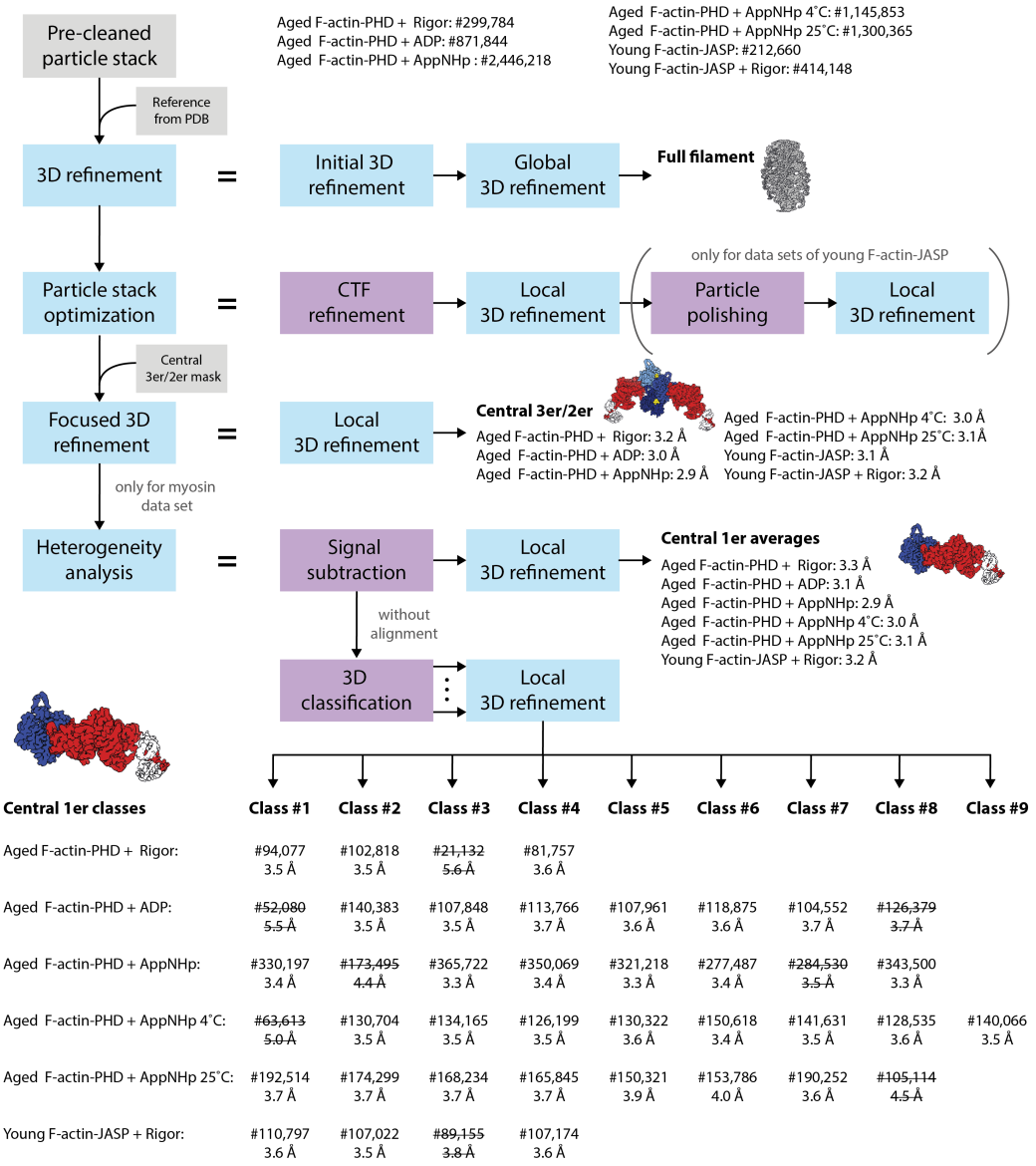

Figure S2: Overview of the processing pipeline used to process the actomyosin complexes. Auto-picked particle stacks were initially pre-cleaned by 2D classification (number of particles stated) and afterwards 3D refinement without a mask against a reference generated from an atomic model of actomyosin (PDB, accession code: 5JLH, von der Ecken et al. (2016)). The resulting 3D density map was used as a reference in a subsequent masked 3D refinement resulting in a first structure of the full actomyosin filament. Based on this, the particle stacks were optimized by CTF refinement and in case of the young F-actin-JASP data sets by particle polishing, followed by a local 3D refinement. By applying a mask including only the central three actin and two myosin subunits (central 3er/2er) the refinement was subsequently focused on the central section of the filament (resolutions stated). To account for the structural heterogeneity observed in actomyosin data sets, a hetereogeinity analysis was performed. Here, particles were initially signal subtracted to remove everything but the central actomyosin molecule (central 1er). This particles were then locally 3D refined to produce average structures (resolutions stated). In addition, signal subtracted particles were 3D classified without alignment to distinct conformations. The number of classes was optimized to result in a maximum number of high-resolution 3D classes. Subsets were finally locally 3D refined resulting in 18 high-resolution structures of the actomyosin complex (final particle numbers and resolutions stated). Classes of insufficient quality are struck through and omitted.

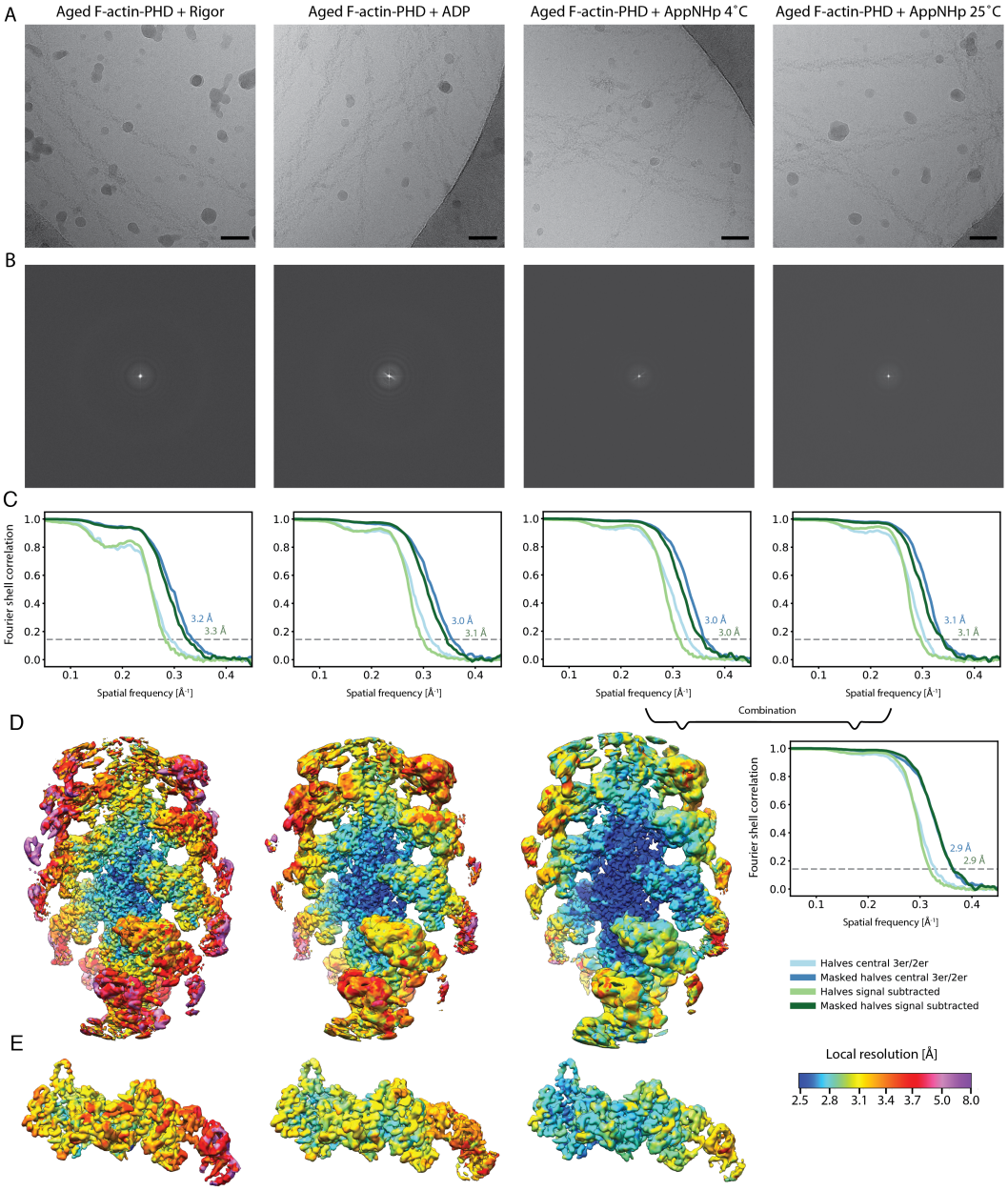

Figure S3: Overview of the cryo-EM data and resolution for F-actin-PHD-aged in complex with myosin in the rigor, ADP and AppNHp state. **(A)** Representative micrographs at -1.3 µm defocus and **(B)** their power spectra. **(C)** Fourier shell correlation (FSC) curves for masked (darker shade, with resolution values) and unmasked (halves, ligher shade) maps including either three actin subunits and two myosin molecules (3er/2er, shades of blue, also see Figure S2) or one actomyosin molecule (signal subtracted, central 1er, shades of green) are shown. **(D)** Color-coded local resolution of full filaments and **(E)** central signal subtracted actomyosin molecules of all three states. Note that the two AppNHp data sets (4 ° and 25 °) were combined to increase the overall resolution. Scale bar 500 Å.

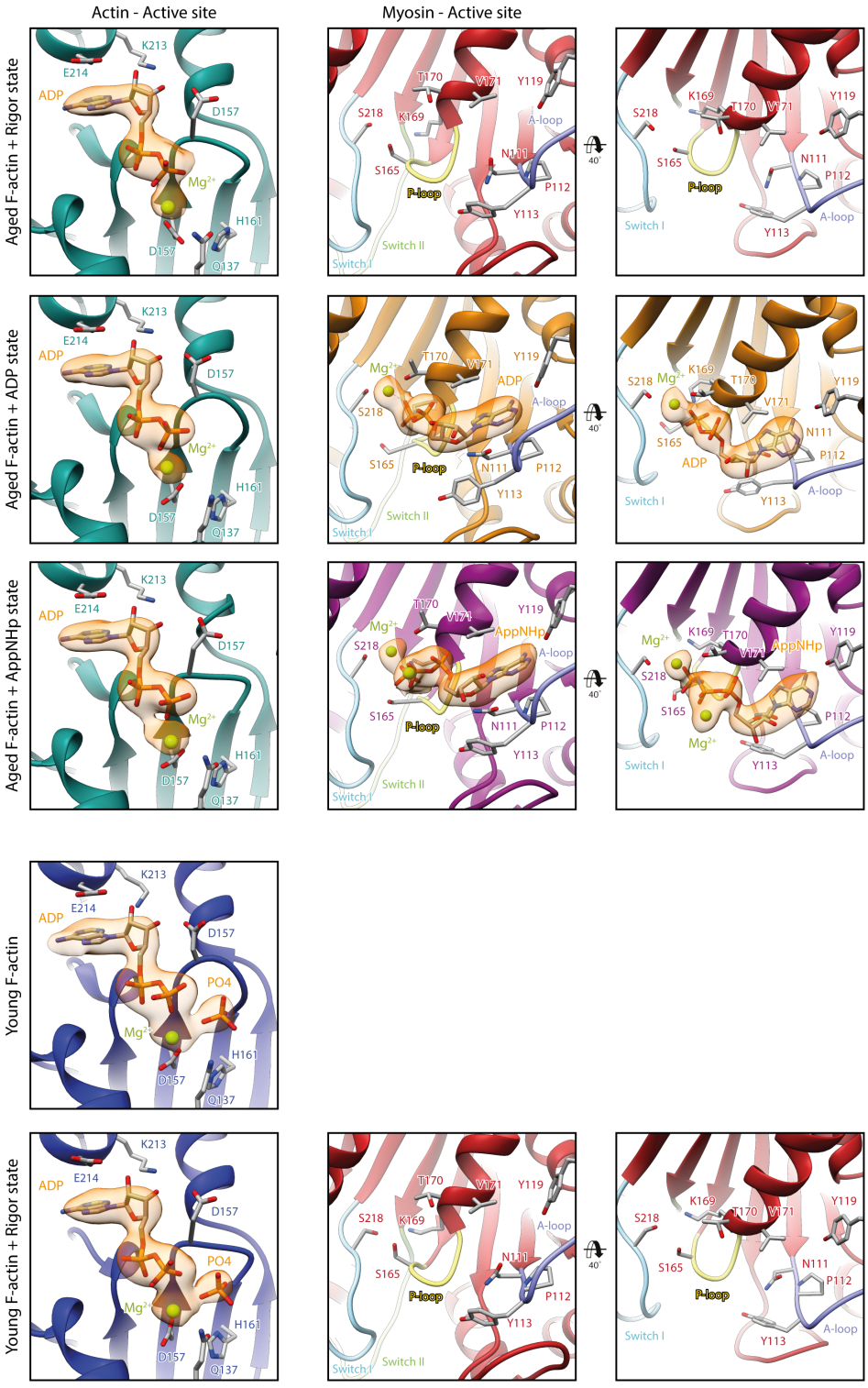

Figure S4: Close-up views of the active site of actin (left column) and myosin (middle and right column) of all actomyosin complexes solved in this thesis. Ribbons are color-coded according to their state (Actin aged-PHD: sea green, young-JASP: blue and myosin rigor: red, ADP: orange and AppNHp: purple). Side chains and nucleotides are colored by heteroatom. Superimposed electron density maps of nucleotides are shown in transparent orange. Key loops of the myosin active site are labeled and highlighted in pastel colors (P-loop: yellow, switch I: blue, switch II: green and A-loop: purple). Densities clearly support the presence of P_i in JASP-stabilized F-actin and coordinating Mg^{2+} ions in all occupied active sites. Interestingly, there is density for two Mg^{2+} ions in case of AppNHp, one next to the γ-phosphate and one in between the α- and β-phosphate.

	Central 3er/2er	Central 1er (subtracted)	Class 2	Class 3	Class 4	Class 5	Class 6	Class 7
Microscopy								
Microscope	Titan Krios (Cs 2.7 mm)							
Voltage [kV]	300							
Camera	K2 (super resolution)							
Energy filter slit width [eV]	20							
Pixel size [Å]	1.06							
Total electron dose [e/Å^2]	82							
Exposure time [s]	15							
Frames per movie	40							
Final electron dose [e/Å^2]	82, Dose weighted							
Defocus range [µm]	0.3 – 3.2							
Number of images[a]	2,304 (4,571)							
3-D refinement statistics								
Number of helical segments	871,844	871,844	140,383	107,848	113,766	107,961	118,875	104,552
Resolution [Å]	3.0	3.1	3.5	3.5	3.7	3.6	3.6	3.7
Map sharpening factor [Å^2]	-60	-60	-78	-78	-94	-86	-83	-88
Atomic model statistics								
Non-hydrogen atoms	23,334	10,171	10,149	10,149	10,086	10,066	10,113	10,139
Cross correlation masked	0.85	0.83	0.83	0.83	0.80	0.82	0.83	0.80
Molprobity score	1.35	1.23	1.28	1.36	1.38	1.36	1.35	1.39
Clashscore	6.28	4.55	5.31	6.45	6.94	6.50	6.37	7.15
EMRinger score[b]	3.42 / 2.83	3.56 / 3.36	3.44 / 3.49	2.83 / 2.92	2.67 / 2.23	2.99 / 2.92	2.92 / 2.52	2.68 / 2.38
Bond RMSD [Å]	0.012	0.005	0.004	0.005	0.005	0.004	0.006	0.008
Angle RMSD [°]	1.07	0.83	0.85	0.89	0.92	0.88	0.93	1.06
Rotamer outliers [%]	0.04	0.09	0.09	0.09	0.09	0.09	0.09	0.09
Ramachandran favored [%]	99.65	99.68	99.76	99.68	99.84	99.84	99.84	99.84
Ramachandran outliers [%]	0.00	0.00	0.00	0.00	0.00	0.00	0.00	0.00
CaBLAM outliers [%]	0.7	0.9	1.1	1.3	1.2	1.0	0.8	1.4

[a]In parenthesis is the initial number of images
[b]Values correspond to score against the post refined map used for real space refinement / a map filtered to local resolution

Figure S5: Data collection, refinement and model building statistics of the ADP actomyosin complex, consisting of aged F-actin-PHD and myosin in the ADP state. See figure legend of Supplementary Figure S1 for details.

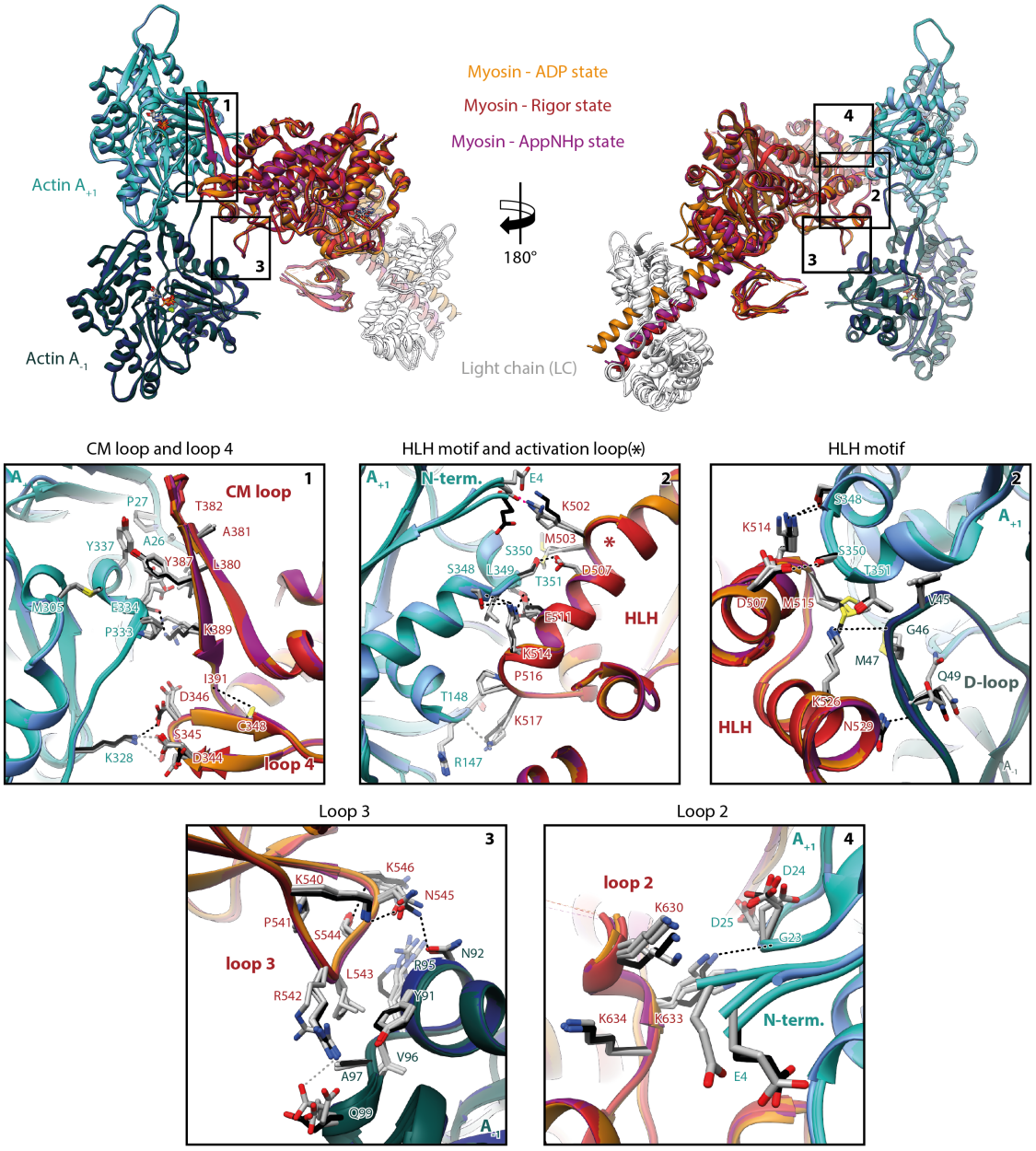

Figure S6: Superposition of atomic models of all three nucleotide states (rigor: red, ADP: orange and AppNHp: purple) of the actomyosin complex, illustrating the conservation of interactions with F-actin. **(Top)** Front and back view of the central myosin molecule and the two actin subunits (shades of green and blue, A_{+1} and A_{-1}) it is bound to. Black boxes indicate the location of close-up views shown below. **(Bottom)** Inserts showing close-up views of all actin-myosin interfaces including the cardiomyopathy (CM) loop, helix-loop-helix (HLH) motif, loops 2-4 and the activation loop (highlighted by an asterisk). Side chains of key residues are displayed and labeled for all states (rigor: black, ADP and AppNHp: gray). Dashed lines indicate hydrogen bonds predicted for the rigor (black) or ADP/AppNHp state (gray).

	Central 3er/2er	Central 1er (subtracted)	Class 2	Class 3	Class 4	Class 5	Class 6	Class 7	Class 8	Class 9
Microscopy										
Microscope	Titan Krios (Cs-corrected)									
Voltage [kV]	300									
Camera	K2 (super resolution)									
Energy filter slit width [eV]	20									
Pixel size [Å]	1.10									
Total electron dose [e/Å^2]	81									
Exposure time [s]	15									
Frames per movie	40									
Final electron dose [e/Å^2]	81, Dose weighted									
Defocus range [μm]	0.3 – 3.0									
Number of images[a]	5,858 (7,121)									
3-D refinement statistics										
Number of helical segments	1,145,853	1,145,853	130,704	134,165	126,199	130,322	150,618	141,631	128,535	140,066
Resolution [Å]	3.0	3.0	3.5	3.5	3.5	3.6	3.4	3.5	3.6	3.5
Map sharpening factor [Å^2]	-88	-109	-80	-85	-77	-86	-76	-87	-84	-78

[a]In parenthesis is the initial number of images

Figure S7: Data collection and refinement statistics of the AppNHp actomyosin complex, consisting of aged F-actin-PHD and myosin in the AppNHp state (4 °C). See figure legend of Supplementary Figure S1 for details.

	Central 3er/2er	Central 1er (subtracted)	Class 1	Class 2	Class 3	Class 4	Class 5	Class 6	Class 7
Microscopy									
Microscope	Titan Krios (Cs-corrected)								
Voltage [kV]	300								
Camera	K2 (super resolution)								
Energy filter slit width [eV]	20								
Pixel size [Å]	1.10								
Total electron dose [e/Å^2]	81								
Exposure time [s]	15								
Frames per movie	40								
Final electron dose [e/Å^2]	81, Dose weighted								
Defocus range [μm]	0.3 – 3.0								
Number of images[a]	6,617 (7,023)								
3-D refinement statistics									
Number of helical segments	1,300,365	1,300,365	192,514	174,299	168,234	165,845	150,321	153,786	190,252
Resolution [Å]	3.1	3.1	3.7	3.7	3.7	3.7	3.9	4.0	3.6
Map sharpening factor [Å^2]	-114	-142	-121	-115	-112	-125	-138	-144	-109

[a]In parenthesis is the initial number of images

Figure S8: Data collection and refinement statistics of the AppNHp actomyosin complex, consisting of aged F-actin-PHD and myosin in the AppNHp state (25 °C). See figure legend of Supplementary Figure S1 for details.

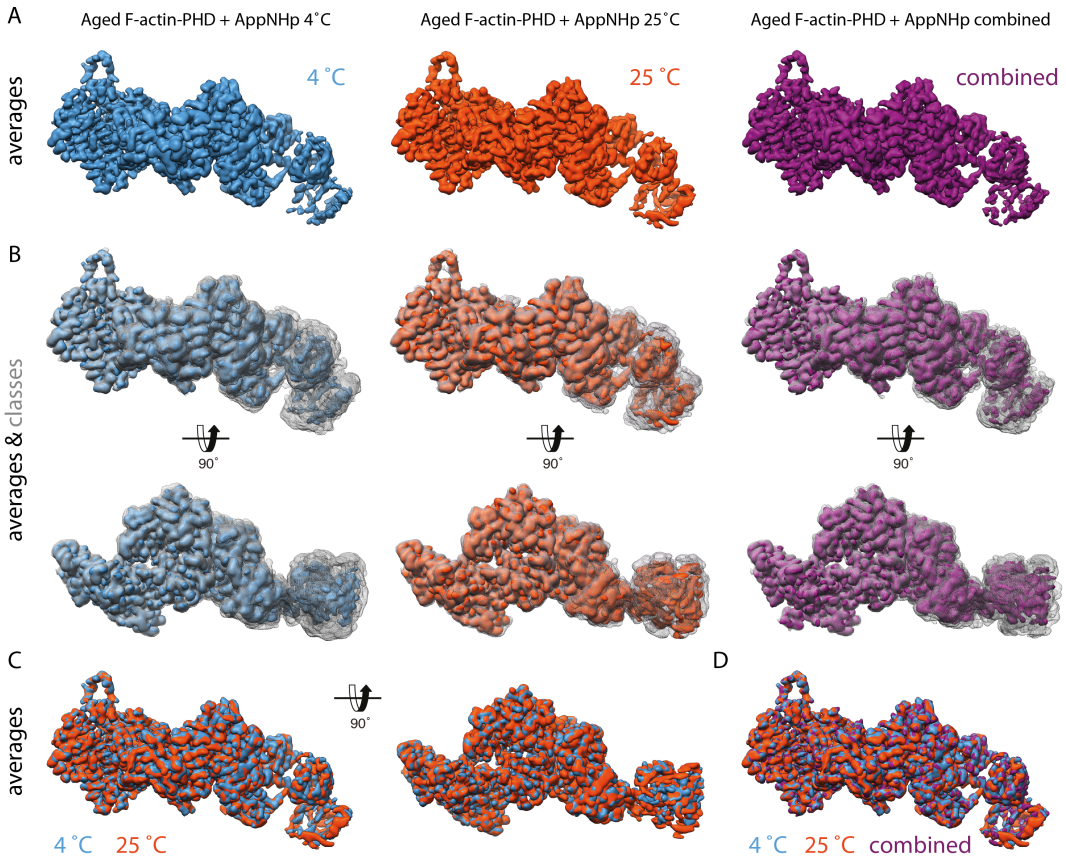

Figure S9: Illustration of the similarity and combination of the AppNHp data sets. **(A)** Comparison of the central 1er electron density map of the 4 °C (blue), 25 °C (red) and combined (purple) AppNHp data set. **(B)** Side and bottom-view of averages shown in (A) and corresponding 3D class averages (transparent grey), illustrating that all data sets span the same conformational space. **(C)** Superposition of average structures from the 4 °C (blue) and 25 °C (red) data sets, highlighting their similarity. **(D)** Superposition of all average structures.

	Central 3er/2er	Central 1er (subtracted)	Class 1	Class 3	Class 4	Class 5	Class 6	Class 8
Microscopy								
Microscope	Titan Krios (Cs-corrected)							
Voltage [kV]	300							
Camera	K2 (super resolution)							
Energy filter slit width [eV]	20							
Pixel size [Å]	1.10							
Total electron dose [e/Å^2]	81							
Exposure time [s]	15							
Frames per movie	40							
Final electron dose [e/Å^2]	81, Dose weighted							
Defocus range [µm]	0.3 – 3.0							
Number of images[a]	12,475							
3-D refinement statistics								
Number of helical segments	2,446,218	2,446,218	330,197	365,722	350,069	321,218	277,487	343,500
Resolution [Å]	2.9	2.9	3.4	3.3	3.4	3.3	3.4	3.3
Map sharpening factor [Å^2]	-80	-100	-113	-106	-114	-106	-111	-104
Atomic model statistics								
Non-hydrogen atoms	23,370	10,189	10,125	10,189	10,154	10,189	10,085	10,189
Cross correlation masked	0.85	0.84	0.84	0.86	0.85	0.85	0.83	0.84
Molprobity score	1.25	1.15	1.17	1.24	1.20	1.26	1.37	1.18
Clashscore	4.76	3.56	3.78	4.64	4.12	4.99	6.74	3.95
EMRinger score[b]	3.29 / 3.45	3.82 / 3.40	3.35 / 3.07	3.58 / 3.45	3.18 / 3.35	2.94 / 2.97	3.01 / 3.01	3.09 / 2.88
Bond RMSD [Å]	0.004	0.012	0.009	0.014	0.009	0.014	0.009	0.005
Angle RMSD [°]	0.78	1.01	0.96	1.15	0.97	1.14	1.08	0.81
Rotamer outliers [%]	0.08	0.09	0.09	0.09	0.09	0.09	0.09	0.09
Ramachandran favored [%]	99.86	99.84	99.84	99.84	99.84	99.84	99.84	99.84
Ramachandran outliers [%]	0.00	0.00	0.00	0.00	0.00	0.00	0.00	0.00
CaBLAM outliers [%]	1.1	1.2	1.1	1.1	1.2	1.2	1.4	0.7

[a]Combined from two data sets (4 ˚C and 25 ˚C)
[b]Values correspond to score against the post refined map used for real space refinement / a map filtered to local resolution

Figure S10: Data collection, refinement and model building statistics of the AppNHp actomyosin complex, consisting of aged F-actin-PHD and myosin in the AppNHp state (combined). See figure legend of Supplementary Figure S1 for details.

Helical symmetry	**Rise [Å]**	**Twist [˚]**	**Pixel size [Å]**
Aged F-actin-PHD + Rigor	27.82 +/- 0.02	167.27 +/- 0.02	1.06
Aged F-actin-PHD + ADP	27.81 +/- 0.02	167.32 +/- 0.02	1.06
Aged F-actin-PHD + AppNHp	27.77 +/- 0.02	167.32 +/- 0.02	1.10
Aged F-actin-PHD (PDB: 6T20)	27.59 +/- 0.02	166.9 +/- 0.1	1.14
Young F-actin-JASP	27.85 +/- 0.08	166.87 +/- 0.02	1.10
Young F-actin-JASP + Rigor	27.72 +/- 0.01	167.06 +/- 0.02	1.10
Young F-actin-JASP (PDB: 5OOD)	27.39	166.41	1.09

Figure S11: Overview of helical symmetry parameters of aged and young actomyosin complexes. For a direct comparison, the parameters of aged F-actin-PHD (PDB: 6T20, Pospich et al. (2020)) and young F-actin-JASP (PDB: 5OOD, Merino et al. (2018)) are shown alongside. Differences in both the helical rise and twist can be readily explained by errors of pixel size, which is not identical for all data sets. Helical parameters were estimated from the atomic model of five consecutive subunits independently fitted to the map, see Pospich et al. (2017) for details. Inaccuracies in the fitting of atomic models, required to determine the symmetry parameters, can also give rise to small deviations. To make results more comparable, only actin molecules were considered during fitting.

	Actin only 3er/2er	Central 3er/2er	Central 1er (subtracted)	Class 1	Class 2	Class 4
Microscopy						
Microscope	Titan Krios (Cs-corrected)					
Voltage [kV]	300					
Camera	K2 (super resolution)					
Energy filter slit width [eV]	20					
Pixel size [Å]	1.10					
Total electron dose [e/Å^2]	80					
Exposure time [s]	15					
Frames per movie	40					
Final electron dose [e/Å^2]	Polished particles					
Defocus range [µm]	0.3 – 2.9			0.3-3.0		
Number of images[a]	936 (1,064)			2,970 (3,336)		
3-D refinement statistics						
Number of helical segments	212,660	414,148	414,148	110,797	107,022	107,174
Resolution [Å]	3.1	3.2	3.2	3.6	3.5	3.6
Map sharpening factor [Å^2]	-56	-83	-50	-55	-49	-54
Atomic model statistics						
Non-hydrogen atoms	8940	23,278	10,149	10,169	10,169	10,156
Cross correlation masked	0.81	0.84	0.83	0.84	0.83	0.83
Molprobity score	1.27	1.29	1.15	1.24	1.26	1.23
Clashscore	5.11	5.46	3.62	4.66	4.91	4.57
EMRinger score[b]	3.11/ 3.08	2.92 / 2.66	3.11 / 2.92	2.89 / 2.96	2.99 / 3.39	2.88 / 2.55
Bond RMSD [Å]	0.004	0.004	0.009	0.005	0.003	0.004
Angle RMSD [°]	0.915	0.780	0.950	0.836	0.807	0.835
Rotamer outliers [%]	0.00	0.00	0.00	0.00	0.00	0.00
Ramachandran favored [%]	100.00	99.86	99.84	99.84	99.84	99.84
Ramachandran outliers [%]	0.00	0.00	0.00	0.00	0.00	0.00
CaBLAM outliers [%]	0.27	0.75	0.90	0.81	0.65	0.49

[a]In parenthesis is the initial number of images
[b]Values correspond to score against the post refined map used for real space refinement / a map filtered to local resolution

Figure S12: Data collection, refinement and model building statistics of the rigor actomyosin complex, consisting of young F-actin-JASP and myosin in the rigor state. See figure legend of Supplementary Figure S1 for details.

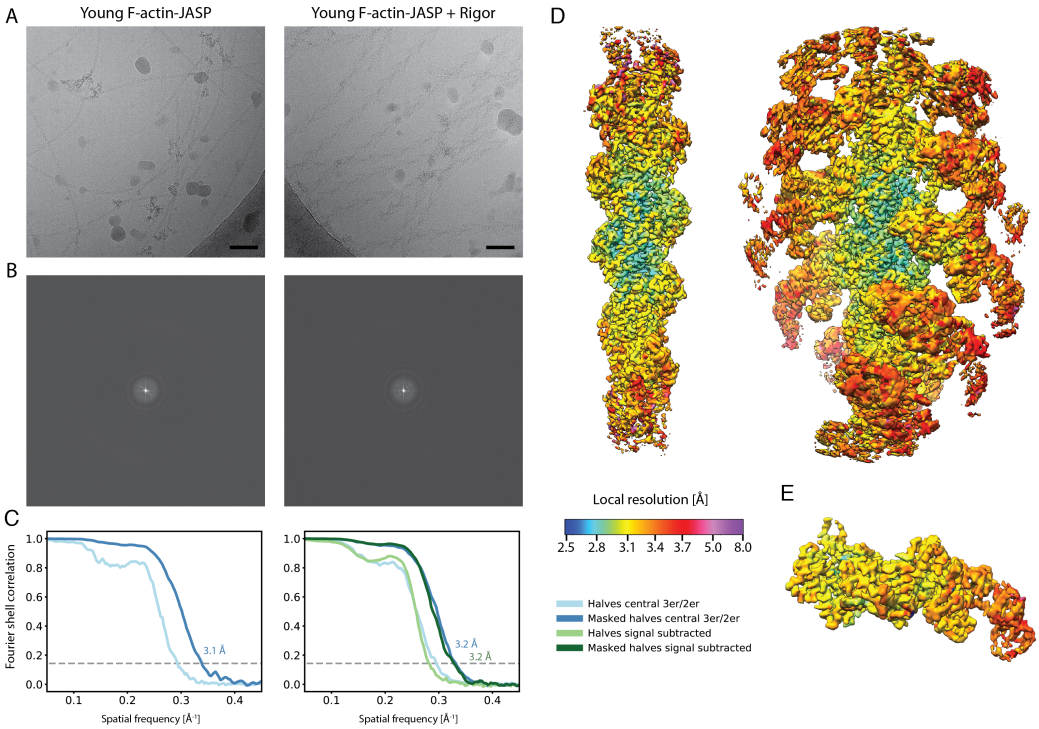

Figure S13: Overview of the cryo-EM data and resolution for young F-actin-JASP alone and in complex with myosin in the rigor state. **(A)** Representative micrographs at -1.3 µm defocus and **(B)** their power spectra. **(C)** Fourier shell correlation (FSC) curves for masked (darker shade, with resolution values) and unmasked (halves, ligher shade) maps. For bare actin only the FSC of a map covering the central three subunits is shown (shades of blue), while for actomyosin either the FSC for three actin subunits and two myosin molecules (3er/2er, shades of blue, also see Figure S2) or for one actomyosin molecule (signal subtracted, central 1er, shades of green) is shown. **(D)** Color-coded local resolution of full filaments for both data sets and of the **(E)** central signal subtracted subunit of the actomyosin complex. Note that signal subtraction was only performed for actomyosin complexes, also see Figure S2. Scale bar 500 Å.